

Electrodeposition and reversibility of Lithium metal
in liquid electrolytes

A Dissertation

Presented to the Faculty of the Graduate School
of Cornell University

In Partial Fulfillment of the Requirements for the Degree of
Doctor of Philosophy

by

Prayag Biswal

May 2021

© 2021 Prayag Biswal

Electrodeposition and reversibility of Lithium metal in liquid electrolytes

Prayag Biswal, Ph. D.

Cornell University 2021

The 21st century has witnessed dramatic changes in the energy harvesting and supply scenario with an appreciable transition from non-renewable energy resources (fossil fuels) to renewable energy resources (wind, solar, hydroelectricity, geothermal), brought on by global efforts to battle climate change associated with elevated greenhouse emissions. This energy transition to meet the world's growing needs for electricity, heating, cooling, and power for transport in a sustainable way is widely considered to be one of the greatest challenges facing humanity in this century. The transition is largely enabled by improvements in generation and storage technologies for energy harvested from renewable, but inherently intermittent supplies. As most of renewable energy technologies provide electricity, development of fast, efficient, and safe electrical energy storage techniques is crucial for further progress. Moreover, growing needs for smaller, lighter, more powerful portable electronic devices, and more powerful electric vehicles suitable for long-range transportation have further fostered the demand for dispatchable and efficient electrical energy storage. In this regard, rechargeable batteries composed of reactive metal anodes such as Lithium, have garnered interest in recent years, primarily due to their potential to significantly improve the energy density compared to current state-of-art Lithium-ion batteries. However, the

commercialization of these Lithium metal batteries has received steady challenges from concerns of short-circuiting and fire hazard, brought on by uneven (dendritic, tree-like) electrodeposition of the reactive metal during several charge-discharge cycles of the batteries. The dendritic electrodeposition is thought to be facilitated by an interplay of morphological and chemical instabilities at the Lithium metal anode during battery charge. The work reported in this thesis utilizes theoretical and experimental tools to fundamentally understand the nature of these instabilities at the initiation step and to thereby develop rational designs of Li anode-electrolyte interphases that delay or eliminate the instabilities at their source. Towards this goal, the physics of nucleation and early-stage growth of Lithium electrodeposits is firstly interrogated and is shown to be consistent across different liquid electrolyte chemistries. Next, based on an understanding of nucleation of Li in liquid electrolytes, certain halide rich electrolytes hypothesized to enhance the surface energetics of Lithium electrodeposition are studied to evaluate their influence on the morphology and chemistry of Lithium electrodeposits. It is shown that these electrolytes do in fact eliminate the morphological and chemical instabilities at the initiation step, and the fine control achieved in physical-chemical features of the Lithium electrodeposits can be translated to achieve greater control of electrodeposit morphology at later stages of electroplating. Finally, custom blends of halide rich electrolytes with beneficial additives are developed to eliminate the instabilities and preserve the therein developed physical-chemical features of Lithium electrodeposits through the deep cycling of Lithium metal anodes. Liquid electrolyte blends developed through rational choice of electrolyte chemistry are shown to improve the electrochemical performance of Lithium metal batteries.

BIOGRAPHICAL SKETCH

Prayag Biswal was born and brought up in Rourkela, a cosmopolitan city in western Odisha, India. He did his schooling at St. Pauls school in Rourkela, where he developed an interest in basic sciences and mathematics. His parents did a great job at fostering the developed interests by connecting him with teachers who are equally passionate. As the interests were further cultivated, they developed into hobbies which he cherishes for rest of his life. The decision to pursue a career in research and academia was consolidated by then.

Later, he received undergrad education in chemical engineering at Indian Institute of Technology (IIT) Kharagpur in India from 2013 to 2017. The diverse range of people and studies he came across in IIT, will help him further grow as a student. Those years were the best years of his life, as the lively campus of IIT fostered late night discussions, sports, and spontaneity. During the junior year of undergrad, he visited the lab of Cooper Langford in University of Calgary, Canada as a research intern. Long hours of conversations with Dr. Langford on fundamental chemistry, inspired him to pursue a doctorate in Chemical Engineering. The professors at the Dept. of Chemical Engineering at the IIT also encouraged him to pursue a Ph.D. degree.

He joined Cornell University, Ithaca in fall of 2017 to pursue Ph.D. in Chemical Engineering with Dr. Lynden Archer. The last four years has been intellectually engaging for him, and he cherishes the friends and memories he made.

Dedicated to my family and all those who have supported me

ACKNOWLEDGMENTS

I would like to express my sincere gratitude to all who have supported me throughout my life and academic journey. Firstly, I would like to thank my thesis advisor Dr. Lynden Archer for his invaluable guidance and encouragement throughout the course of my Ph.D. studies and in further career opportunities. His dedication and commitment towards scientific research inspired me to further improve my research work. He transformed my approach not only towards academics but also towards my life. I would also like to thank my committee members Dr. Don Koch and Dr. Lena Kourkoutis for the research discussions and assistance they have provided.

One of the most satisfying experiences at Cornell has been working with undergraduate students, Atsu Kludze '21 and Joshua Rodriguez '22. We spent countless hours discussing, carrying out new experiments, and equally accepting the success or failure that followed. I am grateful to have had such an opportunity that helped me grow as a mentor. I am also grateful to my colleagues in the Archer research group who have been consistently collaborative and supportive throughout my time here at Cornell. For most of my time here at Cornell, I have also had the pleasure of working in the Cornell Energy Systems Club and as a member of the Teaching Assistant development team for Cornell's Engineering Learning Initiatives. I would like to thank the entire team for the engaging discussions we had, events we organized together, and for the role they played in helping me grow on a personal level.

Last but not least, I would like to express my gratitude for my parents and my family. They have been all the strength and inspiration to bear the hardships during the difficult phases of my life. I will cherish their love and affection forever.

TABLE OF CONTENTS

1. Introduction.....	1
1.1. The Lithium Metal Anode & rechargeable Lithium Metal Batteries	2
1.1.2 Nucleation and growth of electrodeposited Li	8
1.1.3 The Solid Electrolyte Interphase (SEI).....	10
1.2. Outline of this dissertation.....	12
1.3. References.....	15
2. Nucleation and early-stage growth of Li electrodeposits.....	24
2.1. Abstract.....	25
2.2. Introduction.....	26
2.3. Results and Discussions.....	28
2.4. Conclusion.....	48
2.5. Acknowledgement.....	49
2.6. References.....	49
Appendix.....	55
3. The early-stage growth and reversibility of Li electrodeposition in Br-rich electrolytes.....	87
3.1. Abstract.....	88
3.2. Introduction.....	89
3.3. Results and Discussions.....	90
3.4. Conclusion.....	118
3.5. Acknowledgement.....	119
3.6. References.....	119
Appendix.....	130

4. Rational design of Solid Electrolyte Interphase with enhanced energetics for Lithium Metal Anode.....	173
4.1. Abstract.....	174
4.2. Introduction.....	175
4.3. Results and Discussions.....	179
4.4. Conclusion.....	205
4.5. Acknowledgement.....	206
4.6. References.....	206
Appendix.....	213

Chapter 1

Introduction

1.1 The Lithium Metal Anode & rechargeable Lithium Metal Batteries

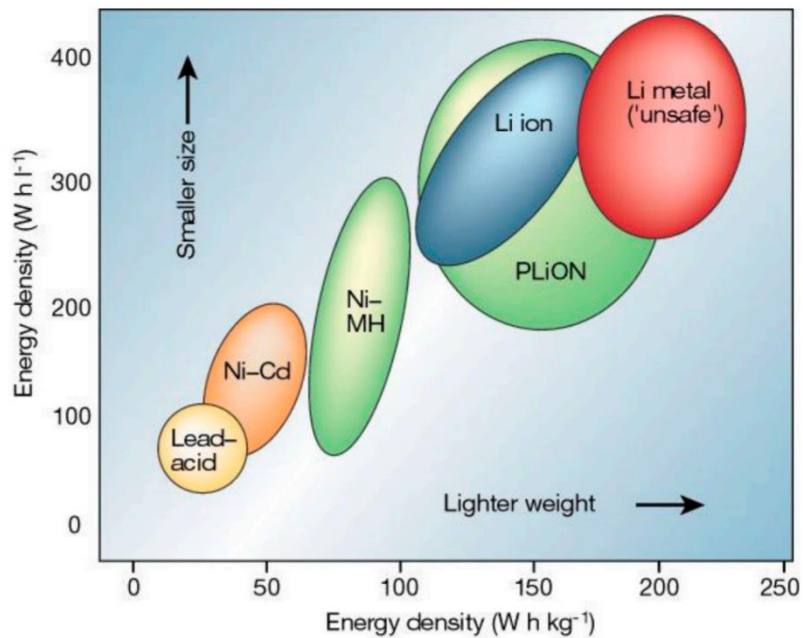


Figure 1.1. Ragone plot of different battery technologies used in EVs (5)

The past four decades have seen a surge in demand for secondary/rechargeable batteries with higher energy densities, lighter weight, improved energy storage capacity, longer cycle life, lower cost, and enhanced safety to meet the growing needs for smaller, lighter, more powerful portable electronic devices, more powerful and long-range electric vehicles (HEV, PHEV, EV), and robust grid scale energy storage. The timeline of the various rechargeable battery architectures brought to bear to address these challenges included Lead-acid battery, Nickel-cadmium battery, Nickel-metal hydride batteries, & Lithium-Ion batteries (LIB) in successive orders of their advancement in power density and year of commercial availability (1). Currently, LIB's based on graphitic anode (for Lithium-ion intercalation) are among the most advanced rechargeable batteries available for commercial use. However, further advancement in power density and cost

of energy storage technology can be realized by substituting the graphitic anode with a film of Lithium metal *i.e.*, the Lithium Metal Anode (LMA) (2-5) (**Figure 1.1**).

Lithium (Li) metal is an ideal anode material for high-energy and light-weight rechargeable batteries due to its extremely high theoretical specific capacity (3860 mAh g⁻¹), the lowest negative electrochemical potential (-3.040 V versus standard hydrogen electrode), and low density (0.534 g cm⁻³) (2-5). Thus, rechargeable Li Metal Batteries (LMB) have been extensively studied for the last 40 years for their prospective application in portable electronics, electric vehicles, and grid-scale energy storage, though not yet commercialized (2-5). The shortcomings in the development of Li metal batteries is primarily attributed to growth of Li dendrites, low Coulombic efficiency (CE) and infinite relative volume expansion during repeated charging/discharging process (C/D cycles). The growth of Li dendrites during C/D cycles leads to internal short-circuit, hence substantially reducing the life cycle of the cell while additionally raising safety hazard concerns due to the potential shorts have for driving thermal runaway. In tandem, dendritic growth of Li increases the electrode surface area and compromises the mechanical integrity of the electrode. The former promotes parasitic reactions with the electrolyte, consuming the electrolyte. The latter causes sections of the deposited metal to break-away from the electrode mass, forming regions of electrically disconnected “dead” Li that is electrochemically inactive. This logically leads to loss of active anode material, thereby loss of capacity, while continuously increasing the cell impedance and lowering the energy density (2-5). With the aim of understanding the electrochemical processes that control these behaviors at an active

metal-electrolyte interface, this dissertation focuses on fundamental mechanistic studies of Li metal dendrite nucleation and growth processes in liquid electrolytes.

The physico-chemical processes that drive Li to electrodeposit in mossy/dendritic morphologies have attracted significant experimental (4-9,13) and theoretical (10-13) interests in recent years. The electrodeposition of Li^+ ion on Lithium anode during charging of LMB is now understood to be a fundamentally unstable process culminating in non-uniform & non-planar Li growth in low-density, morphologically complex structures loosely termed dendrites — although in most cases these structures have no obvious resemblance to trees & are more analogous to a forest of intertwined wires or mosses. An interplay of morphological instability, chemical instability and electroconvective instability at different current densities adds even more complexity; the principal facilitators being unstable ion transport to the Li surface (6), mechanically weak electrolyte (10), and unregulated reactions at Li surface leading to variation of spatial interfacial resistance (6,8). Morphological instability in Li is driven by preferential transport of Li^+ ions to the rough Li metal surface because of unevenly distributed electric field at low current densities (6). Electroconvective instability occurs at higher current densities, having its origins in the formation of a space charge (ion-depleted region) near the Li anode due to diffusion limited transport of Li^+ ions in the electrolyte, leading to electroconvective vortices sweeping Li^+ ions from regions surrounding a growing dendrite, preferentially depositing Li^+ ions on the dendrite tip, enabling further dendrite growth (6,14). The Solid Electrolyte Interphase (SEI) formed at the Li anode surface from insoluble reaction products of Li with the electrolyte, is inhomogeneous and fragile, and further thought to create preferential nucleation sites

for metal reduction and electrolyte loss due to constant breakage during C/D cycles; a phenomenon referred to as chemical instability (**Figure 1.2**) (6,8). A large body of work therefore focuses on developing strategies for prevention of dendritic growth on Li anode through modification of SEI, improvement of mechanical barriers and regulation of ion-transport in the electrolyte (4,6,15,16). These studies lead to a number of suggested best practices for achieving non-dendritic deposition of Li. These range from: **[a] Solvent Design:** solvents such as 1,3-dioxalane forming oligomeric elastic SEI (17); ether based solvents such as glymes forming tough, alkoxy SEI (18,19); fluorinated solvents such as Fluoroethylene carbonate (FEC) (20), Bis(2,2,2-trifluoroethyl) ether (21) forming fluorinated SEI; **[b] Salt Design:** salts such as Lithium nitrate form Nitrooxy (N_xO_y) derivatives in the SEI (22) ; fluorinated salts such as LiTFSI and LiFSI forming fluorinated SEI (17,20,23,24); **[c] Engineered SEIs:** artificial SEI (6,15,16) composed of interconnected amorphous hollow carbon nanospheres (25), graphene (26), Li_3N /PEDOT-co-PEG protecting layer (27), composite protective film (28), ceramic coating film [29,30], LISICON layer (31); **[d] Controlling interfacial ion transport:** modification of ion transport through single ion conductors such as ceramics (LiPON) (32,33), solid solution (thio-LISICON) (34), and polymers (Nafion) (35,36,37); **[e] Mechanically strong and tough electrolytes:** high shear modulus electrolytes such as co-polymers (38,39), cross-linked polymers (40,42), nanocomposites (42,43), solid solutions (thio-LISICON) (34) and ceramics (LiPON) (32,33); **[f] Active regulation of electroreduction:** self-healing electrostatic shield (44) using Cs^+ and Rb^+ as additives in the electrolyte; **[g] Lowering the thermodynamic activity of electrolyte components:** Electrolytes containing high concentrations of

soluble salts (45,46,47) (e.g. LiTFSI and LiFSI) are able to delay/prevent electroreduction of other electrolyte components at the highly reducing deposition potentials for Li metal anode, reducing the thickness and heterogeneity of the SEI; **[h] Physical approaches for homogenizing Li-ion flux:** by increasing the effective surface area of the electrode (16) via advanced current collectors such as 3D Cu current collector (48), graphene (49), carbon fibers (50); **[i] Minimizing Li volume change during electroreduction:** by using stable hosts (16) such as infusion of molten Li into reduced graphene oxide (51); **[j] Designing the current collector:** surface-wrinkling-induced stress relaxation of current collectors on soft substrate (Cu/PDMS) (52) can prevent Li from depositing in wire-like morphologies.

In spite of the vast applications-centered literature that document how and why these various approaches would lead to more stable electrodeposition of Li^+ ions and prevention of dendritic growths on Li anode over several C/D cycles through novel engineering innovations of the LMB battery components, few studies interrogate the initial nucleation and growth behavior of Li metal (53). Even scarcer are studies able to shed light on how the intrinsic reactivity of Li electrodeposits couples with electrolyte chemistry to regulate Li nucleate size, shape, rate of growth, and stability at an electrode.

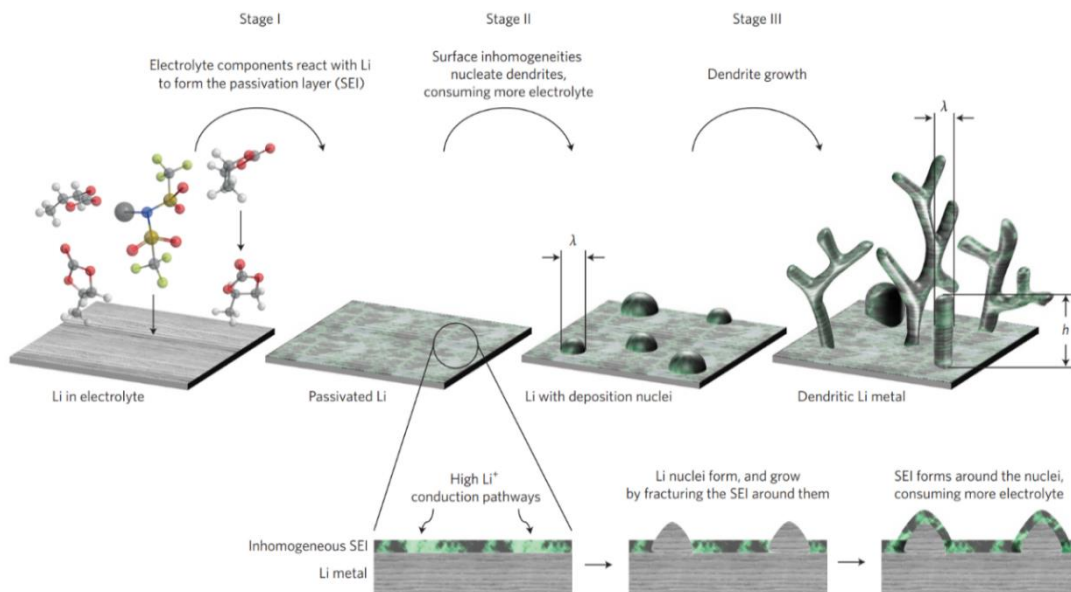


Figure 1.2. Schematic diagram showing hypothesized growth mechanism of Li dendrites. [Upper Row] Formation of SEI (Stage I), nucleation of dendrites due to preferential transport to Li anode surface (Stage II) and further growth due to preferential transport to dendrite tip over time (Stage III). [Lower Row] Chemical instability due to inhomogeneous SEI leading to morphological instability and electrolyte loss. Morphology of dendrites may vary from spherical, mossy dense structures at low current densities to fine, needle like fibrils at high current densities; the structures being highly susceptible to electrolyte composition (6).

1.1.2 Nucleation and growth of electrodeposited Li

In 1962 Barton and Bockris (54) proposed the first theoretical model of dendrite growth and predicted growth initiation/velocity. They showed that cations preferentially diffuse to the dendrite tip rather than valleys, because spherical diffusion dominates over linear diffusion. Shortcomings of the model were identified and remediated by Diggle et al. (55). They introduced Butler-Volmer kinetics to account for the surface kinetics and relaxed Barton & Bockris' assumption that dendrites are static hemispheres. A linear Mullins-Sekerka type instability analysis of a rough interface with spatially periodic undulations was carried out by Aogaki and Makino (56) to account for morphological instability of metals during diffusion-controlled electrodeposition. Sundstrom and Bark (57) extended this model to show that surface tension has only a weakly stabilizing effect on dendrite growth. Monroe and Newman (10) extended the analysis even further to include the effect of electrolyte/separator mechanics on growth kinetics, concluding that dendrite growth could be curbed if the electrolyte modulus exceeded that of the dendritic metal — an important, yet intuitive finding. Tikekar et al. (58,59) developed a single framework combining the effect of elastic deformation of the separator and the electrode and ion transport across the separator on stable electrodeposition of Li. They performed a linear stability analysis to show that morphological instabilities can be suppressed even at relatively high current densities in electrolytes/separators with moderate polymer-like mechanical moduli, provided a small fraction of anions are immobilized in the separator. But like Monroe-Newman analysis, this analysis by Tikekar et al. did not account for the nucleation step and as such cannot provide insight into the important role electrolyte chemistry has been reported to play on stability.

Recently, Stark et al. (60) and Pei et al. (53) studied nanoscale nucleation and growth of electrodeposited Li. Stark et al. showed that while the initial nuclei of Li may be hemispherical, further deposition may lead to tip-based growth due to electrochemically active tip of nuclei followed by extrusion-based growth (mossy dendrites) as a side-effect of pressure buildup because of Li deposition under a strained SEI layer. Pei et al. showed that the dependence of Li nuclei size, shape, and areal density on current density and overpotential are consistent with trends from classical nucleation and growth theory. Wood et al. (13) carried out operando video microscopy to enable synchronized observation of Li electrode morphology and electrochemical behavior during galvanostatic C/D cycling and on that basis developed a continuum-scale model encapsulating Poisson-Nernst-Planck framework with Butler-Volmer kinetics, to understand the electrodeposited Li morphology over time. A weakness ingrained in all of these models is that they begin with the assumption that dendrites are already nucleated on the electrodeposited metal surface and as such provide no insights about steps one might take to prevent dendritic electrodeposition at the formation step. While electroconvective instability (6,14,61) can be perceived as the perpetrator for initiating dendritic growth at high current densities (above diffusion-limited current), limited is the understanding of how morphological and chemical instability may initiate dendrite nucleation at even lower current densities.

1.1.3 The Solid Electrolyte Interphase (SEI)

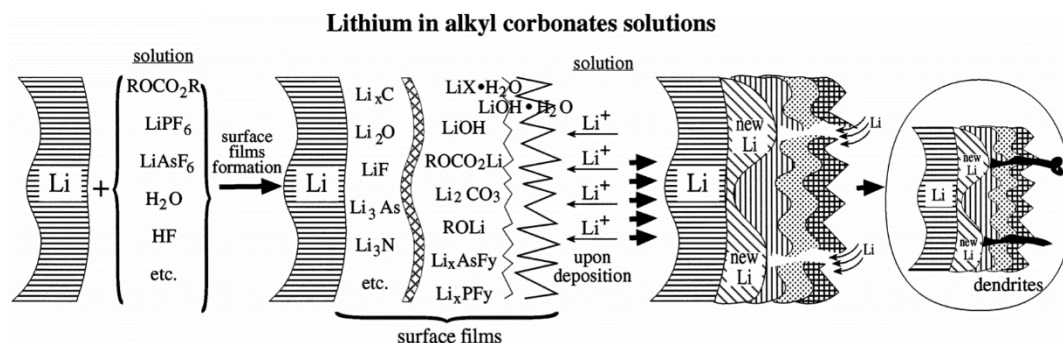


Figure 1.3. A schematic illustration of surface film (SEI) formation on lithium electrodes in alkyl carbonates solutions (64).

A complete investigation of Li dendrite nucleation and growth requires more fundamental understanding of the chemistry, structure, mechanics, transport properties of the SEI formed spontaneously on Li in all electrolytes. Since Peled's first introduced the concept of the SEI in 1979 as an electronically insulating and ionically conducting passivation layer formed between the reactive electrode and electrolyte (62), a fair amount of work has been carried out to understand its formation, morphology, chemistry, electrochemical properties, and stability over C/D cycles (15,63). The role of the SEI on nucleation and growth of Li dendrites is nonetheless essentially unknown. Contrary to the tip-based dendrite growth models (7,54,55) discussed previously, Yamaki et al. (12) showed that non-uniform deposition of Li underneath the SEI creates a stress between the SEI and the underlying Li substrate, eventually causing the SEI to crack, and the rather soft Li to get extruded through the crack to relief the stress. Aurbach et al. (8, 64) proposed that inhomogeneities in the SEI lead to preferential

electrodeposition (non-uniform deposition) at certain sites on the anode causing nucleation and subsequent growth of dendrites, at low/moderate current densities. They further showed that these inhomogeneities stem from the complex chemical nature of the multilayer surface film composed of myriads of organic and inorganic molecules, as shown in **Figure 1.3**. Steiger et al. (65,66,67) suggested that tip-based growth of dendrite occurs behind an inactive deposit of the SEI, when the Li^+ cation can preferentially transport to the tip through an adjacent thin SEI layer. Recently, Choudhury et al. performed equilibrium theoretical calculations using joint density functional analysis in vacuum and generic liquid media (e.g. acetonitrile) to show that surface diffusion barriers for Li are much lower in a SEI composed of pure halide salts (LiF, LiCl, LiBr, LiI), compared to typical SEI salts like LiOH and Li_2CO_3 (**Figure 1.4**) that appear to form spontaneously in the SEI. This indicates that in-plane transport at such interphases may be enhanced substantially if LiX (X = Br > Cl > I > F) species predominate in the SEI. Owing to such varied conclusions and complexity of the SEI, it can be regarded as “the most important but least understood (component) in rechargeable LMB”.

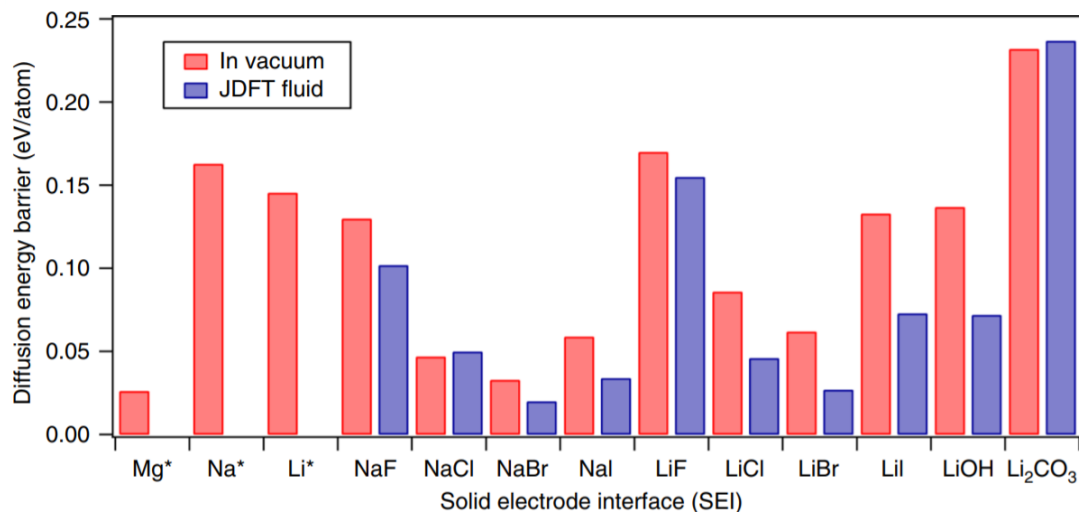


Figure 1.4: Bar Chart showing the surface diffusion barrier for various compounds that typically exist in the SEI of lithium or sodium metal during battery cycling. The *red bars* denote surface in contact with vacuum and *blue bars* indicate the same in presence of acetonitrile (68).

1.2 Outline of this dissertation

This dissertation seeks answers to the following questions: (a) What are the microscopic processes involved in early-stage nucleation and time-dependent physical evolution of the morphology of electrodeposited Li? (b) What is the role of the interphase (SEI) chemistry in dictating the transport-reaction pathway at the interface? (c) What are the steps one can take to prevent dendrite nucleation at the formation step? (d) How can the control of nucleation, growth and kinetic protection of electrodeposited Li be regulated over the life cycle of the LMB?

This work employs a combination of theoretical modelling and microscopy, spectroscopy, data analysis techniques to fundamentally understand the electrode-

electrolyte interphases and proposes rational design concepts for electrolytes to eliminate the morphological and chemical instabilities in Li metal-based batteries.

In **Chapter 2**, we report results from a combined theoretical and experimental study of the early-stage nucleation and growth of electrodeposited lithium at liquid-solid interfaces. We show that ion diffusion in the bulk electrolyte and through the Solid Electrolyte Interphase (SEI) formed spontaneously on the metal play equally important roles on Li nucleation and growth. We show further that the underlying physics dictating bulk and surface diffusion are similar across a range of electrolyte chemistries and measurement conditions and that fluorinated electrolytes (F rich species) produce a distinct flattening of Li electrodeposits at low rates. Our results show that high interfacial energy and high surface ion diffusivity are necessary for uniform Li plating.

In **Chapter 3**, we build upon our work with fluorinated electrolytes in Chapter 2, to investigate the early-stage growth dynamics and reversibility of electrodeposited Lithium in liquid electrolytes infused with brominated additives. We report that it is possible to achieve fine control of the early-stage Li electrodeposit morphology through tuning of surface energetic and ion diffusion properties of interphases formed on Li. This control is shown further to translate to better control of Li electrodeposit morphology and high electrochemical reversibility during deep cycling of the Li metal anode.

In **Chapter 4**, we further build upon our previous work, by studying the role of carbonate and fluorinated electrolytes with/without ether additive on the morphology, chemical composition, interfacial energetics, and electrochemical reversibility of Li electrodeposits during early stages of electrodeposition as well as later stages of deep

cycling of Li anode. The chemical nature of the SEI is deliberately manipulated via electrolytes of contrasting chemistries (carbonate vs fluorinated) to study the physio-chemical nature of Li electrodeposition. The transport-reaction kinetics of the SEI is demonstrated to play an important role in Lithium plating and can be modulated by rational choice of electrolyte components. Furthermore, we demonstrate that incorporation of ether-based additive (diglyme) has a beneficial cleaning effect on Li electroplating and is necessary for preserving the surface energetics (transport-reaction kinetics), chemical nature, and uniform morphology observed at initial stages of electroplating through deep cycling of Li anode. Finally, the electrolyte chemistry (ether enriched fluorinated electrolyte) chosen rationally is shown to have superior electrochemical performance in a LMB. Our results show that understanding and eliminating morphological and chemical instabilities in the initial stages of Li electroplating via deliberately modifying energetics of the Solid Electrolyte Interphase (SEI) is a feasible approach in realization of deeply cyclable reactive metal batteries.

1.3 References

- (1) Scrosati, B. (1995). Challenge of portable power. *Nature*, 373(6515), 557-558.
- (2) Whittingham, M. S. (2012). History, evolution, and future status of energy storage. *Proceedings of the IEEE*, 100(Special Centennial Issue), 1518-1534.
- (3) Tarascon, J. M., & Armand, M. (2011). Issues and challenges facing rechargeable lithium batteries. *Materials for sustainable energy: a collection of peer-reviewed research and review articles from Nature Publishing Group*, 171-179.
- (4) Zhang, J.G., Xu, W. and Henderson, W.A. Lithium metal anodes and rechargeable lithium metal batteries. *Switzerland: Springer International Publishing* (2017).
- (5) Miao, Y., Hynan, P., Von Jouanne, A., & Yokochi, A. (2019). Current Li-ion battery technologies in electric vehicles and opportunities for advancements. *Energies*, 12(6), 1074.
- (6) Tikekar, M. D., Choudhury, S., Tu, Z., & Archer, L. A. (2016). Design principles for electrolytes and interfaces for stable lithium-metal batteries. *Nature Energy*, 1(9), 16114.
- (7) Chianelli RR (1976) Microscopic studies of transition metal chalcogenides. *J Cryst Growth* 34 (2):239–244
- (8) Aurbach D, Zinigrad E, Cohen Y, Teller H (2002) A short review of failure mechanisms of lithium metal and lithiated graphite anodes in liquid electrolyte solutions. *Solid State Ionics* 148:405–416.
- (9) Chandrashekar S, Trease NM, Chang HJ, Du L-S, Grey CP, Jerschow A (2012) 7Li MRI of Li batteries reveals location of microstructural lithium. *Nat Mater* 11(4):311–315.

- (10) Monroe C, Newman J (2005) The impact of elastic deformation on deposition kinetics at lithium/polymer interfaces. *J Electrochem Soc* 152(2):A396–A404
- (11) Tang M, Albertus P, Newman J (2009). *J Electro-chem Soc* 156:A390–A399
- (12) Yamaki J-I (1998) *J Power Sources* 74:219–227
- (13) Wood, Kevin N., Eric Kazyak, Alexander F. Chadwick, Kuan-Hung Chen, Ji-Guang Zhang, Katsuyo Thornton, and Neil P. Dasgupta. "Dendrites and pits: untangling the complex behavior of lithium metal anodes through operando video microscopy." *ACS central science* 2, no. 11 (2016): 790-801.
- (14) Tikekar, M. D., Archer, L. A., & Koch, D. L. (2014). Stability analysis of electrodeposition across a structured electrolyte with immobilized anions. *Journal of The Electrochemical Society*, 161(6), A847-A855.
- (15) Cheng, X. B., Zhang, R., Zhao, C. Z., Wei, F., Zhang, J. G., & Zhang, Q. (2016). A review of solid electrolyte interphases on lithium metal anode. *Advanced Science*, 3(3), 1500213.
- (16) Lin, D., Liu, Y., & Cui, Y. (2017). Reviving the lithium metal anode for high-energy batteries. *Nature nanotechnology*, 12(3), 194.
- (17) Miao, R. *et al.* Novel dual-salts electrolyte solution for dendrite-free lithium metal based rechargeable batteries with high cycle reversibility. *J. Power Sources* 271, 291–297 (2014).
- (18) Qian, J. *et al.* High rate and stable cycling of lithium metal anode. *Nat. Commun.* 6, 6362 (2015).
- (19) Seh, Z. W., Sun, J., Sun, Y. & Cui, Y. A highly reversible room-temperature sodium metal anode. *ACS Cent. Sci.* 1, 449–455 (2015).

- (20) Suo, L., Xue, W., Gobet, M., Greenbaum, S. G., Wang, C., Chen, Y., ... & Li, J. (2018). Fluorine-donating electrolytes enable highly reversible 5-V-class Li metal batteries. *Proceedings of the National Academy of Sciences*, 201712895.
- (21) Gordin, M. L., Dai, F., Chen, S., Xu, T., Song, J., Tang, D., ... & Wang, D. (2014). Bis (2, 2, 2-trifluoroethyl) Ether as an Electrolyte Co-solvent for Mitigating Self-Discharge in Lithium–Sulfur Batteries. *ACS applied materials & interfaces*, 6(11), 8006-8010.
- (22) Aurbach, D., Pollak, E., Elazari, R., Salitra, G., Kelley, C. S., & Affinito, J. (2009). On the surface chemical aspects of very high energy density, rechargeable Li–sulfur batteries. *Journal of The Electrochemical Society*, 156(8), A694-A702.
- (23) Kim, H., Wu, F., Lee, J. T., Nitta, N., Lin, H. T., Oschatz, M., ... & Yushin, G. (2015). In Situ Formation of Protective Coatings on Sulfur Cathodes in Lithium Batteries with LiFSI-Based Organic Electrolytes. *Advanced Energy Materials*, 5(6), 1401792.
- (24) Qian, J., Henderson, W. A., Xu, W., Bhattacharya, P., Engelhard, M., Borodin, O., & Zhang, J. G. (2015). High rate and stable cycling of lithium metal anode. *Nature communications*, 6, 6362.
- (25) Zheng, G., Lee, S.W., Liang, Z., Lee, H.W., Yan, K., Yao, H., Wang, H., Li, W., Chu, S. and Cui, Y., 2014. Interconnected hollow carbon nanospheres for stable lithium metal anodes. *Nature nanotechnology*, 9(8), p.618.
- (26) Zhang, J., Yang, X., Wang, R., Dong, W., Lu, W., Wu, X., Wang, X., Li, H. and Chen, L., 2014. Influences of additives on the formation of a solid electrolyte interphase

on MnO electrode studied by atomic force microscopy and force spectroscopy. *The Journal of Physical Chemistry C*, 118(36), pp.20756-20762.

(27) Zhang, Y.J., Wang, W., Tang, H., Bai, W.Q., Ge, X., Wang, X.L., Gu, C.D. and Tu, J.P., 2015. An ex-situ nitridation route to synthesize Li₃N-modified Li anodes for lithium secondary batteries. *Journal of Power Sources*, 277, pp.304-311.

(28) Lee, H., Lee, D.J., Kim, Y.J., Park, J.K. and Kim, H.T., 2015. A simple composite protective layer coating that enhances the cycling stability of lithium metal batteries. *Journal of Power Sources*, 284, pp.103-108.

(29) Haregewoin, A.M., Wotango, A.S. and Hwang, B.J., 2016. Electrolyte additives for lithium ion battery electrodes: progress and perspectives. *Energy & Environmental Science*, 9(6), pp.1955-1988.

(30) Umeda, G.A., Menke, E., Richard, M., Stamm, K.L., Wudl, F. and Dunn, B., 2011. Protection of lithium metal surfaces using tetraethoxysilane. *Journal of Materials Chemistry*, 21(5), pp.1593-1599.

(31) Wang, X., Hou, Y., Zhu, Y., Wu, Y. and Holze, R., 2013. An aqueous rechargeable lithium battery using coated Li metal as anode. *Scientific reports*, 3, p.1401.

(32) Bates, J. B. *et al.* Electrical properties of amorphous lithium electrolyte thin films. *Solid State Ionics* **53–56**, 647–654 (1992)

(33) Li, J., Ma, C., Chi, M., Liang, C. and Dudney, N.J., 2015. Solid electrolyte: the key for high-voltage lithium batteries. *Advanced Energy Materials*, 5(4), p.1401408.

(34) Kanno, R. & Murayama, M. Lithium ionic conductor thio-LISICON: the Li₂S–GeS₂–P₂S₅ system. *J. Electrochem. Soc.* **148**, 742–746 (2001).

- (35) Lu, Y. *et al.* Stable cycling of lithium metal batteries using high transference number electrolytes. *Adv. Energy Mater.* **5**, 1402073 (2015).
- (36) Song, J., Lee, H., Choo, M.-J., Park, J.-K. & Kim, H.-T. Ionomer-liquid electrolyte hybrid ionic conductor for high cycling stability of lithium metal electrodes. *Sci. Rep.* **5**, 14458 (2015).
- (37) Cheng, X. B. *et al.* Dendrite-free lithium deposition induced by uniformly distributed lithium ions for efficient lithium metal batteries. *Adv. Mater.* **28**, 2888–2895 (2016).
- (38) Stone, G. M. *et al.* Resolution of the modulus versus adhesion dilemma in solid polymer electrolytes for lithium metal batteries. *J. Electrochem. Soc.* **159**, A222–A227 (2012).
- (39) Giles, J. R. M., Gray, F. M., Maccallum, J. R. & Vincent, C. A. Synthesis and characterization of ABA block copolymer-based polymer electrolytes. *Polymer* **28**, 1977–1981 (1987).
- (40) Khurana, R., Schaefer, J. L., Archer, L. A. & Coates, G. W. Suppression of lithium dendrite growth using cross-linked polyethylene/poly(ethylene oxide) electrolytes: a new approach for practical lithium-metal polymer batteries. *J. Am. Chem. Soc.* **136**, 7395–7402 (2014).
- (41) Pan, Q., Smith, D. M., Qi, H., Wang, S. & Li, C. Y. Hybrid electrolytes with controlled network structures for lithium metal batteries. *Adv. Mater.* **27**, 5995–6001 (2015).

- (42) Choudhury, S., Mangal, R., Agrawal, A. & Archer, L. A. A highly reversible room-temperature lithium metal battery based on crosslinked hairy nanoparticles. *Nat. Commun.* **6**, 10101 (2015).
- (43) Gurevitch, I. *et al.* Nanocomposites of titanium dioxide and polystyrenopoly(ethylene oxide) block copolymer as solid-state electrolytes for lithium metal batteries. *J. Electrochem. Soc.* **160**, A1611–A1617 (2013).
- (44) Ding, F., Xu, W., Graff, G.L., Zhang, J., Sushko, M.L., Chen, X., Shao, Y., Engelhard, M.H., Nie, Z., Xiao, J. and Liu, X., 2013. Dendrite-free lithium deposition via self-healing electrostatic shield mechanism. *Journal of the American Chemical Society*, *135*(11), pp.4450-4456.
- (45) Suo, L., Hu, Y.-S., Li, H., Armand, M. & Chen, L. A new class of solvent-in-salt electrolyte for high-energy rechargeable metallic lithium batteries. *Nat. Commun.* **4**, 1481 (2013).
- (46) Qian, J. *et al.* High rate and stable cycling of lithium metal anode. *Nat. Commun.* **6**, 6362 (2015).
- (47) Qian, J. *et al.* Anode-free rechargeable lithium metal batteries. *Adv. Funct. Mater.* **26**, 7094–7102 (2016).
- (48) Yang, C.-P., Yin, Y.-X., Zhang, S.-F., Li, N.-W. & Guo, Y.-G. Accommodating lithium into 3D current collectors with a submicron skeleton towards long-life lithium metal anodes. *Nat. Commun.* **6**, 8058 (2015).
- (49) Zhamu, A. *et al.* Reviving rechargeable lithium metal batteries: enabling nextgeneration high-energy and high-power cells. *Energy Environ. Sci.* **5**, 5701–5707 (2012).

- (50) Ji, X. *et al.* Spatially heterogeneous carbon-fiber papers as surface dendrite-free current collectors for lithium deposition. *Nano Today* **7**, 10–20 (2012).
- (51) Lin, D. *et al.* Layered reduced graphene oxide with nanoscale interlayer gaps as a stable host for lithium metal anodes. *Nat. Nanotech.* **11**, 626–632 (2016)
- (52) Wang, X., Zeng, W., Hong, L., Xu, W., Yang, H., Wang, F., Duan, H., Tang, M. and Jiang, H., 2018. Stress-driven lithium dendrite growth mechanism and dendrite mitigation by electroplating on soft substrates. *Nature Energy*, *3*(3), p.227.
- (53) Pei, A., Zheng, G., Shi, F., Li, Y. and Cui, Y., 2017. Nanoscale nucleation and growth of electrodeposited lithium metal. *Nano letters*, *17*(2), pp.1132-1139.
- (54) J. L. Barton, J. O'M. Bockris, "The electrolytic growth of dendrites from ionic solutions", *Proc R Soc London, Ser A*, **268**, 485 (1962)
- (55) J. W. Diggle, A. R. Despic, and J. O'M. Bockris, "The mechanism of dendritic electrocrystallization of zinc", *J Electrochem Soc*, **116**, 1503 (1969).
- (56) R. Aogaki, T. Makino, "Theory of powdered metal formation in electrochemistry – morphology instability in galvanostatic crystal growth under diffusion control", *Electrochim Acta*, **26**, 1509 (1981).
- (57) Sundström, L.G. and Bark, F.H., 1995. On morphological instability during electrodeposition with a stagnant binary electrolyte. *Electrochimica acta*, *40*(5), pp.599-614.
- (58) Tikekar, M.D., Archer, L.A. and Koch, D.L., 2014. Stability analysis of electrodeposition across a structured electrolyte with immobilized anions. *Journal of The Electrochemical Society*, *161*(6), pp.A847-A855.

- (59) Tikekar, M.D., Archer, L.A. and Koch, D.L., 2016. Stabilizing electrodeposition in elastic solid electrolytes containing immobilized anions. *Science advances*, 2(7), p.e1600320.
- (60) Stark, J.K., Ding, Y. and Kohl, P.A., 2013. Nucleation of electrodeposited lithium metal: dendritic growth and the effect of co-deposited sodium. *Journal of The Electrochemical Society*, 160(9), pp.D337-D342.
- (61) J. N. Chazaviel, “Electrochemical aspects of the generation of ramified metallic electrodeposits”, *Phys Rev A*, **42**, 7355 (1990).
- (62) E. Peled, “The electrochemical behavior of alkali and alkaline earth metals in nonaqueous battery Systems—The solid electrolyte interphase model”, *J Electrochem Soc*, **126**, 2047 (1979).
- (63) Wang, A., Kadam, S., Li, H., Shi, S. and Qi, Y., 2018. Review on modeling of the anode solid electrolyte interphase (SEI) for lithium-ion batteries. *npj Computational Materials*, 4(1), p.15.
- (64) Aurbach, D. (2000). Review of selected electrode–solution interactions which determine the performance of Li and Li ion batteries. *Journal of Power Sources*, 89(2), 206-218.
- (65) Steiger J, Kramer D, Mönig R (2014a) Mechanisms of dendritic growth investigated by in situ light microscopy during electrodeposition and dissolution of lithium. *J Power Sources* 261:112–119.
- (66) Steiger J, Kramer D, Mönig R (2014b) Microscopic observations of the formation, growth and shrinkage of lithium moss during electrodeposition and dissolution. *Electrochim Acta* 136:529–536.

(67) Steiger J, Richter G, Wenk M, Kramer D, Mönig R (2015) Comparison of the growth of lithium filaments and dendrites under different conditions. *Electrochem Commun* 50:11–14.

(68) Choudhury, S., Wei, S., Ozhabes, Y., Gunceler, D., Zachman, M.J., Tu, Z., Shin, J.H., Nath, P., Agrawal, A., Kourkoutis, L.F. and Arias, T.A., 2017. Designing solid-liquid interphases for sodium batteries. *Nature communications*, 8(1), pp.1-10.

Chapter 2

Nucleation and early-stage growth of Li electrodeposits

Adapted with permission from

Biswal, P., Stalin, S., Kludze, A., Choudhury, S., & Archer, L. A. (2019). Nucleation and early stage growth of Li electrodeposits. *Nano letters*, 19(11), 8191-8200.

2.1 Abstract

The morphologies metal electrodeposits adopt during the earliest stages of electrodeposition are known to play a critical role in the recharge of electrochemical cells that use metals as anodes. Here we report results from a combined theoretical and experimental study of the early-stage nucleation and growth of electrodeposited lithium at liquid-solid interfaces. The spatial characteristics of Lithium electrodeposits are studied via Scanning Electron Microscopy in tandem with Image analysis. Comparisons of Li nucleation and growth in multiple electrolytes provide a comprehensive picture of the initial nucleation and growth dynamics. We report that ion diffusion in the bulk electrolyte and through the Solid Electrolyte Interphase (SEI) formed spontaneously on the metal play equally important roles on Li nucleation and growth. We show further that the underlying physics dictating bulk and surface diffusion are similar across a range of electrolyte chemistries and measurement conditions and that fluorinated electrolytes produce a distinct flattening of Li electrodeposits at low rates. These observations are rationalized using X-ray Photoelectron Spectroscopy (XPS), Electrochemical Impedance Spectroscopy (EIS), and contact angle goniometry to probe the interfacial chemistry and dynamics. Our results show that high interfacial energy and high surface ion diffusivity are necessary for uniform Li plating.

2.2 Introduction

Lithium (Li) metal is among the most promising anode materials for high-energy and light-weight rechargeable batteries due to its extremely high theoretical specific capacity (3860 mAh g⁻¹), the lowest negative electrochemical potential (-3.040 V versus standard hydrogen electrode), and low density (0.534 g cm⁻³) (1). Rechargeable Li Metal Batteries (LMBs) have been extensively studied for over forty years for prospective applications in portable electronics, electric vehicles and grid-scale energy storage, though not yet commercialized (1-4). These studies have revealed multiple shortcomings of Li metal anodes, including the metal's tendency to deposit during charging in low-density mossy morphologies, loosely termed *dendrites*; its low reversibility and poor Columbic efficiency (CE) in liquid electrolyte media; propensity to proliferate in the electrode space to short-circuit the battery producing thermal runaway; and to undergo large volume changes during repeated cycles of charge and discharge (1-6). The “dendritic/mossy” growth of Li exacerbates all of these problems and, additionally, imparts fragility to the metal electrodeposits that can cause them to break away from the electronic circuitry of an electrode, producing so-called “orphaned/dead” Li. The orphaned Li has recently been reported to play an important, perhaps even dominant, role in the poor reversibility and low CE of Li metal anodes. Significant experimental (1,3,5-9,13) and theoretical (10-13) efforts have been made in recent years to understand and control mossy/dendritic Li electrodeposition. The electrodeposition is presently understood to be destabilized at current densities, i , below the classical diffusion limit ($i_L = 4FcD_+/\delta_D$) by at least two processes: (i) morphological instability produced by heterogeneous nucleation of Li deposits in less

passivated (faster ion transport) regions of an electrode (5,7); and (ii) metal extrusion due to heterogeneous interfacial stresses, which produces root-growth of fibrous structures (8,12,14). For $i > i_L$ morphological instability couples to the classical hydrodynamic instability known as electroconvection to produce much faster dendrite growth (15). A variety of technical approaches have been reported to be effective in eliminating/slowing Li dendrite proliferation by addressing one or more of these instability modes. Among the most effective are: (i) liquid electrolytes containing additives that change the chemistry and transport properties of the solid-electrolyte interphase (SEI) formed in contact with Li (16-22); (ii) artificial SEIs which simultaneously passivate the Li surface and enable fast & less heterogeneous ion transport (5,23-31); ion-transport regulators that may alter either the ion-flux to the electrode or size distribution the electrodeposition structures (32-37); (iii) high-shear modulus solid and viscoelastic liquid electrolytes that slow localized growth of dendritic structures by mechanical and/or polymer stresses (38-43); and (iv) advanced current collectors that enable dissipation of localized stresses developed in the metal during deposition (14,44-46) or which facilitate continuous electrical connection and, thereby, electrochemical access to orphaned metal deposits (44). While the majority of these studies emphasize the ability to produce anodes with non-dendritic morphology after several charge/discharge cycles, the recent work by Zheng et al. raises doubt about whether one is every truly able to achieve dendrite-free electrodeposition of Li on continuum length scales and in liquid electrolytes (47).

2.3 Results and Discussions

Here, we investigate the initial nucleation and growth dynamics of metallic Lithium in liquid electrolytes with/without components believed to make the deposition non-dendritic. We show that ionic diffusion in the solid-electrolyte interphase formed spontaneously on a Li electrodeposit plays a crucial role in the development and growth of electrodeposited Li nuclei. We show further that by combining theoretical analysis of the early-stage electrodeposit growth dynamics with experiments, it is possible to develop a comprehensive picture of the Lithium electrodeposition process. The study builds upon the existing nucleation and growth framework proposed by Barton et al. (48) and the recent work of Pei et al. (49) to elucidate the role interphases formed on Li play in regulating ionic transport to the growing nuclei. Lithium ions are galvanostatically electrodeposited onto a heterogeneous surface composed of polished stainless-steel (rms roughness = 9.12 ± 8.78 nm) from the bulk electrolyte (**Figure 2.1(a)**). The electrodeposition is carried out at different current densities in carbonate liquid electrolytes with/without fluorinated carbonated additives reported to suppress the chemical and morphological instability of Li (18, 50-52). The spatial characteristics (morphology, size, number density) of Li nuclei formed in the process are analyzed ex-situ using Scanning Electron Microscopy (SEM) and the interphases formed on the deposits studied using electrochemical impedance spectroscopy (EIS), goniometry and x-ray photoelectron spectroscopy (XPS).

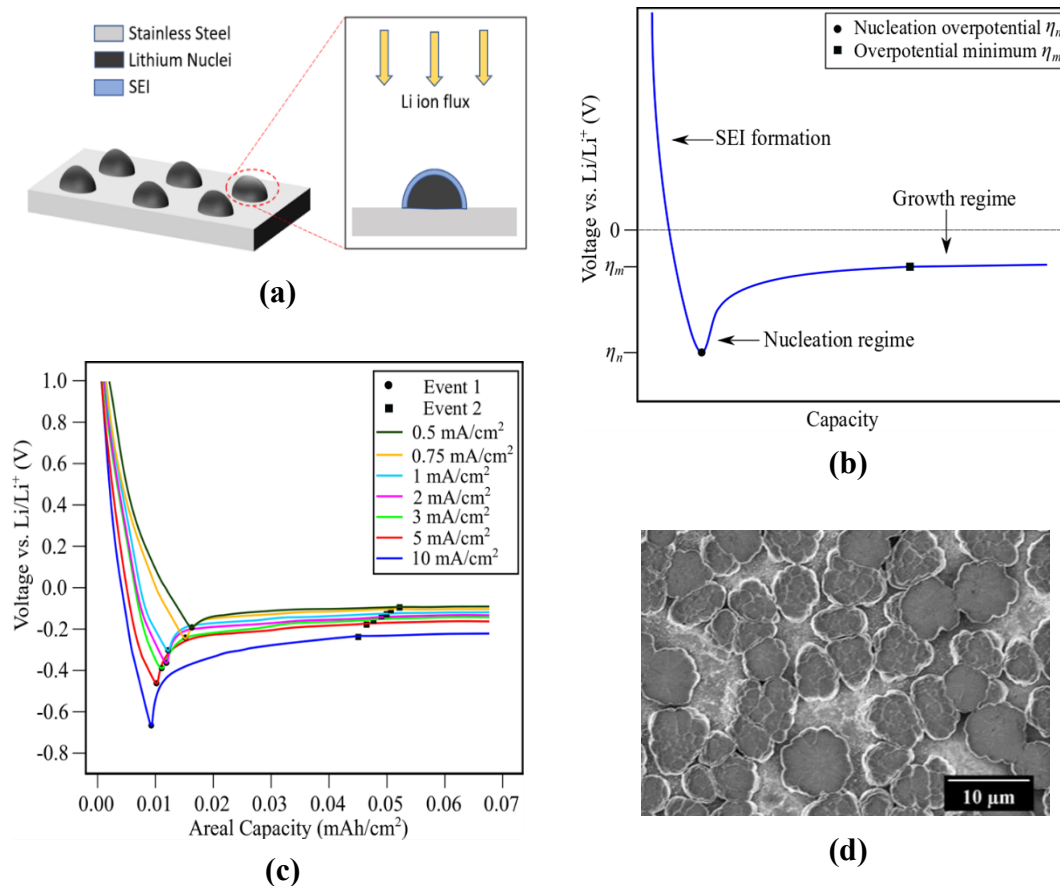


Figure 2.1. Fundamentals of lithium nucleation and growth. **(a)** Schematic showing electrodeposition of Li ion from the bulk electrolyte through the SEI on the stainless-steel substrate **(b)** Schematic plot showing a typical voltage profile of galvanostatic Li deposition (black). Nucleation Overpotential and Overpotential minimum are marked by Event 1 and Event 2 **(c)** Experimental voltage profiles of galvanostatic Li deposition for a range of current densities. The electrolyte is 1M LiPF_6 in EC:DMC (1:1 vol.%). Nucleation Overpotential and Overpotential minimum are marked by Event 1 and Event 2. **(d)** SEM image of the electrodeposited Lithium morphology captured at a current density of 0.5 mA/cm^2 and an areal capacity corresponding to that of Overpotential minimum. The electrolyte is 1M LiPF_6 in EC:DMC (1:1 vol.%).

To form nuclei of a particular size r at an electrode, reduced metal ions at the electrode must overcome a nucleation barrier that can be conveniently manipulated by adjusting the electrochemical supersaturation at the electrified interface. A measurable physical parameter characteristic of the electrochemical supersaturation is the overpotential. The driving force for nucleation may therefore be divided into three components: the charge transfer overpotential, diffusion overpotential, and interfacial (surface) energy overpotential (48,49,53,54). An additional consideration in the nucleation of reactive metals like Li concerns barriers to ionic transport through the SEI formed spontaneously at the metal/electrolyte interface (**Figure 2.1(a)**). These effects are captured theoretically by extending the nucleation and growth model for non-interacting hemispherical nuclei proposed by Barton et al. (48), to account for SEI diffusion:

$$\eta = \frac{RT}{\alpha F} \ln \frac{i}{i_0} + \frac{irRT}{D_B C_B F^2} + \frac{2\gamma V}{Fr} + \frac{ir^2 RT}{D_S C_S F^2} \quad (1)$$

Here η is the net overpotential due to all of the processes referenced above; i and i_0 are the current density and exchange current density respectively; r is the radius of the nuclei; D_B and C_B are the bulk electrolyte Li ion diffusivity and concentration respectively; D_S and C_S are the SEI Li ion diffusivity and concentration respectively, γ is the interfacial energy and α , V , R , T , F are charge transfer coefficient, molar volume of metal, universal gas constant, temperature and Faraday constant respectively.

Deconvoluting each of these overpotential contributions from the voltage response during galvanostatic Li electrodeposition is difficult as each of these overpotentials arise due to electrochemical processes occurring simultaneously. At current densities $i < i_L$,

the galvanostatic voltage response curve (**Figure 2.1(b)**) may nevertheless be divided into three distinct regimes: (a) An initial steep voltage drop, which is thought to be the result of reduction of the electrolyte components at the onset of electrode of polarization to produce an ion-conductive, solid-state electrolyte interphase (SEI) at the electrified interface. Because the SEI in typical carbonate liquids is self-limiting, for a clean heterogeneous interface with minimal intercalation or alloying, the capacity corresponding to the SEI formation step is quite low (7). (b) A sharp voltage spike corresponding to formation of Li nuclei at the electrified interface. The voltage spike reflects the electrochemical supersaturation needed to overcome the nucleation barrier. The voltage at the spike is therefore referred to as Nucleation Overpotential (η_n) and is marked as Event 1 in **Figure 2.1(b)**. The nucleation overpotential is a consequence of simultaneous charge transfer process and Li-solution interface formation process. Hence, it can be interpreted as a combination of charge transfer overpotential and interfacial formation overpotential. (c) A final regime in which the voltage initially rises before approaching a final plateau. This regime corresponds to the post-nucleation growth phase. The overpotential is mainly due to mass-transfer of Lithium ions from the bulk electrolyte through the SEI to the newly formed Li nuclei. The onset of voltage plateau is associated with an Overpotential Minimum (η_m), marked as Event 2 in **Figure 2.1(b)**. The minimum has been reported to show a gradual transition of rate-limiting step from charge transfer/interface formation controlled to mass transfer controlled (49). The plateau following the Overpotential minimum event can be attributed to a combination of bulk diffusion overpotential and SEI surface diffusion overpotential. Understanding how each of these three events is influenced by electrolyte chemistry is

the focus of this study. Anticipating comparisons with SEM experiments of electrodeposits, we first consider the prediction of equation 1 for η_m . Minimizing the net overpotential (η) with respect to the characteristic size (radius) of the nuclei, an inverse relationship between current density (i) and radius (r) of the nuclei is apparent (Equation 2).

$$i = \frac{1}{\tilde{r}^2 A' + \tilde{r}^3 B'} \quad \text{where } A' = \frac{RT}{2\gamma V D_B C_B F} \text{ and } B' = \frac{RT}{\gamma V D_S C_S F} \quad (2)$$

This minimum in the net overpotential is associated with a certain characteristic nuclei size, \tilde{r} , and a particular Li electrodeposition capacity (**Figure 2.1(b),(c)**). Equation 2 indicates that ionic diffusion in the bulk is associated with the term quadratic in \tilde{r}^2 , while ionic transport in the SEI produces a stronger, \tilde{r}^3 term in the current. Equation 2 also implies that the coefficients, A' and B' , associated with the \tilde{r}^2 and \tilde{r}^3 terms can be used, respectively, to infer information about the bulk ($C_B D_B$) and surface ($C_S D_S$) ionic conductivity. In other words, from measurements of the electrodeposit size at the beginning of the growth phase, it is possible to deduce information about the bulk and interfacial ion transport in an electrolyte.

We investigated electrodeposition of Li under galvanostatic conditions at a range of current densities (**Figure 2.1(c)**) followed by an ex-situ SEM observation of the Nuclei size, morphology (**Figure 2.1(d)**) and distribution. A conventional carbonate electrolyte, i.e. 1M LiPF₆ in EC:DMC (1:1 vol.%), was used in the study. At all current densities studied, the Overpotential Minimum, η_m , was observed at a relatively small areal capacity of the electrodeposited lithium (between 0.045 - 0.052 mAh/cm², depending

on the current density. If the Li electrodeposit density is assumed to be the same as the bulk metal, an equivalent of 250-300 nm of Li metal is deposited by η_m . The capacities for Nucleation Overpotential and Overpotential Minimum (**Figure 2.1(c)**) are higher for lower current densities. This may be due to extra capacity required owing to simultaneous formation of nascent SEI and Lithium nuclei at a lower rate of electrodeposition (49). A lower value of voltage at Overpotential Minimum than Nucleation Overpotential suggests that it is favorable for Li ions to electrodeposit on preexisting nuclei's rather than forming new nuclei embryos (**Figure 2.1(c)**).

To facilitate comprehensive postmortem studies, multiple replicates of Li electrodeposited on polished stainless-steel substrates were collected and analyzed via SEM and XPS. The areal capacity for a given current density was kept fixed for each of the replicates. The morphology of the Li electrodeposits obtained from SEM analysis is reported in **Figure 2.2(A)**. The bare bright stainless-steel substrate can be seen underneath the Li nuclei. The nuclei are distinct in size for different current densities, with smaller and densely distributed nuclei occurring at higher current densities. Larger conjoining blob-like-nuclei are visible at lower current densities, while smaller, distinct ones can be seen at higher current densities. At the lowest current density of 0.5 mA/cm² nuclei twice the size (2.25 μm compared to 1.18 μm) of those formed at the highest current density of 10 mA/cm² are observed. Also, higher nucleation overpotentials (*e.g.* 0.67 V at 10 mA/cm² compared to 0.19 V at 0.5 mA/cm²) and plateau overpotentials (*e.g.* 0.23 V at 10 mA/cm² compared to 0.09 V at 0.5 mA/cm²) are observed at higher current densities. These observations can be rationalized as follows. A higher current density imparts a higher activation overpotential and mass transfer overpotential

causing the overpotentials needed for the critical events to be higher. A higher nucleation overpotential η_n ensures the competing factors in nuclei formation i.e. Gibbs bulk free energy ($-\frac{4}{3}\pi r^3 F\eta_n/V$) and the compensating surface free energy ($4\pi r^2\gamma$) are larger. A larger compensating surface free energy is attained through an increased overpotential required for surface formation ($\frac{2\gamma V}{Fr}$), at the expense of inversely proportional critical size of the nuclei r . Hence, this leads to formation of greater number of smaller nuclei on the electrode surface at higher current densities (49). A greater number of nuclei embryos ensures less capacity of lithium ions deposited per nucleus in the subsequent growth phase, hence smaller lithium nuclei are observed as compared to the low current density case. A similar argument can explain the densely distributed nuclei observed at higher current densities.

The electrolyte chemistry has been reported to play an important role in Lithium electrodeposition (1,5,7,13). Fluorinated additives, in particular, have received intensive attention because of their reported influence on the morphology of Li electrodeposits formed in charge/discharge battery cycling experiments (16-19,22,50-52). We studied galvanostatic electrodeposition of Lithium in electrolytes containing Fluoroethylene carbonate (FEC) as a fluorinated additive. Previous studies showed that this additive breaks down to form LiF and Vinylene Carbonate (VC), which may electropolymerize at the reducing anode potentials to form a SEI enriched in fluorinated species (18,50-52). In order to determine the role of FEC on the morphology and interfacial properties of Li electrodeposit nuclei, 1M LiPF₆-EC/DMC electrolytes containing 0 to 50 wt.% of FEC were studied. The areal capacity at Overpotential Minimum η_m was observed to

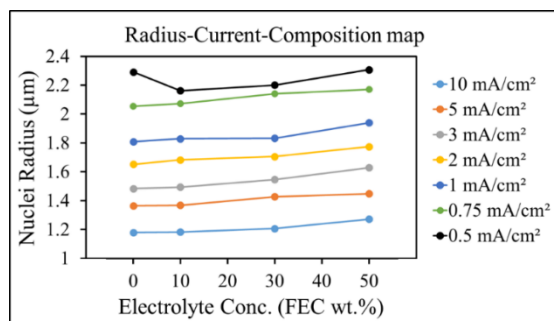
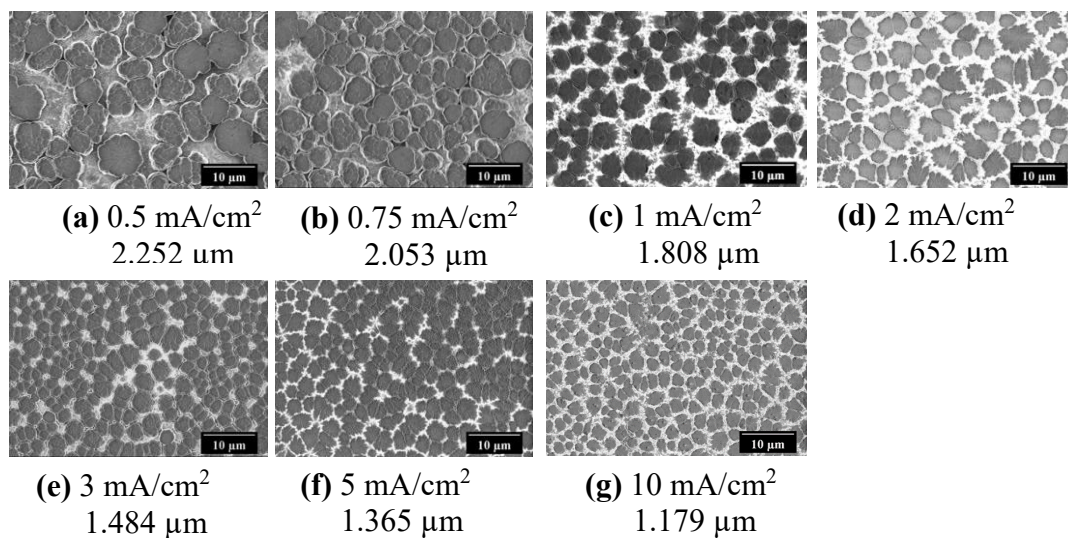
vary with electrolyte composition (*i.e.*, 0.041 - 0.05 mAh/cm² for 10 wt. % FEC, 0.037 - 0.045 mAh/cm² for 30 wt. % FEC, and 0.034 - 0.043 mAh/cm² for 50 wt. % FEC), over the range of current densities investigated (**Supplementary Figure 2.1**).

The morphology of Li electrodeposit nuclei in the FEC-enriched electrolytes are reported in **Supplementary Figure 2.2, 2.3, 2.4**, respectively, for electrolytes containing 10 wt.%, 30 wt.% and 50 wt.% FEC. The results show that at a fixed current density, the nuclei are enlarged and, particularly at low current density, noticeably flatter (*i.e.*, ink-stain-like, as opposed to hemispherical) at the higher FEC concentrations. The results reported in **Figure 2.2(B)** show that the average radius of Li electrodeposit nuclei at η_m measured in the FEC-enriched electrolytes decrease with increasing current density, in essentially the same manner as observed in the baseline 1M LiPF₆ EC:DMC case. The distribution of nuclei sizes was recovered from the images using the image analysis software ImageJ and represented as histograms in **Supplementary Figure 2.5, 2.6, 2.7, 2.8**. For all electrolytes, the distribution is noticeably broader at lower current densities. For example, for the baseline electrolyte (*i.e.* no FEC additive), at 0.5 mA/cm² the relative standard deviation of nuclei sizes is about 27%, compared to 22% at 10 mA/cm² (**Supplementary Figure 2.5**). It is also apparent that in most cases the nuclei size distributions can be crudely fitted to a normal distribution, implying that the demarcations in **Figure 2.1(b)** are at best crude. Specifically, while a large population of nuclei appear to form at a certain time, the breadth of the distribution suggest that smaller populations of nuclei may develop at later times and grow independently during the early stages of Li deposition.

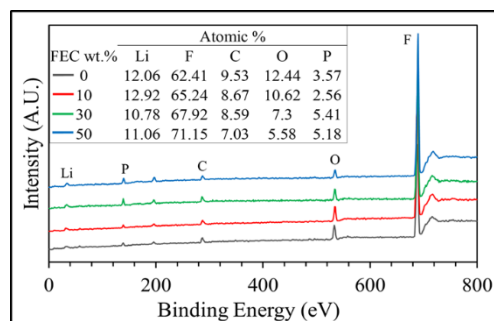
Simultaneously growing nuclei arising from instantaneous nucleation would lead to a sharper (more peaked distribution), whereas strictly continuous nucleation would lead to a flatter distribution of sizes. The situation is further complicated by the fact that a gaussian size dispersion can also arise from coalescence/fusing of instantaneously formed nuclei and/or heterogeneous ion transport (*e.g.*, due to a non-uniform distribution of inter-nucleus distances produced by the finite roughness of the electrode surface) to instantaneously formed nuclei (49,55,56,57). A broader distribution at lower current densities may also indicate that inter-nuclei diffusion coupling is important at low rates of electrodeposition (49).

X-ray Photoelectron spectroscopy (XPS) was performed to investigate the surface chemistry of SEI formed in electrolytes containing FEC. The results are reported in **Figure 2.2(C),(D),(E)** and **Supplementary Table 2.1**. While the average nuclei sizes are indifferent to the addition of FEC, distinct changes in the chemical composition of the SEI can be observed. A single dominant peak corresponding to fluorine is observed at about 685 eV; the peak increases in height as FEC content rises in the electrolytes. Analyzing the atomic % it can be inferred that a FEC-enriched electrolyte has greater concentration of Fluorine groups in the SEI, i.e. 71.15 at.% F for 50 wt.% FEC compared to 62.41 at.% F for 0 wt.% FEC (**Figure 2.2(C)**). Similarly by contrasting the atomic %, it can also be inferred that the Fluorine to Oxygen at.% ratio (F:O) in the SEI increases significantly with addition of FEC. For 50 wt.% FEC the F:O ratio is 12.75, which is approximately 250% higher than the corresponding ratio (5.02) at 0 wt.% FEC.

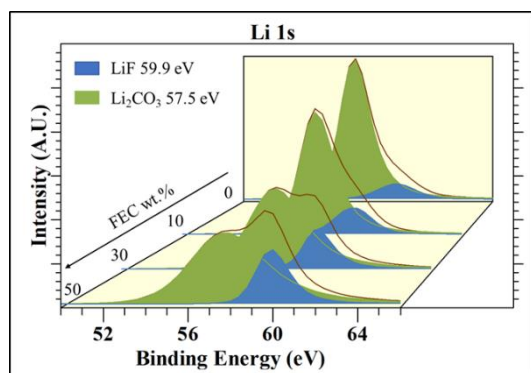
(A)



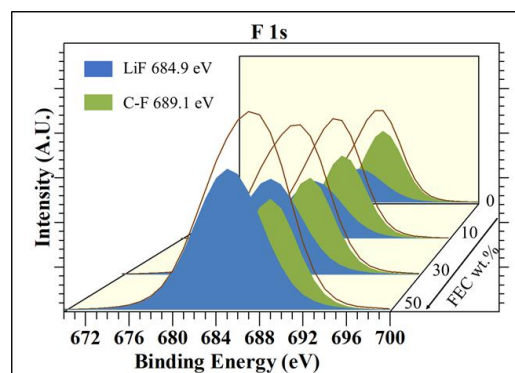
(B)



(C)



(D)



(E)

Figure 2.2. Effect of current density and electrolyte chemistry on the morphology and interfacial chemistry of Lithium electrodeposits. **(A)** Ex situ SEM images of Li deposited on stainless-steel at current densities of **(a)** 0.5 **(b)** 0.75 **(c)** 1 **(d)** 2 **(e)** 3 **(f)** 5 **(g)** 10 mA/cm², respectively. At lower current densities, the stainless-steel substrate is visible underneath the sparsely distributed Li nuclei. The electrolyte is 1M LiPF₆ in EC: DMC (1:1 vol.%). **(B)** Plot of Nuclei radius for a range of current densities for varying concentration of FEC (0, 10, 30, 50 wt.%) in 1M LiPF₆ EC: DMC (1:1 vol.%). **(C)** Chemical spectra of the SEI layer induced by varying concentrations of FEC (0, 10, 30, 50 wt.%) in 1M LiPF₆ EC: DMC (1:1 vol.%). **(D)**, **(E)** Li 1s and F 1s spectra of the SEI layer induced by varying concentrations of FEC (0, 10, 30, 50 wt.%) in 1M LiPF₆ EC: DMC (1:1 vol.%). The total areal capacity corresponds to that of Overpotential Minimum (Event 2).

A closer look at the high-resolution individual element spectra of Lithium and Fluorine is necessary to further understand the nature of bonding in the FEC-induced SEI. There are two peaks observed in the Li 1s spectra: LiF at 59.9 eV and Li₂CO₃ at 57.5 eV (**Figure 2.2(D)**). The LiF peak is enhanced for higher wt.% of FEC i.e., 25.12% LiF, 74.88% Li₂CO₃ at 50 wt.% FEC compared to 10.96% LiF, 89.04% Li₂CO₃ at 0 wt.% FEC (**Supplementary Table 2.1**). Similar inferences can be drawn for the F 1s spectra where two peaks are also observed: LiF at 684.9 eV and C-F at 689.1 eV (**Figure 2.2(E)**). Along with similar enhancement of the LiF peak, FEC-induced SEI shows a higher proportion of LiF than C-F i.e., 61.65% LiF, 38.35% C-F at 50 wt.% FEC contrasted to 37.42% LiF, 62.56% C-F at 0 wt.% FEC. The XPS results are consistent with earlier reports (18,50-52) and corroborate the fact that LiF-rich fluorinated SEI is formed via the decomposition of the FEC, even during the earliest stages of Li electrodeposition.

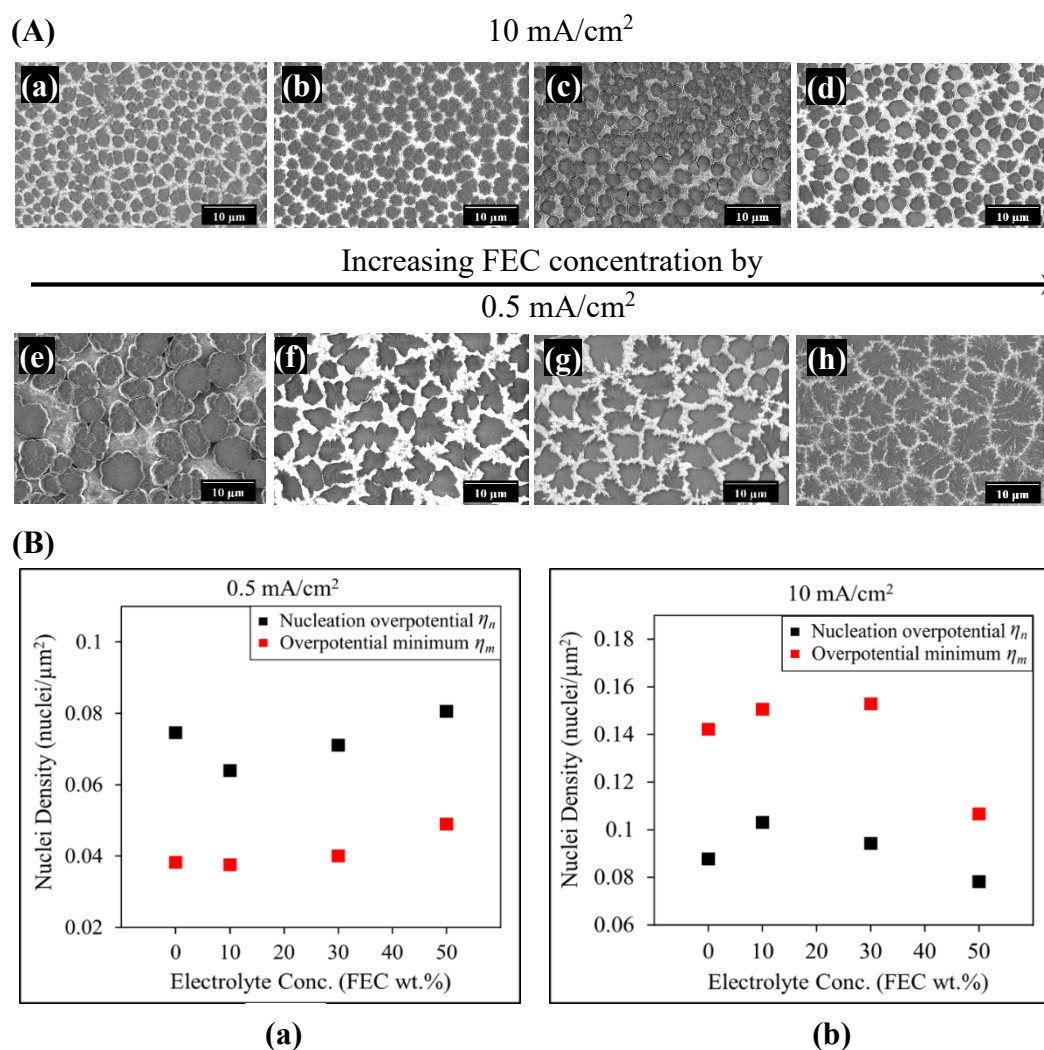


Figure 2.3. Effect of electrolyte chemistry on the morphology and nuclei density of Lithium electrodeposits at contrasting current densities. **(A)** Ex situ SEM images of Li nuclei deposited on stainless-steel for current densities of 10 mA/cm^2 and 0.5 mA/cm^2 for increasing concentration of FEC **(a,e)** 0 **(b,f)** 10 **(c,g)** 30 **(d,h)** 50 wt.% in 1M LiPF_6 EC: DMC (1:1 vol.%). The total areal capacity corresponds to that of Overpotential Minimum (Event 2). **(B)** Plot of the Nuclei Density for varying concentration of FEC (0, 10, 30, 50 wt.%) in 1M LiPF_6 EC: DMC (1:1 vol.%) at **(a)** 0.5 mA/cm^2 **(b)** 10 mA/cm^2 . The Nucleation Overpotential and Overpotential Minimum are shown in black and red respectively.

A closer look at the spatial evolution of these nuclei between the two critical events (Nucleation Overpotential and Overpotential Minimum) shall aid our understanding of the nucleation process and growth dynamics. We performed detailed galvanostatic electrodeposition studies at two contrasting current densities (0.5 mA/cm² and 10 mA/cm²) followed by ex-situ SEM observation of the Nuclei size and morphology (**Supplementary Figure 2.9**). The areal capacity at the Nucleation Overpotential (η_n) were recorded under these conditions: 0.009 - 0.016 mAh/cm² for 0 wt.% FEC, 0.008 - 0.014 mAh/cm² for 10 wt. % FEC, 0.007 - 0.012 mAh/cm² for 30 wt. % FEC, and 0.006 - 0.011 mAh/cm² for 50 wt. % FEC depending on 0.5 mA/cm² or 10 mA/cm² respectively. **Figure 2.3(A)** reports the analogous areal capacities recorded at η_m . The areal density of the nuclei for both events were also estimated from the SEM images and plotted in **Figure 2.3(B)**. Overall, densely distributed nuclei occur for the higher current density (10 mA/cm²) at both events and at all electrolyte compositions. As mentioned earlier, a high current density gives rise to a higher nucleation overpotential at the interface, which leads to formation of a greater number of nuclei (49). At the lower current density of 0.5 mA/cm², the nuclei sizes observed at η_n are smaller than at η_m . For example, for 0 wt.% FEC, the average nucleus size (radius) is about 1.81 μm compared to 2.25 μm at η_m (**Supplementary Figure 2.9(e)** vs **Figure 2.3(A)(e)**). The areal coverage of the nuclei is also higher at η_m . (e.g., for 0 wt.% FEC at 0.5 mA/cm², the nuclei density is about 0.075 nuclei/ μm^2 at η_n compared to 0.038 nuclei/ μm^2 at η_m). This observation spans all electrolyte chemistries and suggests that as the formed nuclei grow, they also tend to agglomerate/fuse (49). The decreasing overpotential after the peaking and subsequent plateauing of the Overpotential Curve (**Figure 2.1(c)**,

Supplementary Figure 2.1) in between these events is consistent with growth on preexisting nuclei. Simultaneous growth and agglomeration would lead to less dense, larger nuclei at low current density.

There is a significant change in morphology of the electrodeposits at a lower current density for the FEC-enriched electrolytes as is apparent from **Figure 2.3(A)(e),(f),(g),(h)** (at η_m) and **Supplementary Figure 2.9(e),(f),(g),(h)** (at η_n). At 0.5 mA/cm², the nuclei size and density increase with the incorporation of FEC. The morphology of the nuclei transition from hemispherical 3-D spherical structures to flat 2-D structures. These differences are apparent even at 10 wt.% FEC but are more pronounced at higher FEC content. **Supplementary Figure 2.10** shows the effect the fluorinated electrolyte chemistry at an even lower current density of 0.05 mA/cm². The planarizing effect is evident at even lower FEC contents and the nuclei appear to flow into each other, more fully utilizing the surface area of the stainless-steel substrate. The capacities at the critical events are also lower (see **Supplementary Figure 2.11(a)**), implying that the 2-D nuclei require lower capacity to nucleate and grow at low current densities. None of these electrolyte-chemistry dependent effects are observed at a high current density of 10 mA/cm² (see **Figure 2.3(A)(a),(b),(c),(d)**) indicating that their origins are associated with changes in deposition dynamics induced by the FEC. Previously, XPS analysis revealed that the SEI formed on Li in a FEC-containing electrolyte is enriched in fluorine containing species, including LiF. And a LiF-rich SEI has been postulated to have high surface energy and to pose lower barriers to surface diffusion (58-61). Higher interphase mobility enhances rearrangement of Li ions prior to deposition, facilitating more uniform and compact electrodeposition. Hence, it is

relevant to investigate the role of physical parameters such as interfacial energy and surface diffusion in the planarizing effect of fluorinated additives.

The theory correlating the current density with the observed nuclei size (**Equation 2**) serves as a useful tool for unravelling the contributions made by surface energetic, bulk, and surface transport parameters. The squared/cubic relationship of the nuclei radius

with the applied current density i.e., $i = \frac{1}{\tilde{r}^2 A' + \tilde{r}^3 B'}$ contains coefficients (A' and B')

which have surface diffusivity (D_S), surface concentration (C_S) and interfacial energy (γ) embedded in them. A proof of concept analysis was performed to fit the current density with the observed nuclei size \tilde{r} at η_m using **Equation 2** (see SI on Curve fitting). Three

distinct cases were considered to determine the relevance of each mass transfer overpotential in the growth phase as demonstrated in **Figure 2.4(a),(b),(c)**. In Case 1

(**Figure 2.4(a)**), we ignore surface diffusion (i.e., $A' \gg B'$) and in Case 2 (**Figure**

2.4(b)) we ignore the contribution to the transport overpotential originating from ion migration in the electrolyte bulk (i.e., $B' \gg A'$). In Case 3 (**Figure 2.4(c)**) we consider

the case where the surface and bulk diffusion make comparable contributions to the transport overpotential. The vastly improved quality of the fit for Case 3, relative to

Cases 1 and 2 confirm that a combination of mass transfer overpotentials due to bulk diffusion and SEI diffusion are important in determining η_m . A similar proof of concept

analysis was carried out for all of the fluorinated/non-fluorinated carbonate-based electrolyte compositions studied as shown in **Supplementary Figure 2.12**. Motivated

by the ability of Equation 2 to quantitatively replicate the i versus \tilde{r} data for the full set of carbonate electrolytes used in the study, we also compared the model predictions to

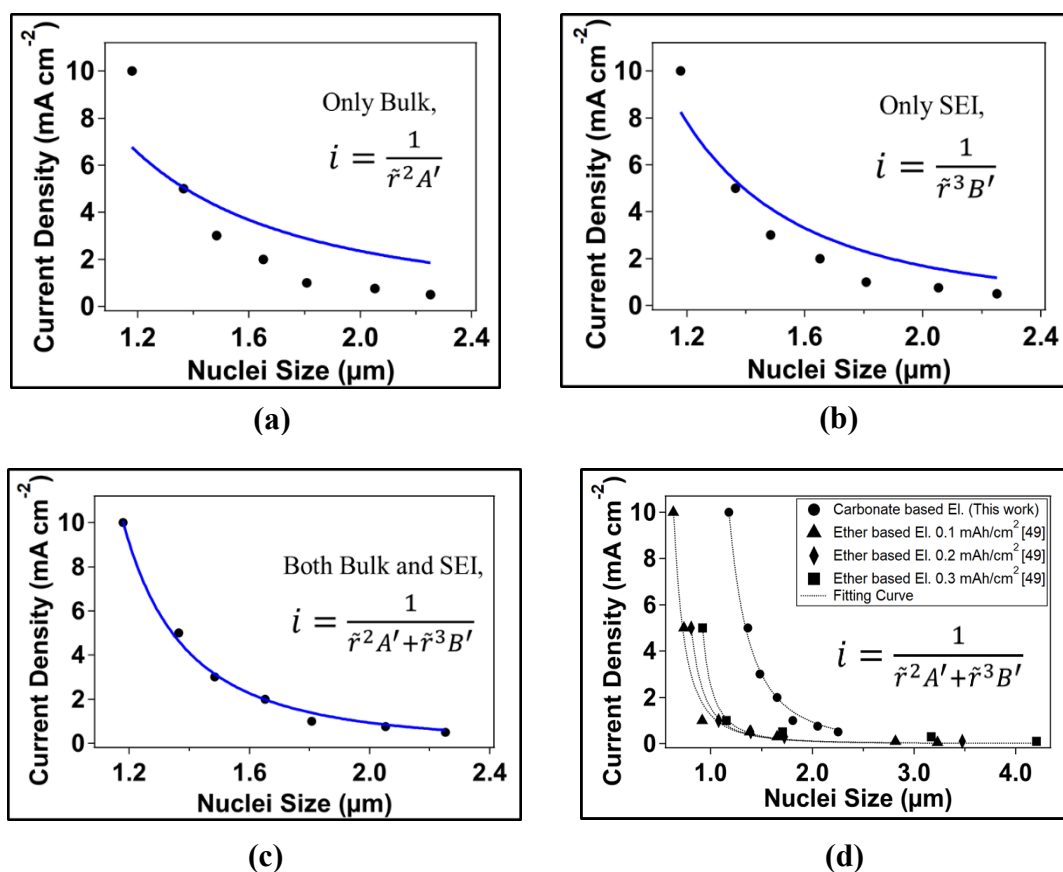


Figure 2.4. Proof of concept curve fitting at Overpotential Minimum and growth capacities. **(a)** The dependency of average nuclei radius on current density has been restricted to the effects of bulk diffusion overpotential only. **(b)** The dependency of average nuclei radius on current density has been restricted to the effects of SEI surface diffusion overpotential only. **(c)** The dependency of average nuclei radius on current density involving the synergistic effects of bulk diffusion overpotential and SEI diffusion overpotential. The electrolyte is 1M LiPF₆ in EC: DMC (1:1 vol.%) and the nuclei data is collected for areal capacities corresponding to Overpotential Minimum (Event 2). **(d)** The dependency of average nuclei radius on current density involving the synergistic effects of bulk diffusion and SEI diffusion overpotential for nuclei formed from carbonate-based electrolyte (this work) and ether-based electrolyte (49).

literature results for ether-based electrolyte compositions studied in the work of Pei et al. (49). The results reported in **Figure 2.4(d)** show that the model predictions are in quantitative accord with the observations reported by Pei et al. (49); the corresponding parameters are provided in **Supplementary Table 2.2**. We therefore conclude that in every situation, the Case 3 physics provide the best description of available \tilde{r} versus i data, for Li electrodeposition in liquid electrolytes.

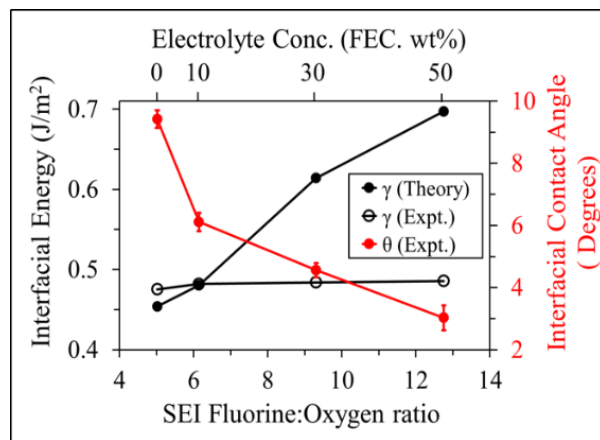
We estimated the interfacial energy (γ) for Lithium in carbonate electrolytes with different FEC contents using contact angle measurements performed in an Argon-filled glove box. The results reported in **Figure 2.5(a)**, **Supplementary Table 2.3** show that γ increases gradually from 475 mJ/m² to 486 mJ/m² as the FEC content is increased from 0 to 50 wt.%. Electrolyte wetting of studies (**Supplementary Figure 2.13**) indeed reveal better Li wettability at higher concentration of FEC. The average contact angle formed between the electrolyte and Li ranges from 9.42° to 3.03° when the FEC content ranges from 0 wt.% FEC to 50 wt.% (**Figure 2.5(a)**). The lowering of the contact angle is consistent with the higher γ . Using the best-fit values of A' and B' obtained by fitting the empirical \tilde{r} versus i data using **Equation 2**, we calculate the actual γ values under conditions of the electrodeposition experiments. The results (**Figure 2.5(a)**) show that while the values of γ are comparable to the ones estimated from the contact angle experiment, those obtained by fitting the Li nucleate size data are a stronger function of FEC content (γ ranges from 454 mJ/m² to 697 mJ/m² with the addition of FEC). The mismatch between the experimentally estimated and theoretical values of γ can be two-fold. First, Young's equation employed to calculate the interfacial energy is valid for

interfaces with lower interfacial energy than the solid substrate (in this case Lithium) (62). Second, the interphases formed on Li by reduction of FEC under the deposition conditions are more enriched in fluorinated species than those formed on Li in contact with the electrolyte under ambient conditions.

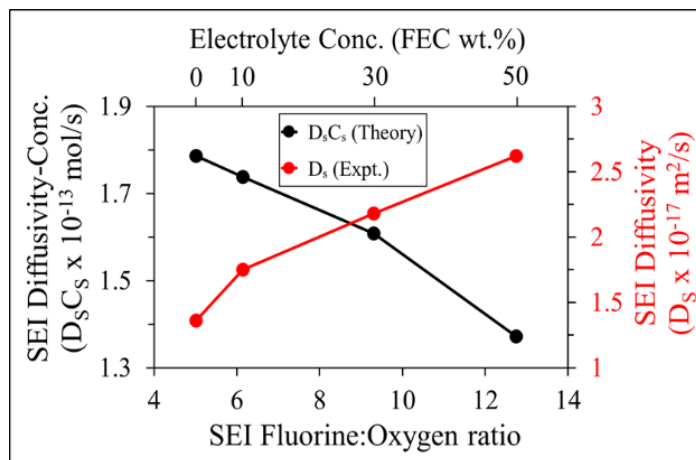
Electrochemical Impedance Spectroscopy was performed on Lithium electrodeposited on polished stainless steel to determine the surface and bulk transport characteristics (**Supplementary Figure 2.15, Figure 2.5(b)**). The product of surface diffusivity and surface concentration decreases with the incorporation of FEC as shown in **Figure 2.5(b)**. However, the surface diffusivity of Li ions is observed to increase with increasing concentration of FEC (e.g., D_S is $2.62 \times 10^{-17} \text{ m}^2/\text{s}$ at 50 wt.% FEC contrasted to $1.36 \times 10^{-17} \text{ m}^2/\text{s}$ at 0 wt.% FEC), a roughly two-fold increase in D_S . A decreasing $C_S D_S$ value therefore means that the surface concentration of Li ions at the electrode decreases quite rapidly as FEC concentration rises (**Supplementary Table 2.4**). The surface concentration C_S is $1.313 \times 10^4 \text{ mol/m}^2$ at 0 wt.% FEC compared to $0.523 \times 10^4 \text{ mol/m}^2$ at 50 wt.% FEC, i.e. more than a two-fold decrease in the concentration, which is consistent with the two-step (surface ion transport \rightarrow Li-ion reduction) reaction assumed in **Equation 2** when the surface ion transport is rate limiting.

A higher surface diffusivity indicates relatively easier 2-D migration of Li ions in the fluorinated SEI, promoting more spread-out/delocalized electrodeposition. Assuming fast reduction kinetics of Li-ions at the electrode, a higher D_S would also lower the concentration of Li ions in the SEI. This also explains the lowering of the SEI and charge transfer resistance evident in **Supplementary Figure 2.15. (c)** and is consistent with

previous reports (50). Synergistically, high surface diffusivity and high interfacial energy of the fluorinated SEI facilitates planar electrodeposits as observed earlier for fluorinated electrolytes (10 – 50 wt.% FEC). On the other hand, the carbonated electrolyte (0 wt.% FEC) lacking such interfacial advantages forms 3-D, blob like nuclei which have higher probability of succumbing to the morphological instability that drives growth of mossy/dendritic Li electrodeposit morphologies. Recent modelling studies have shown the SEI diffusivity (63-66) to be anywhere in between 10^{-16} m²/s to 10^{-26} m²/s and SEI surface energy (12,67-69) to be in between 0.18 J/m² to 0.84 J/m², with higher values (10^{-16} m²/s and 0.84 J/m²) reported for a purely LiF interface. The range of surface diffusivity and interfacial energy values deduced by fitting Equation 2 to the empirical \tilde{r} are in rough agreement with these values. **Supplementary Figure 2.15 (d)** shows further that the bulk diffusivity (10^{-10} m²/s) of Li ions is about seven order of magnitude higher than the surface diffusivity (10^{-17} m²/s), implying that even a highly fluorinated interphase has a *throttling* effect on transport of Li-ions arriving from the bulk. This mismatch in bulk and interphase diffusivities will produce a rapid piling-up of ions at the electrolyte/electrode interface, ultimately leading to non-planar mossy/dendritic electrodeposition of Li even in fluorinated electrolytes. Similarly, accumulation of Li ion vacancies underneath the SEI during Li anode stripping has been shown to be detrimental for the adherence/passivity of the SEI layer (70). Electrolyte and interphases that lower the bulk/surface diffusivity ratio are therefore predicted to be essential for achieving compact, planar electrodeposition of Li in liquid electrolytes.



(a)



(b)

Figure 2.5. Effect of electrolyte chemistry/surface chemistry on the interfacial energy, interfacial contact angle, surface diffusivity, and concentration and of the SEI. **(a)** Plot of SEI interfacial energy (theoretically/experimentally determined) and interfacial contact angle (experimentally determined) for varying concentration of FEC (0, 10, 30, 50 wt.%) in 1M LiPF₆ EC: DMC (1:1 vol.%) electrolyte and corresponding Fluorine to Oxygen ratio in the SEI layer. **(b)** Plot of SEI surface diffusivity-concentration (theoretically determined) and SEI surface diffusivity (experimentally determined) for varying concentration of FEC (0, 10, 30, 50 wt.%) in 1M LiPF₆ EC: DMC (1:1 vol.%) electrolyte and corresponding Fluorine to Oxygen ratio in the SEI layer.

2.4 Conclusion

In summary, we study the effect of electrolyte chemistry on the morphology, size, density, spatial distribution, surface chemistry of early-stage Li nuclei formed at different rates of electrodeposition. The underlying physics of Lithium (reactive metal) nucleation and growth through electrodeposition is elucidated. A comprehensive understanding of the galvanostatic Overpotential curve and the square-cubic inverse dependency of nuclei radius on current density is demonstrated and experimentally correlated. Such a dependency reveals both bulk ion diffusion and surface ion diffusion to play equally important role in Lithium electroplating. Theoretical formulations along with aptly designed experiments also reveal interfacial dynamics of the SEI. Designing interfaces with high surface energy and high surface diffusivity is a feasible solution to eliminate dendritic morphology of electrodeposited Lithium. Additional studies dealing with understanding the nucleation and growth dynamics of reactive metals are cardinal to understand the morphological and chemical instabilities originating at early stages of electrodeposition. Understanding and elimination of the instabilities at the initiation step would enable uniform and compact plating of reactive metals.

2.5 Acknowledgement

The research was supported as part of the Center for Mesoscale Transport Properties, an Energy Frontier Research Center supported by the U.S. Department of Energy (DOE), Office of Science, Basic Energy Sciences, under Award DE-SC0012673. The electron microscopy facilities made use of the Cornell Center for Materials Research Shared Facilities which are supported through the NSF MRSEC program (DMR-1719875). The interface characterization work made use of the facilities available in CESI, Cornell.

2.6 References

- (1) Zhang, J.G.; Xu, W.; Henderson, W.A. *Lithium metal anodes and rechargeable lithium metal batteries*; Springer International Publishing: Switzerland, **2017**.
- (2) Whittingham, M. S. History, evolution, and future status of energy storage. *Proc. IEEE*, **2012**, *100*, 1518-1534.
- (3) Aurbach, D.; Cohen, Y. *J. Electrochem. Soc.* **1996**, *143*, 3525-3532.
- (4) Xu, W.; Wang, J.; Ding, F.; Chen, X.; Nasybulin, E.; Zhang, Y.; Zhang, J.G. *Energy Environ. Sci.* **2014**, *7*, 513–537.
- (5) Tikekar, M. D.; Choudhury, S.; Tu, Z.; Archer, L. A. *Nat. Energy* **2016**, *1*, 16114.
- (6) Chianelli, R.R. *J. Cryst. Growth* **1976**, *34*, 239-244.
- (7) Aurbach, D.; Zinigrad, E.; Cohen, Y.; Teller, H. *Solid State Ionics* **2002**, *148*, 405-416.
- (8) Zachman, M. J.; Tu, Z.; Choudhury, S.; Archer, L. A.; Kourkoutis, L. F. *Nature* **2018**, *560*, 345.

- (9) Chandrashekar, S.; Trease, N. M.; Chang, H. J.; Du, L. S.; Grey, C.P.; Jerschow, A. *Nat. Mater.* **2012**, *11*, 311-315.
- (10) Monroe, C.; Newman, J. *J. Electrochem. Soc.* **2005**, *152*, A396-A404.
- (11) Tang, M.; Albertus, P.; Newman, J. *J. Electrochem. Soc.* **2009**, *156*, A390-A399.
- (12) Yamaki, J. I. *J. Power Sources* **1998**, *74*, 219-227.
- (13) Wood, K. N.; Kazyak, E.; Chadwick, A. F.; Chen, K. H.; Zhang, J. G.; Thornton, K.; Dasgupta, N. P. *ACS Cent. Sci.* **2016**, *2*, 790-801.
- (14) Wang, X.; Zeng, W.; Hong, L.; Xu, W.; Yang, H.; Wang, F.; Duan, H.; Tang, M.; Jiang, H. *Nat. Energy* **2018**, *3*, 227.
- (15) Li, G.; Archer, L. A.; Koch, D. L. *Phys. Rev. Lett.* **2019**, *122*, 124501.
- (16) Miao, R.; Yang, J.; Feng, X.; Jia, H.; Wang, J.; Nuli, Y. *J. Power Sources* **2014**, *271*, 291-297.
- (17) Qian, J.; Henderson, W. A.; Xu, W.; Bhattacharya, P.; Engelhard, M.; Borodin, O.; Zhang, J.-G. *Nat. Commun.* **2015**, *6*, 6362.
- (18) Suo, L.; Xue, W.; Gobet, M.; Greenbaum, S. G.; Wang, C.; Chen, Y.; Yang, W.; Li, Y.; Li, J. *Proc. Natl. Acad. Sci.* **2018**, *115*, 1156-1161.
- (19) Gordin, M. L.; Dai, F.; Chen, S.; Xu, T.; Song, J.; Tang, D.; Azimi, N.; Zhang, Z.; Wang, D. *ACS Appl. Mater. Interfaces* **2014**, *6*, 8006–8010.
- (20) Aurbach, D.; Pollak, E.; Elazari, R.; Salitra, G.; Kelley, C. S.; Affinito, J. *J. Electrochem. Soc.* **2009**, *156*, A694-A702.
- (21) Kim, H.; Wu, F.; Lee, J. T.; Nitta, N.; Lin, H.-T.; Oschatz, M.; Cho, W. I.; Kaskel, S.; Borodin, O.; Yushin, G. *Adv. Energy Mater.* **2014**, *5*, 1401792.
- (22) Choudhury, S.; Archer, L. A. *Adv. Electron. Mater.* **2016**, *2*, 1500246.

- (23) Cheng, X.-B.; Zhang, R.; Zhao, C.-Z.; Wei, F.; Zhang, J.-G.; Zhang, Q. *Adv. Sci.* **2015**, *3*, 1500213.
- (24) Lin, D.; Liu, Y.; Cui, Y. *Nat. Nanotechnol.* **2017**, *12*, 194-206.
- (25) Zheng, G.; Lee, S. W.; Liang, Z.; Lee, H.-W.; Yan, K.; Yao, H.; Wang, H.; Li, W.; Chu, S.; Cui, Y. *Nat. Nanotechnol.* **2014**, *9*, 618-623.
- (26) Zhang, J.; Yang, X.; Wang, R.; Dong, W.; Lu, W.; Wu, X.; Wang, X.; Li, H.; Chen, L. *J. Phys. Chem. C* **2014**, *118*, 20756-20762.
- (27) Zhang, Y.; Wang, W.; Tang, H.; Bai, W.; Ge, X.; Wang, X.; Gu, C.; Tu, J. *J. Power Sources* **2015**, *277*, 304-311.
- (28) Lee, H.; Lee, D. J.; Kim, Y.-J.; Park, J.-K.; Kim, H.-T. *J. Power Sources* **2015**, *284*, 103-108.
- (29) Haregewoin, A. M.; Wotango, A. S.; Hwang, B.-J. *Energy Environ. Sci.* **2016**, *9*, 1955-1988.
- (30) Umeda, G. A.; Menke, E.; Richard, M.; Stamm, K. L.; Wudl, F.; Dunn, B. *J. Mater. Chem.* **2011**, *21*, 1593-1599.
- (31) Wang, X.; Hou, Y.; Zhu, Y.; Wu, Y.; Holze, R. *Sci. Rep.* **2013**, *3*, 1401.
- (32) Bates, J. B.; Dudney, N. J.; Gruzalski, G. R.; Zuhr, R. A.; Choudhury, A.; Luck, C. F.; Robertson, J. D. *Solid state ionics* **1992**, *53*, 647-654.
- (33) Li, J.; Ma, C.; Chi, M.; Liang, C.; Dudney, N. J. *Adv. Energy Mater.* **2015**, *5*(4), 1401408.
- (34) Kanno, R.; Murayama, M. *J. Electrochem. Soc.* **2001**, *148*, 742-746.
- (35) Lu, Y.; Tikekar, M.; Mohanty, R.; Hendrickson, K.; Ma, L.; Archer, L.A. *Adv. Energy Mater.* **2015**, *5*, 1402073.

- (36) Song, J.; Lee, H.; Choo, M.-J.; Park, J.-K.; Kim, H.-T. *Sci. Rep.* **2015**, *5*, 14458.
- (37) Cheng, X. B.; Hou, T. Z.; Zhang, R.; Peng, H. J.; Zhao, C. Z.; Huang, J. Q.; Zhang, Q. *Adv. Mater.* **2016**, *28*, 2888-2895.
- (38) Stone, G. M.; Mullin, S. A.; Teran, A. A.; Hallinan, D. T.; Minor, A. M.; Hexemer, A.; Balsara, N. P. *J. Electrochem. Soc.* **2012**, *159*, A222–A227.
- (39) Giles, J. R. M.; Gray, F. M.; Maccallum, J. R.; Vincent, C. A. *Polymer* 1987, *28*, 1977-1981.
- (40) Khurana, R.; Schaefer, J. L.; Archer, L. A.; Coates, G. W. *J. Am. Chem. Soc.* **2014**, *136*, 7395-7402.
- (41) Pan, Q.; Smith, D. M.; Qi, H.; Wang, S.; Li, C. Y. *Adv. Mater.* 2015, *27*, 5995-6001.
- (42) Choudhury, S.; Mangal, R.; Agrawal, A.; Archer, L. A. *Nat. Commun.* **2015**, *6*, 10101.
- (43) Gurevitch, I.; Buonsanti, R.; Teran, A. A.; Gludovatz, B.; Ritchie, R. O.; Cabana, J.; Balsara, N. P. *J. Electrochem. Soc.* **2013**, *160*, A1611–A1617.
- (44) Yang, C. P.; Yin, Y. X.; Zhang, S. F.; Li, N. W.; Guo, Y. G. *Nat. Commun.* **2015**, *6*, 8058.
- (45) Zhamu, A.; Chen, G.; Liu, C.; Neff, D.; Fang, Q.; Yu, Z.; Xiong, W.; Wang, Y.; Wang, X.; Jang, B.Z. *Energy Environ. Sci.* **2012**, *5*, 5701-5707.
- (46) Ji, X.; Liu, D.Y.; Prendiville, D.G.; Zhang, Y.; Liu, X.; Stucky, G.D. 2012. *Nano Today* **2012**, *7*, 10-20.
- (47) Zheng, J.; Tang, T.; Zhao, Q.; Liu, X.; Deng, Y.; Archer, L. A. *ACS Energy Lett.* **2019**, *4*, 6, 1349-1355.
- (48) Barton, J. L.; Bockris, J. O. M. *Proc. R. Soc. London, Ser. A* **1962**, *268*, 485-505.

- (49) Pei, A.; Zheng, G.; Shi, F.; Li, Y.; Cui, Y. *Nano letters* **2017**, *17*, 1132-1139.
- (50) Zhang, X. Q.; Cheng, X. B.; Chen, X.; Yan, C.; Zhang, Q. *Adv. Funct. Mater.* **2017**, *27*, 1605989.
- (51) Markevich, E.; Salitra, G.; Chesneau, F.; Schmidt, M.; Aurbach, D. *ACS Energy Lett.* **2017**, *2*, 1321-1326.
- (52) Zhang, X.Q.; Chen, X.; Cheng, X.B.; Li, B.Q.; Shen, X.; Yan, C.; Huang, J.Q.; Zhang, Q. *Angew. Chem., Int. Ed.* **2018**, *57*, 5301-5305.
- (53) Winand, R. *J. Appl. Electrochem.* **1991**, *21*, 377-385.
- (54) Vetter, K. *J. Electrochemical Kinetics Theoretical Aspects*; Elsevier Science: Burlington, **2013**.
- (55) Fransaer, J. L.; Penner, R. M. *J. Phys. Chem. B* **1999**, *103*, 7643-7653.
- (56) Penner, R. M. *J. Phys. Chem. B* **2002**, *106*, 3339-3353.
- (57) Serruya, A.; Mostany, J.; Scharifker, B. R. *J. Chem. Soc., Faraday Trans.* **1993**, *89*, 255-261.
- (58) Lu, Y.; Tu, Z.; Archer, L. A. *Nat. Mater.* **2014**, *13*, 961.
- (59) Gunceler, D.; Letchworth-Weaver, K.; Sundararaman, R.; Schwarz, K. A.; Arias, T. A. *Modell. Simul. Mater. Sci. Eng.* **2013**, *21*, 074005.
- (60) Michan, A. L.; Parimalam, B. S.; Leskes, M.; Kerber, R. N.; Yoon, T.; Grey, C. P.; Lucht, B. L. *Chem. Mater.* **2016**, *28*, 8149-8159.
- (61) Sun, H. H.; Dolocan, A.; Weeks, J. A.; Rodriguez, R.; Heller, A.; Mullins, C. B. *J. Mater. Chem. A* **2019**, *7*, 17782-17789.
- (62) Zhu, D.; Liao, X.; Dai, P. *Chin. Sci. Bull.* **2012**, *57*, 4517-4524.
- (63) Benitez, L.; Seminario, J. M. *J. Electrochem. Soc.* **2017**, *164*, E3159-E3170.

- (64) Guan, P.; Liu, L.; Lin, X. *J. Electrochem. Soc.* **2015**, *162*, A1798-A1808.
- (65) Yildirim, H.; Kinaci, A.; Chan, M. K.; Greeley, J. P. *ACS Appl. Mater. Interfaces* **2015**, *7*, 18985-18996.
- (66) Tasaki, K.; Goldberg, A.; Lian, J. J.; Walker, M.; Timmons, A.; Harris, S. J. *J. Electrochem. Soc.* **2009**, *156*, A1019-A1027.
- (67) Liu, Z.; Qi, Y.; Lin, Y. X.; Chen, L.; Lu, P.; Chen, L. Q. *J. Electrochem. Soc.* **2016**, *163*, A592-A598.
- (68) Jand, S. P.; Kaghazchi, P. *J. Phys.: Condens. Matter* **2014**, *26*, 262001.
- (69) Kokko, K.; Salo, P. T.; Laihia, R.; Mansikka, K. *Surf. Sci.* **1996**, *348*, 168-174.
- (70) Shi, F.; Pei, A.; Boyle, D.T.; Xie, J.; Yu, X.; Zhang, X.; Cui, Y. *Proc. Natl. Acad. Sci.* **2018**, *115*, 8529-8534.

Appendix

Supplementary information for Chapter 2

This appendix includes details of theoretical model and curve fitting, voltage response plots, nuclei distributions, SEM, XPS, Impedance spectroscopy, and goniometer characterizations, coin cell fabrication, electrochemical testing methods, image analysis, and additional figures.

Theoretical model

A theoretical model of nucleation and growth like that of Barton et al. (1), involving charge transfer overpotential, bulk diffusion overpotential, interfacial energy overpotential, and SEI diffusion overpotential respectively is as follows:

$$\eta = \frac{RT}{\alpha F} \ln \frac{i}{i_0} + \frac{irRT}{D_B C_B F^2} + \frac{2\gamma V}{Fr} + \frac{ir^2 RT}{D_S C_S F^2} \quad (1)$$

where η is the net overpotential due to all the processes, i and i_0 are the current density and exchange current density respectively, r is the radius of the nucleus, D_B and C_B (mol/m³) are the bulk electrolyte Li ion diffusivity and concentration respectively, D_S and C_S (mol/m²) are the SEI Li ion diffusivity and concentration respectively, and α , V , R , T , F are charge transfer coefficient, molar volume of metal, universal gas constant, temperature and Faraday constant respectively.

- The charge transfer overpotential is accounted for via the Tafel equation (2-3):

$$\eta = \frac{RT}{\alpha F} \ln \frac{i}{i_0}$$

- The interfacial energy overpotential is accounted for by considering the Gibbs energy of nucleation (1-5). The Gibbs energy of a nucleus formed as a cluster of atoms and as a function of size (hemisphere approximation of nucleus radius) is the sum of bulk free energy and surface free energy.

$$\Delta G_{\text{Nuc}} = -\frac{4}{3}\pi r^3 \Delta G_v + 4\pi r^2 \gamma \quad \text{where,} \quad \Delta G_v = F |\eta| / V$$

$$\frac{\partial \Delta G_{\text{Nuc}}}{\partial r} = 0 \quad \text{hence} \quad r_{\text{crit}} = 2\gamma V / F |\eta|$$

Rearranging the terms, and generalizing the expression for early stages of growth (small radius), we obtain the contribution of interfacial (SEI surface) energy of metal – solution to the overpotential as

$$\eta = \frac{2\gamma V}{Fr}$$

- The bulk diffusion overpotential is derived from the Nernst-Planck equation by eliminating the convective term and the concentration term. This assumption is only valid for bulk electrolyte experiencing minimal convective mass transfer of ions and concentration gradient ion diffusion effects. In our study, the current densities and time of electrodeposition are adjusted such that there is no current due to convective mass transfer effect. This is achieved by keeping the time of electrodeposition well below the sands time (6) for the current density. The concentration gradient of ions in the bulk (away from the electrode) is generally small and is often overshadowed by the effect of electric field. In such a system, the total current is generally carried by the migration of ions in response to the electric field. The contribution of ion-migration in the bulk electrolyte to the overpotential is as follows (2):

$$\eta = \frac{irRT}{D_B C_B F^2}$$

For the sake of simplicity, a linear variation of electric field over the length of ion-transport (i.e., radius of nucleus, r) in the bulk electrolyte is assumed. This follows directly from the work of Barton et al. (1), in which the authors demonstrated that for migration of ions from the bulk electrolyte to a hemispherical nucleus, the length

of ion transport is numerically equivalent of the radius of the hemispherical nucleus provided that the radius of the nucleus is smaller than 55 μm . The sizes of nuclei presented in our work are below 5 μm , hence justifying the assumption to be valid for the study.

- The SEI diffusion overpotential is accounted for via the following assumptions:
 - The SEI is a thin layer i.e., much thinner than the length of the ion transport in the bulk. Hence, the SEI acts as a 2-D layer as compared to the 3-D bulk electrolyte. For our study, the length of ion transport in the bulk is in micrometers (equivalent to the radius of the nuclei). The assumption is valid as the SEI thickness is usually in nanometers for low electrodeposition capacities.
 - The primary mode of ion transport in the SEI is via surface diffusion, as the SEI is a 2-D layer. For a 3-D bulk electrolyte, the primary mode of ion transport is bulk ion diffusion in response to the applied electric field.
 - The overpotential due to ion migration in the bulk electrolyte must have the same order of magnitude as that of the SEI. In other words, the ionic fluxes in the bulk electrolyte and the SEI must be equal. This can be mathematically demonstrated as follows:

$$\frac{D_B C_B}{r} \approx \frac{D_S C_S}{r^2}$$

The ionic flux in the bulk electrolyte over ion transport length r should be the same as ionic flux in the SEI over transport area r^2 . The bulk electrolyte ion concentration C_B has the units mol/m^3 while the SEI surface ion concentration

C_S has units of mol/m². Hence, the overpotential due to ion transport in the SEI can be derived as:

$$\eta = \frac{ir^2RT}{D_S C_S F^2}$$

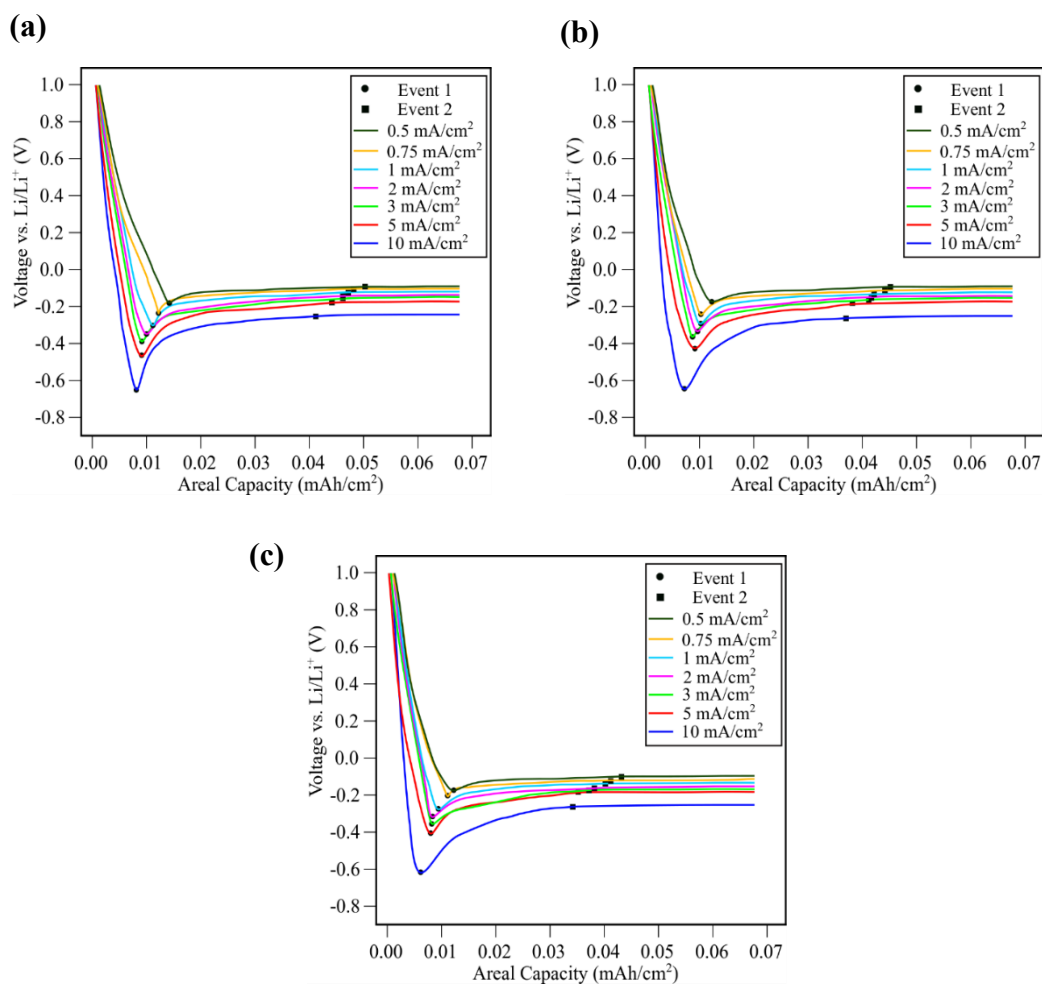
The expression is very similar to the overpotential due to ion transport in the bulk electrolyte, except for the r^2 dependency instead of the r dependency.

A note on Curve fitting and extraction of parameters

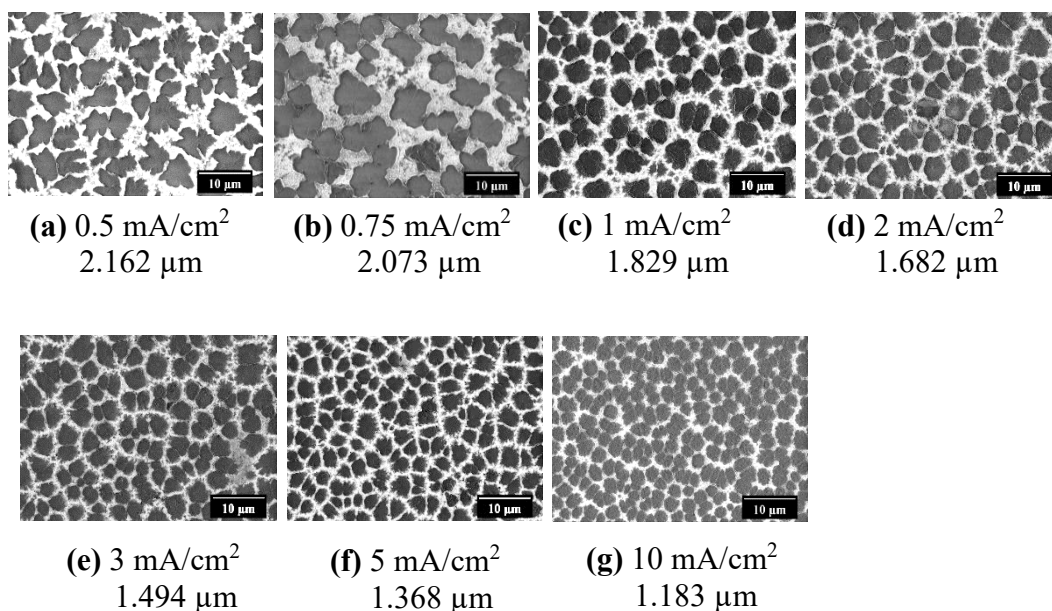
The curve fitting of the average nuclei radius (with error bars) against current density was performed by keeping the coefficients (A' and B') were kept unrestricted to any value (**Supplementary Figure 2.12**).

$$i = \frac{1}{\bar{r}^2 A' + \bar{r}^3 B'} \text{ where } A' = \frac{RT}{2\gamma V D_B C_B F} \text{ and } B' = \frac{RT}{\gamma V D_S C_S F} \quad (2)$$

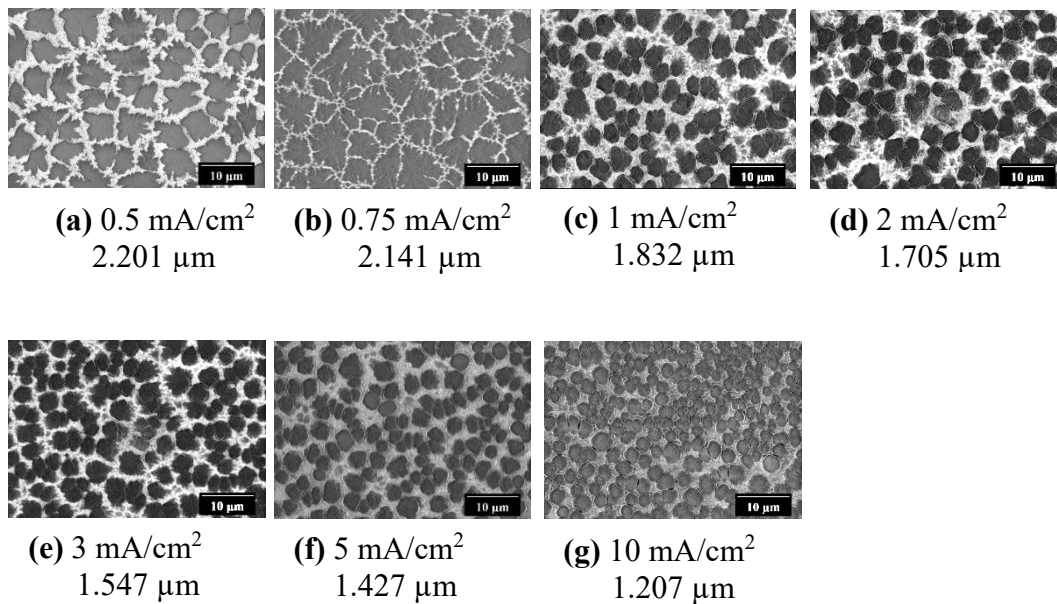
The division of the fitted coefficients (A'/B') gives the ratio of $D_S C_S / D_B C_B$. The value of C_B is already known as it is the concentration of lithium ions in the bulk electrolyte. D_B was determined through impedance spectroscopy (**Supplementary Figure 2.15**). Hence, the parameter $D_S C_S$ was determined and presented in **Supplementary Figure 2.12, Figure 2.5(b)**. Similarly, the fitted coefficient A' was used to determine interfacial energy γ as presented in **Figure 2.5(a)**.



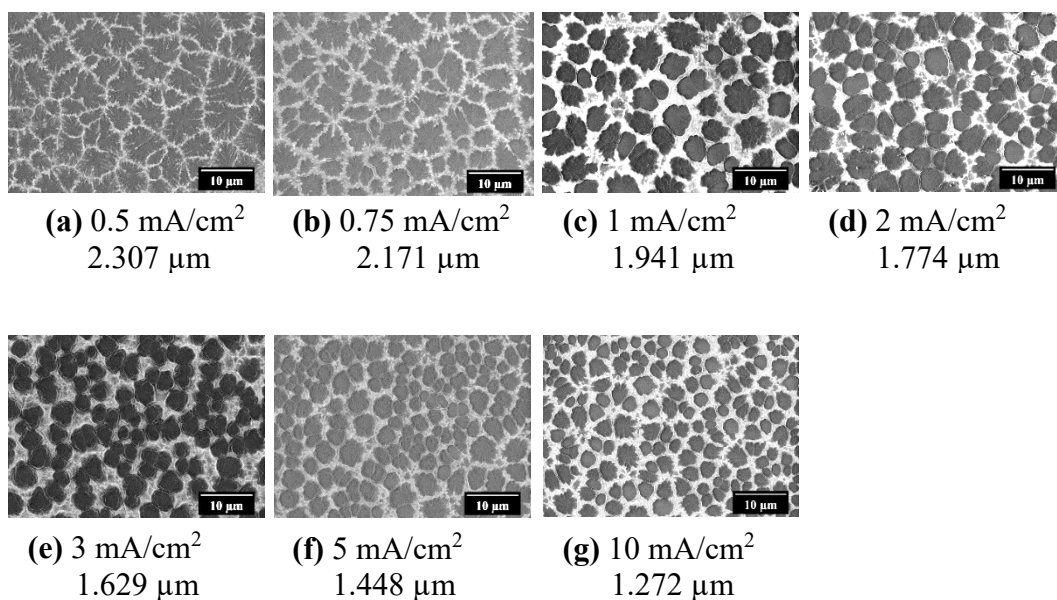
Supplementary Figure 2.1. Experimental voltage profiles of galvanostatic Li deposition for a range of current densities. The electrolyte is 1M LiPF₆ in EC:DMC (1:1 vol.%) with **(a)** 10 wt.% FEC **(b)** 30 wt.% FEC **(c)** 50 wt.% FEC. Nucleation Overpotential and Overpotential minimum are marked by Event 1 and Event 2.



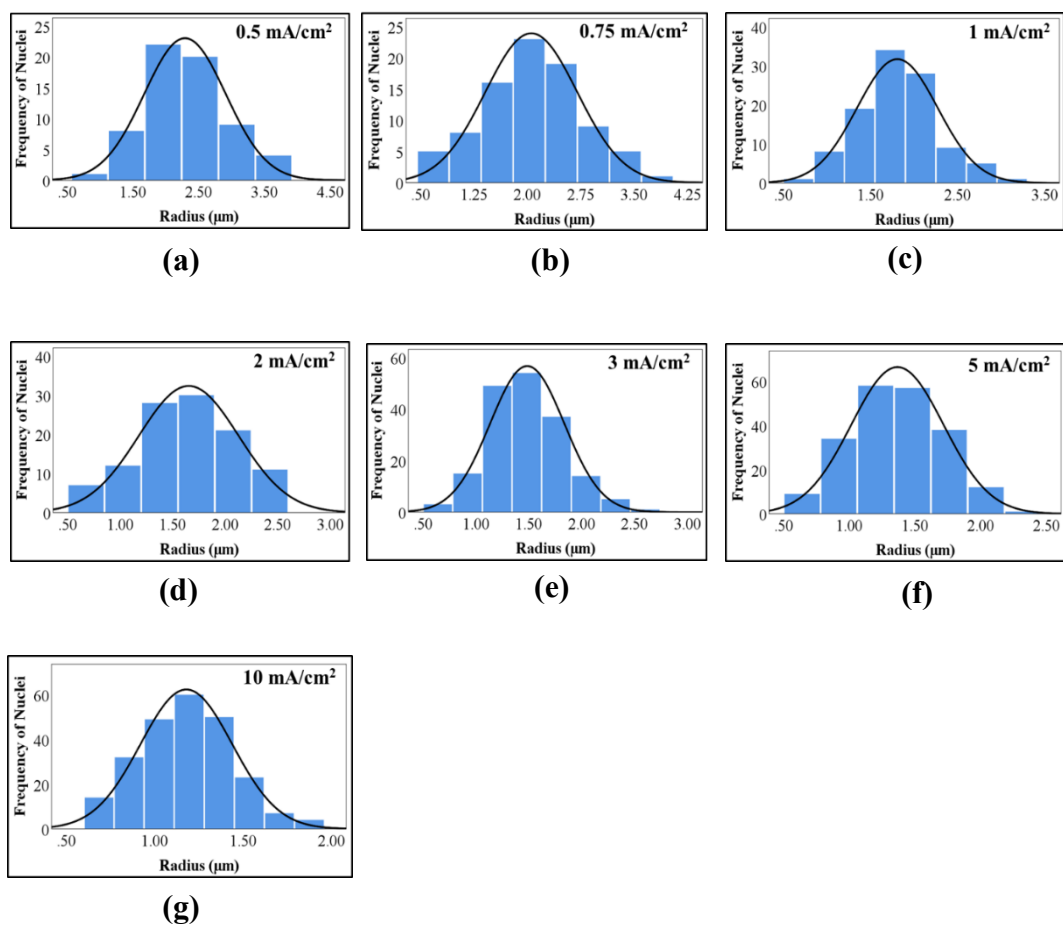
Supplementary Figure 2.2. Morphology map of Lithium electrodeposits. Ex situ SEM images of Li nuclei deposited on stainless-steel at current densities of (a) 0.5 (b) 0.75 (c) 1 (d) 2 (e) 3 (f) 5 (g) 10 mA/cm², respectively, for a total areal capacity corresponding to that of Overpotential Minimum (Event 2). At lower current densities, the stainless-steel substrate is visible underneath the sparsely distributed Li nuclei. The electrolyte is 1M LiPF₆ in EC:DMC (1:1 vol.%) with 10 wt.% FEC.



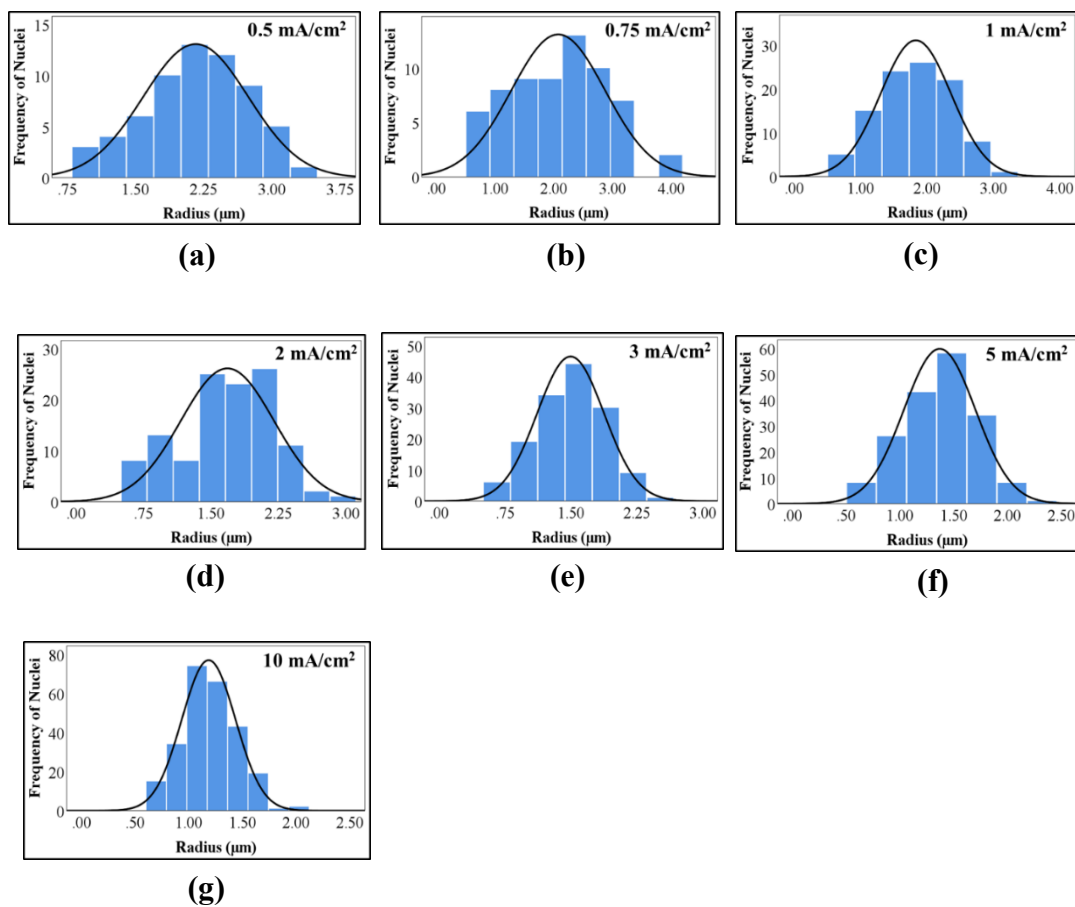
Supplementary Figure 2.3. Morphology map of Lithium electrodeposits. Ex situ SEM images of Li nuclei deposited on stainless-steel at current densities of (a) 0.5 (b) 0.75 (c) 1 (d) 2 (e) 3 (f) 5 (g) 10 mA/cm², respectively, for a total areal capacity corresponding to that of Overpotential Minimum (Event 2). At lower current densities, the stainless-steel substrate is visible underneath the sparsely distributed Li nuclei. The electrolyte is 1M LiPF₆ in EC:DMC (1:1 vol.%) with 30 wt.% FEC.



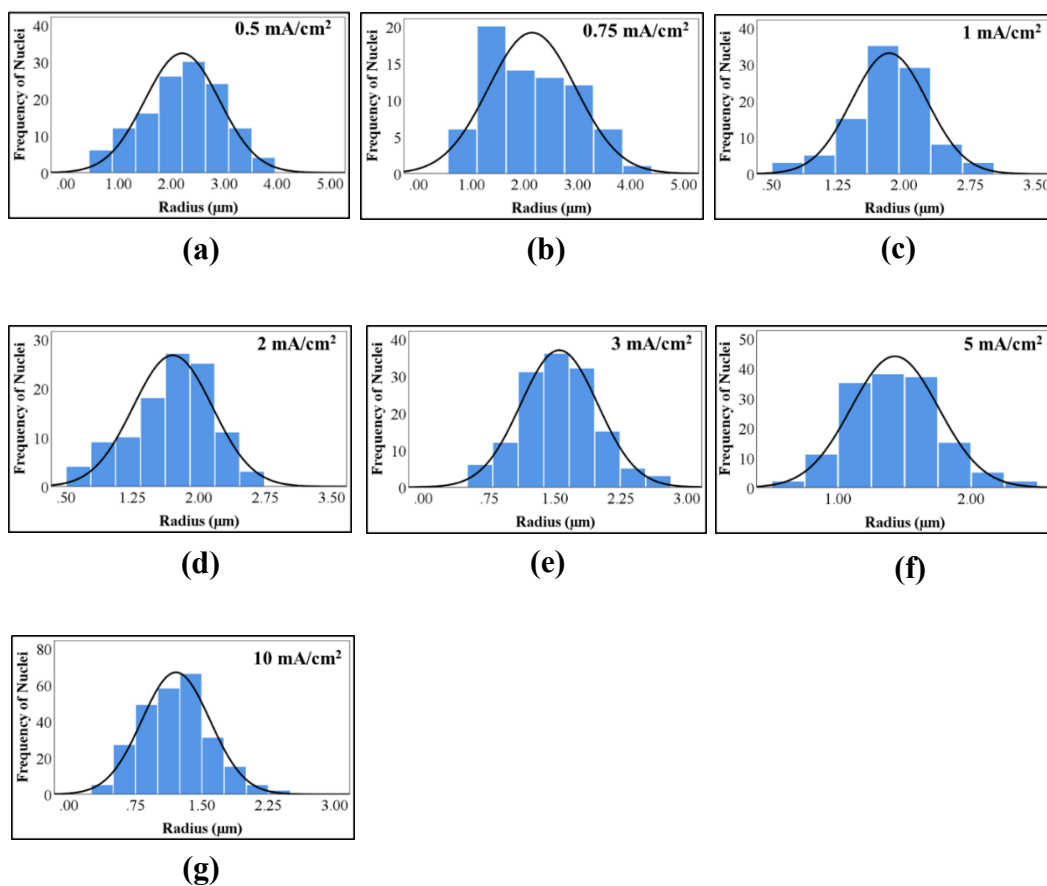
Supplementary Figure 2.4. Morphology map of Lithium electrodeposits. Ex situ SEM images of Li nuclei deposited on stainless-steel at current densities of (a) 0.5 (b) 0.75 (c) 1 (d) 2 (e) 3 (f) 5 (g) 10 mA/cm², respectively, for a total areal capacity corresponding to that of Overpotential Minimum (Event 2). At lower current densities, the stainless-steel substrate is visible underneath the sparsely distributed Li nuclei. The electrolyte is 1M LiPF₆ in EC:DMC (1:1 vol.%) with 50 wt.% FEC.



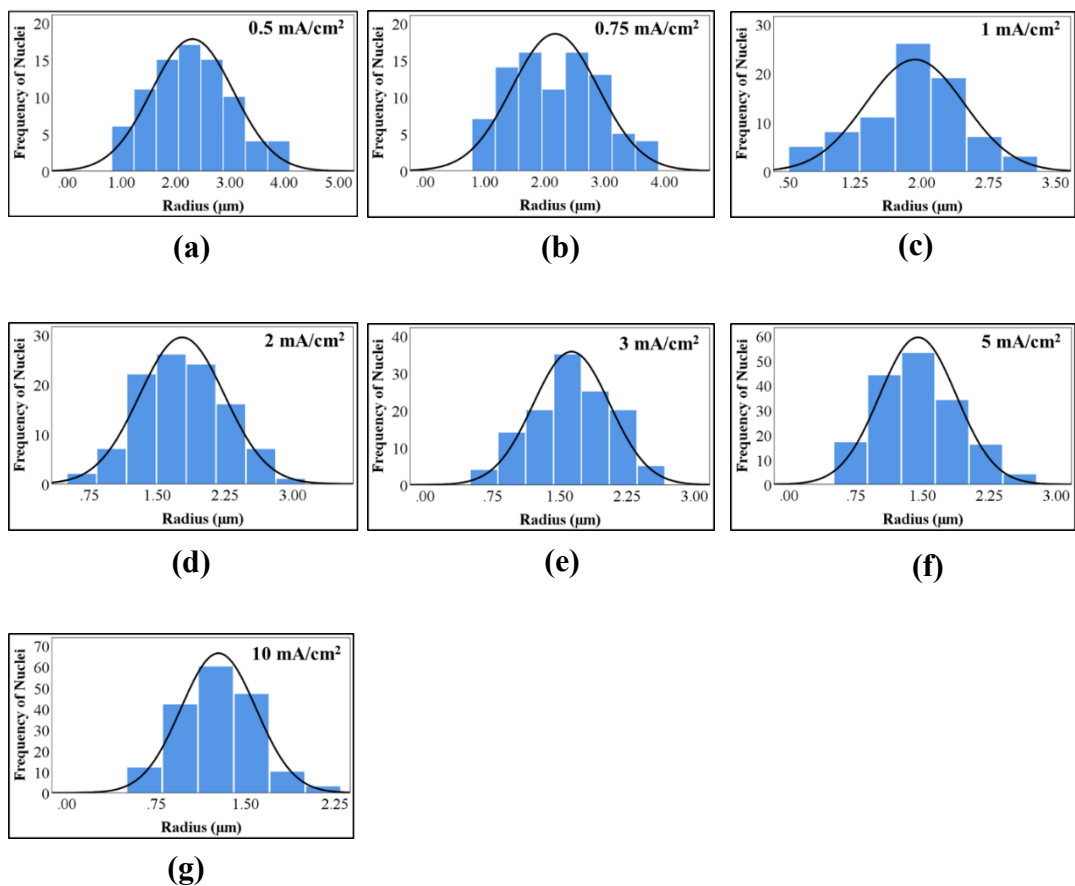
Supplementary Figure 2.5. Nuclei size distribution map of Lithium electrodeposits. Histograms of Li nuclei deposited on stainless-steel at current densities of (a) 0.5 (b) 0.75 (c) 1 (d) 2 (e) 3 (f) 5 (g) 10 mA/cm², respectively, for a total areal capacity corresponding to that of Overpotential Minimum (Event 2). The electrolyte is 1M LiPF₆ in EC:DMC (1:1 vol.%).



Supplementary Figure 2.6. Nuclei size distribution map of Lithium electrodeposits. Histograms of Li nuclei deposited on stainless-steel at current densities of (a) 0.5 (b) 0.75 (c) 1 (d) 2 (e) 3 (f) 5 (g) 10 mA/cm^2 , respectively, for a total areal capacity corresponding to that of Overpotential Minimum (Event 2). The electrolyte is 1M LiPF_6 in EC:DMC (1:1 vol.%) with 10 wt.% FEC.



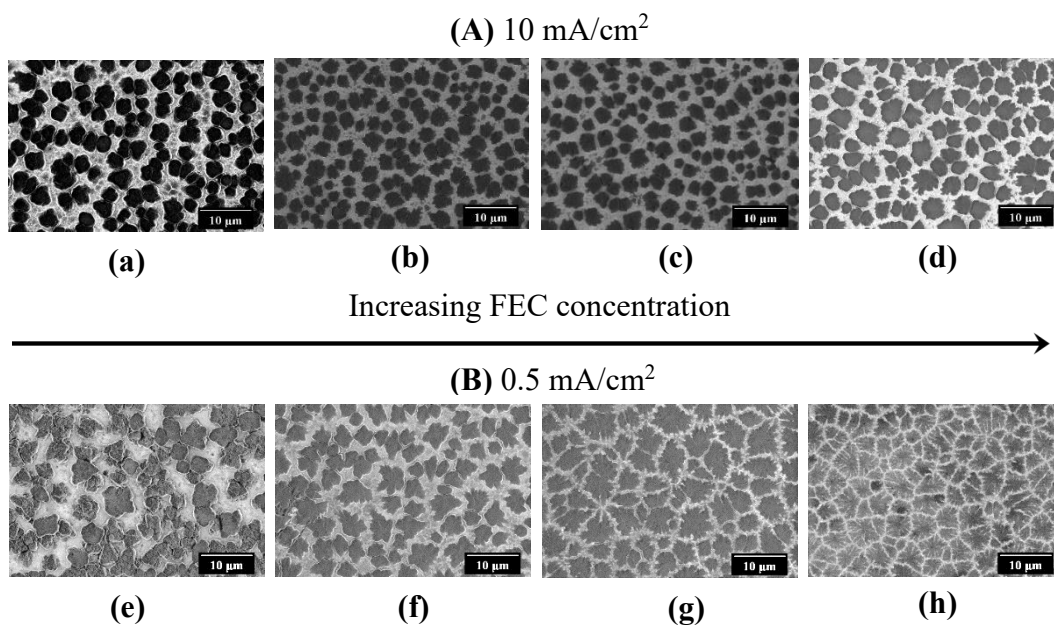
Supplementary Figure 2.7. Nuclei size distribution map of Lithium electrodeposits. Histograms of Li nuclei deposited on stainless-steel at current densities of (a) 0.5 (b) 0.75 (c) 1 (d) 2 (e) 3 (f) 5 (g) 10 mA/cm², respectively, for a total areal capacity corresponding to that of Event 2. The electrolyte is 1M LiPF₆ in EC:DMC (1:1 vol.%) with 30 wt.% FEC.



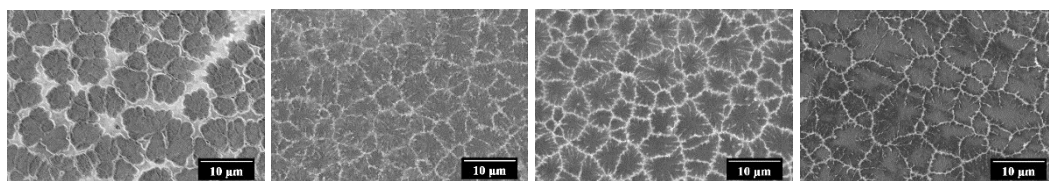
Supplementary Figure 2.8. Nuclei size distribution map of Lithium electrodeposits. Histograms of Li nuclei deposited on stainless-steel at current densities of (a) 0.5 (b) 0.75 (c) 1 (d) 2 (e) 3 (f) 5 (g) 10 mA/cm², respectively, for a total areal capacity corresponding to that of Event 2. The electrolyte is 1M LiPF₆ in EC:DMC (1:1 vol.%) with 50 wt.% FEC.

	% Concentration			
	Li 1s		F 1s	
FEC wt.%	LiF	Li ₂ CO ₃	LiF	C-F
0	10.96	89.04	37.42	62.58
10	17.38	82.62	46.73	53.27
30	21.12	78.88	55.53	44.47
50	25.12	74.88	61.65	38.35

Supplementary Table 2.1. Li 1s and F 1s chemical analysis via XPS spectra of the FEC-induced SEI layer.

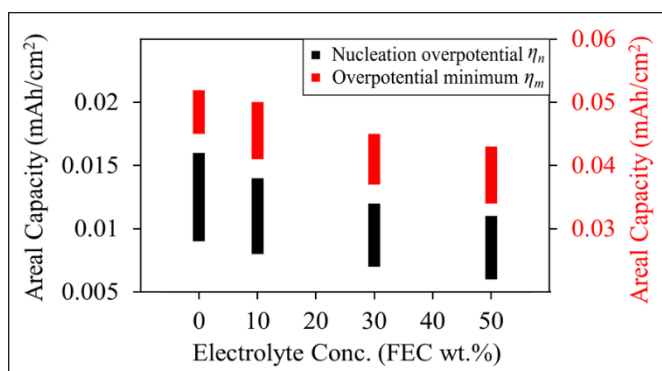


Supplementary Figure 2.9. Morphology comparison of Lithium electrodeposits at contrasting current densities. Ex situ SEM images of Li nuclei deposited on Stainless steel for current densities of **(A)** 10 mA/cm² and **(B)** 0.5 mA/cm² for increasing concentration of FEC **(a)** 0 **(b)** 10 **(c)** 30 **(d)** 50 wt.% in 1M LiPF₆ EC: DMC (1:1 vol.%). The total areal capacity corresponds to that of Nucleation Overpotential (Event 1).

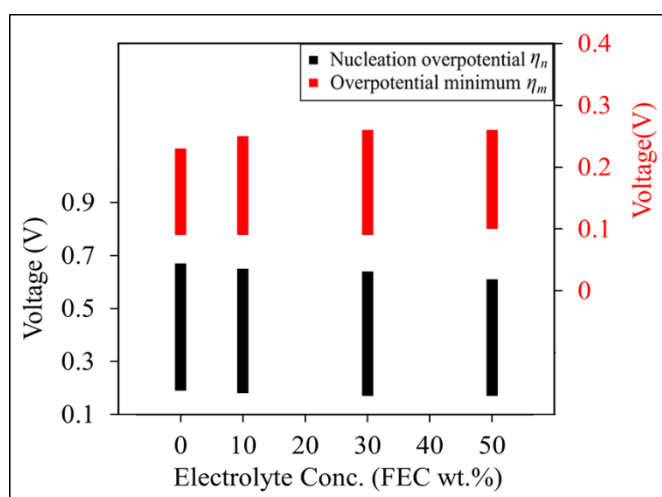


(a) 0 wt.% FEC **(b)** 10 wt.% FEC **(c)** 30 wt.% FEC **(d)** 50 wt.% FEC

Supplementary Figure 2.10. Effect of electrolyte chemistry on the Morphology of Lithium electrodeposits at a low current density. Ex situ SEM images of Li nuclei deposited on stainless-steel at a current density of 0.05 mA/cm^2 and for varying concentration of FEC **(a)** 0 **(b)** 10 **(c)** 30 **(d)** 50 wt.% in 1M LiPF_6 EC:DMC (1:1 vol.%). The total areal capacity corresponds to that of Overpotential Minimum (Event 2).

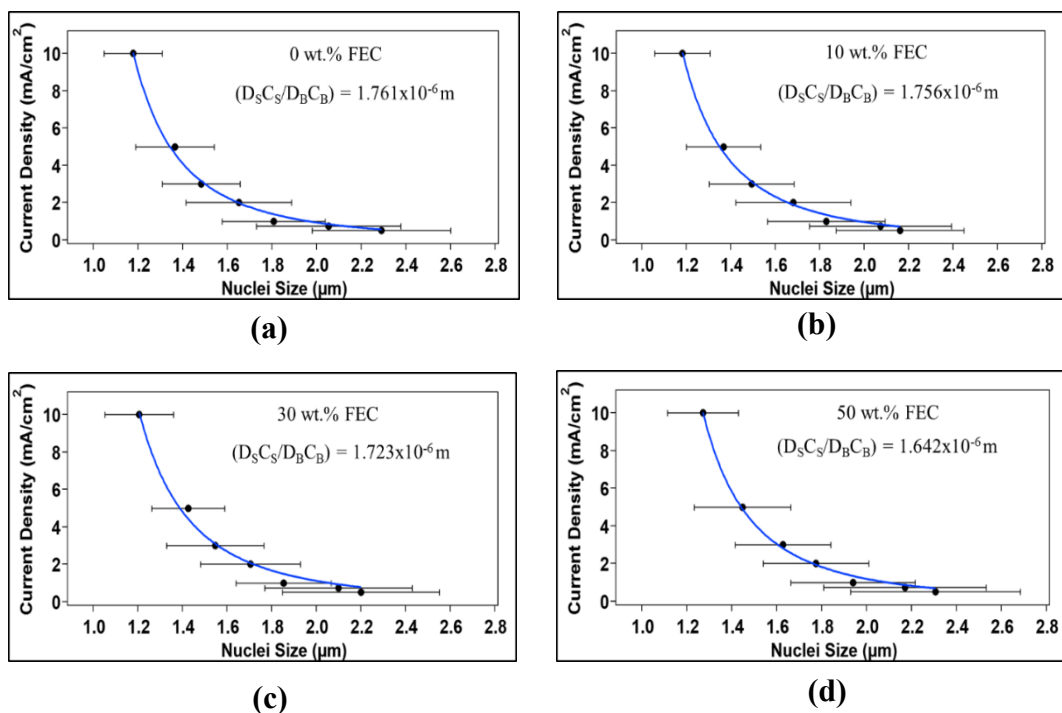


(a)



(b)

Supplementary Figure 2.11. Effect of electrolyte chemistry on the areal capacities and overpotentials of the Nucleation Overpotential and Overpotential Minimum events. **(a)** Plot of Areal Capacities for all the current densities and varying concentration of FEC (0, 10, 30, 50 wt.%) in 1M LiPF₆ EC: DMC (1:1 vol.%). **(b)** Plot of Overpotentials for all the current densities and varying concentration of FEC (0, 10, 30, 50 wt.%) in 1M LiPF₆ EC: DMC (1:1 vol.%). The Nucleation Overpotential and Overpotential Minimum are shown in black and red respectively.



Supplementary Figure 2.12. Proof of Concept curve fitting for electrolyte with different chemistries. Curve fitting of Current Density with average Nuclei Size through square-cubic relationship (**Equation 2**) for 1M LiPF₆ in EC:DMC (1:1 vol.%) with (a) 0 wt.% FEC (b) 10 wt.% FEC (c) 30 wt.% FEC (d) 50 wt.% FEC. The areal capacity at which the nuclei sizes are analyzed corresponds to that of Overpotential Minimum (Event 2). The extracted diffusivity-concentration parameters are mentioned.

	Capacity (mAh/cm ²)		
Parameters	0.1	0.2	0.3
A'	7.25E+10	1.16E+11	1.59E+11
γ (mJ/m ²)	71.13	44.33	32.41

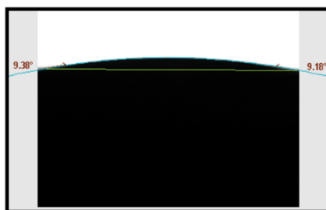
Supplementary Table 2.2. Interfacial energy for Ether-based electrolyte as calculated for nuclei data available in literature for different capacities of electrodeposition (4).

The theoretical γ values calculated for Lithium nuclei formed from Ether-based electrolyte are lower than those obtained for the corresponding Carbonate-based systems. The Ether-based electrolyte nuclei are also smaller in size (4). As the nuclei size can be roughly correlated to interfacial energy as $\tilde{r} = 2\gamma V/F\eta$, a smaller nucleus should exhibit a smaller critical radius, hence lower interfacial energy, assuming the overpotential in the growth regime to be comparable for the two different chemistries. This is consistent with what we see experimentally.

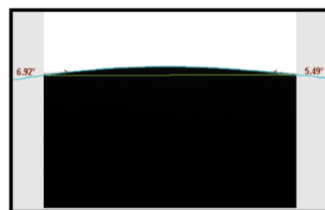
Interfacial energy at the electrode-electrolyte interface



(a) 0 wt.% FEC with Polished Stainless-Steel
Contact Angle: 43.89°



(b) 0 wt.% FEC with Lithium Substrate
Contact Angle: 9.42°



(c) 10 wt.% FEC with Lithium Substrate
Contact Angle: 6.11°



(d) 30 wt.% FEC with Lithium Substrate
Contact Angle: 4.56°



(e) 50 wt.% FEC with Lithium Substrate
Contact Angle: 3.03°

Supplementary Figure 2.13. Effect of fluorinated electrolyte chemistry on the wetting of Polished stainless-steel and Lithium substrate. Average Contact Angle of Polished Stainless-Steel Substrate with **(a)** 0 wt.% FEC in 1M LiPF₆ EC: DMC (1:1 vol.%). Similarly, Average Contact Angle of Lithium Substrate with 1M LiPF₆ EC: DMC (1:1 vol.%) containing **(b)** 0 wt.% FEC **(c)** 10 wt.% FEC **(d)** 30 wt.% FEC **(e)** 50 wt.% FEC. All measurements were performed in an Argon atmosphere at 20 °C.

A combination of Zisman approach and Young's equation was used to determine the interfacial energy of the Electrode-Electrolyte interphase.⁷⁻⁹

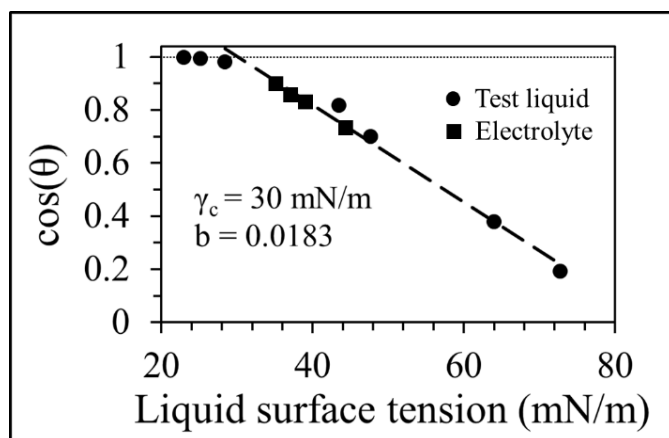
$$\gamma_L \cos(\theta) = \gamma_S - \gamma_{SL} \quad (1)$$

$$\cos(\theta) = 1 - b(\gamma_L - \gamma_C) \quad (2)$$

Where γ_L is the experimentally determined surface energy (surface tension) of the liquid (electrolyte), θ is the contact angle, γ_S is the surface energy of the solid (lithium: 0.52 J m^{-2}), γ_{SL} is the solid/liquid interfacial energy, b is the slope of the regression line and γ_C is the critical surface tension when $\cos(\theta) = 1$. The contact angle of the electrolytes (0, 10, 30, 50 wt.% FEC) on the surface of clean lithium metal was measured using an optical tensiometer in an argon-filled enclosure as shown in **Supplementary Figure 2.13**. Prior to that, the critical surface tension γ_C and b the slope of regression were determined for a polished stainless steel using common test liquids with known surface tension (Isopropanol 23 mN/m, Acetone 25.2 mN/m, Toluene 28.4 mN/m, DMSO 43.54 mN/m, Ethylene Glycol 47.7 mN/m, Glycerol 64 mN/m, Water 72.8 mN/m) as shown in figure **Supplementary Figure 2.14**. The surface tension of each electrolyte was calculated via Zisman approach (eq. 2) by measuring their respective contact angles with the polished stainless steel as shown in **Supplementary Table 2.3**. Finally, the obtained information was used to determine the interfacial energy of Li-electrolyte interphase via Young's (eq. 1).

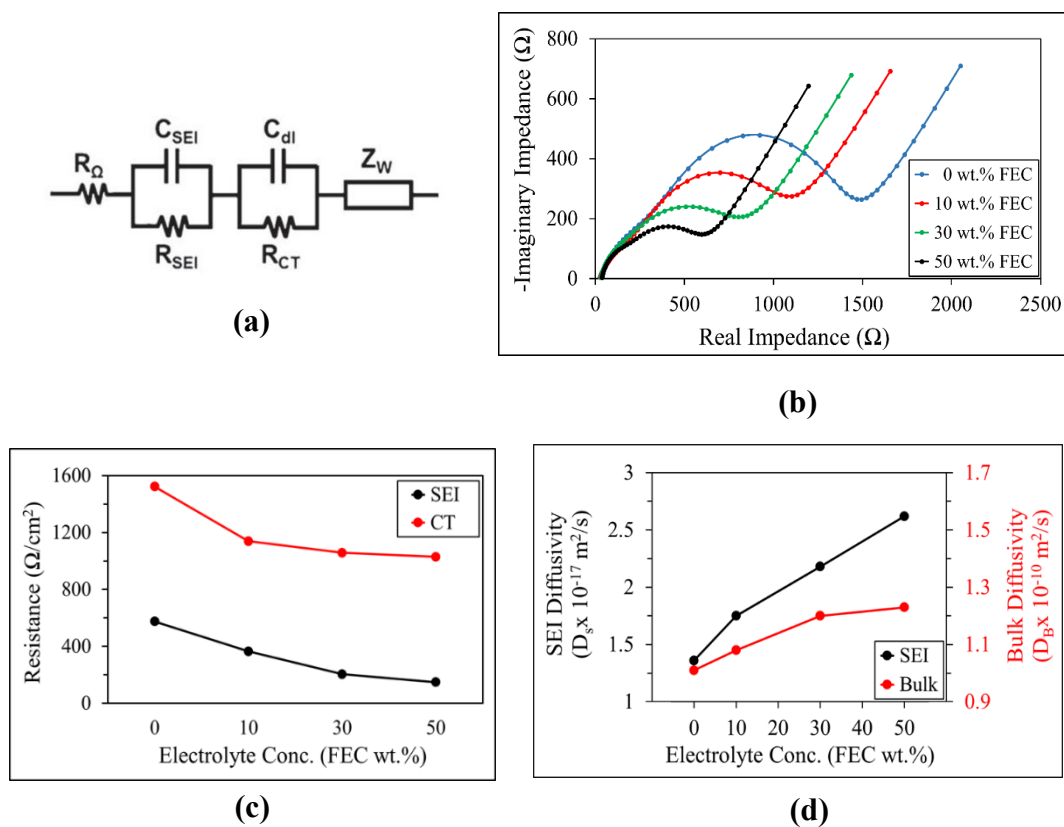
Electrolyte	C.A. (θ_{ss})	$\cos(\theta_{ss})$	γ_L (mJ/m^2)	C.A. (θ_{Li})	$\cos(\theta_{Li})$	γ_{SL} (mJ/m^2)
0 wt.% FEC	43.89	0.721	45.25	9.42	0.987	475.36
10 wt.% FEC	31.74	0.851	38.16	6.11	0.994	482.05
30 wt.% FEC	27.65	0.886	36.23	4.56	0.997	483.88
50 wt.% FEC	22.98	0.921	34.33	3.03	0.999	485.72

Supplementary Table 2.3. Contact angles, electrolyte surface tensions (γ_L) and Li-electrolyte interfacial energy (γ_{SL}) for a range of electrolyte compositions. Lithium: 0.52 J m^{-2} , θ_{ss} contact angle w.r.t Polished stainless-steel, θ_{Li} contact angle with respect to Lithium.



Supplementary Figure 2.14. Zisman plot ($\cos(\theta)$ vs γ_L) for different test liquids and electrolytes on Polished stainless steel. A linear regression between \cos of contact angle and the surface tension of test liquids (Isopropanol 23 mN/m, Acetone 25.2 mN/m, Toluene 28.4 mN/m, DMSO 43.54 mN/m, Ethylene Glycol 47.7 mN/m, Glycerol 64 mN/m, Water 72.8 mN/m) as estimated by Zisman approach. The estimated surface tension for each electrolyte as in 1M LiPF_6 EC:DMC containing 0, 10, 30, 50 wt.% FEC. All measurements were performed in an Argon atmosphere at $20 \text{ }^\circ\text{C}$.

Impedance spectroscopy of early-stage Li electrodeposits

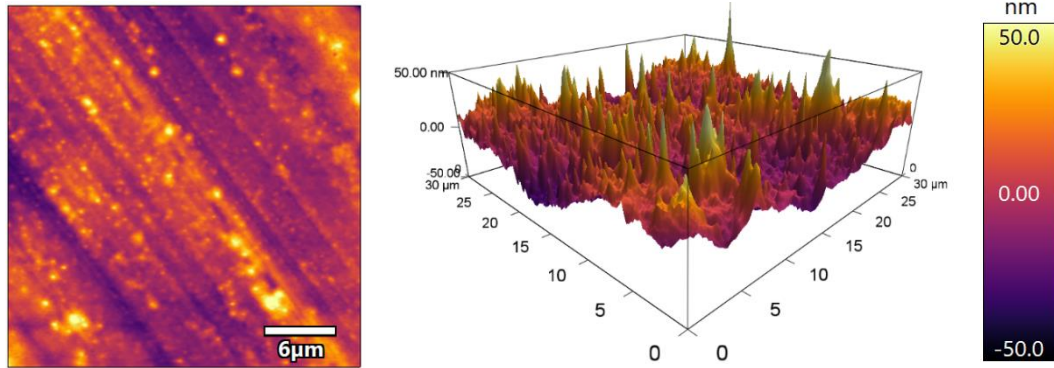


Supplementary Figure 2.15. Effect of fluorinated electrolyte chemistry on the surface and bulk transport characteristics. Electrochemical Impedance Spectroscopy (EIS) analysis of Lithium electrodeposited on Polished Stainless-Steel substrate in contact with electrolyte having different fluorinated concentrations. (a) EIS model (10-13) used to fit the electrochemical spectrum data (b) Model fitting of the Nyquist plots of the electrochemical spectrum data (c) Areal SEI and Charge Transfer resistance as extracted from the fitted model (d) SEI and Bulk diffusivity as calculated from the extracted data of the fitted model.

- The R_{SEI} and R_{CT} are averaged over the electrode area in contact with the electrolyte, as reported in **Supplementary Figure 2.15(c)**.
- Nernst-Einstein equation is used to correlate the bulk electrolyte resistance (R_{Ω}) with the ambipolar bulk ion diffusivity. The transference number of bulk Li ion is calculated using Bruce-Vincent method (14) after performing potentiostatic polarization and impedance spectroscopy. The bulk Li ion diffusivity (D_B) is calculated as the product of ambipolar bulk ion diffusivity and bulk Li ion transference number. (**Supplementary Figure 2.15(d)**)
- The SEI diffusivity (D_S) is calculated from the Warburg coefficient (15). The Warburg coefficient is calculated from the plot of low frequency real impedance of Z_w vs $1/\sqrt{\omega}$. The transference number of Li ions in the SEI is assumed to be 1.

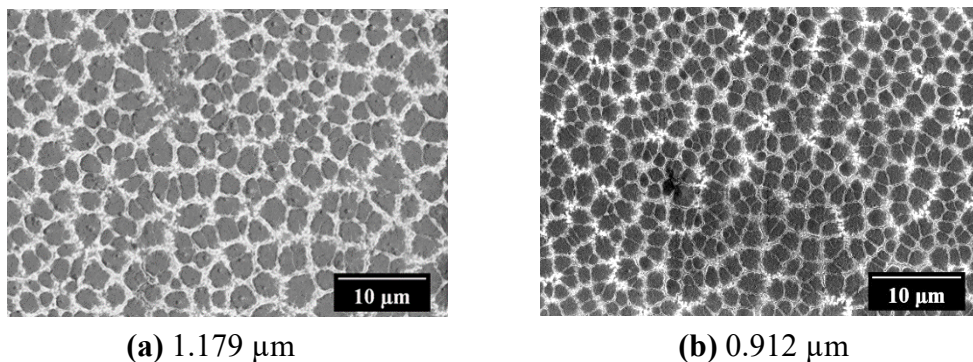
FEC conc.	$D_S C_S \times 10^{-13}$ (mol/s)	$D_S \times 10^{-17}$ (m²/s)	$C_S \times 10^4$ (mol/m²)
0 wt.%	1.786	1.36	1.313
10 wt.%	1.738	1.75	0.993
30 wt.%	1.608	2.18	0.737
50 wt.%	1.372	2.62	0.523

Supplementary Table 2.4. Effect of fluorinated electrolyte chemistry on the interfacial characteristics. The $D_S C_S$ is theoretically determined while the D_S is experimentally determined through the EIS. The C_S is obtained by dividing $D_S C_S$ with D_S .



Average surface roughness (Ra) = 9.12 +/- 8.78

Supplementary Figure 2.16. AFM image of the surface topography of polished stainless-steel.



Supplementary Figure 2.17. Morphology of Lithium electrodeposits formed at a high current density of 10 mA/cm^2 on different substrates. (a) Polished Stainless steel (b) Copper. The electrolyte is 1M LiPF_6 in EC: DMC (1:1 vol.%) and the areal capacities are about 0.045 mAh/cm^2 (corresponding to that of Overpotential Minimum observed on stainless steel).

Material and Methods

Polishing/cleaning method: The stainless-steel 304 substrate was polished to a surface roughness of $R_a < 10\text{nm}$ through chemical mechanical polishing (CMP) method. The unpolished stainless-steel substrates were fixed in an Alumina slurry of 0.3 Micron particles on a bed of Final-POL Adhesive Back Disc (Allied High-Tech products) in a vibratory polisher at an amplitude of 50% for about 2 days. The polished stainless-steel substrates were cleaned through ultrasonication in a bath of acetone for about 1 hour.

Supplementary Figure 2.16 shows the AFM image of the surface topography of the stainless-steel to have average roughness of about 10 nm. The polished cleaned substrates were stored in a vial of acetone and ultrasonicated again with fresh acetone prior to any usage.

Electrochemical method: 2032-type coin cells with the polished stainless-steel working electrodes and Li foil (Alfa Aesar 0.75 mm width) counter/reference electrodes were assembled in an argon-filled glove box (MBraun). A Teflon O-ring of internal diameter 0.25 inches was used between the two electrodes and 200 μL of electrolyte was added to each cell. 1 M Lithium hexafluorophosphate (LiPF_6) in Ethylene Carbonate: Dimethyl Carbonate (1:1 V) electrolyte (Sigma-Aldrich) with varying wt.% of Fluoroethylene Carbonate (FEC) (Sigma-Aldrich) as an additive was used as the electrolyte. Galvanostatic deposition was conducted using an 8-channel battery testing unit from Neware Instruments and MACCOR series 4000 battery tester system. The stainless-steel electrode was discharged to 0.5 V vs. Li/Li^+ by applying 0.5 mA/cm^2 current, then charged back to 2 V at -0.5 mA/cm^2 to initialize SEI formation and remove

surface impurities. Then, a fixed amount of charge was passed galvanostatically at different current rates depending on the experiment. In this work, the point in overpotential curve at which 99-100% of the plateau overpotential is attained after the nucleation peak, is referred to as Overpotential Minimum, and the corresponding areal capacity as Overpotential Minimum Capacity. To accurately determine the Overpotential Minimum, galvanostatic electrodeposition of Li ions was carried out on multiple replicates of Polished stainless-steel for capacities of about 0.2 mAh/cm². The overpotential minimum capacity was then fixed by examining the Overpotential curve, and marking the capacity corresponding to 99-100% plateau overpotential. It was found that the capacity at overpotential minimum is almost constant ($\pm 1\%$ error) for a fixed current density and electrolyte chemistry. Subsequent electrodeposition and postmortem analysis were carried out for the fixed capacity at Overpotential Minimum. Minute care was undertaken for the cleanliness and purity of the coin cell components, which ensures reproducibility of the fixed capacity. Similar electrodeposition methodology was carried out on copper substrate (Alfa Aesar 1mm width) and the general morphology is shown in **Supplementary Figure 2.17**.

A Solartron workstation with frequency analyzer was used for obtaining impedance spectra at room temperature. The frequency range was adjusted to be in between 1 MHz to 1 mHz at an amplitude of 10mV. Prior to the impedance spectroscopy, Lithium of areal capacity corresponding to the Overpotential Minimum (Event 2) was electrodeposited on to the polished stainless-steels through the electrochemical method mentioned previously. These electrodes were extracted and re-assembled in a symmetric cell fashion in 2032-type coin cells. The assembly consisted of electrolyte in a Teflon

O-ring (0.25 inches) in between two Polished stainless-steel with electrodeposited Lithium.

An Attention Theta-lite Optical tensiometer (Biolin Scientific) was used in an argon-filled glove box for obtaining the contact angle data. The contact angles (C.A.) were measured according to the sessile drop method at room temperature (20 °C). A single drop of the test electrolyte (drop volume ca. 4–5 μL) was placed on the Lithium substrate via a microliter syringe. Dynamic contact angles were measured from the optical image of the steady droplet using the live acquisition mode of the software. For each electrolyte, the contact angle was determined for 6 different Lithium substrates, and the average values are reported. The initial few dynamic Contact angle readings at the start of an experiment were discarded owing to unsteady state of the droplet (Advancing/Receding contact lines). For each electrolyte, the standard deviation for C.A. measurements were less than 10% of the reported data.

Electrode Characterization: After Li electrodeposition onto stainless-steel, the cells were opened in the Argon glove box and the stainless-steel electrodes were rinsed with fresh Dimethyl Carbonate and dried. Electrodes were mounted onto SEM stages and sealed in Argon filled transfer vessels for immediate SEM observation (Zeiss Gemini SEM). Unavoidable contact with air was brief and may have slightly altered the surface features of the electrodeposited Lithium metal seen in SEM images. The images were captured at 2 kV with an aperture of 20 μm .

The chemical composition of the surface of Li electrodeposits were analyzed using a Surface Science Instruments SSX-100 with operating pressure $< 2 \times 10^{-9}$ Torr and

monochromatic AlK α X- rays at 200 W, 1486.6 eV. The diameter of the analyzed area was 1mm. Photoelectrons were collected at an angle of 55-degrees from the surface normal and analyzed with a hemispherical analyzer having pass energy of 150 V for wide/survey scans, and 50 V for high resolution scans. High resolution sensitivity scan was performed to capture Li 1s data at the same acquisition parameters. The data analysis was performed with CasaXPS software, with Tougaard background fitting of the peaks.

Image / Data Analysis: Nuclei sizes were measured using ImageJ software. Gaussian blurring to remove excessive noise, Thresholding to restrict color contrast of images to black and white, and adjustable watershed to identify nuclei were performed. Between 100-500 particles were averaged for each current density and for every electrolyte composition. The radius of a Nuclei was calculated by assuming the nuclei to be hemispherical and the projected area was approximated to that of a circle. Nuclei density was calculated by counting number of visible nucleus in each image and dividing by the area of the SEM image. Igor Pro 8 was used to curve fit the average nuclei radius (with error bars) against current density. The coefficients (A' and B') were kept unrestricted to any value. The fitted coefficients were analyzed, and physical parameters were extracted. The ether-based electrolyte data was obtained from the work of Pei et al.⁴

References for Appendix

- (1) Barton, J. L.; Bockris, J. O. M. *Proceedings of the Royal Society of London. Series A. Mathematical and Physical Sciences* **1962**, 268(1335), 485-505.
- (2) Bard, A. J., Faulkner, L. R., Leddy, J., & Zoski, C. G. *Electrochemical methods: fundamentals and applications* (Vol. 2) **1980**, New York: Wiley.
- (3) Budevski, E. B., Staikov, G. T., & Lorenz, W. J. *Electrochemical phase formation and growth: an introduction to the initial stages of metal deposition* **2008**, John Wiley & Sons.
- (4) Pei, A.; Zheng, G.; Shi, F.; Li, Y.; Cui, Y. *Nano letters* **2017**, 17,1132-1139.
- (5) Plieth, W. *Electrochemistry for materials science* **2008**, Elsevier.
- (6) Brissot, C., Rosso, M., Chazalviel, J. N., & Lascaud, S. *Journal of power sources* **1999**, 81, 925-929.
- (7) Zisman, W. A. *Ind. Eng. Chem.* **1963**, 55, 18-38.
- (8) Gindl, M.; Sinn, G.; Gindl, W.; Reiterer, A.; Tschegg, S. *Colloids Surf., A* **2001**, 181, 279-287.
- (9) Dahbi, M.; Violleau, D.; Ghamouss, F.; Jacquemin, J.; Tran-Van, F.; Lemordant, D.; Anouti, M. *Ind. Eng. Chem. Res.* **2012**, 51, 5240-5245.
- (10) Zhang, S. S.; Xu, K.; Jow, T. R. *Electrochim. Acta* **2006**, 51, 1636-1640.
- (11) Xiang, H.; Shi, P.; Bhattacharya, P.; Chen, X.; Mei, D.; Bowden, M.E.; Zheng, J.; Zhang, J.G.; Xu, W. *J. Power Sources* **2018**, 318, 170-177.

- (12) Huang, J.; Li, Z.; Ge, H.; Zhang, J. *J. Electrochem. Soc.* **2015**, *162*, A7037-A7048.
- (13) Guo, J.; Sun, A.; Chen, X.; Wang, C.; Manivannan, A. *Electrochim. Acta* **2011**, *56*, 3981-3987.
- (14) Bruce, P. G.; Evans, J.; Vincent, C. A. *Solid State Ionics* **1988**, *28*, 918-922.
- (15) Warburg, E. *Ann. Phys. (Berlin, Ger.)* **1899**, *303*, 493-499.

Chapter 3

The early-stage growth and reversibility of Li electrodeposition in Br-rich electrolytes

Adapted with permission from

Biswal, P., Kludze, A., Rodrigues, J., Deng, Y., Moon, T., Stalin, S., Zhao, Q., Yin, J., Kourkoutis, L.F. and Archer, L.A. (2021). The early-stage growth and reversibility of Li electrodeposition in Br-rich electrolytes. *Proceedings of the National Academy of Sciences*, 118(2).

3.1 Abstract

The physio-chemical nature of reactive metal electrodeposits during the early stages of electrodeposition is rarely studied but known to play an important role in determining the electrochemical stability and reversibility of electrochemical cells that utilize reactive metals as anodes. We investigated the early-stage growth dynamics and reversibility of electrodeposited Lithium in liquid electrolytes infused with brominated additives. On the basis of equilibrium theories, we hypothesize that by regulating the surface energetics and surface ion/adatom transport characteristics of the interphases formed on Li, Br-rich electrolytes alter the morphology of early-stage Li electrodeposits; enabling late-stage control of growth and high electrode reversibility. A combination of Scanning Electron Microscopy (SEM), Image analysis, X-ray Photoelectron Spectroscopy (XPS), Electrochemical Impedance Spectroscopy (EIS) and Contact Angle Goniometry are employed to evaluate this hypothesis by examining the physical-chemical features of the material phases formed on Li. We report that it is possible to achieve fine control of the early-stage Li electrodeposit morphology through tuning of surface energetic and ion diffusion properties of interphases formed on Li. This control is shown further to translate to better control of Li electrodeposit morphology and high electrochemical reversibility during deep cycling of the Li metal anode. Our results show that understanding and eliminating morphological and chemical instabilities in the initial stages of Li electroplating via deliberately modifying energetics of the Solid Electrolyte Interphase (SEI) is a feasible approach in realization of deeply cyclable reactive metal batteries.

3.2 Introduction

The development of practical rechargeable Li metal batteries (LMB) has been of significant research interest for over 40 years for prospective applications in portable electronics, electric vehicles, and grid-scale energy storage (1-5). Multiple features of the metallic Li anode are known to drive this interest. The most important include the extremely high theoretical specific capacity (3860 mAh g^{-1}), Li's lowest reduction potential (-3.040 V versus standard hydrogen electrode), and low density (0.534 g cm^{-3}) (1-5). Unfortunately, the list of technical shortcomings of a Li metal anode is almost as long. First, in liquid electrolyte media parasitic reactions between the electrode and electrolyte lead to poor electrode reversibility and limited battery rechargeability (1-7). Second, at current densities well below the classical diffusion limit ($i_L = 4FcD_+/\delta_D$), Li deposits in mossy, low-density structures that may either grow to short the cell internally or break-away from the electrode mass to form electrochemically disconnected structures, which further lowers electrode reversibility (6-12). Finally, the inorganic or organic-inorganic interphases formed spontaneously on Li invariably have much lower ionic conductivity than bulk liquid electrolytes, which leads to large polarization, and accelerated electrochemical degradation of the electrolyte (13).

All of these shortcomings are to a large extent traceable to the lack of control of the chemical, physical, and transport properties of the Solid-Electrolyte Interphases (SEI) formed spontaneously on Li. Significant experimental efforts have consequently been made in recent years to control the composition of the SEI. For example, borrowing from successes of electrolyte additives in creating favorable SEI chemistries on the

graphite anode in the Lithium-ion battery, recent efforts have focused on the role of molecular and salt, including large salt concentrations, on the SEI composition and properties (14-22). Other efforts have focused on creating polymeric and ceramic interphases based on high-modulus materials with the aim of mechanically constraining the deposition to a small volume to maximize electrodeposit density (23 – 43). Yet other efforts have focused on designing of 3-D stable hosts and current collectors aimed at facilitating continuous electronic connection to metal electrodeposits as well as dissipate any interfacial stress build-up during electroplating (44-47). In most cases, the success of the approach is quantified using electrode- or cell-level measures of reversibility such as coulombic efficiency, compactness of the Li plated particularly at high electrodeposit capacity and number of cycles Li metal can be stripped and plated from the anode without inducing failure by dendrite-induced short circuits.

3.3 Results and Discussions

Here, we investigate the initial nucleation and growth dynamics of metallic Lithium in liquid electrolytes with/without components (brominated additives) believed to make the deposition non-dendritic. We hypothesize that regulation of the morphology of these early-stage electrodeposits is crucial for achieving late-stage control and high electrode reversibility. Recent works of Pei et al. (48) and Lopez et al. (49) have shown that interphases on Li play a key role in modulating the size, shape, rate of growth in the initial stages of electrodeposition. In a previous study (50), we reported that these effects can be described quantitatively by an analytical model in which transport through the electrolyte bulk and SEI on metallic Li are described as independent processes. An

additional motivation for the study comes from predictions from recent Joint Density Functional Theory (JDFT) work by Choudhury et al. (51) which show that interphases on Li enriched by LiBr salt offer the lowest known barrier to Li ad-atom transport in the SEI. Consistent with these predictions, we find that LiBr additives in carbonate does facilitate fast interphase ion transport and dramatically improves the uniformity of Li electrodeposit nuclei. More in-depth analysis of the interphases formed on Li in LiBr-enriched electrolytes nonetheless show that the source of the faster interphase transport and higher spatial uniformity of Li nuclei is not the salt itself, but an oligomeric species that appears to arise from polymerization of the electrolyte solvent initiated by LiBr. Electrochemical studies based on cycling life, coulombic efficiency, and optical visualization of Li electrodeposition with/without the brominated additive reveal that the benefits they impart in the nucleation step translate to higher reversibility, longer cycle life and decidedly non-dendritic morphology for the Lithium metal anode.

Lithium ions were galvanostatically electrodeposited onto a heterogeneous surface composed of polished stainless-steel (rms roughness = 9.12 ± 8.78 nm) from various liquid electrolytes. To investigate the effect of LiBr on nucleation and early stage growth of Li electrodeposits, experiments were performed at different current densities in carbonate liquid electrolyte with/without LiBr. The spatial characteristics (morphology, size) of Li nuclei formed in the process were analyzed ex-situ using Scanning Electron Microscopy (SEM); the interphases formed on the deposits studied using electrochemical impedance spectroscopy (EIS), goniometry and x-ray photoelectron spectroscopy (XPS); and the late-stage plating/stripping of Li studied using

galvanostatic symmetric cell cycling, coulombic efficiency, and optical visualization of Li electroplating.

To analyze the effect of ion transport in the electrolyte bulk and at the interphase on Li electrodeposition, we utilize a simple two-layer model for decoupled ion transport to a reactive metal nuclei of radius r at a heterogeneous surface. Reduction of the metal at the surface may either cause new deposits to nucleate or existing nucleates to grow. The nucleation barrier is a function of the electrochemical supersaturation (overpotential) of all the electrochemical processes involved: (a) migration of metal ions from the bulk electrolyte to the SEI, $\frac{irRT}{D_B C_B F^2}$; (b) migration of the incoming metal ions through the SEI to the electrified heterogeneous surface, $\frac{ir^2RT}{D_S C_S F^2}$; and (c) charge transfer of the metal ions to the heterogeneous surface ($\frac{RT}{\alpha F} \ln \frac{i}{i_0}$) and the formation of metal nuclei underneath the SEI ($\frac{2\gamma V}{Fr}$) (50, 52).

$$\eta = \frac{irRT}{D_B C_B F^2} + \frac{ir^2RT}{D_S C_S F^2} + \frac{RT}{\alpha F} \ln \frac{i}{i_0} + \frac{2\gamma V}{Fr} \quad (1)$$

Here η is the net overpotential due to all of the processes referenced above; i and i_0 are the current density and exchange current density respectively; r is the radius of the nuclei; D_B (m^2/s) and C_B (mol/m^3) are the bulk electrolyte Li ion diffusivity and concentration respectively; D_S (m^2/s) and C_S (mol/m^2) are the SEI Li ion diffusivity and concentration respectively, γ is the interfacial energy and α , V , R , T , F are charge transfer coefficient, molar volume of metal, universal gas constant, temperature and Faraday constant respectively.

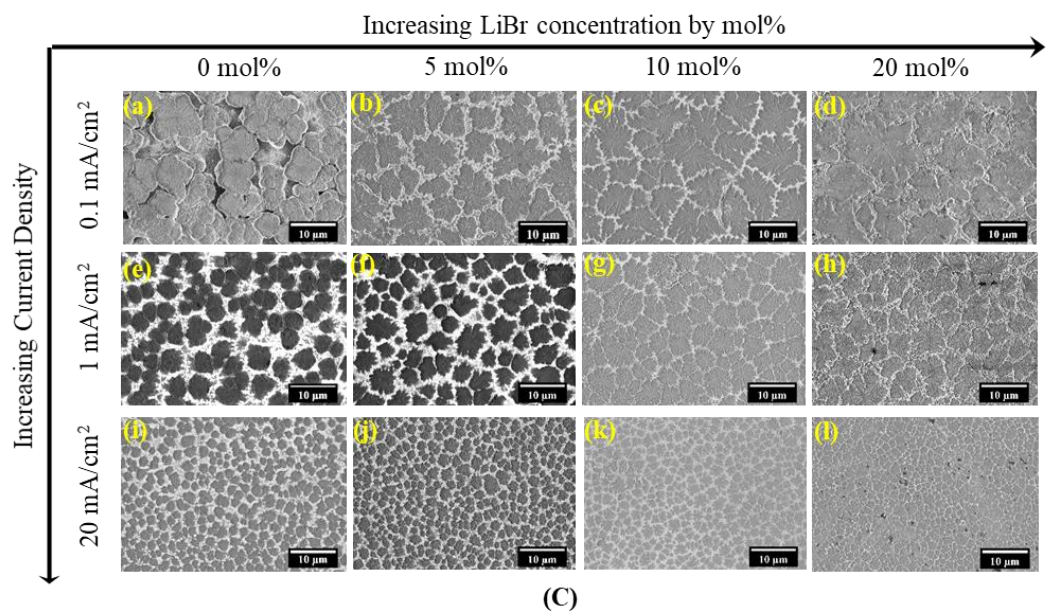
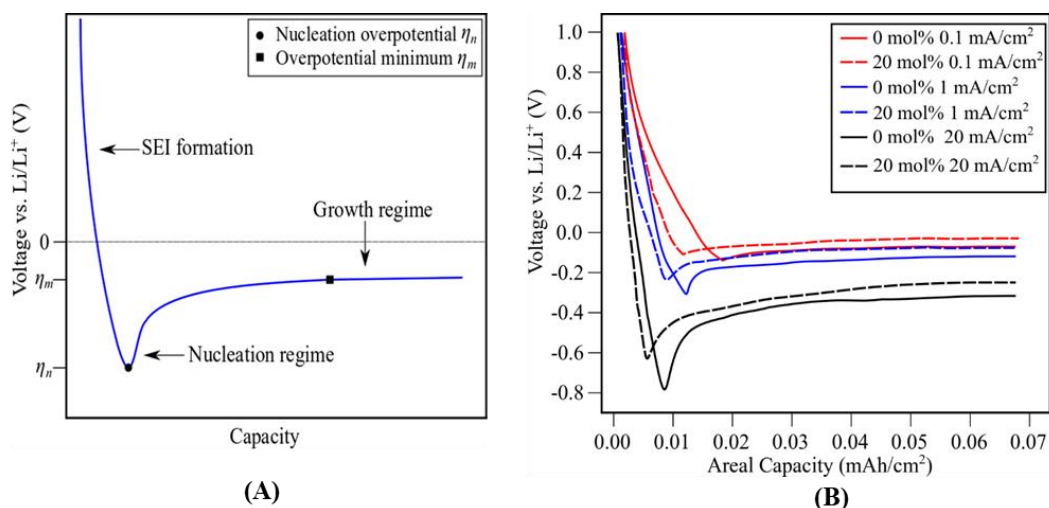


Figure 3.1. Fundamentals of lithium nucleation and growth and effect of electrolyte chemistry on morphology of Li electrodeposits. **(A)** Schematic plot showing a typical voltage profile of galvanostatic Li deposition. **(B)** Experimental voltage profiles of galvanostatic Li deposition for a range of current densities (0.1,1,20 mA/cm²) and different electrolyte compositions (0, 20 mol% LiBr) **(C)** Ex-situ SEM images of the electrodeposited Lithium morphology captured for a range of current densities of **(a-d)** 0.1 mA/cm², **(e-h)** 1 mA/cm², **(i-l)** 20 mA/cm² and electrolyte compositions **(a,e,i)** 0, **(b,f,j)** 5, **(c,g,k)** 10, **(d,h,l)** 20 mol% LiBr. The base electrolyte is 1M LiPF₆ in EC: DMC (1:1 vol.%) and the areal capacity of electrodeposition is 0.05 mAh/cm² (corresponding to Overpotential minimum).

The ion movement and charge transfer processes typically occur simultaneously during galvanostatic electrodeposition of Li ions, therefore deconvoluting and identifying contributions each make to the net overpotential is difficult. It is possible nonetheless to identify characteristics of the net overpotential curve (voltage response curve) that facilitate qualitative delineation of the various effects (48, 50). At currents densities $i < i_L$, the net overpotential curve (**Figure 3.1(A)**) due to galvanostatic deposition of Li ions has three distinct regimes: an initial drastic drop in voltage due to SEI formation; followed by a negative peak in voltage (local maxima) due to extra energy required for nucleation of Li metal from Li ions; and an eventual plateauing of the voltage curve as a result of post nucleation growth phase of Li nuclei. The overpotential at the voltage peak of nucleation is referred to as Nucleation overpotential (η_n), a combination of charge transfer overpotential and interfacial formation overpotential in the formation of the nuclei, while the overpotential in the growth phase voltage plateau region is referred to as the Overpotential minimum (η_m), a combination of mass transfer overpotentials due to ion diffusion through the bulk electrolyte and SEI to the growing nuclei. η can be minimized with respect to the characteristic size (radius) of the nuclei, to yield an inverse relationship between current density (i) and radius (r) of the nuclei (**Equation 2**).

$$i = \frac{1}{\tilde{r}^2 A' + \tilde{r}^3 B'} \quad \text{where } A' = \frac{RT}{2\gamma V D_B C_B F} \quad \text{and } B' = \frac{RT}{\gamma V D_S C_S F} \quad (2)$$

The Overpotential minimum is associated with a certain characteristic nuclei size, \tilde{r} , and a particular Li electrodeposition capacity (**Figure 3.1(A)**). From Equation 2 we see that ionic diffusion in the bulk is associated with the term quadratic in \tilde{r}^2 , while ionic

transport in the SEI produces a stronger, \tilde{r}^3 term in the current. The coefficients, A' and B' , associated with the \tilde{r}^2 and \tilde{r}^3 terms can be used, respectively, to infer information about the bulk ($C_B D_B$) and surface ($C_S D_S$) ionic conductivity. Thus, from measurements of the electrodeposit size at the beginning of the growth phase, it is possible to deduce information about the bulk and interfacial ion transport in an electrolyte (50).

We investigated electrodeposition of Li under galvanostatic conditions for a range of current densities and LiBr compositions (**Supplementary Figure 3.1, 3.2**) in standard 2032 coin-cells in which polished stainless steel was the working electrode and Li metal foil the counter electrode. A conventional carbonate electrolyte 1M LiPF₆ in EC:DMC (1:1 vol.%) reinforced with increasing concentrations of Lithium bromide (LiBr) additive (0, 5, 10, 20 mol%) was used in the study to investigate the effect of the salt additive on nucleation of Li electrodeposits. By means of ex-situ postmortem SEM analysis we characterized the size and morphology of Li nucleates formed on stainless-steel electrodes harvested from cells under the various electrolyte and cell running conditions (**Supplementary Figure 3.3, 3.4, 3.5, 3.6**). The net overpotential (galvanostatic voltage response) curves across all current densities (0.1 – 20 mA/cm²) and electrolyte chemistries (0 – 20 mol% LiBr) (**Supplementary Figure 3.1**) show typical behavior of voltage dip due to SEI formation, voltage peak at about capacity of 0.005 – 0.02 mAh/cm² due to metal nucleation and voltage plateauing (Overpotential Minimum (η_m)) at about 0.05 mAh/cm² ($\pm 5\%$) due to subsequent electroplating of ions onto the nuclei in the growth phase. These voltage-capacity features are further elaborated in **Supplementary Figure 3.2**. The small areal capacities are equivalent to

electrodeposit film thickness of 20 –120 nm (0.005 – 0.02 mAh/cm²) and 270 – 330 nm (0.05 mAh/cm² (\pm 5%)) if Li electrodeposits have the same density as that of bulk Li metal. The capacity for Nucleation overpotential (η_n) is higher for lower current densities as a lower rate of electrodeposition may result in simultaneous formation of SEI and Li nuclei (48,50), while the capacity at the Overpotential minimum (η_m) is slightly higher for higher current densities, as a high rate of electrodeposition may result in nucleation first followed by formation of SEI as shown in **Supplementary Figure 3.1, 3.2(a)**. It is also observed that the absolute value of voltage corresponding to Nucleation overpotential (η_n) and Overpotential minimum (η_m) increases with increase in current density for any electrolyte chemistry (**Supplementary Figure 3.1, 3.2(b)**). This is also apparent from Equation 1, which shows that any increase in current density contributes positively to charge transfer overpotential ($\frac{RT}{\alpha F} \ln \frac{i}{i_0}$) and mass transfer overpotentials ($\frac{irRT}{D_B C_B F^2} + \frac{ir^2 RT}{D_S C_S F^2}$) and therefore, to the net overpotential (η).

Comprehensive post-mortem analysis of multiple replicates of the Li electrodeposits were carried out via ex-situ SEM and XPS. The areal capacities were fixed at about 0.05 mAh/cm² corresponding to the Overpotential minimum (See SI). The morphology and size of the electrodeposits formed under different brominated electrolyte chemistries (0, 5, 10, 20 mol%) for a range of current densities (0.1 – 20 mA/cm²) is reported in **Supplementary Figure 3.3, 3.4, 3.5, 3.6**. A subset of the results obtained from the studies performed at the extremes, *i.e.*, widely differing current densities (*e.g.* 0.1 mA/cm², 1mA/cm², 20 mA/cm²) and electrolyte compositions (0 – 20 mol% LiBr) is presented in **Figure 3.1(B),(C)**, to facilitate the discussion. The first minimum in the

overpotential curve is noticeably deeper at higher current density. The corresponding Nucleation overpotential (η_n) is in the range 0.63 – 0.79 V at 20 mA/cm² compared to 0.1 – 0.16 V at 0.1 mA/cm². The Overpotential minimum (η_m) is also markedly lower (from 0.24 – 0.32 V at 20 mA/cm²) to (0.04 – 0.07 V at 0.1 mA/cm²). The spread in the respective η_n and η_m values, with lower values occurring for higher mol% LiBr, reflect the additional effect of LiBr composition (0 mol% - 20 mol%) in the electrolytes (**Supplementary Figure 3.2(b)**). It is also observed that the areal capacity values and spread at Nucleation overpotential (η_n) for the brominated electrolyte (20 mol% LiBr) is significantly lower than the standard electrolyte (0 mol% LiBr) for the range of current densities studied (**Supplementary Figure 3.2(a)**). The areal capacity at Overpotential minimum (η_m) shows a similar trend but a much weaker dependence on LiBr mol%, therefore remains within the limit of 0.05 mAh/cm² (\pm 5%) across all current densities and electrolyte chemistries studied. Our findings of are consistent with the notion that the LiBr additive enhances ion transport through the SEI which lowers the nucleation barrier and critical capacity at which Li electrodeposit nuclei form. These inferences are consistent with results reported in reference (50) as well as in the JDFT analysis (51).

The morphology of Li electrodeposits deduced from SEM analysis are reported in **Figure 3.1(C)**. At lower current densities, the bare bright stainless-steel substrate can be clearly seen underneath the nuclei. The nuclei exist as distinct structures with a well-defined size for any given current density and electrolyte composition, with bigger nuclei occurring at lower current densities (*e.g.* the nuclei formed at 0.1 mA/cm² for 0

mol% LiBr (**Figure 3.1(C)(a)**) are more than twice the size (2.643 μm compared to 1.061 μm) of those formed at 20 mA/cm² (**Figure 3.1(C)(i)**). It is also apparent that the number density of nuclei is higher at higher current densities. These observations can be rationalized in a straightforward way: a higher current density imparts higher activation (nucleation) overpotential to form nuclei (**Supplementary Figure 3.1, 3.2**), and the nuclei size is inversely proportional to the activation overpotential (48,50), therefore rendering greater number of smaller nuclei for a constant capacity of electrodeposition. The nuclei sizes do not change appreciably with addition of LiBr for a fixed current density (e.g. nuclei formed at 0.1 mA/cm² for 0 mol% LiBr (**Figure 3.1(C)(a)**) are of comparable size (2.643 μm compared to 3.034 μm) to those formed at 20 mol% LiBr (**Figure 3.1(C)(d)**). **Supplementary Figure 3.7** summarizes all of the information on the effect of current density and electrolyte composition on the average nuclei size of Li electrodeposits.

Closer analysis of **Figure 3.1(C)** shows that at any current density, LiBr produces a significant change in morphology of the Li electrodeposits. Comparing the morphology across the panel of SEM images for a fixed current density (**Figure 3.1(C)(a-d),(e-h),(i-l)**), a clear transition from blob-like, three-dimensional (3-D) electrodeposit structures, to more planar, 2-D, structures, is apparent. It is also apparent that the 2-D structures are less isolated and in fact appear to be flowing into each other. This *planarizing* effect of LiBr is even more evident at a lower current density of 0.1 mA/cm² and 20 mol% LiBr (**Figure 3.1(C)(d)**), where the spatial coverage of the 2-D nuclei renders the bright stainless-steel background virtually invisible. This observation is further examined by cross-sectional SEM via the Cryo-FIB technique as shown in **Supplementary Figure**

3.8. The Li nuclei in the 0 mol% LiBr case exhibit more three-dimensional (3-D) features as opposed to the planar Li deposit observed in the 20 mol% LiBr case. Similar two-dimensional (2-D) nuclei are also observed in electrolytes reinforced with other halide salts (LiCl and LiI) as shown in **Supplementary Figure 3.9**.

Bromide additives and intermediates have been argued in the literature to facilitate uniform plating of Li by altering the chemical composition of the SEI (21, 47, 51). To identify root causes for our observations, we first studied the effect of LiBr on the chemical composition of the SEI in these early stages of Li electrodeposition. X-ray Photoelectron spectroscopy (XPS) was performed to investigate the surface chemistry of the SEI formed in electrolytes containing LiBr. The results are reported in **Figure 3.2** and **Supplementary Table 3.1, 3.2**. Distinct changes in the chemical composition of the SEI can be readily observed. The survey spectra in **Figure 3.2(A)** shows multiple atomic peaks of which Lithium 1s (55.5 eV), Carbon 1s (284.5 eV), Oxygen 1s (531.6 eV), Phosphorous 2p (133 eV), Fluorine 1s (684.9 eV), and Bromine 3p (185 eV) are relevant. It is observed further that the concentration of Br increases from 0 to 1.34 at% in the SEI with increasing LiBr concentration. However, when compared to the amount of LiBr added into the electrolyte, the rise in Bromine at% in the SEI is meagre (*e.g.*, for 20 mol% LiBr electrolyte, the amount of Br in the electrolyte is 1.5 wt% compared to 0.07 wt% in the SEI (**Supplementary Table 3.1**)). It is also observed that the at% of Carbon and Oxygen increases dramatically with the addition of LiBr (*e.g.*, the at% of Carbon and Oxygen in the SEI are 13.17% and 9%, respectively, for 0 mol% LiBr compared to 36.7% and 25.3%, respectively for 20 mol% LiBr electrolyte. The at% of Li and Fluorine on the other hand decreases with increased LiBr content (*e.g.*, the at%

of Li and F in the SEI are 42.47% and 32.38% respectively for 0 mol% LiBr compared to 19.37% and 13.43% respectively for the electrolyte containing 20 mol% LiBr). The Carbon to Lithium ratio (C: Li) and Oxygen to Lithium ratio (O: Li) in the SEI therefore increases significantly with addition of LiBr. For 20 mol% LiBr, the C:Li and O:Li ratio are, respectively, 1.89 and 1.31; approximately 500% higher than the corresponding values of 0.31 and 0.21 at 0 mol% LiBr.

A closer look at the high-resolution spectra of Carbon is necessary to further understand the nature of bonding between Carbon, Oxygen and Lithium in the SEI that might produce these observations. There are three distinct peaks observed in the C 1s spectra: Li_2CO_3 at 289.05 eV, C-C-O at 285.6 eV, and C-C/C-H at 283.8 eV (**Figure 3.2(B)**). The Li_2CO_3 and C-C-O peaks are enhanced and the C-C/C-H peak is diminished for higher mol% of LiBr i.e. 26.74% Li_2CO_3 , 50.93% C-C-O, 22.35% C-C/C-H at 20 mol% LiBr compared to 17.97% Li_2CO_3 , 42.14% C-C-O, 39.18% C-C/C-H at 0 mol% LiBr (**Supplementary Table 3.2**).

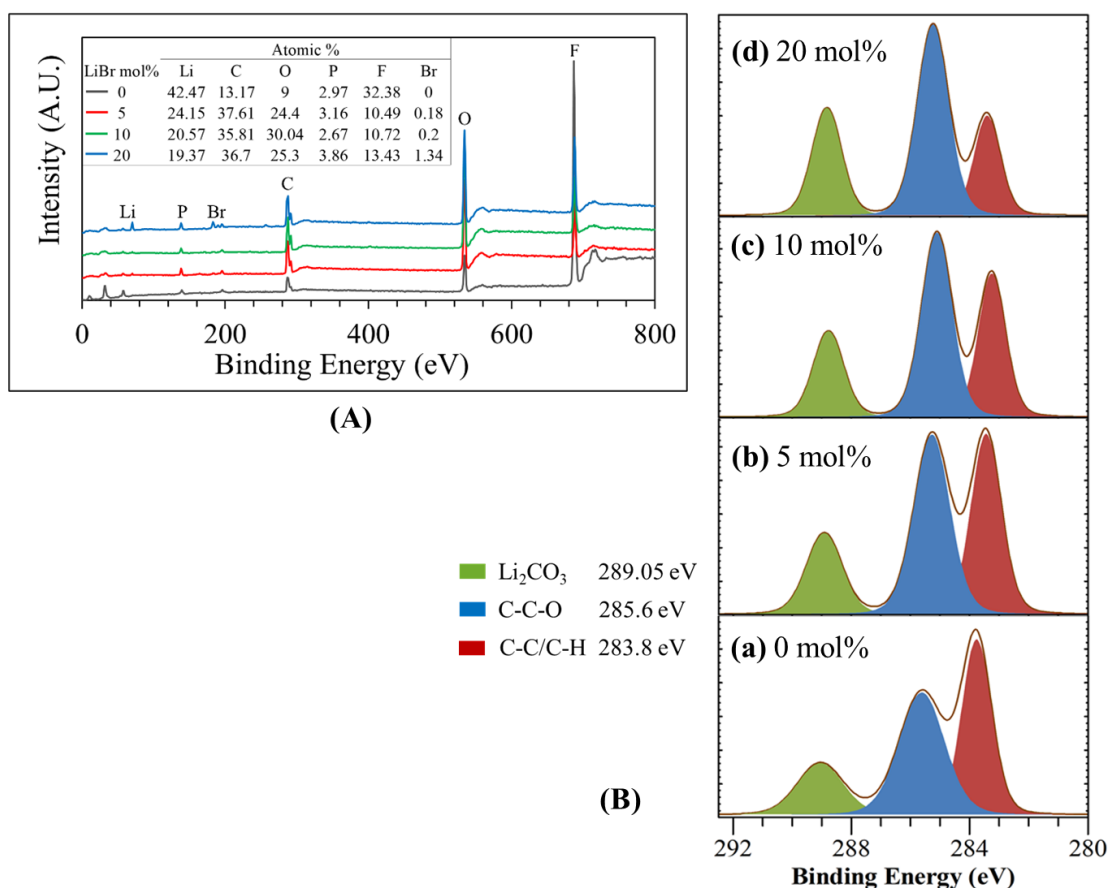


Figure 3.2. Interfacial chemistry of Lithium electrodeposits formed at low capacities. **(A)** Chemical spectra of the SEI layer induced by varying concentrations of LiBr (0, 5, 10, 20 mol%) in 1M LiPF₆ EC: DMC (1:1 vol.%) on Li electrodeposits formed at current density of 1 mA/cm² and areal capacities of 0.05 mAh/cm². **(B)** C 1s high-resolution spectra of SEI layer on Li electrodeposits formed at current density of 1 mA/cm² for areal capacities of 0.05 mAh/cm² induced by varying concentration of (a) 0 mol%, (b) 5 mol%, (c) 10 mol%, (d) 20 mol% LiBr in 1M LiPF₆ EC: DMC (1:1 vol.%).

We hypothesize that the increase in the C:Li, O:Li ratio and %Li₂CO₃, %C-C-O in the SEI that accompanies LiBr introduction is produced by LiBr, a Lewis acid (53, 54), induced formation of carbon rich SEI by enhancing decomposition of the Ethylene carbonate and Dimethyl carbonate solvent during electrodeposition. The carbon rich SEI contains greater amounts of Lithium carbonate (Li₂CO₃) and ethylene oxide oligomers (C-C-O) terminated with alkyl (C-H) as its major components. Existing literature shows that oligomerization of carbonate electrolytes via ring opening and/or anionic mechanisms can occur at the reducing potentials during Li electrodeposition (13, 30, 55 – 57). LiBr therefore appears to be enhancing this process. The percentage of C-C-O relative to C-C/C-H can be used to crudely assess the relative sizes of the formed oligomers. That this percentage is increased by LiBr, which our results show is in fact not enhanced in the SEI compared to other elements, supports our earlier hypothesis about LiBr.

Further, 1-H NMR spectroscopy of the cycled electrolyte w/o LiBr was performed to detect evidence of oligomers formed during the electrodeposition of Li (**Supplementary Figure 3.10**). Li was galvanostatically plated onto stainless steel at a low current density of 0.1 mA/cm² and capacity of 0.5 mAh/cm², and subsequently stripped to a potential of 1 V. The electrolyte was collected with DMSO-d₆ solvent, followed by 1-H NMR spectroscopy. The low current density and high capacity is to ensure significant formation of reduced electrolyte products at the stainless-steel interface that can be detected via NMR. **Supplementary Figure 3.10(b) & 3.10(c)** can be contrasted to observe any significant effects of LiBr additive over the base carbonate electrolyte. It is apparent that in the presence of LiBr, the reduction of EC/DMC

electrolyte is accelerated during electrodeposition, and results in a splitting of DMC peak at around 3.7 ppm (x peak) and minor side peaks around 4.05 ppm (y peak) and 3.48 ppm (z peak) as shown in **Supplementary Figure 3.10(c)**. No such peaks are apparent in the base electrolyte post cycling (**Supplementary Figure 3.10(b)**). **Supplementary Figure 3.10(d)** provides a closer comparison of the ^1H NMR spectra of the electrolyte with 0 mol% and 20 mol% LiBr additive post cycling, with several noticeable differences as mentioned above. The x peak formed at around 3.7 ppm is associated with the formation of Lithium ethylene di-carbonate (LEDC), while the minor peaks i.e. quadruplet peak y formed at around 4.05 ppm and peak z at around 3.48 ppm has been identified to be the characteristic peaks of Lithium methyl carbonate (LMC) and Lithium ethylene mono-carbonate (LEMC) (57). The oligomeric products LEDC, LMC, and LEMC typically found in the long term cycled standard carbonate electrolyte (57), are formed in higher concentrations even in the first cycle due to accelerated electrolyte reduction in presence of LiBr additive. These oligomeric products intrinsic to any SEI formed by carbonates, have ethylene oxide (C-C-O) linkage present in their backbone, further corroborating the results of XPS chemical analysis and the hypothesis of a carbon rich oligomeric SEI.

A carbon rich SEI with ethylene-oxide oligomeric linkage (C-C-O) is postulated to regulate electrodeposition of Li ions by modification of the interfacial energy and surface diffusion properties of the SEI, quite similar to Li^+ ion regulation exhibited by anionic backbone of elastic and resilient ethylene oxide polymer networks (58 – 61) during Li electrodeposition. Higher interphase mobility and surface energy enhances rearrangement of Li ions prior to deposition, facilitating more uniform and compact

electrodeposition. Hence, it is relevant to investigate the role of physical parameters such as surface energy and interfacial ion diffusion in the planarizing effect of bromine enriched SEI.

Equation 2 may be used as a tool for resolving the contributions made by surface energetic, bulk, and surface transport parameters. A proof of concept analysis was performed to fit the current density with the observed nuclei size \tilde{r} at η_m (0.05 mAh/cm²) using **Equation 2** (see **Appendix**). The observed nuclei size \tilde{r} correspond to the 4-sample averaged values obtained from multiple repeat measurements at each current density and electrolyte composition (**Supplementary Figure 3.3 – 3.6**). **Figure 3(a)** compares the predicted and measured values under three scenarios. In Case 1, we ignore surface diffusion (*i.e.* $A' \gg B'$, $i = \frac{1}{\tilde{r}^2 A'}$) and in Case 2 we ignore the contribution to the transport overpotential originating from ion migration in the electrolyte bulk (*i.e.* $B' \gg A'$, $i = \frac{1}{\tilde{r}^3 B'}$). Finally, in Case 3 we consider a scenario where the surface and bulk diffusion make comparable contributions to the transport overpotential (*i.e.* $i = \frac{1}{\tilde{r}^2 A' + \tilde{r}^3 B'}$). The vastly improved quality of the fit for Case 3, relative to Cases 1 and 2 confirm that a combination of mass transfer overpotentials due to bulk diffusion and SEI diffusion are relevant during the initial stages of Li electrodeposition. A similar proof of concept analysis for the LiBr-reinforced carbonate electrolytes reported in **Supplementary Figure 3.11** and **Figure 3.3(b)** lead to the same conclusion. Further, to elucidate the universality of the physics underlying **Equation 2** and governing Li electrodeposition in liquid electrolyte of any chemical composition, in **Supplementary Figure 3.12** we compare the predictions of this equation with experimental data for a wide range of electrolytes — carbonate, fluorinated (50), brominated, and ether-based electrolytes reported by Pei et al. (48). It is seen that the equation provides a good account of the experimental observations in every case. We therefore conclude that in

every situation, the Case 3 physics leading to $(i = \frac{1}{\tilde{r}^2 A' + \tilde{r}^3 B'})$ provide the best description of available \tilde{r} versus i data, for Li electrodeposition in liquid electrolytes. The interfacial energy (γ) for Lithium metal in a carbonate electrolyte with different LiBr content was estimated using contact angle goniometry in an Argon filled glovebox (see **Appendix**, for method to determine interfacial energy); the measured values are reported in **Supplementary Table 3.3** and **Figure 3.3(c)**. The interfacial energy (γ expt.) increases from 475 mJ/m² to 488 mJ/m² when the LiBr concentration rises from 0 to 20 mol%. The interfacial energy (γ theory) estimated from the best fit values of A' and B' obtained by fitting the Li nucleate size (\tilde{r}) versus applied current density (i) data using **Equation 2**, is a stronger function of LiBr content ranging from 471 mJ/m² to 712 mJ/m². While the increasing trend in interfacial energy with addition of LiBr is similar for both experimentally and theoretically determined γ , a mismatch between the values is apparent. We suspect this mismatch arises mostly from the fact that the experimental determination of γ employs Young's equation, which by its formulation underestimates the interfacial energy in comparison to canonical values for solid substrates (*e.g.*, γ Li = 520 mJ/m²) (62). Moreover, the SEI formed on Li by physical placement of liquid electrolyte on the Lithium substrate may not share the exact physical and chemical nature as that of the one formed during electrodeposition.

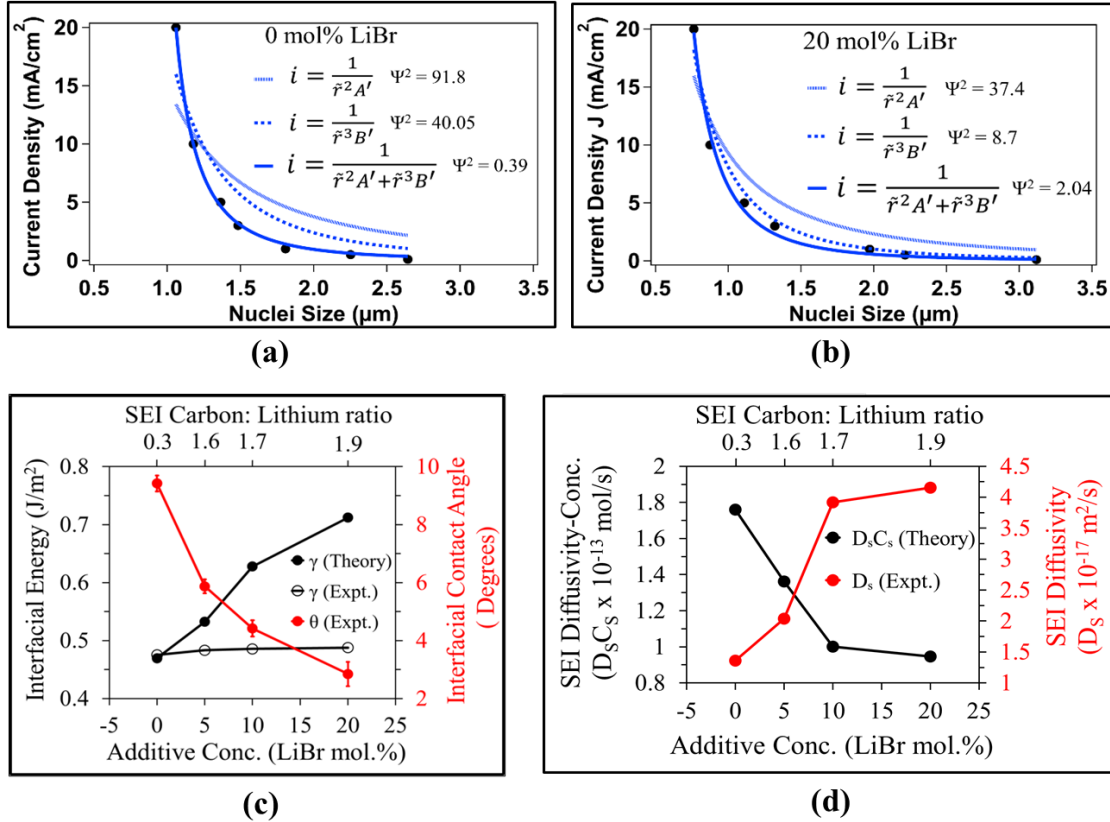


Figure 3.3. Proof of concept curve fitting at Overpotential minimum and effect of electrolyte chemistry/interfacial chemistry on the interfacial energy, interfacial contact angle, surface diffusivity, and concentration and of the SEI. The dependency of average nuclei radius on current density has been restricted to the effects of bulk diffusion overpotential, SEI surface diffusion overpotential, and combined effect of both for 1M LiPF₆ in EC: DMC (1:1 vol.%) reinforced with **(a)** 0 mol% LiBr **(b)** 20 mol% LiBr. **(c)** Plot of SEI interfacial energy (theoretically/experimentally determined) and interfacial contact angle (experimentally determined) for varying concentration of LiBr (0, 5, 10, 20 wt.%) in 1M LiPF₆ EC: DMC (1:1 vol.%) electrolyte and corresponding Carbon to Lithium ratio in the SEI layer. **(d)** Plot of SEI surface diffusivity-concentration (theoretically determined) and SEI surface diffusivity (experimentally determined) for varying concentration of LiBr (0, 5, 10, 20 wt.%) in 1M LiPF₆ EC: DMC (1:1 vol.%) electrolyte and corresponding Carbon to Lithium ratio in the SEI layer.

Electrochemical impedance spectroscopy performed on the Li electrodeposits on the stainless-steel reveals transport characteristics of the SEI and the bulk electrolyte as shown in **Supplementary Figure 3.14** and **Figure 3.3(d)**. The product of surface diffusivity and surface concentration $C_S D_S$ decreases with LiBr as shown in **Figure 3.3(d)**. However, the surface diffusivity of Li ions increases roughly three-fold with increase in concentration of LiBr (*e.g.* $D_S = 4.2 \times 10^{-17} \text{ m}^2/\text{s}$ for 20 mol% LiBr, compared with $D_S = 1.36 \times 10^{-17} \text{ m}^2/\text{s}$ at 0 mol% LiBr). Decreasing $C_S D_S$ value and an increasing D_S implies that the surface concentration of Li ions (C_S) is significantly lower electrolytes containing LiBr, as shown in **Supplementary Table 3.4**. These findings can be rationalized as follows. Li electrodeposition at the heterogeneous surface involves transport and delocalization of metal ions in the SEI followed by reduction of metal ions at the heterogeneous surface. A higher surface diffusivity implies easier 2-D migration of Li ions in the SEI, promoting more spread-out/delocalized electrodeposition. Assuming fast reduction kinetics of Li-ions at the electrode, a higher D_S would also lower the concentration of Li ions in the SEI. This also explains the lowering of the SEI and charge transfer resistance evident in **Supplementary Figure 3.14(c)**. Synergistically, high surface diffusivity and high interfacial energy of the SEI formed in electrolytes containing LiBr facilitates planar electrodeposits as observed earlier for brominated electrolytes (5 – 20 mol% LiBr). On the other hand, the standard carbonated electrolyte lacking such advantages of surface energetics forms 3-D, blob like nuclei and is expected eventually to succumb to morphological instability that drives growth of mossy/dendritic Li electrodeposit morphologies (50). This inference is in good agreement with the properties of polymeric/oligomeric SEI as reported (6, 13, 61, 63,

64) to have high interfacial conductivity and surface energy (via elasticity) (58) enough to stabilize Li electrodeposition.

Li-ion diffusivity in polymeric/oligomeric networks is also far faster ($D_{\text{Li}} \sim 10^{-12} - 10^{-14}$ m²/s) (61, 65, 66) in comparison to the solid inorganic compounds (e.g. Li₂CO₃/ Li₂O/ LiF ($D_{\text{Li}} \sim 10^{-16} - 10^{-20}$ m²/s) (67, 68) and inorganic-organic composites commonly found at Li electrodes cycled in carbonate electrolytes. Recent modelling studies have in fact shown the SEI diffusivity (67 – 72) to be anywhere in between 10^{-16} m²/s to 10^{-20} m²/s and SEI surface energy (10, 73 – 75) to be in between 180 mJ/m² to 840 mJ/m². These values are in rough agreement with those determined by fitting Equation 2 to our experimental results.

It is noticeable that despite the three-fold increase in surface diffusivity of Li ions for a bromine enriched oligomeric interface, the surface diffusivity (10^{-17} m²/s) is still seven orders of magnitude lower than the bulk diffusivity (10^{-10} m²/s) as shown in **Supplementary Figure 3.14(d)**. Contrasting the ratio of ion relaxation times for bulk diffusion (τ_{B} , ion transport length $\sim \tilde{r}$) and surface diffusion (τ_{S} , ion transport length \sim SEI thickness 100 nm (9)) for Li interphases in the control carbonate electrolyte (0 mol% LiBr) and LiBr-reinforced electrolyte, the latter has an order of magnitude higher ratio of relaxation times ($\tau_{\text{B}}/\tau_{\text{S}} = 2.8 \times 10^{-4}$ for brominated vs 4×10^{-5} for carbonate), and therefore considerably faster ion relaxation. However, the ratios are evidently much less than 1, implying that the Li ions relaxes much slower in the SEI than the bulk electrolyte. Taken together with the orders of magnitude mismatch between the interphase and bulk diffusivities, this slower transport might be expected to produce a

rapid piling-up of ions at the electrolyte/electrode interface, which could produce non-planar mossy/dendritic electrodeposition of Li. Electrolyte and interphases that lower the bulk/surface diffusivity ratio are therefore predicted to be essential for achieving compact, planar electrodeposition of Li in liquid electrolytes.

The analysis above provides insights into the role of surface energetics on the uniform plating of Li at low capacities. However, it remains to be determined if the surface energetics, chemical nature, and uniform morphology observed at low capacities translates to similar morphology and surface energetics at later stage (higher capacity) relevant for applications in practical Li metal batteries. In this context, we study the morphology, chemical composition, and surface energetics of electrodeposited Lithium at higher capacities (**Figure 3.4**). We further investigate the electrochemical reversibility and morphology of Li electrodeposits via galvanostatic stripping/plating, coulombic efficiency, and optical microscopy (**Figure 3.5**).

Li was galvanostatically electrodeposited onto polished stainless substrate at current densities of 1 mA/cm² from liquid electrolyte with/without LiBr, for higher capacities of 0.5 mAh/cm² i.e., about an order of magnitude higher than the low capacity of 0.05 mAh/cm². **Figure 3.4(A)** shows panel of SEM images at contrasting capacities of 0.05 mAh/cm² (**Figure 3.4(A)(a-d)**) and 0.5 mAh/cm² (**Figure 3.4(A)(e-h)**) for the range of LiBr concentration in electrolyte. It can be observed that the morphology of Li electrodeposits is entwined wire-like mossy dendrites for 0 mol% LiBr (**Figure 3.4(A)(e)**) contrasted to relatively smooth morphology observed for 20 mol% LiBr (**Figure 3.4(A)(h)**). In other words, the entwined wire-like dendrites observed for 0 mol% LiBr case have no resemblance to have grown out of the nuclei at lower capacity

(**Figure 3.4(A)(a)**), while the smooth morphology observed for 20 mol% LiBr retains the spatial uniformity in nuclei morphology observed at lower capacity (**Figure 3.4(A)(d)**). The panel of SEM images (**Figure 3.4(A)(e-h)**) show a gradual increase in non-dendritic morphology with addition of LiBr to the electrolyte. The chemical composition of the SEI during late-stage electroplating (0.5 mAh/cm²) is examined via XPS survey spectra (**Supplementary Figure 3.15, Supplementary Table 3.5**) along with high-resolution C 1S spectra (**Supplementary Figure 3.16**). For brevity of discussion, the results are briefly summarized and contrasted to that of lower capacity in **Figure 3.4(B),(C)**. The SEI is still bromine enriched (**Supplementary Figure 3.15**) with meagre percent of LiBr (**Supplementary Table 3.5**) in it compared to the brominated liquid electrolyte. Similar to the lower capacity case, the C: Li and O: Li ratio increases about 150%, with increase in ethylene oxide C-C-O linkage (from 45.17 to 56.41%) and decrease in alkane/ alkyl C-C/C-H linkage (from 29.43 to 17.72%) across the range of brominated electrolyte chemistry (0 to 20 mol% LiBr) as shown in **Figure 3.4(B),(C)**. Crudely, this suggests that the oligomeric SEI formed at lower capacities is retained in its nature of chemical composition at higher capacities of electrodeposition as well.

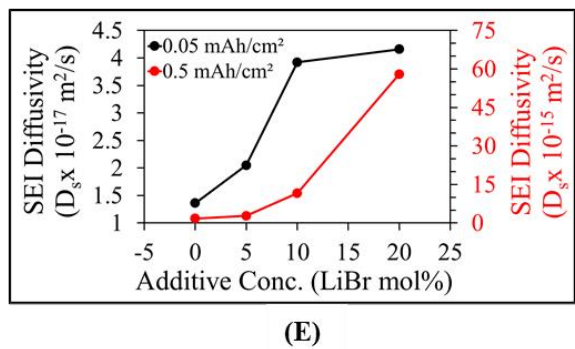
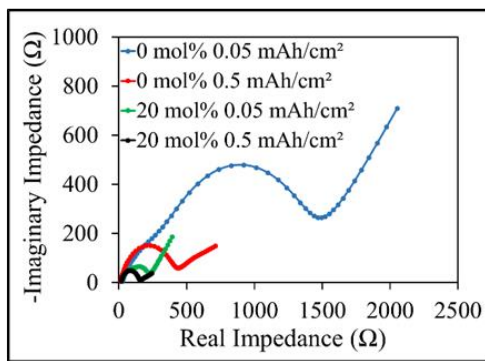
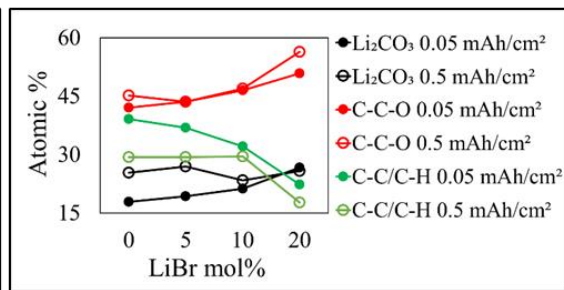
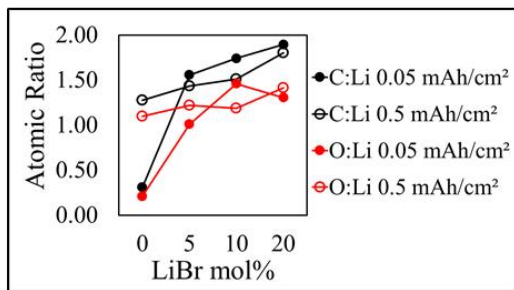
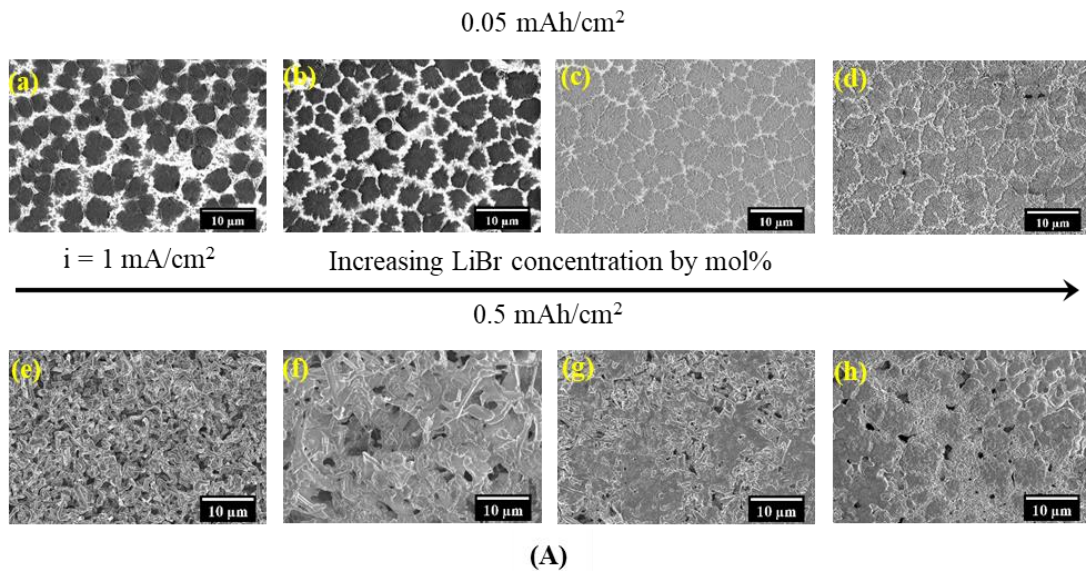
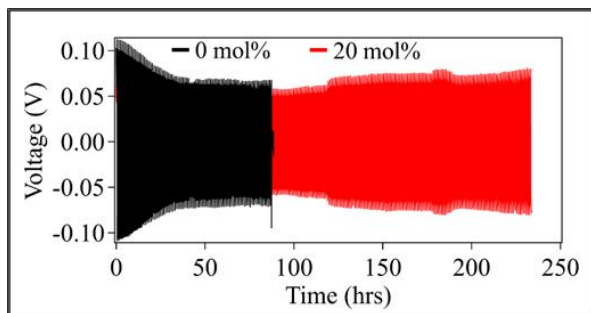


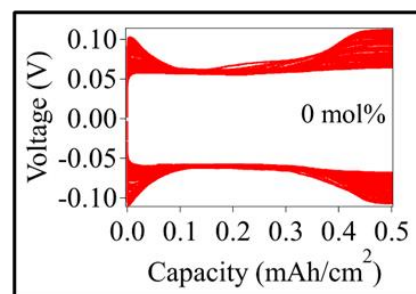
Figure 3.4. Effect of electrolyte chemistry/interfacial chemistry on the morphology of Li electrodeposits and physical transport characteristics of Li ion at the interface at contrasting capacities of electrodeposition. **(A)** Ex-situ SEM images of the electrodeposited Lithium morphology captured at current density of 1 mA/cm² at increasing capacities of **(a-d)** 0.05 mAh/cm² and **(e-f)** 0.5 mAh/cm² for different electrolyte compositions of 1M LiPF₆ in EC:DMC (1:1 vol.%) reinforced with **(a,e)** 0 mol%, **(b,f)** 5 mol%, **(c,g)** 10 mol%, **(d,h)** 20 mol% LiBr. **(B)** Plot of atomic ratio of Carbon to Lithium of the SEI formed at different capacities of 0.05 mAh/cm² and 0.5 mAh/cm² for electrolyte compositions of LiBr (0, 5, 10, 20 wt.%) in 1M LiPF₆ EC: DMC (1:1 vol.%), derived from survey spectra of XPS. **(C)** Plot of atomic % of components of Carbon 1s high resolution spectra of the SEI formed at different capacities of 0.05 mAh/cm² and 0.5 mAh/cm² for electrolyte compositions of LiBr (0, 5, 10, 20 wt.%) in 1M LiPF₆ EC: DMC (1:1 vol.%). **(D)** Nyquist plots showing electrochemical impedance spectra of Li electrodeposits at two contrasting mol% of LiBr and capacities of electrodeposition. **(E)** Plot of SEI Li ion diffusivity for Li electrodeposited at different capacities from LiBr reinforced electrolyte as calculated from the Nyquist plots.

Electrochemical impedance spectroscopy performed on higher capacity (0.5 mAh/cm²) electrodeposited Li for the range of electrolyte composition (0 – 20 mol% LiBr) is shown in **Supplementary Figure 3.17** and contrasted to that of lower capacity (0.05 mAh/cm²) in **Figure 3.4(D),(E)**. The impedance loops in Nyquist plots are relatively smaller for higher capacity than that of lower capacity with the smallest for the 20 mol% brominated electrolyte (**Figure 3.4(D)**), indicating lower SEI and charge transfer resistance for higher capacity (**Supplementary Figure 3.17(B),(C)**) and the lowest of any resistance for the bromine enriched interface formed in 20 mol% brominated electrolyte. Comparing the SEI ion diffusivity across the contrasting capacities and

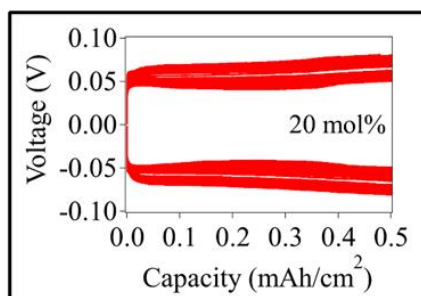
electrolyte compositions (**Figure 3.4(E)**), we observe that higher capacities ($\sim 10^{-15}$ m²/s) have two order of magnitudes higher diffusivity than lower capacity electrodeposits ($\sim 10^{-17}$ m²/s), and bromine enriched SEI (20 mol% LiBr) has exceptionally higher diffusivity (5.7×10^{-14} m²/s) than any of its counterparts i.e. for e.g. the SEI formed in the standard electrolyte (0 mol% LiBr) has ion diffusivity 1.7×10^{-15} m²/s. The above observations can be rationalized as follows: The nascent SEI formed in the initial stages of electrodeposition at lower capacities matures into a well-formed SEI at higher capacities, enhancing ion transport through it as it grows. The bromine enriched SEI being of oligomeric nature has exceptionally fast ion transport closely resembling that of ion diffusion through bulk polymer networks ($\sim 10^{-12} - 10^{-14}$ m²/s) (61, 65, 66), as compared to the non-brominated SEI which has more than an order of magnitude lower ion diffusivity and resembles more of an inorganic SEI ($\sim 10^{-16} - 10^{-20}$ m²/s) (67, 68). The bromine enriched SEI also had higher surface ion diffusion and higher surface energy in its initial stages of formation. The non-dendritic morphology in a brominated electrolyte at higher capacities in **Figure 3.4(A)(h)** is an outcome of this effect, while as predicted the standard carbonate electrolyte lacking such interfacial advantages eventually succumbs to the morphological instability that drives mossy/wire like dendritic growth of Li electrodeposits.



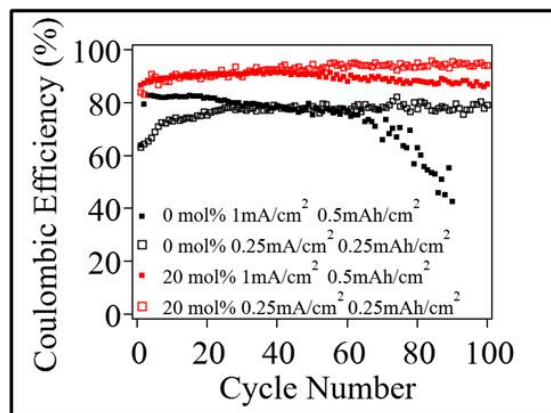
(A)



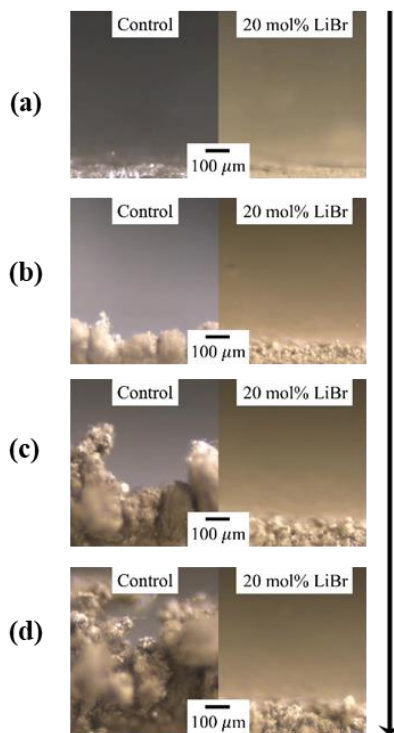
(B)



(C)

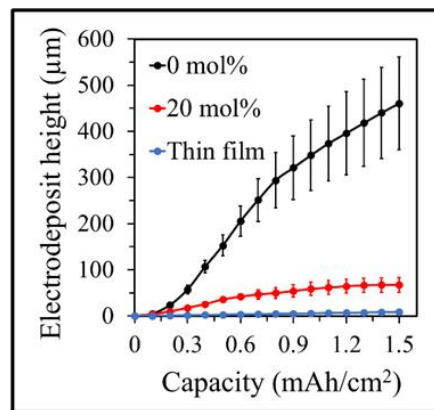


(D)



(E)

Increasing Areal Capacity of Electrodeposition



(F)

Figure 3.5. Reversibility and cyclability of Li electrodeposits formed under the influence of brominated electrolyte chemistry. **(A)** Galvanostatic plating stripping voltage profile of symmetric Lithium at a current density of 1 mA/cm² and capacity of 0.5 mAh/cm² in 1M LiPF₆ EC: DMC (1:1 vol.%) reinforced with 0 mol% and 20 mol% LiBr. Plot of voltage vs areal capacity for **(B)** 0 mol% and **(C)** 20 mol% LiBr. **(D)** Coulombic efficiency of electrodeposited Lithium on polished stainless steel for 100 cycles at different electrolyte compositions (0,20 mol% LiBr) and varying cycling conditions. **(E)** Optical snapshots of Li electrodeposition from video (**SI, Video S1**) for increasing capacities **(a)** 0 **(b)** 0.5 **(c)** 1 **(d)** 1.5 mAh/cm² in 1M LiPF₆ EC: DMC (1:1 vol.%) reinforced with 0 mol% (control) and 20 mol% LiBr. **(F)** Plot of electrodeposit height for increasing capacities of Li electrodeposition for 0 mol%, 20 mol% LiBr and Lithium as a thin film. The electrodeposit height is calculated from **Supplementary Video 3.1 in Appendix**.

The electrochemical reversibility of Li electrodeposits under the influence of the LiBr additive is shown in **Figure 3.5**. Galvanostatic plating stripping experiments performed at a current density of 1 mA/cm² and capacity of 0.5 mAh/cm² show a three-fold enhancement in cycle life for the standard electrolyte reinforced with 20 mol% LiBr additive. The resulting voltage profiles can be contrasted as well to understand the role of the LiBr additive on the interfacial transport during repeated plating/stripping as shown in **Figure 3.5(B)** (0 mol%) and **Figure 3.5(C)** (20 mol%). The voltage profile for the standard electrolyte (0 mol% LiBr) case (**Figure 3.5(B)**) shows three distinct regimes: a voltage peak of about 0.06 – 0.1V at around 0.01 mAh/cm², typical of Li dendrites nucleation on the Li anode at beginning of electroplating; followed by a gradual transition to extended voltage plateau of about 0.06 - 0.08V from roughly 0.1 mAh/cm² to 0.35 mAh/cm², typical of mass transfer of Li ions onto the formed nuclei

on the Li anode as well as electrodisolution of Li dendrites on the Li cathode; subsequently followed by a gradual voltage spike of about 0.08 – 0.1V from around 0.35 mAh/cm² to 0.5 mAh/cm², typical of switch from ongoing electrodisolution of Li dendrites to pitting of Li bulk cathode i.e. due to diminished accessibility of orphaned and electrochemically-dead Lithium present in dendrites on the Li cathode (76). The presence of nucleation and pitting peaks in the cycling voltage profile during repeated plating stripping cycles suggests significant barrier to ion transport at the interface and low electrochemical reversibility of electrodeposited Lithium. However, the cycling voltage profile for the standard electrolyte reinforced with 20 mol% LiBr is devoid of any such peaks even for 3-fold longer cycle life (**Figure 3.5(A),(C)**). The voltage varies between 0.05 – 0.08 V for the entire capacity of cycling i.e., lower than the voltage range of the standard electrolyte (0 mol%). This is indicative of facile ion transport being promoted by the bromine enriched SEI and relatively better electrochemical reversibility of the Li electrodeposits in the brominated electrolyte. Coulombic efficiency (CE) tests performed at a similar current density of 1 mA/cm² and capacity of 0.5 mAh/cm² corroborate the above inference (**Figure 3.5(D)**). The 20 mol% LiBr reinforced electrolyte shows a consistent CE of 87 – 88% at 80 – 100 cycles contrasted to drastically dropping CE between 60 – 40 % at 80 – 90 cycles for the standard electrolyte (0 mol% LiBr). Coulombic efficiency performed at more moderate current densities (0.25 mA/cm²) and capacities (0.25 mAh/cm²) show consistent CE for 100 cycles for both electrolyte compositions with LiBr reinforced electrolyte showing higher CE (94 – 95%) than the standard electrolyte (78 – 80%).

Optical visualization of the growth of electrodeposited Lithium on a stainless-steel substrate at a current density of 3 mA/cm² and capacity of 1.5 mAh/cm² for the contrasting electrolyte chemistries is shown in **Supplementary Video 3.1** and as snapshots in **Figure 3.5(E)**. It is seen that the morphology of electrodeposits (**Figure 3.5(E)(a-d)**) evolves rapidly as large mossy dendrites in the standard electrolyte (0 mol% LiBr) compared to the brominated electrolyte (20 mol% LiBr) which has a smooth morphology and is essentially dendrite-free, with a visually slower growth rate. Semi-quantitative analysis of electrodeposit height (μm) and roughness (error-bars) as a function of capacity is performed on the snapshots using ImageJ software and is presented in **Figure 3.5(F)**. The thickness (height) of a thin film of Lithium (i.e. if Li electrodeposited dendrite free and at the same density of bulk anode) for a capacity of 1.5 mAh/cm² is about 9 μm . Mossy dendritic electrodeposits formed in the standard electrolyte drastically evolve over the capacity of electrodeposition to heights of about 450 μm with largely uneven morphology of roughness \pm 100 μm . However, the electrodeposits in the brominated electrolyte are relatively less dendritic with a smoother morphology and show an order of magnitude lower height (\sim 70 μm) and roughness (\sim 16 μm). Essentially, the electrodeposits formed in the presence of LiBr enriched electrolyte and SEI, have a closer resemblance to thin film lithium than that of a standard carbonate electrolyte. These results further imply that the brominated electrolyte has a stabilizing effect on the morphology of electrodeposition. Together, the galvanostatic stripping/plating, Coulombic efficiency tests and optical visualization of Li electroplating show that the brominated electrolyte enhances the electrochemical reversibility and stability of electrodeposited Li by maintaining facile transport of ions

through the bromine enriched SEI i.e., an ongoing effect of increased surface energetics (surface diffusion and interfacial energy) deciphered previously at initial stages of Li electrodeposition.

3.4 Conclusion

In conclusion, we studied the role of brominated electrolytes on the morphology, chemical composition, interfacial energetics, and electrochemical reversibility of Li electrodeposits during early as well as later stages of electroplating. Theoretical formulations with aptly tailored experiments shed light into the surface energetics of the SEI. Ion transport (diffusion) through bulk electrolyte and the surface (SEI) is demonstrated to play equally important role in Li electroplating across a range of electrolyte chemistries (carbonate-based, fluorinated, brominated, ether-based) studied in this work or previously in literature. Further, we demonstrated that surface energetics, chemical nature, and uniform morphology observed at initial stages of electroplating do translate to electrochemical stability at later stages of electroplating and has a positive effect on the reversibility of Li electrodeposits during deep cycling. Designing interfaces with high surface energy and high surface diffusivity is a feasible solution to stabilize electrodeposition of reactive metals such as Lithium. Additional studies dealing with the fundamental approach of understanding and eliminating morphological and chemical instabilities at the initiation step of dendrite nucleation for a reactive metal electrodeposition are paramount to accelerate the realization of high energy density, high performance reactive metal batteries.

3.5 Acknowledgement

The research was supported as part of the Center for Mesoscale Transport Properties, an Energy Frontier Research Center supported by the U.S. Department of Energy (DOE), Office of Science, Basic Energy Sciences, under Award DE-SC0012673. The electron microscopy facilities made use of the Cornell Center for Materials Research Shared Facilities which are supported through the NSF MRSEC program (DMR-1719875). The interface characterization work made use of the facilities available in CESI, Cornell.

3.6 References

- (1) Zhang, J. G., Xu, W., & Henderson, W. A. (2017). Lithium metal anodes and rechargeable lithium metal batteries. *Springer International Publishing: Switzerland*.
- (2) Whittingham, M. S. (2012). History, evolution, and future status of energy storage. *Proc. IEEE, 100*, 1518-1534.
- (3) Aurbach, D., & Cohen, Y. (1996). The application of atomic force microscopy for the study of Li deposition processes. *Journal of the Electrochemical Society, 143*(11), 3525-3532.
- (4) Xu, W., Wang, J., Ding, F., Chen, X., Nasybulin, E., Zhang, Y., & Zhang, J. G. (2014). Lithium metal anodes for rechargeable batteries. *Energy & Environmental Science, 7*(2), 513-537.
- (5) Lin, D., Liu, Y., & Cui, Y. (2017). Reviving the lithium metal anode for high-energy batteries. *Nature nanotechnology, 12*(3), 194.
- (6) Tikekar, M. D., Choudhury, S., Tu, Z., & Archer, L. A. (2016). Design principles for electrolytes and interfaces for stable lithium-metal batteries. *Nature Energy, 1*(9), 1-7.

- (7) Chianelli, R. R. (1976). Microscopic studies of transition metal chalcogenides. *Journal of Crystal Growth*, 34(2), 239-244.
- (8) Aurbach, D., Zinigrad, E., Cohen, Y., & Teller, H. (2002). A short review of failure mechanisms of lithium metal and lithiated graphite anodes in liquid electrolyte solutions. *Solid state ionics*, 148(3-4), 405-416.
- (9) Zachman, M. J., Tu, Z., Choudhury, S., Archer, L. A., & Kourkoutis, L. F. (2018). Cryo-STEM mapping of solid-liquid interfaces and dendrites in lithium-metal batteries. *Nature*, 560(7718), 345-349.
- (10) Yamaki, J. I., Tobishima, S. I., Hayashi, K., Saito, K., Nemoto, Y., & Arakawa, M. (1998). A consideration of the morphology of electrochemically deposited lithium in an organic electrolyte. *Journal of Power Sources*, 74(2), 219-227.
- (11) Wang, X., Zeng, W., Hong, L., Xu, W., Yang, H., Wang, F., ... & Jiang, H. (2018). Stress-driven lithium dendrite growth mechanism and dendrite mitigation by electroplating on soft substrates. *Nature Energy*, 3(3), 227-235.
- (12) Zheng, J., Tang, T., Zhao, Q., Liu, X., Deng, Y., & Archer, L. A. (2019). Physical orphaning versus chemical instability: is dendritic electrodeposition of Li fatal?. *ACS Energy Letters*, 4(6), 1349-1355.
- (13) Zheng, J., Kim, M. S., Tu, Z., Choudhury, S., Tang, T., & Archer, L. A. (2020). Regulating electrodeposition morphology of lithium: towards commercially relevant secondary Li metal batteries. *Chemical Society Reviews*.
- (14) Miao, R., Yang, J., Feng, X., Jia, H., Wang, J., & Nuli, Y. (2014). Novel dual-salts electrolyte solution for dendrite-free lithium-metal based rechargeable batteries with high cycle reversibility. *Journal of Power Sources*, 271, 291-297.

- (15) Qian, J., Henderson, W. A., Xu, W., Bhattacharya, P., Engelhard, M., Borodin, O., & Zhang, J. G. (2015). High rate and stable cycling of lithium metal anode. *Nature communications*, 6(1), 1-9.
- (16) Suo, L., Xue, W., Gobet, M., Greenbaum, S. G., Wang, C., Chen, Y., ... & Li, J. (2018). Fluorine-donating electrolytes enable highly reversible 5-V-class Li metal batteries. *Proceedings of the National Academy of Sciences*, 115(6), 1156-1161.
- (17) Gordin, M. L., Dai, F., Chen, S., Xu, T., Song, J., Tang, D., ... & Wang, D. (2014). Bis(2, 2, 2-trifluoroethyl) ether as an electrolyte co-solvent for mitigating self-discharge in lithium–sulfur batteries. *ACS applied materials & interfaces*, 6(11), 8006-8010.
- (18) Aurbach, D., Pollak, E., Elazari, R., Salitra, G., Kelley, C. S., & Affinito, J. (2009). On the surface chemical aspects of very high energy density, rechargeable Li–sulfur batteries. *Journal of The Electrochemical Society*, 156(8), A694-A702.
- (19) Kim, H., Wu, F., Lee, J. T., Nitta, N., Lin, H. T., Oschatz, M., ... & Yushin, G. (2015). In situ formation of protective coatings on sulfur cathodes in lithium batteries with LiFSI-based organic electrolytes. *Advanced Energy Materials*, 5(6), 1401792.
- (20) Choudhury, S. (2019). Lithium fluoride additives for stable cycling of lithium batteries at high current densities. In *Rational Design of Nanostructured Polymer Electrolytes and Solid–Liquid Interphases for Lithium Batteries* (pp. 81-94). Springer, Cham.
- (21) Lu, Y., Tu, Z., Shu, J., & Archer, L. A. (2015). Stable lithium electrodeposition in salt-reinforced electrolytes. *Journal of Power Sources*, 279, 413-418.

- (22) Zhang, X. Q., Cheng, X. B., Chen, X., Yan, C., & Zhang, Q. (2017). Fluoroethylene carbonate additives to render uniform Li deposits in lithium metal batteries. *Advanced Functional Materials*, 27(10), 1605989.
- (23) Stone, G. M., Mullin, S. A., Teran, A. A., Hallinan, D. T., Minor, A. M., Hexemer, A., & Balsara, N. P. (2012). Resolution of the modulus versus adhesion dilemma in solid polymer electrolytes for rechargeable lithium metal batteries. *Journal of The Electrochemical Society*, 159(3), A222-A227.
- (24) Giles, J. R. M., Gray, F. M., MacCallum, J. R., & Vincent, C. A. (1987). Synthesis and characterization of ABA block copolymer-based polymer electrolytes. *Polymer*, 28(11), 1977-1981.
- (25) Gao, Y., Yan, Z., Gray, J. L., He, X., Wang, D., Chen, T., ... & Mallouk, T. E. (2019). Polymer–inorganic solid–electrolyte interphase for stable lithium metal batteries under lean electrolyte conditions. *Nature materials*, 18(4), 384-389.
- (26) Pan, Q., Smith, D. M., Qi, H., Wang, S., & Li, C. Y. (2015). Hybrid electrolytes with controlled network structures for lithium metal batteries. *Advanced Materials*, 27(39), 5995-6001.
- (27) Choudhury, S. (2019). A Highly Reversible Room-Temperature Lithium Metal Battery Based on Cross-Linked Hairy Nanoparticles. In *Rational Design of Nanostructured Polymer Electrolytes and Solid–Liquid Interphases for Lithium Batteries* (pp. 35-57). Springer, Cham.
- (28) Gurevitch, I., Buonsanti, R., Teran, A. A., Gludovatz, B., Ritchie, R. O., Cabana, J., & Balsara, N. P. (2013). Nanocomposites of titanium dioxide and polystyrene-poly

(ethylene oxide) block copolymer as solid-state electrolytes for lithium metal batteries. *Journal of The Electrochemical Society*, 160(9), A1611-A1617.

(29) Choudhury, S., Stalin, S., Vu, D., Warren, A., Deng, Y., Biswal, P., & Archer, L. A. (2019). Solid-state polymer electrolytes for high-performance lithium metal batteries. *Nature communications*, 10(1), 1-8.

(30) Cheng, X. B., Zhang, R., Zhao, C. Z., Wei, F., Zhang, J. G., & Zhang, Q. (2016). A review of solid electrolyte interphases on lithium metal anode. *Advanced Science*, 3(3), 1500213.

(31) Zheng, G., Lee, S. W., Liang, Z., Lee, H. W., Yan, K., Yao, H., ... & Cui, Y. (2014). Interconnected hollow carbon nanospheres for stable lithium metal anodes. *Nature nanotechnology*, 9(8), 618-623.

(32) Zhang, J., Yang, X., Wang, R., Dong, W., Lu, W., Wu, X., ... & Chen, L. (2014). Influences of additives on the formation of a solid electrolyte interphase on MnO electrode studied by atomic force microscopy and force spectroscopy. *The Journal of Physical Chemistry C*, 118(36), 20756-20762.

(33) Zhang, Y. J., Wang, W., Tang, H., Bai, W. Q., Ge, X., Wang, X. L., ... & Tu, J. P. (2015). An ex-situ nitridation route to synthesize Li₃N-modified Li anodes for lithium secondary batteries. *Journal of Power Sources*, 277, 304-311.

(34) Lee, H., Lee, D. J., Kim, Y. J., Park, J. K., & Kim, H. T. (2015). A simple composite protective layer coating that enhances the cycling stability of lithium metal batteries. *Journal of Power Sources*, 284, 103-108.

- (35) Haregewoin, A. M., Wotango, A. S., & Hwang, B. J. (2016). Electrolyte additives for lithium ion battery electrodes: progress and perspectives. *Energy & Environmental Science*, 9(6), 1955-1988.
- (36) Umeda, G. A., Menke, E., Richard, M., Stamm, K. L., Wudl, F., & Dunn, B. (2011). Protection of lithium metal surfaces using tetraethoxysilane. *Journal of Materials Chemistry*, 21(5), 1593-1599.
- (37) Wang, X., Hou, Y., Zhu, Y., Wu, Y., & Holze, R. (2013). An aqueous rechargeable lithium battery using coated Li metal as anode. *Scientific reports*, 3, 1401.
- (38) Bates, J. B., Dudney, N. J., Gruzalski, G. R., Zuhr, R. A., Choudhury, A., Luck, C. F., & Robertson, J. D. (1992). Electrical properties of amorphous lithium electrolyte thin films. *Solid state ionics*, 53, 647-654.
- (39) Li, J., Ma, C., Chi, M., Liang, C., & Dudney, N. J. (2015). Solid electrolyte: the key for high-voltage lithium batteries. *Advanced Energy Materials*, 5(4), 1401408.
- (40) Kanno, R., & Murayama, M. (2001). Lithium ionic conductor thio-LISICON: the $\text{Li}_2\text{S GeS}_2 \text{P}_2\text{S}_5$ system. *Journal of the electrochemical society*, 148(7), A742-A746.
- (41) Lu, Y., Tikekar, M., Mohanty, R., Hendrickson, K., Ma, L., & Archer, L. A. (2015). Stable cycling of lithium metal batteries using high transference number electrolytes. *Advanced Energy Materials*, 5(9), 1402073.
- (42) Song, J., Lee, H., Choo, M. J., Park, J. K., & Kim, H. T. (2015). Ionomer-liquid electrolyte hybrid ionic conductor for high cycling stability of lithium metal electrodes. *Scientific reports*, 5, 14458.
- (43) Cheng, X. B., Hou, T. Z., Zhang, R., Peng, H. J., Zhao, C. Z., Huang, J. Q., & Zhang, Q. (2016). Dendrite-free lithium deposition induced by uniformly distributed

lithium ions for efficient lithium metal batteries. *Advanced materials*, 28(15), 2888-2895.

(44) Yang, C. P., Yin, Y. X., Zhang, S. F., Li, N. W., & Guo, Y. G. (2015). Accommodating lithium into 3D current collectors with a submicron skeleton towards long-life lithium metal anodes. *Nature communications*, 6(1), 1-9.

(45) Zhamu, A., Chen, G., Liu, C., Neff, D., Fang, Q., Yu, Z., ... & Jang, B. Z. (2012). Reviving rechargeable lithium metal batteries: enabling next-generation high-energy and high-power cells. *Energy & Environmental Science*, 5(2), 5701-5707.

(46) Ji, X., Liu, D. Y., Prendiville, D. G., Zhang, Y., Liu, X., & Stucky, G. D. (2012). Spatially heterogeneous carbon-fiber papers as surface dendrite-free current collectors for lithium deposition. *Nano Today*, 7(1), 10-20.

(47) Duan, H., Zhang, J., Chen, X., Zhang, X. D., Li, J. Y., Huang, L. B., ... & Guo, Y. G. (2018). Uniform nucleation of lithium in 3D current collectors via bromide intermediates for stable cycling lithium metal batteries. *Journal of the American Chemical Society*, 140(51), 18051-18057.

(48) Pei, A., Zheng, G., Shi, F., Li, Y., & Cui, Y. (2017). Nanoscale nucleation and growth of electrodeposited lithium metal. *Nano letters*, 17(2), 1132-1139.

(49) Lopez, J., Pei, A., Oh, J. Y., Wang, G. J. N., Cui, Y., & Bao, Z. (2018). Effects of polymer coatings on electrodeposited lithium metal. *Journal of the American Chemical Society*, 140(37), 11735-11744.

(50) Biswal, P., Stalin, S., Kludze, A., Choudhury, S., & Archer, L. A. (2019). Nucleation and Early Stage Growth of Li Electrodeposits. *Nano Letters*, 19(11), 8191-8200.

- (51) Choudhury, S., Wei, S., Ozhabes, Y., Gunceler, D., Zachman, M. J., Tu, Z., & Arias, T. A. (2017). Designing solid-liquid interphases for sodium batteries. *Nature communications*, 8(1), 1-10.
- (52) Barton, J. L., & Bockris, J. O. M. (1962). The electrolytic growth of dendrites from ionic solutions. *Proceedings of the Royal Society of London. Series A. Mathematical and Physical Sciences*, 268(1335), 485-505.
- (53) Charette, A. B., Barbay, J. K., & He, W. (2001). Lithium Bromide. *Encyclopedia of Reagents for Organic Synthesis*.
- (54) Mojtahedi, M. M., Akbarzadeh, E., Sharifi, R., & Abaee, M. S. (2007). Lithium Bromide as a Flexible, Mild, and Recyclable Reagent for Solvent-Free Cannizzaro, Tishchenko, and Meerwein–Ponndorf–Verley Reactions. *Organic letters*, 9(15), 2791-2793.
- (55) Tavassol, H., Buthker, J. W., Ferguson, G. A., Curtiss, L. A., & Gewirth, A. A. (2012). Solvent oligomerization during SEI formation on model systems for Li-ion battery anodes. *Journal of The Electrochemical Society*, 159(6), A730-A738.
- (56) Aurbach, D. (2000). Review of selected electrode–solution interactions which determine the performance of Li and Li ion batteries. *Journal of Power Sources*, 89(2), 206-218.
- (57) Wang, L., Menakath, A., Han, F., Wang, Y., Zavalij, P.Y., Gaskell, K.J., Borodin, O., Iuga, D., Brown, S.P., Wang, C., & Xu, K., (2019). Identifying the components of the solid–electrolyte interphase in Li-ion batteries. *Nature chemistry*, 11(9), pp.789-796.

- (58) Stalin, S., Tikekar, M., Biswal, P., Li, G., Johnson, H.E.N., Deng, Y., Zhao, Q., Vu, D., Coates, G.W. and Archer, L.A., 2020. Designing Polymeric Interphases for Stable Lithium Metal Deposition. *Nano Letters*, 20 (8), 5749-5758.
- (59) Choudhury, S. (2019). Confining electrodeposition of metals in structured electrolytes. In *Rational Design of Nanostructured Polymer Electrolytes and Solid-Liquid Interphases for Lithium Batteries* (pp. 59-79). Springer, Cham.
- (60) Khurana, R., Schaefer, J. L., Archer, L. A., & Coates, G. W. (2014). Suppression of lithium dendrite growth using cross-linked polyethylene/poly (ethylene oxide) electrolytes: a new approach for practical lithium-metal polymer batteries. *Journal of the American Chemical Society*, 136(20), 7395-7402.
- (61) Xue, Z., He, D., & Xie, X. (2015). Poly (ethylene oxide)-based electrolytes for lithium-ion batteries. *Journal of Materials Chemistry A*, 3(38), 19218-19253.
- (62) Zhu, D., Liao, X., & Dai, P. (2012). Theoretical analysis of reactive solid-liquid interfacial energies. *Chinese Science Bulletin*, 57(34), 4517-4524.
- (63) Song, J. Y., Wang, Y. Y., & Wan, C. C. (1999). Review of gel-type polymer electrolytes for lithium-ion batteries. *Journal of power sources*, 77(2), 183-197.
- (64) Stephan, A. M., & Nahm, K. S. (2006). Review on composite polymer electrolytes for lithium batteries. *Polymer*, 47(16), 5952-5964.
- (65) Brooks, D. J., Merinov, B. V., Goddard III, W. A., Kozinsky, B., & Mailoa, J. (2018). Atomistic Description of Ionic Diffusion in PEO-LiTFSI: Effect of Temperature, Molecular Weight, and Ionic Concentration. *Macromolecules*, 51(21), 8987-8995.

- (66) Savoie, B. M., Webb, M. A., & Miller III, T. F. (2017). Enhancing cation diffusion and suppressing anion diffusion via Lewis-acidic polymer electrolytes. *The journal of physical chemistry letters*, *8*(3), 641-646.
- (67) Ramasubramanian, A., Yurkiv, V., Foroozan, T., Ragone, M., Shahbazian-Yassar, R., & Mashayek, F. (2019). Lithium diffusion mechanism through solid–electrolyte interphase in rechargeable lithium batteries. *The Journal of Physical Chemistry C*, *123*(16), 10237-10245.
- (68) Iddir, H., & Curtiss, L. A. (2010). Li ion diffusion mechanisms in bulk monoclinic Li₂CO₃ crystals from density functional studies. *The Journal of Physical Chemistry C*, *114*(48), 20903-20906.
- (69) Benitez, L., & Seminario, J. M. (2017). Ion diffusivity through the solid electrolyte interphase in lithium-ion batteries. *Journal of The Electrochemical Society*, *164*(11), E3159-E3170.
- (70) Guan, P.; Liu, L.; Lin, X. *J. Electrochem. Soc.* **2015**, *162*, A1798-A1808.
- (71) Yildirim, H., Kinaci, A., Chan, M. K., & Greeley, J. P. (2015). First-principles analysis of defect thermodynamics and ion transport in inorganic SEI compounds: LiF and NaF. *ACS applied materials & interfaces*, *7*(34), 18985-18996.
- (72) Tasaki, K., Goldberg, A., Lian, J. J., Walker, M., Timmons, A., & Harris, S. J. (2009). Solubility of lithium salts formed on the lithium-ion battery negative electrode surface in organic solvents. *Journal of The Electrochemical Society*, *156*(12), A1019-A1027.

- (73) Liu, Z., Qi, Y., Lin, Y. X., Chen, L., Lu, P., & Chen, L. Q. (2016). Interfacial study on solid electrolyte interphase at Li metal anode: implication for Li dendrite growth. *Journal of The Electrochemical Society*, 163(3), A592-A598.
- (74) Jand, S. P., & Kaghazchi, P. (2014). The role of electrostatic effects in determining the structure of LiF-graphene interfaces. *Journal of Physics: Condensed Matter*, 26(26), 262001.
- (75) Kokko, K., Salo, P. T., Laihia, R., & Mansikka, K. (1996). First-principles calculations for work function and surface energy of thin lithium films. *Surface science*, 348(1-2), 168-174.
- (76) Wood, K. N., Kazyak, E., Chadwick, A. F., Chen, K. H., Zhang, J. G., Thornton, K., & Dasgupta, N. P. (2016). Dendrites and pits: Untangling the complex behavior of lithium metal anodes through operando video microscopy. *ACS central science*, 2(11), 790-801.

Appendix

Supplementary information for Chapter 3

This appendix includes details of the theoretical model and curve fitting, voltage response plots, SEM, XPS, NMR, Impedance spectroscopy, and goniometer characterizations, optical microscopy video, coin cell fabrication, polishing, electrochemical testing methods and electrolyte characterization, rationale of methods chosen, image analysis, and additional figures.

Theoretical model

A theoretical model of nucleation and growth (previously derived in **Chapter 2, Supplementary information**), involving charge transfer overpotential, bulk diffusion overpotential, interfacial energy overpotential, and SEI diffusion overpotential respectively is as follows:

$$\eta = \frac{RT}{\alpha F} \ln \frac{i}{i_0} + \frac{irRT}{D_B C_B F^2} + \frac{2\gamma V}{Fr} + \frac{ir^2 RT}{D_S C_S F^2} \quad (1)$$

where η is the net overpotential due to all the processes, i and i_0 are the current density and exchange current density respectively, r is the radius of the nucleus, D_B and C_B (mol/m³) are the bulk electrolyte Li ion diffusivity and concentration respectively, D_S and C_S (mol/m²) are the SEI Li ion diffusivity and concentration respectively, and α , V , R , T , F are charge transfer coefficient, molar volume of metal, universal gas constant, temperature and Faraday constant respectively.

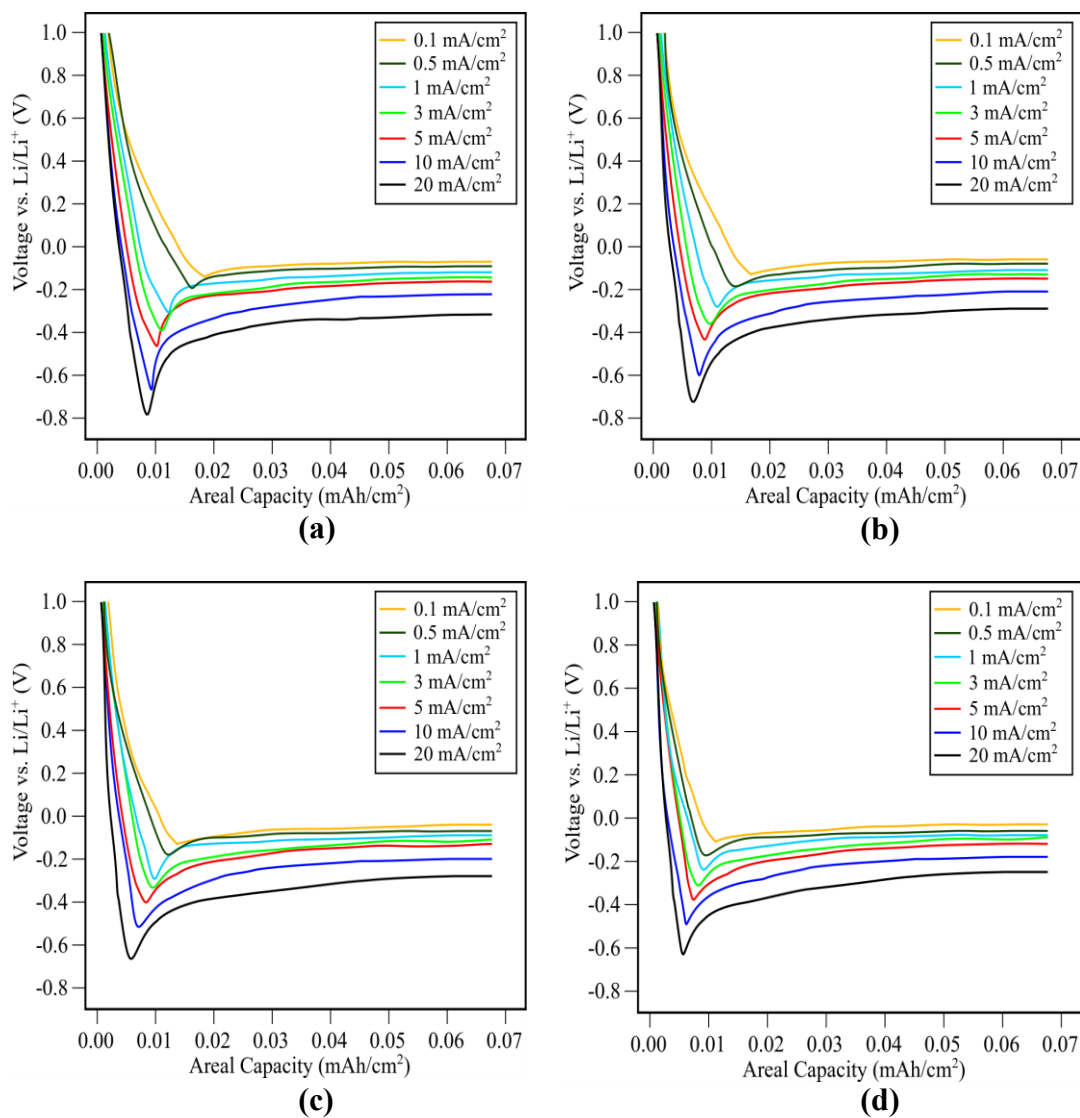
A note on Curve fitting and extraction of parameters

The curve fitting of the average nuclei radius (with error bars) against current density was performed by keeping the coefficients (A' and B') were kept unrestricted to any value (**Supplementary Figure 3.8**).

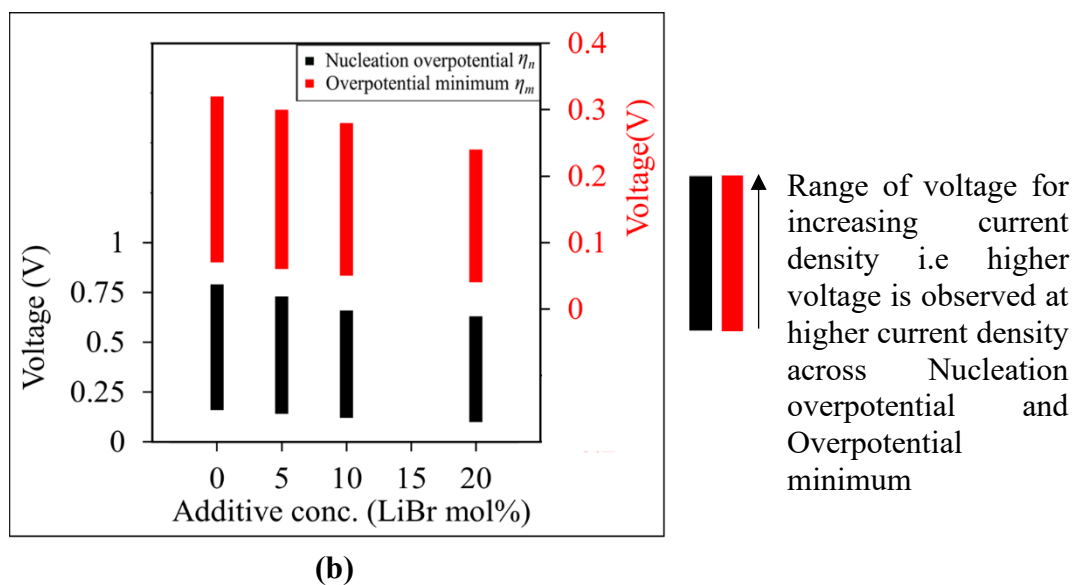
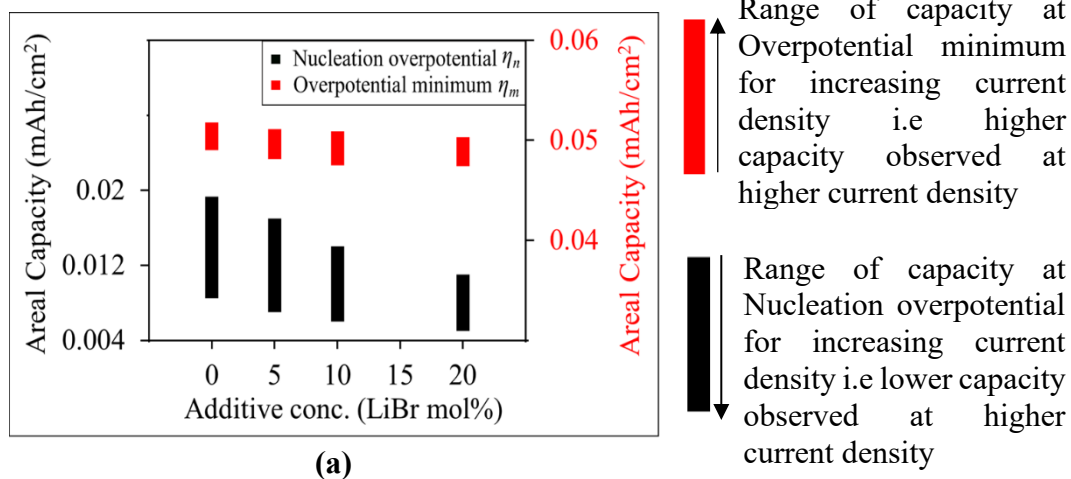
$$i = \frac{1}{\tilde{r}^2 A' + \tilde{r}^3 B'} \quad \text{where } A' = \frac{RT}{2\gamma V D_B C_B F} \quad \text{and } B' = \frac{RT}{\gamma V D_S C_S F} \quad (2)$$

The division of the fitted coefficients (A'/B') gives the ratio of $D_S C_S / D_B C_B$. The value of C_B is already known as it is the concentration of lithium ions in the bulk electrolyte. D_B was determined through impedance spectroscopy (**Supplementary Figure 3.14**).

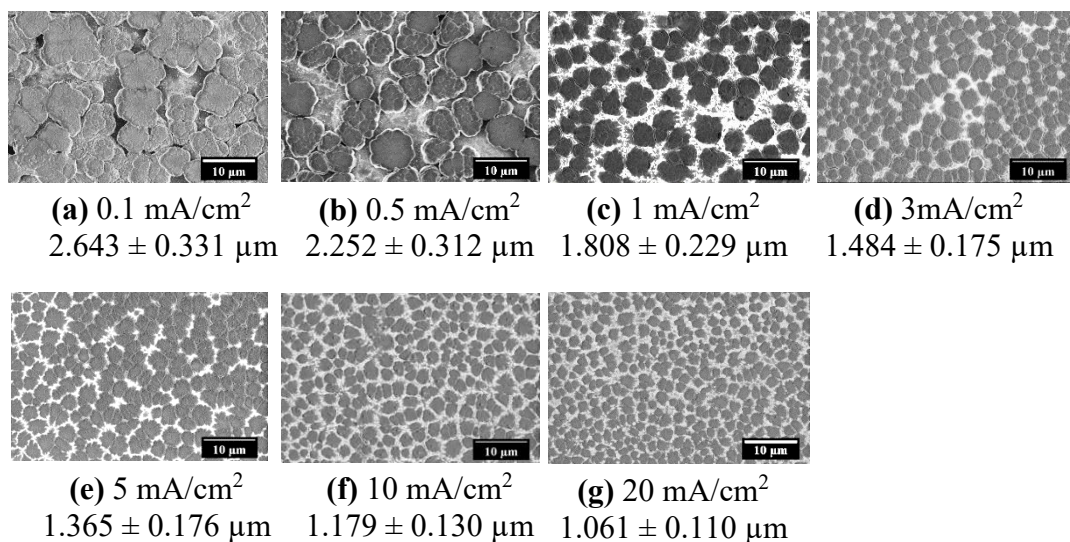
Hence, the parameter $D_S C_S$ was determined and presented in **Supplementary Table 3.4**, **Figure 3.3(d)**. Similarly, the fitted coefficient A' was used to determine interfacial energy γ as presented in **Figure 3.3(c)**.



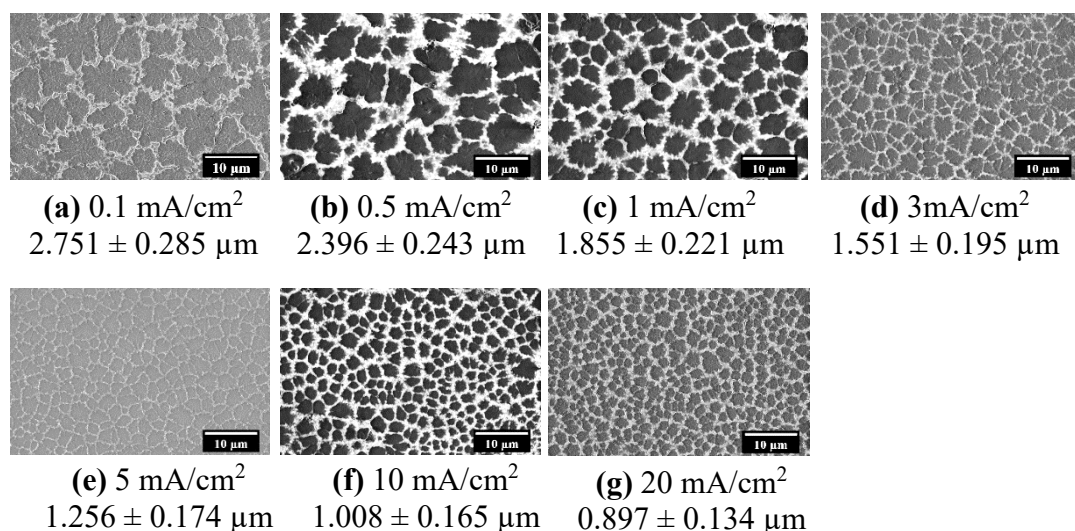
Supplementary Figure 3.1. Experimental voltage profiles of galvanostatic Li deposition for a range of current densities and different electrolyte compositions. The electrolyte is 1M LiPF_6 in EC:DMC (1:1 vol.%) with **(a)** 0 mol% **(b)** 5 mol% **(c)** 10 mol% **(d)** 20 mol% LiBr.



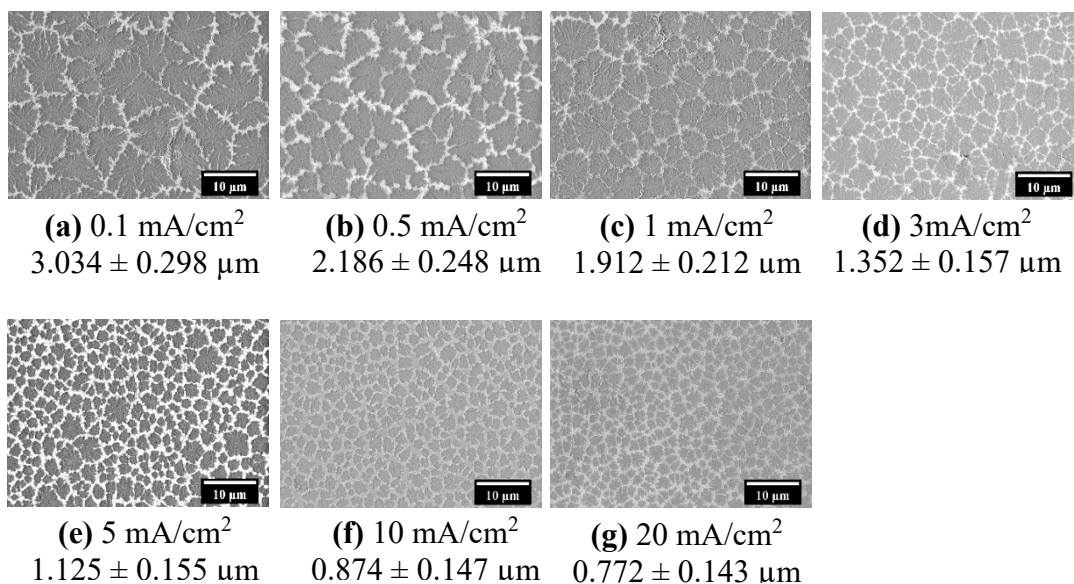
Supplementary Figure 3.2. Effect of electrolyte chemistry on the areal capacities and overpotentials of the Nucleation overpotential and Overpotential minimum events. **(a)** Plot of Areal Capacities for all the current densities and varying concentration of LiBr additive (0, 5, 10, 20 mol%) in 1M LiPF₆ EC: DMC (1:1 vol.%). **(b)** Plot of overpotentials for all the current densities and varying concentration of LiBr additive (0, 5, 10, 20 mol%) in 1M LiPF₆ EC: DMC (1:1 vol.%). The Nucleation Overpotential and Overpotential Minimum are shown in black and red, respectively. The range of capacities and voltages reported are extracted from **Supplementary Figure 3.1**.



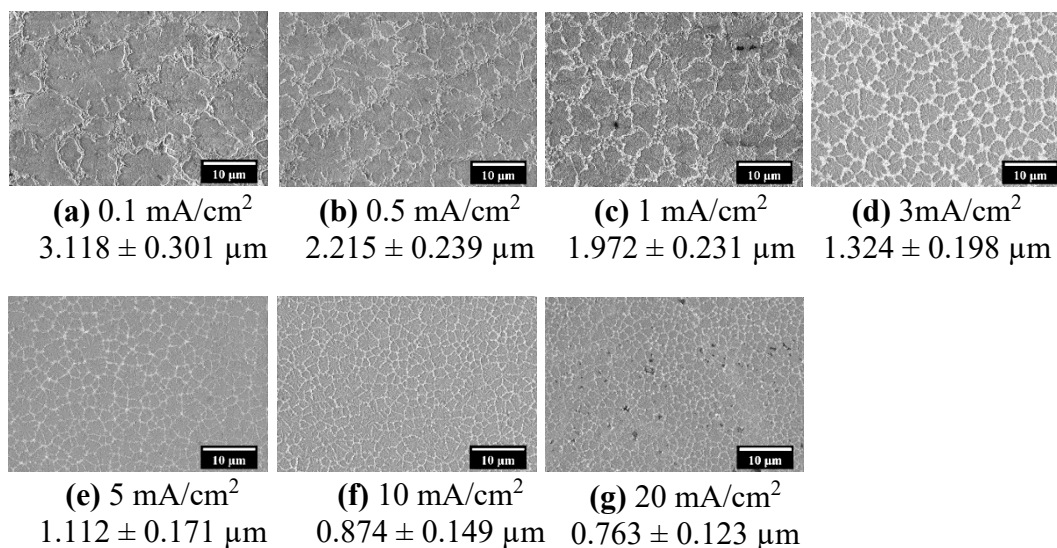
Supplementary Figure 3.3. Morphology map of Lithium electrodeposits formed under 1M LiPF₆ in EC:DMC (1:1 vol.%) with 0 mol% LiBr. Ex situ SEM images of Li nuclei deposited on stainless-steel at current densities of (a) 0.1 (b) 0.5 (c) 1 (d) 3 (e) 5 (f) 10 (g) 20 mA/cm², respectively, for a total areal capacity corresponding to that of Overpotential Minimum, about 0.05 mAh/cm². At lower current densities, the stainless-steel substrate is visible underneath the sparsely distributed Li nuclei. The average nuclei size with error bar is reported for average of 4 samples per current density and electrolyte composition including these ones.



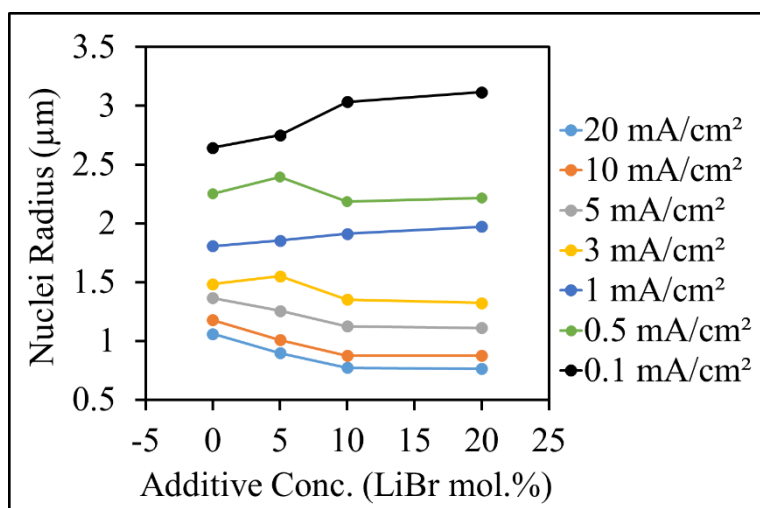
Supplementary Figure 3.4. Morphology map of Lithium electrodeposits formed under 1M LiPF₆ in EC:DMC (1:1 vol.%) with 5 mol% LiBr. Ex situ SEM images of Li nuclei deposited on stainless-steel at current densities of **(a)** 0.1 **(b)** 0.5 **(c)** 1 **(d)** 3 **(e)** 5 **(f)** 10 **(g)** 20 mA/cm², respectively, for a total areal capacity corresponding to that of Overpotential Minimum, about 0.05 mAh/cm². At lower current densities, the stainless-steel substrate is visible underneath the sparsely distributed Li nuclei. The average nuclei size with error bar is reported for an average of 4 samples per current density and electrolyte composition including



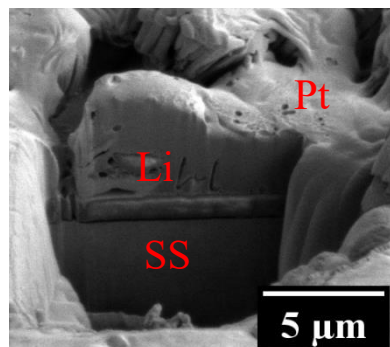
Supplementary Figure 3.5. Morphology map of Lithium electrodeposits formed under 1M LiPF₆ in EC:DMC (1:1 vol.%) with 10 mol% LiBr. Ex situ SEM images of Li nuclei deposited on stainless-steel at current densities of (a) 0.1 (b) 0.5 (c) 1 (d) 3 (e) 5 (f) 10 (g) 20 mA/cm², respectively, for a total areal capacity corresponding to that of Overpotential Minimum, about 0.05 mAh/cm². At lower current densities, the stainless-steel substrate is visible underneath the sparsely distributed Li nuclei. The average nuclei size with error bar is reported for average of 4 samples per current density and electrolyte composition including these ones.



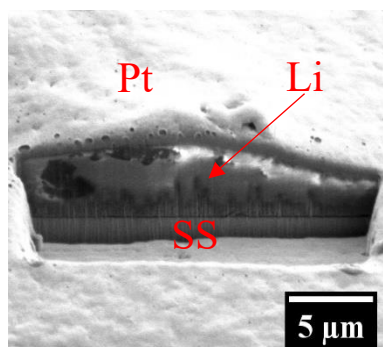
Supplementary Figure 3.6. Morphology map of Lithium electrodeposits formed under 1M LiPF₆ in EC:DMC (1:1 vol.%) with 20 mol% LiBr. Ex situ SEM images of Li nuclei deposited on stainless-steel at current densities of **(a)** 0.1 **(b)** 0.5 **(c)** 1 **(d)** 3 **(e)** 5 **(f)** 10 **(g)** 20 mA/cm², respectively, for a total areal capacity corresponding to that of Overpotential Minimum, about 0.05 mAh/cm². The average nuclei size with error bar is reported for average of 4 samples per current density and electrolyte composition including these ones.



Supplementary Figure 3.7. Effect of current density and electrolyte chemistry on the average size of Lithium electrodeposits. Plot of Nuclei radius for a range of current densities for varying concentration of LiBr (0, 5, 10, 20 mol%) in 1M LiPF₆ EC: DMC (1:1 vol.%). The areal capacity at which nuclei radius are analyzed is 0.05 mAh/cm². The average nuclei size is reported for an average of 4 samples per current density and electrolyte composition including these ones.

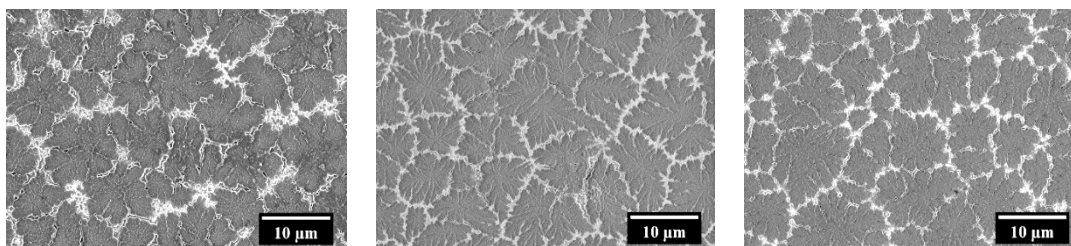


(a) 0 mol% LiBr



(a) 20 mol% LiBr

Supplementary Figure 3.8. Cross-sectional morphology of Lithium electrodeposits formed under the influence of (a) 0 mol% LiBr (b) 20 mol% LiBr in 1M LiPF₆ EC: DMC (1:1 vol.%) at a current density of 0.1 mA/cm² and capacity of 0.05 mAh/cm². The platinum layer is approximately 1 μm thick.



(a) LiCl

(b) LiBr

(c) LiI

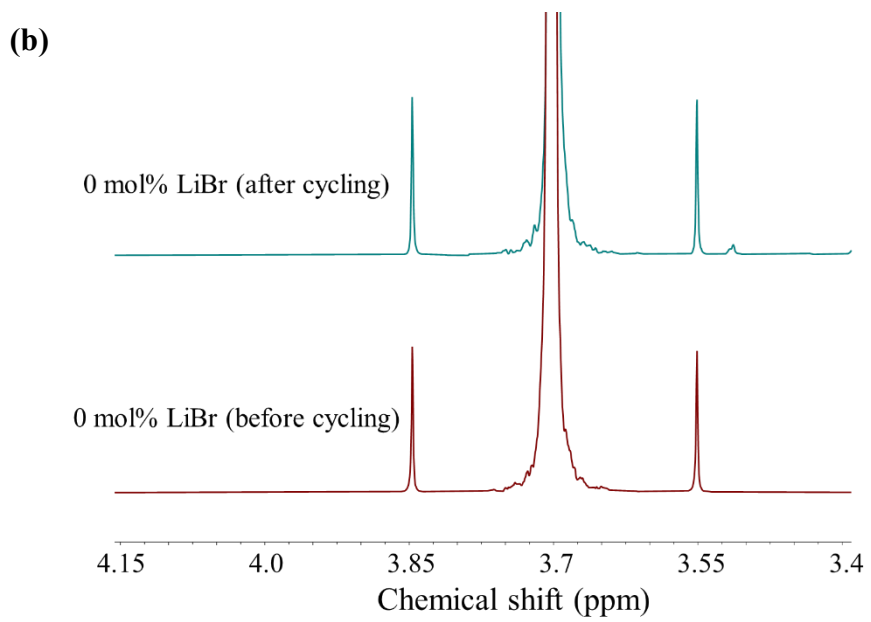
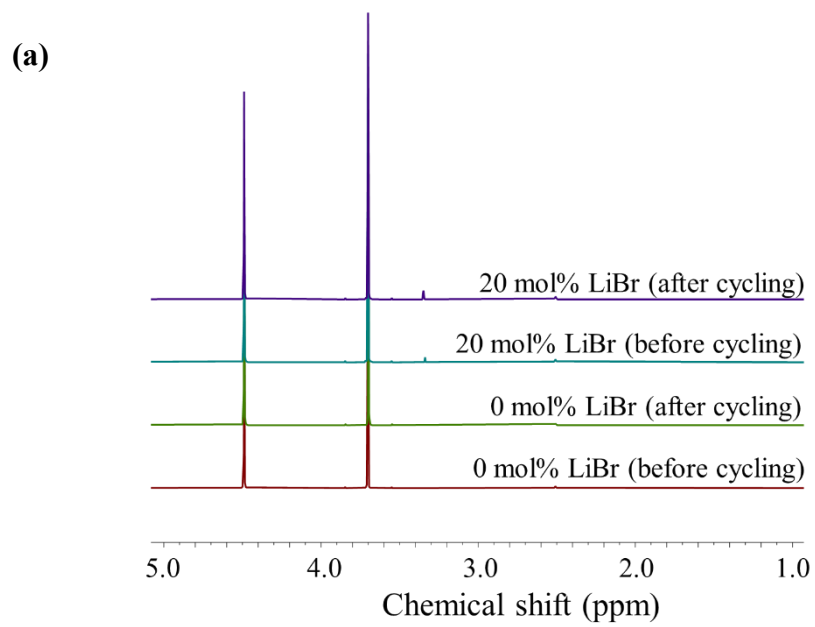
Supplementary Figure 3.9. Morphology of Lithium electrodeposits formed under the influence of different halide salts present in 1M LiPF₆ EC: DMC (1:1 vol.%) at a current density of 0.1 mA/cm² and capacity of 0.05 mAh/cm². (a) 10 mol% LiCl (b) 10 mol% LiBr (c) 10 mol% LiI.

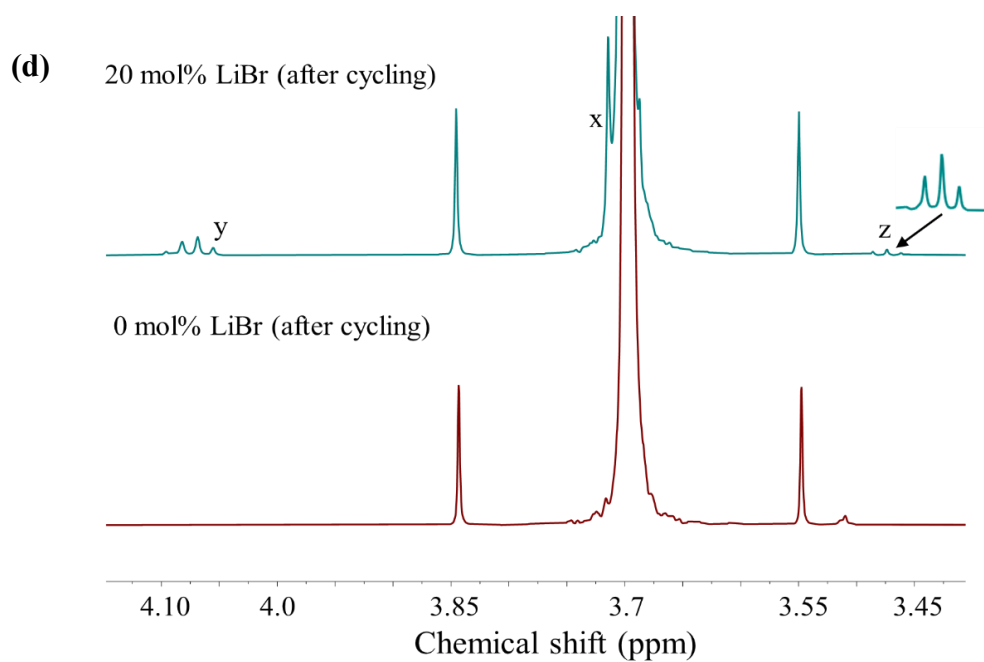
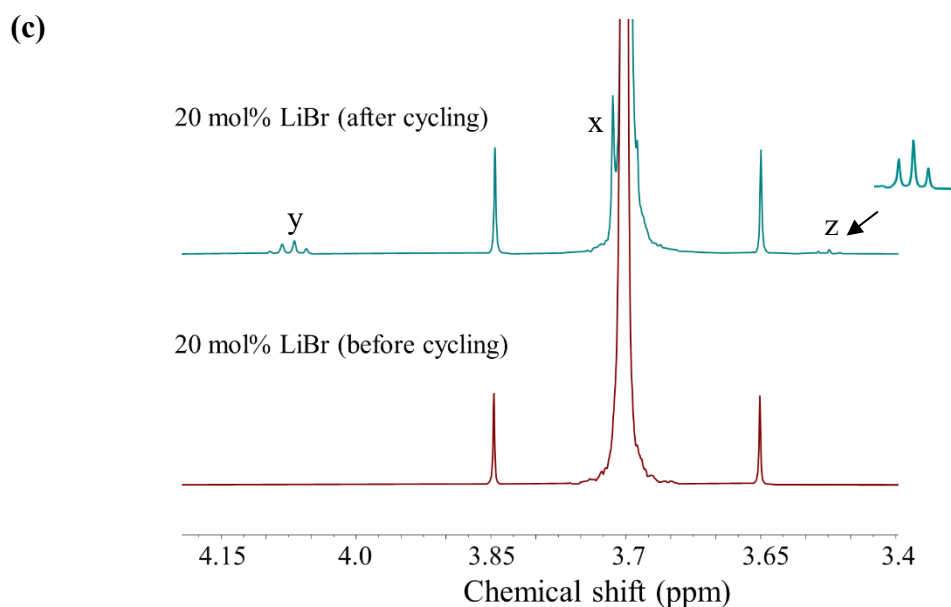
LiBr mol% electrolyte	Br wt% electrolyte	Br wt% SEI 0.05 mAh/cm²
0	0.000	0.000
5	0.323	0.011
10	0.663	0.012
20	1.509	0.073

Supplementary Table 3.1. Concentration comparison of Br anion in electrolyte vs SEI at 0.05 mAh/cm² capacity of electrodeposition. The data for Br wt% in SEI is obtained by calculation from at% reported by XPS survey spectra.

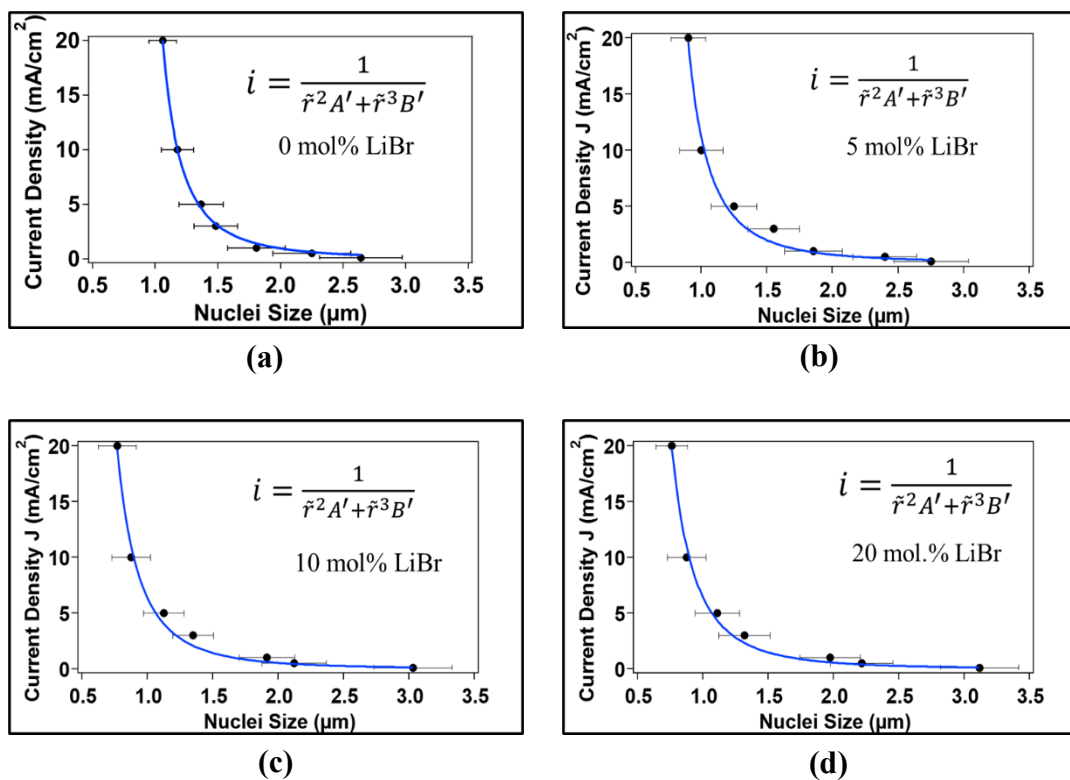
LiBr mol%	Li₂CO₃ %	C-C-O %	C-C/C-H %
0	17.97	42.14	39.18
5	19.37	43.65	36.98
10	21.29	46.52	32.19
20	26.73	50.93	22.35

Supplementary Table 3.2. Chemical components of high-resolution C 1s spectra obtained via XPS spectra of the LiBr induced SEI layer at capacities of 0.05 mAh/cm².

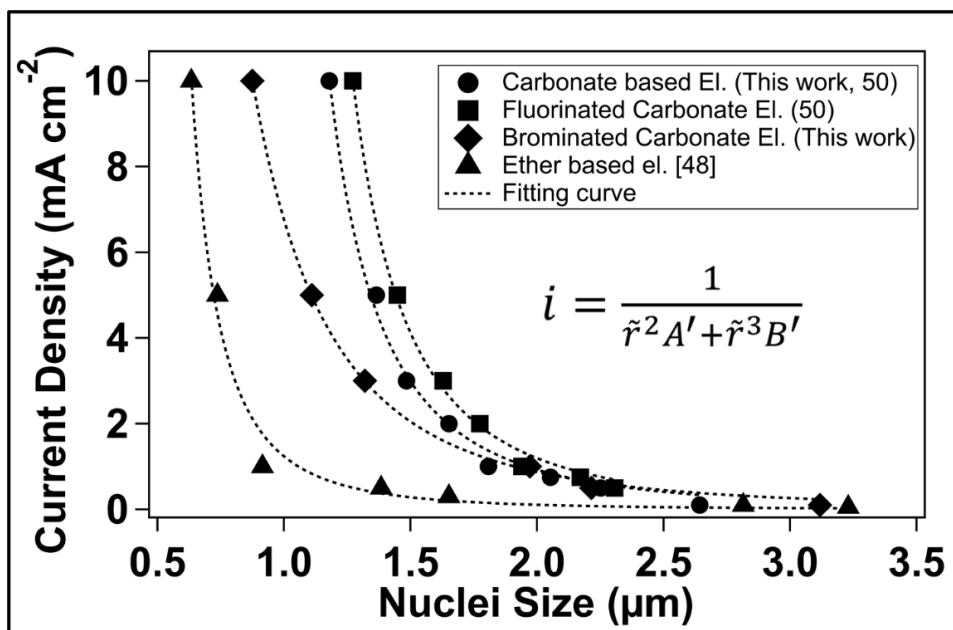




Supplementary Figure 3.10. ^1H NMR spectroscopy of 1M LiPF_6 EC: DMC (1:1 vol.%) electrolyte w/o LiBr additive before/after Li electrodeposition. Chemical shift observed for (a) 0 mol% and 20 mol% LiBr before/after Li electrodeposition (b) 0 mol% LiBr before/after Li electrodeposition (c) 20 mol% LiBr before/after Li electrodeposition (d) 0 mol% and 20 mol% LiBr after Li electrodeposition. x,y,z shows differentiated peaks between the two spectra.



Supplementary Figure 3.11. Proof of Concept curve fitting for electrolyte with different bromide compositions. Curve fitting of Current Density with average Nuclei Size through square-cubic relationship for 1M LiPF₆ in EC:DMC (1:1 vol.%) with (a) 0 mol% (b) 5 mol% (c) 10 mol% (d) 20 mol% LiBr. The areal capacity at which nuclei radius are analyzed is 0.05 mAh/cm², corresponding to that of Overpotential minimum.



Supplementary Figure 3.12. Proof of Concept curve fitting for electrolyte with different chemistries. The ether-based electrolyte data was obtained from the work of Pei et al. (48 Main text, 1 Appendix).

Interfacial energy at the electrode-electrolyte interface

A combination of Zisman approach and Young's equation was used to determine the interfacial energy of the Electrode-Electrolyte interphase. (2-4)

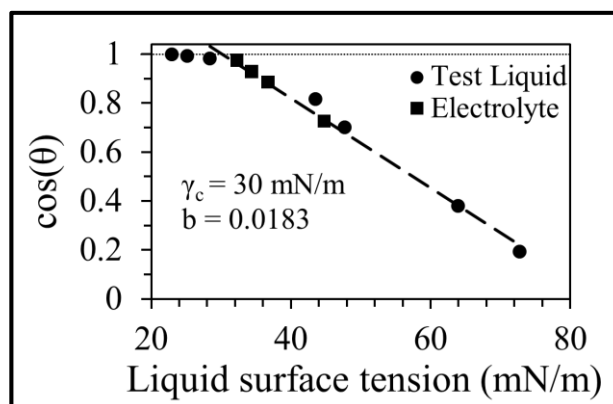
$$\gamma_L \cos(\theta) = \gamma_S - \gamma_{SL} \quad (1)$$

$$\cos(\theta) = 1 - b(\gamma_L - \gamma_C) \quad (2)$$

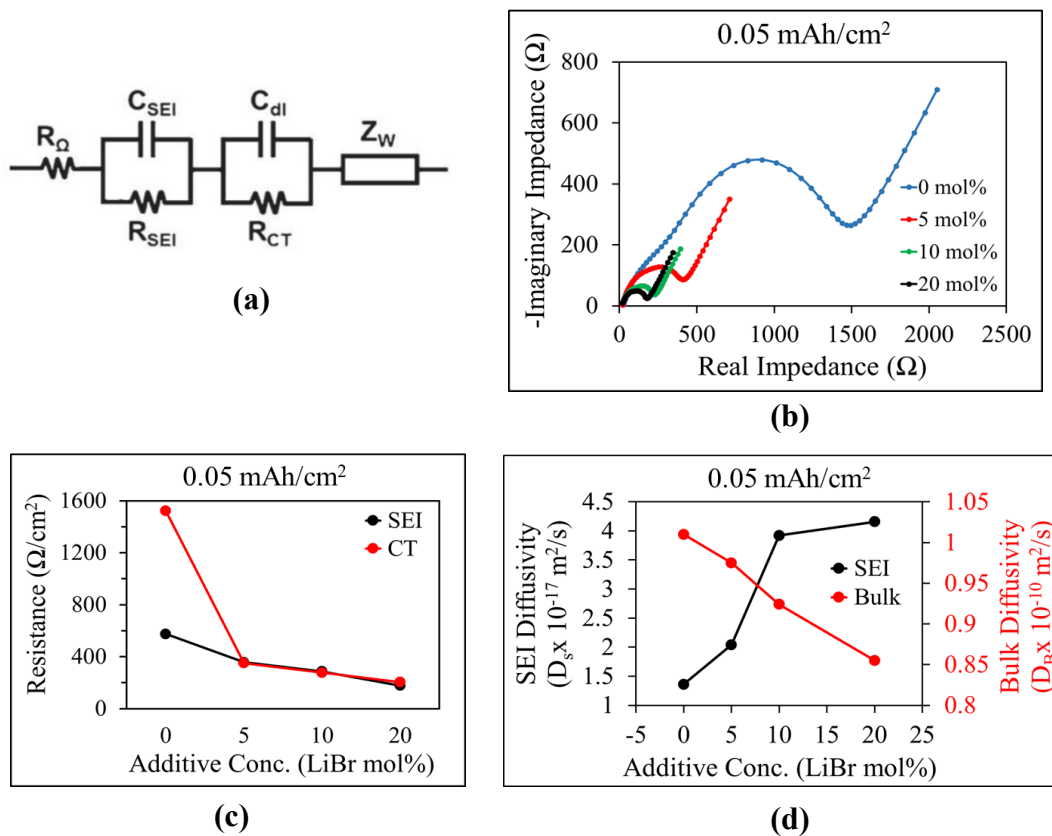
Where γ_L is the experimentally determined surface energy (surface tension) of the liquid (electrolyte), θ is the contact angle, γ_S is the surface energy of the solid (lithium: 0.52 J m^{-2}), γ_{SL} is the solid/liquid interfacial energy, b is the slope of the regression line and γ_C is the critical surface tension when $\cos(\theta) = 1$. The contact angle of the electrolytes (0, 5, 10, 20 mol% LiBr) on the surface of clean lithium metal was measured using an optical tensiometer in an argon-filled enclosure as shown in **Supplementary Table 3.3**. Prior to that, the critical surface tension γ_C and b the slope of regression were determined for a polished stainless steel using common test liquids with known surface tension (Isopropanol 23 mN/m, Acetone 25.2 mN/m, Toluene 28.4 mN/m, DMSO 43.54 mN/m, Ethylene Glycol 47.7 mN/m, Glycerol 64 mN/m, Water 72.8 mN/m) as shown in **Supplementary Figure 3.13**. The surface tension of each electrolyte was calculated via Zisman approach (eq. 2) by measuring their respective contact angles with the polished stainless steel as shown in **Supplementary Table 3.3**. Finally, the obtained information was used to determine the interfacial energy of Li-electrolyte interphase via Young's (eq. 1).

Electrolyte	C.A. (θ_{ss})	$\cos(\theta_{ss})$	γ_L (mJ/m ²)	C.A. (θ_{Li})	$\cos(\theta_{Li})$	γ_{SL} (mJ/m ²)
0 mol% LiBr	43.89	0.721	45.25	9.42	0.987	475.36
5 mol% LiBr	28.74	0.877	36.72	5.87	0.995	483.47
10 mol% LiBr	22.65	0.923	34.21	4.42	0.997	485.89
20 mol% LiBr	15.98	0.961	32.11	2.85	0.999	487.93

Supplementary Table 3.3. Contact angles, electrolyte surface tensions (γ_L) and Li-electrolyte interfacial energy (γ_{SL}) for a range of electrolyte compositions. Lithium: 0.52 J m⁻², θ_{ss} contact angle w.r.t Polished stainless-steel, θ_{Li} contact angle w.r.t to Lithium.



Supplementary Figure 3.13. Zisman plot ($\cos(\theta)$ vs γ_L) for different test liquids and electrolytes on Polished stainless steel. A linear regression between \cos of contact angle and the surface tension of test liquids (Isopropanol 23 mN/m, Acetone 25.2 mN/m, Toluene 28.4 mN/m, DMSO 43.54 mN/m, Ethylene Glycol 47.7 mN/m, Glycerol 64 mN/m, Water 72.8 mN/m) as estimated by Zisman approach. The estimated surface tension for each electrolyte as in 1M LiPF₆ EC:DMC containing 0, 5, 10, 20 mol% LiBr. All measurements were performed in an Argon atmosphere at 20 °C.

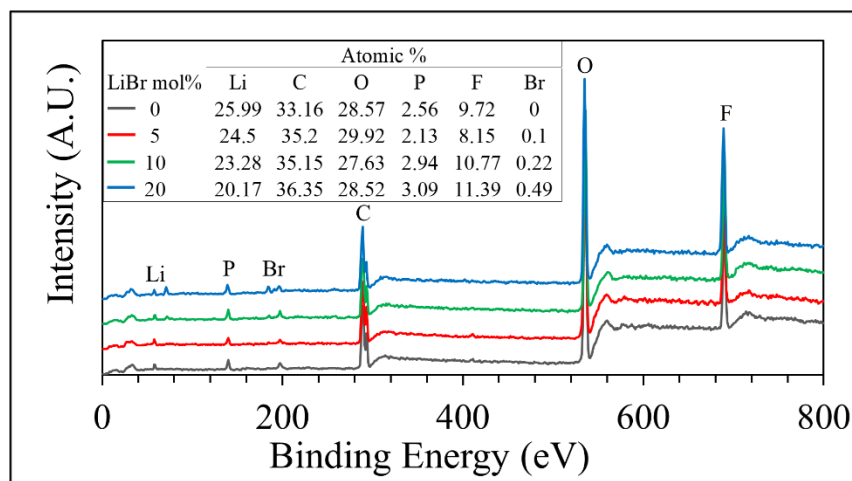


Supplementary Figure 3.14. Effect of electrolyte chemistry on the surface and bulk transport characteristics at lower capacities. Electrochemical Impedance Spectroscopy (EIS) of Lithium electrodeposited on polished substrate in contact with electrolyte having different brominated additive concentration (0, 5, 10, 20 mol% LiBr). **(a)** EIS model (5-8) used to fit the electrochemical spectrum data **(b)** Model fitting of the Nyquist plots of the electrochemical spectrum data **(c)** Areal SEI and Charge Transfer resistance as extracted from the fitted model **(d)** SEI and Bulk diffusivity as calculated from the extracted data of the fitted model.

- The R_{SEI} and R_{CT} are averaged over the electrode area in contact with the electrolyte, as reported in **Supplementary Figure 3.14(c)**.
- Nernst-Einstein equation is used to correlate the bulk electrolyte resistance (R_{Ω}) with the ambipolar bulk ion diffusivity. The transference number of bulk Li ion is calculated using Bruce-Vincent method (9) after performing potentiostatic polarization and impedance spectroscopy. The bulk Li ion diffusivity (D_B) is calculated as the product of ambipolar bulk ion diffusivity and bulk Li ion transference number (**Supplementary Figure 3.14(d)**).
- The SEI diffusivity (D_S) is calculated from the Warburg coefficient (10). The Warburg coefficient is calculated from the plot of low frequency real impedance of Z_w vs $1/\sqrt{\omega}$. The transference number of Li ions in the SEI is assumed to be 1.

LiBr conc.	$D_S C_S \times 10^{-13}$ (mol/s)	$D_S \times 10^{-17}$ (m²/s)	$C_S \times 10^4$ (mol/m²)
0 mol%	1.79	1.36	1.31
5 mol%	1.36	2.04	0.67
10 mol%	1.00	3.92	0.26
20 mol%	0.95	4.16	0.23

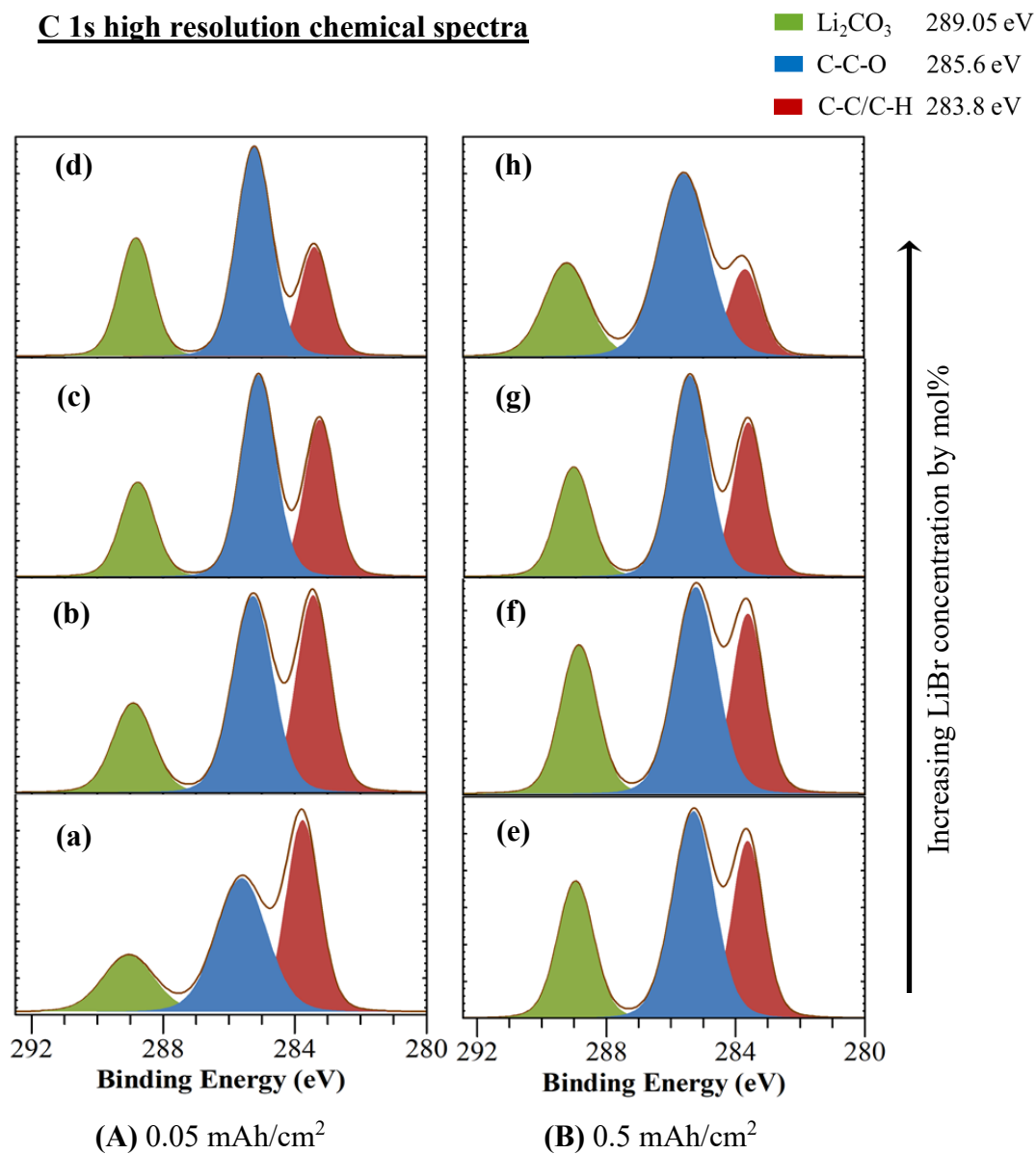
Supplementary Table 3.4. Effect of brominated electrolyte chemistry on the interfacial transport characteristics. The $D_S C_S$ is theoretically determined while the D_S is experimentally determined through the EIS. The C_S is obtained by dividing $D_S C_S$ with D_S .



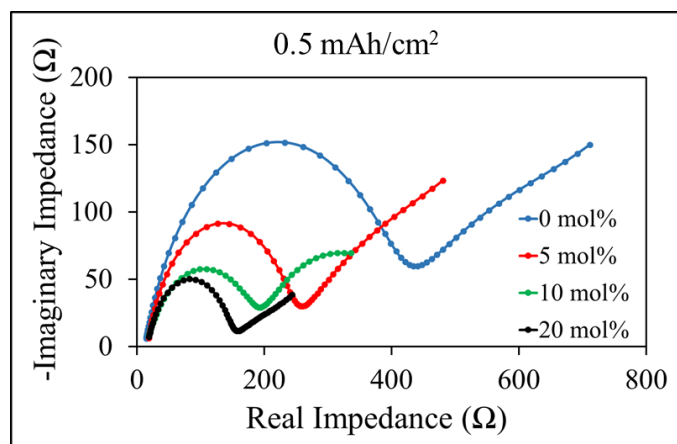
Supplementary Figure 3.15. Effect of electrolyte chemistry on interfacial chemistry of Lithium electrodeposits at different capacities of electrodeposition. Chemical spectra of the SEI layer induced by varying concentrations of LiBr (0, 5, 10, 20 mol%) in 1M LiPF₆ EC: DMC (1:1 vol.%) on Li electrodeposits formed at current density of 1 mA/cm² and areal capacities of 0.5 mAh/cm².

LiBr mol% electrolyte	Br wt% electrolyte	Br wt% SEI 0.05 mAh/cm ²	Br wt% SEI 0.5 mAh/cm ²
0	0.000	0.000	0.000
5	0.323	0.011	0.006
10	0.663	0.012	0.013
20	1.509	0.073	0.028

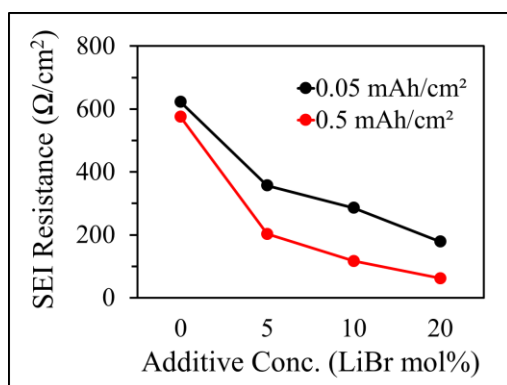
Supplementary Table 3.5. Concentration comparison of Br anion in electrolyte vs SEI at different capacities of electrodeposition. The data for Br wt% in SEI is obtained by calculation from at% reported by XPS survey spectra.



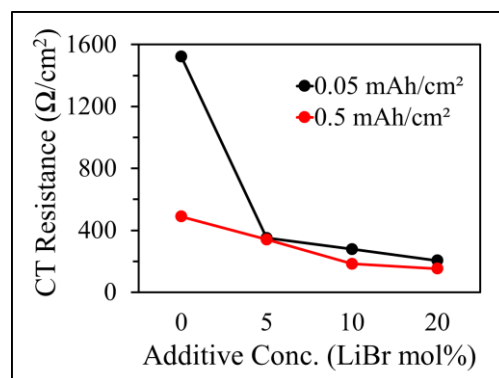
Supplementary Figure 3.16. Effect of electrolyte chemistry on the interfacial chemistry (C 1s) of Li electrodeposits at different capacities of electrodeposition. C 1s high-resolution spectra of SEI layer on Li electrodeposits formed at current density of 1 mA/cm² for areal capacities of (A) 0.05 mA/h/cm² and (B) 0.5 mA/h/cm², induced by varying concentration of (a,e) 0 mol%, (b,f) 5 mol%, (c,g) 10 mol%, (d,h) 20 mol% of LiBr in 1M LiPF₆ EC: DMC (1:1 vol.%)



(a)



(b)

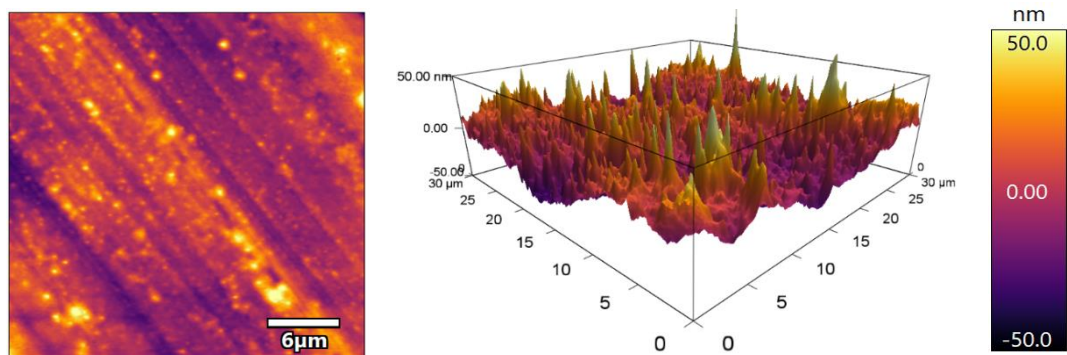


(c)

Supplementary Figure 3.17. Effect of electrolyte chemistry on the surface and bulk transport characteristics at higher capacities. Electrochemical Impedance Spectroscopy (EIS) of Lithium electrodeposited on polished substrate in contact with electrolyte having different brominated additive concentration (0,5,10,20 mol% LiBr) at a capacity of 0.5 mAh/cm². **(a)** Fitting of the Nyquist plots of the electrochemical spectrum data with model mentioned in Figure S9. (a). **(b)** Areal SEI and **(c)** Charge Transfer resistance as extracted from the fitted model contrasting for different capacities of 0.05 mAh/cm² and 0.5 mAh/cm².

<https://movie-usa.glencoesoftware.com/video/10.1073/pnas.2012071118/video-1>

Supplementary Video 3.1. Optical visualization of Li electrodeposition onto stainless steel at a current density of 3 mA/cm² and capacity of 1.5 mAh/cm² for 1M LiPF₆ EC: DMC (1:1 vol.%) electrolyte reinforced with 0 mol% (control) and 20 mol% LiBr.

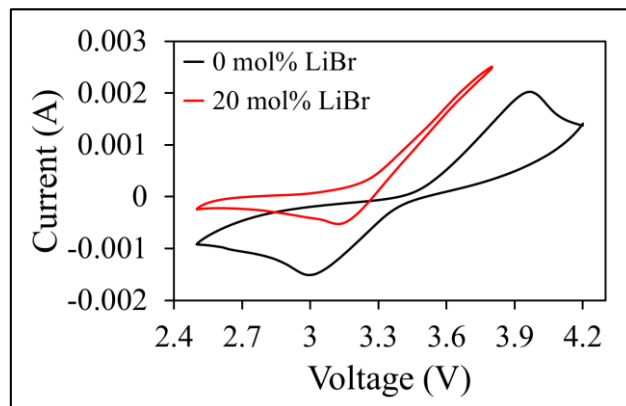


Average surface roughness (Ra) = 9.12 +/- 8.78 nm

Supplementary Figure 3.18. AFM image of the surface topography of polished stainless-steel.

LiBr mol%	Conductivity (mS/cm)	Transference number
0	10.2	0.38
5	10.3	0.38
10	10.5	0.37
20	10.6	0.37

Supplementary Table 3.6. Conductivity and Transference number of 1M LiPF₆ EC: DMC (1:1 vol.%) electrolyte reinforced with LiBr additive measured at 20° C.



Supplementary Figure 3.19. Electrochemical stability from cyclic voltammogram of 0 mol% and 20 mol% LiBr in 1M LiPF₆ in EC: DMC (1:1 vol.%). The measurements were conducted in a Li || LFP cell at a rate of 0.5 mV s⁻¹ and working voltage range of 2.5 – 4.2 V.

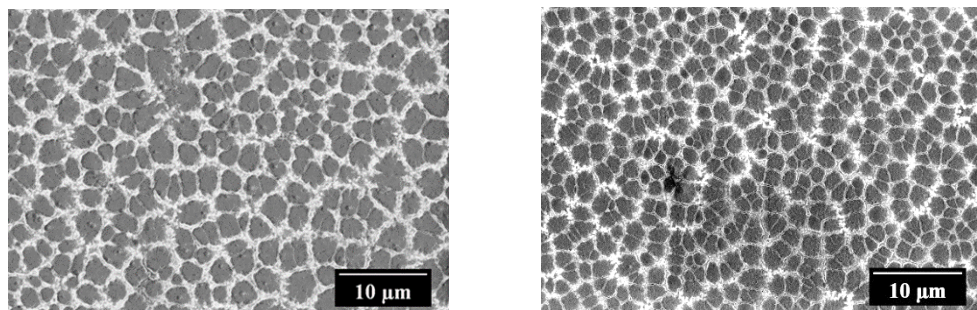
Discussion: **Supplementary Table 3.6** shows the conductivity and transference number 1M LiPF₆ EC: DMC (1:1 vol.%) electrolyte reinforced with LiBr additive measured at 20° C. The conductivity and transference number is not significantly altered by the additive, as the additive proportion is much lower than the primary salt 1M LiPF₆. However, the oxidative stability window of 20 mol% LiBr electrolyte is significantly lowered as inferred via cyclic voltammetry test shown in **Supplementary Figure 3.19**. While the reduction peaks occurring at about 3-3.2 V have similar shape across both electrolytes, the LiBr reinforced electrolyte shows no prominent oxidation peak, indicative of persistent oxidation at voltages as low as 3.5 V.

LiBr additive mol%	Current Density			
	0.1 mA/cm ²	1 mA/cm ²	20 mA/cm ²	
0 mol%	0.0505 ± 0.023	0.051 ± 0.018	0.051 ± 0.019	Overpotential minimum capacity in mAh/cm ²
5 mol%	0.050 ± 0.022	0.050 ± 0.017	0.051 ± 0.011	
10 mol%	0.049 ± 0.018	0.050 ± 0.011	0.0505 ± 0.008	
20 mol%	0.049 ± 0.014	0.049 ± 0.016	0.050 ± 0.012	

Supplementary Table 3.7. Average areal capacities with maximum range for the Overpotential minimum event observed during galvanostatic deposition of Li at different current densities and from 1M LiPF₆ EC: DMC (1:1 vol.%) electrolyte with varying mol% of LiBr additive. 8 number of multiple replicates of polished stainless steel were used as substrate for galvanostatic deposition of Li ions for a fixed current density and LiBr mol%.

Discussion: **Supplementary Table 3.7** above shows the areal capacity at which Overpotential minimum was observed for 8-sample average of Li galvanostatically deposited onto stainless steel for a fixed current density and LiBr additive mol%. The Overpotential minimum corresponds to the onset of the plateau regime, i.e., the capacity at which the voltage reaches the plateau value (Refer **Figure 3.1(a)**). Because of unavoidable sampling limitations, measurement error, and asymptotic nature of voltage curve, the exact capacity value at which the overpotential plateau first appears cannot be determined, particularly at high current densities. Here we estimate it by assuming an exponential growth model as the capacity where the voltage rises from the minimum overpotential to reach 99% of the plateau value. Consistent with the work reported by, Pei, A., Zheng, G., Shi, F., Li, Y., & Cui, Y. (2017), Nanoscale nucleation and growth of electrodeposited lithium metal. *Nano letters*, 17(2), 1132-1139 (Reference 48 in main text), we find that on clean surfaces the plateau remains well defined at early times, even at moderately high current densities, which increases confidence in the values deduced. More fundamentally, because the plateau overpotential is in the mass-transfer controlled zone for a self-limiting SEI, any decrease in the plateau overpotential at capacities below the Sands value is indicative of impurities or side-reactions. Clean pristine planar substrates minimize these artifacts.

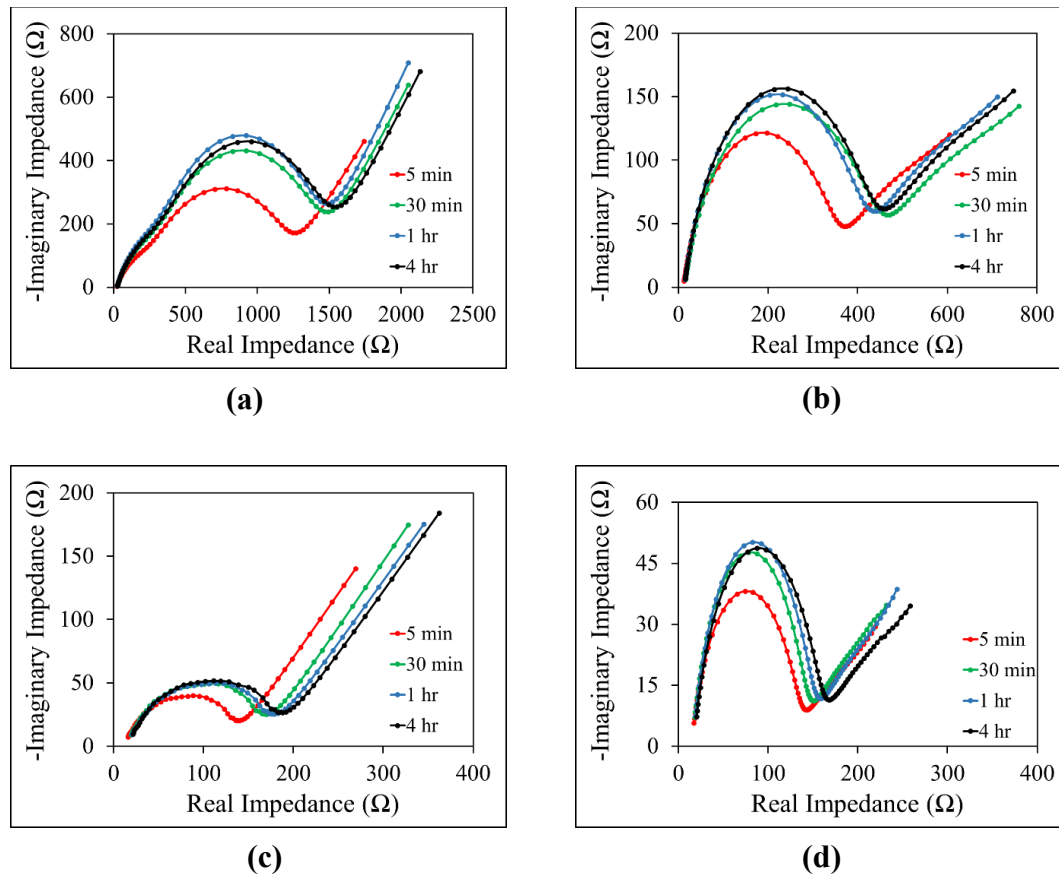
Prior to galvanostatic electrodeposition, a SEI formation and cleaning step is necessary and carried out in-situ, by electrodepositing a certain amount of Lithium and stripping it back to 1V as mentioned in the Electrochemical Method section of Materials and Method section of Supporting information. To accurately determine the Overpotential Minimum, galvanostatic electrodeposition was carried out on multiple replicates (8 per current density and LiBr mol%) of Polished stainless steel for capacities of about 0.2 mAh/cm². The overpotential minimum capacity was then fixed by examining the Overpotential curve, and marking the capacity corresponding to 99% plateau overpotential. It was found that the capacity at overpotential minimum is almost constant (maximum of $\pm 5\%$ error) (Refer **Supplementary Table 3.7**) for a fixed current density and electrolyte chemistry and can be estimated as (0.05 mAh/cm² $\pm 5\%$ error) for the entire spectrum of current density and electrolyte chemistries studied in this work. Subsequent electrodeposition and postmortem analysis were carried out for the fixed capacity (0.05 mAh/cm²) at Overpotential Minimum (as mentioned in **Materials and Methods**) to keep the analysis simple and easily reproducible. Minute care was undertaken for the cleanliness of the coin cell components, which ensures reproducibility.



(a) 1.18 μm

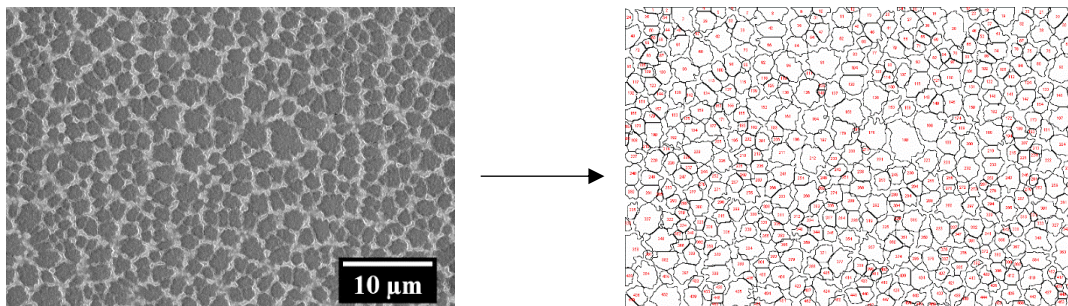
(b) 0.91 μm

Supplementary Figure 3.20. Morphology of Lithium electrodeposits formed at a current density of 10 mA/cm² on different substrates. (a) Polished Stainless steel (b) Copper. The electrolyte is 1M LiPF₆ in EC: DMC (1:1 vol.%). There is no significant difference in morphology of Li electrodeposits seen across both substrates.



Supplementary Figure 3.21. Electrochemical impedance spectra of Li electrodeposits on Stainless Steel at different open circuit potential resting time for different electrolyte compositions and capacities of electrodeposition. a) 0 mol% LiBr, 0.05 mAh/cm² b) 0 mol% LiBr, 0.5 mAh/cm² c) 20 mol% LiBr, 0.05 mAh/cm² d) 20 mol% LiBr, 0.5 mAh/cm². The base electrolyte is 1M LiPF₆ in EC: DMC (1:1 vol.%).

Discussion: **Supplementary Figure 3.21** shows the open circuit voltage (OCV) time dependent impedance spectra of low/high capacity Li electrodeposits formed under the carbonate electrolyte w/o LiBr additive. It is apparent that the impedances offered by the electrodeposits grows significantly between 5 min to 30 min, while remaining mostly stable from 30 min to 4 hr. Therefore, the impedance spectroscopy of Li electrodeposits at any capacity and electrolyte composition performed in this study is after 1 hr OCV resting time.



Supplementary Figure 3.22. ImageJ analysis of Li nuclei size. The software counts the number and projected area of each nuclei and the results are obtained in nm significant figures. The average radius (with standard deviation) of nuclei are obtained from the projected area reported. Gaussian blurring, thresholding, adjustable watershed are typical image processing tools employed within Image

Material and Methods

Polishing/cleaning method: The stainless-steel 304 substrate was polished to a surface roughness of $R_a < 10\text{nm}$ through chemical mechanical polishing (CMP) method. The unpolished stainless-steel substrates were fixed in an Alumina slurry of 0.3 Micron particles on a bed of Final-POL Adhesive Back Disc (Allied High-Tech products) in a vibratory polisher at an amplitude of 50% for about 2 days. The polished stainless-steel substrates were cleaned through ultrasonication in a bath of acetone for about 1 hour.

Supplementary Figure 3.18 shows the AFM image of the surface topography of the stainless-steel to have average roughness of about 10 nm. The polished cleaned substrates were stored in a vial of acetone and ultrasonicated again with fresh acetone prior to any usage.

Electrochemical method: 2032-type coin cells with the polished stainless-steel working electrodes (thickness 1.7 mm) and Li foil (Alfa Aesar 0.75 mm width) counter/reference electrodes were assembled in an argon-filled glove box (MBraun). A hard Teflon O-ring of internal diameter 0.25 inches and thickness of 0.8 mm was used between the two electrodes and 200 μL of electrolyte was added to each cell. The Teflon O-ring ensures holding of free liquid electrolyte and minimal stacking pressure. The coin cell crimping pressure is kept at a minimum (< 100 psi) to avoid deformation of Li electrode and subsequent short-circuiting. 1 M Lithium hexafluorophosphate (LiPF_6) in Ethylene Carbonate: Dimethyl Carbonate (1:1 V) electrolyte (Sigma-Aldrich) with varying mol% of Lithium Bromide (Sigma-Aldrich) as an additive was used as the electrolyte. The solubility limit of Lithium Bromide salt in the 1 M Lithium

hexafluorophosphate (LiPF_6) in Ethylene Carbonate: Dimethyl Carbonate (1:1 V) electrolyte is at about 30 mol%. The conductivity and transference number of the electrolyte infused with LiBr doesn't change significantly, while the oxidative potential window of the electrolyte is significantly altered by the LiBr additive (See **SI Supplementary Table 3.6** and **Supplementary Figure 3.19**). Galvanostatic deposition was conducted using an 8-channel battery testing unit from Neware Instruments and MACCOR series 4000 battery tester system. The stainless-steel electrode was discharged to 0 V vs. Li/Li^+ by applying 0.05 mA/cm^2 current, then charged back to 1 V at -0.05 mA/cm^2 to initialize SEI formation and remove surface impurities. Then, a fixed amount of charge was passed galvanostatically at different current rates depending on the experiment. In this work, the point in overpotential curve at which 99% of the plateau overpotential is attained after the nucleation peak, is referred to as Overpotential minimum, and the corresponding areal capacity as Overpotential minimum capacity. To accurately determine the Overpotential minimum, galvanostatic electrodeposition of Li ions was carried out on multiple replicates of Polished stainless-steel for capacities of about 0.2 mAh/cm^2 . The overpotential minimum capacity was then fixed by examining the Overpotential curve, and marking the capacity corresponding to 99% plateau overpotential. It was found that the capacity at Overpotential minimum is almost constant for a fixed current density and electrolyte chemistry and is observed at an areal capacity of 0.05 mAh/cm^2 ($\pm 5\%$ error) for entire spectrum of current densities and electrolyte chemistries (See **Supplementary Table 3.7** and discussion). Subsequent electrodeposition and postmortem analysis were carried out for the fixed capacity (0.05 mAh/cm^2) at Overpotential Minimum to keep the analysis simple and easily

reproducible. Minute care was undertaken for the cleanliness and purity of the coin cell components, which ensures reproducibility of the fixed capacity.

The preselection of substrate involved electrodeposition of Li via above galvanostatic procedure onto Polished Stainless-Steel and Polished Copper (**Supplementary Figure 3.20**) to examine any morphological differences in the nucleated Li. There is no significant difference in morphology observed. Therefore, both are viable substrates for the study. However, employing polished Copper as the primary substrate is difficult due to a) Copper tends to bend and deform under the vibrations of polishing action producing uneven surface b) Polished Copper substrates oxidized within a few days' time frame severely compromising their reusability in the experiments. The polished stainless-steel substrate proves superior in all these aspects, and therefore employed as the primary substrate in this study.

Similarly, the Galvanostatic deposition for higher capacities 0.5 mAh/cm^2 , symmetric cell cycling, and Coulombic efficiency cycling were conducted using an 8-channel battery testing unit from Neware Instruments. The galvanostatic deposition for higher capacities of 0.5 mAh/cm^2 involved discharging the stainless-steel electrode to 0 V vs. Li/Li^+ by applying 0.05 mA/cm^2 current, then charging back to 1 V at -0.05 mA/cm^2 to initialize SEI formation and remove surface impurities, followed by electrodeposition at a current of 1 mA/cm^2 for 30 minutes. The cell setup being like previously described asymmetric arrangement of Lithium and polished stainless steel with a sandwiched Teflon O-ring electrolyte holder. The symmetric cell cycling consisted of two lithium electrodes of diameter 1.27 cm (0.5 in) with a celgard 2320 as the separator, holding 60

μl of electrolyte. An initial SEI formation plating/stripping 10 cycles were carried out at low current density of 0.05 mA/cm^2 and 0.05 mAh/cm^2 capacity, followed by repeated plating/stripping cycles at higher current density of 1 mA/cm^2 and 0.5 mAh/cm^2 . The Coulombic efficiency test had an asymmetric cell setup of Lithium electrode (1.27 cm (0.5 in) diameter) and polished stainless steel electrode with a celgard 2320 as the separator, holding $60 \mu\text{l}$ of electrolyte. The stainless-steel electrode was discharged to 0 V vs. Li/Li^+ by applying 0.05 mA/cm^2 current, then charged back to 1 V at -0.05 mA/cm^2 for 10 cycles to initialize SEI formation, followed by 100 cycles of plating/stripping of Li onto/from the stainless steel at a fixed current density and capacity.

A Solartron workstation with frequency analyzer was used for obtaining impedance spectra at room temperature. The frequency range was adjusted to be in between 1 MHz to 1 mHz at an amplitude of 10mV. Prior to the impedance spectroscopy, Lithium of areal capacity corresponding to 0.05 mAh/cm^2 ($\pm 5\%$ error) or 0.5 mAh/cm^2 was electrodeposited on to the polished stainless-steel through the electrochemical method mentioned previously. These electrodes were extracted and re-assembled in a symmetric cell fashion in 2032-type coin cells. The assembly consisted of electrolyte in a Teflon O-ring (0.25 inches in diameter) in between two Polished stainless-steel with electrodeposited Lithium. A 1 hr resting OCV time was ensured before impedance spectroscopy to allow the SEI to fully mature, the rationale of which is shown in **Supplementary Figure 3.21**. Further impedance spectroscopy performed on symmetric Li cells with Teflon O-ring holding the electrolyte were used to determine conductivity and transference number of Li ions in the electrolyte.

The cyclic voltammetry experiments were performed using a Gamry potentiostat. The measurements were conducted in a Li || LFP cell at a rate of 0.5 mV s^{-1} and working voltage range of 2.5 – 4.2 V. The cell consisted of celgard infused with the electrolyte (with or without LiBr additive). The LFP cathode was procured from NEI corporation, and has active material loading of 90%, standard capacity of $1.25 \text{ mAh/cm}^2 \pm 5\%$, nominal voltage vs. Li/Li⁺ of 3.2V and nominal capacity at 0.1C rate of greater than or equal to 160 mAh/g.

Goniometry: An Attention Theta-lite Optical tensiometer (Biolin Scientific) was used in an argon-filled glove box for obtaining the contact angle data. The contact angles (C.A.) were measured according to the sessile drop method at room temperature (20 °C). A single drop of the test electrolyte (drop volume ca. 4–5 μL) was placed on the pristine Lithium substrate via a microliter syringe. Dynamic contact angles were measured from the optical image of the steady droplet using the live acquisition mode of the software. For each electrolyte, the contact angle was determined for 6 different Lithium substrates, and the average values are reported. The initial few dynamic Contact angle readings at the start of an experiment were discarded owing to unsteady state of the droplet (Advancing/Receding contact lines). For each electrolyte, the standard deviation for C.A. measurements were less than 10% of the reported data.

Electrode Characterization: After Li electrodeposition onto stainless-steel, the cells were opened in the Argon glove box and the stainless-steel electrodes were rinsed with fresh Dimethyl Carbonate for about 5 seconds and vacuum dried in the antechamber of the glovebox. Electrodes were mounted onto SEM stage puck and sealed in Argon filled

transfer vessels for immediate SEM observation (Zeiss Gemini SEM). Unavoidable contact with air was brief (< 10 secs) and may have slightly altered the surface features of the electrodeposited Lithium metal seen in SEM images. The images were captured at 2 kV with an aperture of 20 μm .

The chemical composition of the surface of Li electrodeposits were analyzed using a Scienta Omicron ESCA-2SR with operating pressure ca. 1×10^{-9} mBar. Monochromatic Al K α X-rays (1486.6 eV) were generated at 300W (15kV; 20mA). Analysis spot size was 2 mm in diameter with a 0° photoemission angle and a source to analyzer angle of 54.7° . A hemispherical analyzer determined electron kinetic energy, using a pass energy of 200 eV for wide/survey scans and 50 eV for high resolution scans. A flood gun was used for charge neutralization of non-conductive samples. The data analysis was performed with CasaXPS software, with Tougaard background fitting of the peaks.

The cross-sectional images were prepared using cryogenic FIB/SEM in a FEI Strata 400 and the Quorum PP3010T cryo-preparation station. Samples washed with DMC were transferred in an Argon filled container, subsequently were plunge frozen in slush nitrogen and transferred in vacuum into the microscope chamber. To mitigate charging and damage from both the ion and electron beams, the samples were first sputter coated with a thin gold-palladium layer, and then covered in a platinum layer approximately 1 μm thick. Cross-sections were milled using a 30 kV gallium ion beam, first at 2.8 nA for a rough trench, then cleaned at 0.93 nA. Images were collected at 2 kV and 0.84 nA.

Electrolyte Characterization: The electrolyte (0 mol% and 20 mol% LiBr) was reduced galvanostatically at a current density of 1 mA/cm^2 for 30 mins (0.5 mAh/cm^2).

The setup included flat rectangular pieces of Lithium and stainless steel co-facing each other arranged in a 3.5 mL electrolyte filled cuvette purchased from Science Outlet with paired caps made in the laboratory (Refer to work of Deng et al. (16) for detailed arrangement of setup with schematics), as electrodes connected with stainless-steel transmission line to Neware battery tester. After the galvanostatic electrodeposition (discharge cycle) for 30 mins, a charging cycle of lithiated stainless steel to 1 V at 1 mA/cm² was performed to ensure the stripping of deposited Lithium and modest dissolution of SEI components formed on the lithiated stainless steel. About 50 uL of the cycled electrolyte was collected in a standard NMR tube with 50 uL DMSO-d₆ solvent. The 1-HNMR spectra were collected on a Bruker AV III HD (1H, 500MHz) spectrometer with a broad band Prodigy cryoprobe.

Image / Data Analysis: Nuclei sizes were measured using ImageJ software as shown in **Supplementary Figure 3.22**. Gaussian blurring to remove excessive noise, Thresholding to restrict color contrast of images to black and white, and adjustable watershed to identify nuclei were performed. 4 samples with Li electrodeposits per current density and electrolyte composition were analyzed and averaged. Roughly, between 100-500 particles from these samples were averaged for each current density and for every electrolyte composition. The radius of a Nuclei was calculated by assuming the nuclei to be hemispherical and the projected area was approximated to that of a circle. Igor Pro 8 was used to curve fit the average nuclei radius (with error bars) against current density. The coefficients (A' and B') were kept unrestricted to any value. The fitted coefficients were analyzed, and physical parameters were extracted.

Visualization method: Visualization cells were quartz 3.5 mL cuvette purchased from Science Outlet with paired caps made in the laboratory (Refer to work of Deng et al. (11) for detailed arrangement of setup with schematics). Flat rectangular pieces of Lithium and stainless steel co-facing each other were arranged in an electrolyte filled cuvette, as electrodes connected with stainless-steel transmission line to Neware battery tester. The cuvette arrangement was placed under an Optical microscope (OLYMPUS DP 80) camera with a x100 magnification, such that the direction of gravity is perpendicular to the direction of electric field during cell polarization. The images captured were analyzed using ImageJ software. All measurements were carried under room temperature and pressure.

References for Appendix

- (1) Pei, A., Zheng, G., Shi, F., Li, Y., & Cui, Y. (2017). Nanoscale nucleation and growth of electrodeposited lithium metal. *Nano letters*, 17(2), 1132-1139.
- (2) Zisman, W. A. (1963). Influence of constitution on adhesion. *Industrial & Engineering Chemistry*, 55(10), 18-38.
- (3) Gindl, M., Sinn, G., Gindl, W., Reiterer, A., & Tschegg, S. (2001). A comparison of different methods to calculate the surface free energy of wood using contact angle measurements. *Colloids and Surfaces A: Physicochemical and Engineering Aspects*, 181(1-3), 279-287.
- (4) Dahbi, M., Violleau, D., Ghamouss, F., Jacquemin, J., Tran-Van, F., Lemordant, D., & Anouti, M. (2012). Interfacial properties of LiTFSI and LiPF6-based electrolytes in

binary and ternary mixtures of alkylcarbonates on graphite electrodes and celgard separator. *Industrial & engineering chemistry research*, 51(14), 5240-5245.

(5) Zhang, S. S., Xu, K., & Jow, T. R. (2006). EIS study on the formation of solid electrolyte interface in Li-ion battery. *Electrochimica acta*, 51(8-9), 1636-1640.

(6) Xiang, H., Shi, P., Bhattacharya, P., Chen, X., Mei, D., Bowden, M. E., ... & Xu, W. (2016). Enhanced charging capability of lithium metal batteries based on lithium bis (trifluoromethanesulfonyl) imide-lithium bis (oxalato) borate dual-salt electrolytes. *Journal of Power Sources*, 318, 170-177.

(7) Huang, J., Li, Z., Ge, H., & Zhang, J. (2015). Analytical solution to the impedance of electrode/electrolyte interface in lithium-ion batteries. *Journal of The Electrochemical Society*, 162(13), A7037-A7048.

(8) Guo, J., Sun, A., Chen, X., Wang, C., & Manivannan, A. (2011). Cyclability study of silicon-carbon composite anodes for lithium-ion batteries using electrochemical impedance spectroscopy. *Electrochimica Acta*, 56(11), 3981-3987.

(9) Bruce, P. G., Evans, J., & Vincent, C. A. (1988). Conductivity and transference number measurements on polymer electrolytes. *Solid State Ionics*, 28, 918-922.

(10) Warburg, E. (1899). Ueber das Verhalten sogenannter unpolarisierbarer Elektroden gegen Wechselstrom. *Annalen der Physik*, 303(3), 493-499.

(11) Deng, Y., Zheng, J., Warren, A., Yin, J., Choudhury, S., Biswal, P., Zhang, D. and Archer, L.A., 2019. On the Reversibility and Fragility of Sodium Metal Electrodes. *Advanced Energy Materials*, 9(39), p.1901651.

Chapter 4

Rational design of Solid Electrolyte Interphase with enhanced energetics for Lithium Metal Anode

4.1 Abstract

The spatial variations in chemical composition and transport properties of the interphase formed on reactive metal electrodeposits plays a critical role in dictating the electrochemical stability and reversibility of electrochemical cells that use reactive metals as anodes. Here, we report on the influence of carbonate and fluorinated electrolytes infused with ethers as additives on the physical-chemical characteristics and electrochemical reversibility of metallic Lithium (Li) during early stages of electrodeposition, as well as on later stages of deep cycling of Li metal anode. We hypothesize that regulation and preservation of the surface energetics of the interphase through the cycle life of Li electrodeposits is crucial in achieving high reversibility. We hypothesize further that a feasible strategy for achieving such interphases is through the simultaneous use of sacrificial electrolyte components that undergo electroreduction to enrich the interphase with fluorinated species and in tandem introduce electrolyte components that promote dissolution and removal of less desirable carbonaceous compounds. A combination of electron microscopy (SEM) and spectroscopy (EDX, XPS, EIS) techniques are employed to evaluate this hypothesis by examining the spatial homogeneity, chemical composition, transport-reaction characteristics of the material phases formed on Li. We report that it is possible to control, regulate, and preserve the surface energetics of Li electrodeposits through rational choice of electrolyte components consisting of fluorinated electrolyte solvents infused with ether additive. We consider the practical benefits of the approach and show that it translates to high electrochemical reversibility during deep cycling of the Li metal anode and improved performance of full-cell LMBs. Our results show that designing and preserving

interfaces with enhanced transport-reaction kinetics is a feasible strategy for achieving high Li metal reversibility and for controlling electrodeposition morphology of reactive metals such as Li.

4.2 Introduction

The spatial variations in chemical composition and transport properties of the solid electrolyte interphase (SEI) formed on Li metal in liquid electrolytes are thought to be responsible for the propensity of Li metal electrodes to electrodeposit in irregular, nonplanar morphologies during repeated charging/discharging cycles (1). The origin of these spatial variations is thought to be parasitic reactions of Li with electrolyte components (solvent, salt, additives), forming a spectrum of inorganic and organic products *i.e.*, Li_2CO_3 , LiF, LiOH, Li_2O , LiH, & ROLi, ROCO_2Li class oligomers at the interface (1,2). A chemically inhomogeneous solid electrolyte interphase (SEI) means that ion transport and mechanics vary from location to location on Li, which is thought to favor Li electrodeposition at specific points during charging (3). The nascent deposits formed serve as centers of concentrated electric field lines of incoming Li ions, directing the electrodeposition thereon, and grow disproportionately to micrometer sizes within a short period of time (4,5). As these deposits grow, they break through the inherent SEI, further reacting with the electrolyte to form a fresh SEI composed of decomposition products. During the discharging phase, these spatial variations in the SEI enable non-uniform local dissolution of Li from the electrode, leading to pitting of the electrode and further collapse of the SEI due to pits formed in the process (5,6). This process is further

exacerbated by repeated charging/discharging cycles of the metal electrode, leading to mechanical loss of active metal and chemical loss of electrolyte components, deteriorating electrochemical reversibility of a Li metal battery. Further, the continuous reaction of the electrodeposited Li with the electrolyte throughout the cycles results in a thicker SEI and lower interfacial ionic conductivity, relative to the electrolyte bulk, which increases polarization and accelerates decomposition of the electrolyte (7).

A growing body of work reports that selectively modifying the chemistry and transport properties of the SEI via incorporating certain additives in liquid electrolytes is an effective approach for achieving highly reversible Li electrodeposition in liquid electrolytes (8-16). Further, equilibrium theoretical calculations using joint density functional analysis in vacuum and generic liquid (*e.g.*, acetonitrile) media have also shown that in plane transport at such interphases is enhanced substantially if LiX (X = Br > Cl > F) species are the only components of the SEI (17). Previous work (4,18) summarized in **chapters 2 & 3** builds upon this hypothesis to investigate whether deliberate incorporation of these halide (F, Br) species into the SEI via partially fluorinated/ brominated electrolytes affects the early-stage growth and reversibility of Li electrodeposits. The results show improvement in the surface energetics (ion diffusivity, interfacial energy) of the SEI and also indicate that Li electrodeposits with more uniform morphology form in the early stages of electrodeposition. However, the improvements observed in the reversibility of the electrodeposits during long-term, deep cycling of Li are at best modest, when compared to conventional carbonate electrolytes. We hypothesize that the failure to realize deep cycling of the Li anode in halide-enriched electrolytes stems from at least three reasons. First, conventional carbonate electrolyte

which serves as the carrier medium for halide rich additives, actively decomposes into carbonaceous compounds (Li_2CO_3 , ROCO_2Li *etc.*) at the reducing potentials (-3.04V vs SHE) at which Li^+ reduces to form Li at the anode during battery charge. Second, the formed carbonate compounds ultimately dominate the composition of the SEI fundamentally alter the interfacial ion transport properties, ultimately negating any benefits of the fluorinated components. To demonstrate this point more concretely, we note that a purely Li_2CO_3 rich SEI has about 5 times higher energy barrier for diffusion of in-plane Li adatoms than a purely LiF SEI (17). Similarly, the ion diffusion properties of the SEI are also hindered by the presence of Li_2CO_3 as discussed in previous **chapters 2 & 3**. Repeated plating/stripping cycles of the anode generates significant amount of these compounds at the SEI in the long run which negate any beneficial effects of the halide additives in the early stage. Finally, mitigating the parasitic reactions and preserving the halide rich SEI over repeated plating/stripping cycles of the Li anode provides a strategy for realizing high electrochemical reversibility for deep cycled Li.

An approach to reduce the parasitic reactions at the interphase is to substitute the conventional carbonate electrolyte with a fully fluorinated electrolyte. This can be realized by either adding large amounts of easily reduced fluorine-rich salts (*e.g.*, LiPF_6 , LiFSI) into the conventional carbonate or ether-based solvents (*e.g.*, Ethylene Carbonate/ Dimethyl Carbonate or Dimethyl Ether/ Dioxolane) to create a highly concentrated electrolyte where the salt dominates over the solvent in regulating the SEI (9,10,19-21), or simply replacing the base solvent with a fluorinated analog (Fluoroethylene Carbonate) (10). The later approach is studied here because it is

considered more feasible, as the high cost of salt in a highly concentrated electrolyte can easily outweigh any potential benefit of a Li metal anode (21). Fluoroethylene Carbonate (FEC) is selected here because it has often been employed as an electrolyte additive due to its reported beneficial influence on the morphology of Li electrodeposits formed in charge/discharge battery cycling experiments (10, 16, 22). In chapter 2, we in fact showed that carbonate electrolytes containing FEC as additive, even in low weight percentages (~10 wt%), yield more uniform plating morphology of Lithium. By means of XPS analysis, this behavior was attributed to FEC's ability to form a fluorine rich SEI. Further, FEC is also expected to serve dual purpose role of stabilizing Li anode imparted by LiF-rich SEI formation as well as enhancing oxidative stability of electrolyte (10,23). Recently, its role as a single component electrolyte solvent in enabling highly reversible 5V class Li metal batteries has garnered attention (10). While FEC can stabilize the SEI, realizing elimination of any parasitic side reactions and unwanted side products over hundreds of charge/discharge cycles of the anode is a requirement for progress towards practically relevant Li metal batteries. Specifically, FEC, a fluorinated carbonic ester having structural similarity to that of the conventional carbonate solvents (Ethylene Carbonate), is expected to generate carbonaceous compounds (Li_2CO_3 , ROCO_2Li) as side products. This means that the beneficial fluoride enriched interphase formed in the early stages of Li deposition can be easily overwhelmed by carbonates. The fluoride-rich interface can however be sustained via a solubilizing/cleaning agent capable of dissolving the side products from the SEI. A cleaning agent of choice can be glycol ethers (glymes), a group of saturated non-cyclic polyethers commonly used in paints and cleaners (24) for precisely that purpose.

4.3 Results and Discussions

We investigated the physiochemical characteristics and electrochemical reversibility of metallic Lithium in carbonate and fluorinated electrolytes with/without glymes. Electrodeposition of Li is carried out across a set of carbonate (Ethylene Carbonate: Dimethyl Carbonate, EC:DMC) and fluorinated (Fluoroethylene Carbonate, FEC) electrolyte chemistries incorporated with glyme additive (Diglyme, G2), namely 1M LiPF₆ in EC:DMC (50:50), 1M LiPF₆ in EC:DMC:G2 (45:45:10), 1M LiPF₆ in FEC, 1M LiPF₆ in FEC:G2 (90:10). We hypothesize that regulation and preservation of the surface energetics of the SEI through the cycle life of Li electrodeposits is crucial in achieving high reversibility, and this is feasible through the SEI fluorine enrichment mechanism of FEC in tandem with the cleaning action of the diglyme. The spatial and chemical characteristics of electrodeposited Li are studied via a combination of Scanning Electron Microscopy (SEM), Energy Dispersive X-Ray (EDX), X-ray Photoelectron Spectroscopy (XPS), and Electrochemical Impedance spectroscopy (EIS) techniques. Consistent with our previous reports (4) from Chapter 2, we show that fluorine enriched SEI is spatially homogeneous and has favorable kinetics for uniform Li deposition in early stages of Li electrodeposition. We also show that the glyme additive (diglyme) even in modest proportions can solubilize the unwanted carbonaceous compounds and preserve the pristine fluorine enriched SEI for later cycles, enabling higher reversibility, longer cycle life, and decidedly nondendritic morphology for the lithium metal anode. Further, cycling studies in electrochemical cells composed of thin metallic Li anodes (50 μm) and commercial-grade nickel cobalt manganese oxide (NCM) cathodes further reveals that the fluorinated electrolyte with a

glyme additive enable high coulombic efficiency (CE) and stable long-term cell operations.

The solid electrolyte interphase (SEI) was formed via galvanostatic polarization of bulk electrolyte onto a heterogenous surface composed of polished stainless steel (SS; rms roughness, 9.12 ± 8.78 nm). To investigate the effect of fluorinated electrolytes (FEC) and the glyme additive (diglyme) on the spatial homogeneity of the interphase, the SEI was formed from electrolytes of different compositions (1M LiPF₆ in EC:DMC (50:50), 1M LiPF₆ in EC:DMC:G2 (45:45:10), 1M LiPF₆ in FEC, 1M LiPF₆ in FEC:G2 (90:10)) by discharging the Li||SS cell at current density of 0.5 mA/cm² till the potential dropped to 50 mV vs Li⁺/Li as shown in **Figure 4.1(A)**. The terminal discharge potential of 50 mV was chosen to avoid any substantial underpotential deposition of Li, which is likely at around 0V. Thereon, the cell was galvanostatically charged back to 1.5V at low currents of 0.1 mA/cm², to strip the underpotentially deposited Li, if any. The areal capacity of SEI formation is observed to decrease almost two fold between the carbonate electrolyte and the fluorinated electrolyte (i.e. 0.047 mAh/cm² for EC:DMC compared to 0.027 mAh/cm² for FEC) as shown in **Figure 4.1(A)**. Both electrolytes are known to actively reduce at potentials above 0V to form products that can electronically passivate the stainless-steel (25-27). This capacity is a measurable indicator of the amount of electrolyte reduced at a fixed current to form the SEI on the stainless steel. This formation step occurring over a range of potentials involves competing reactions which often results in several side products. The lower capacity observed in the formation of the SEI for the fluorinated electrolyte suggests fewer side reactions and quicker electronic passivation of the heterogenous surface than the carbonate electrolyte.

Further, no change in areal capacities were observed between the base electrolytes and diglyme-infused variants (*i.e.*, EC:DMC vs. EC:DMC:G2, & FEC vs. FEC:G2), indicating that the diglyme acts as inert to decomposition in the SEI formation, plausibly due to its low reduction potential against Li (calculated to be between -0.8V and -0.2V vs Li⁺/Li) (28) and significantly lower proportion in the electrolyte mixtures.

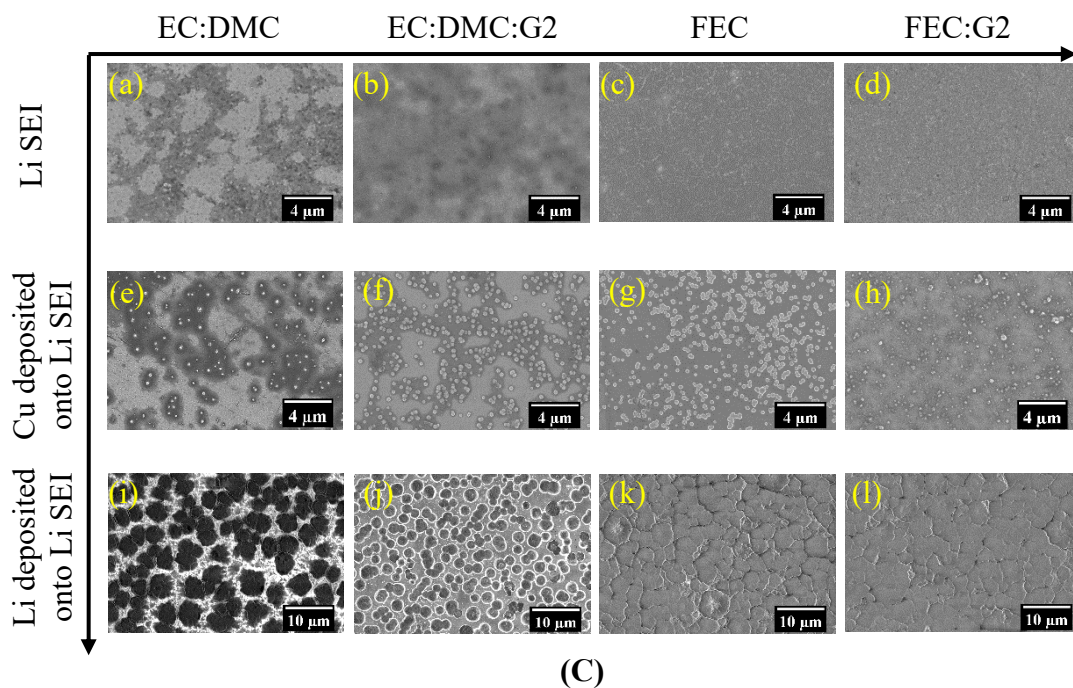
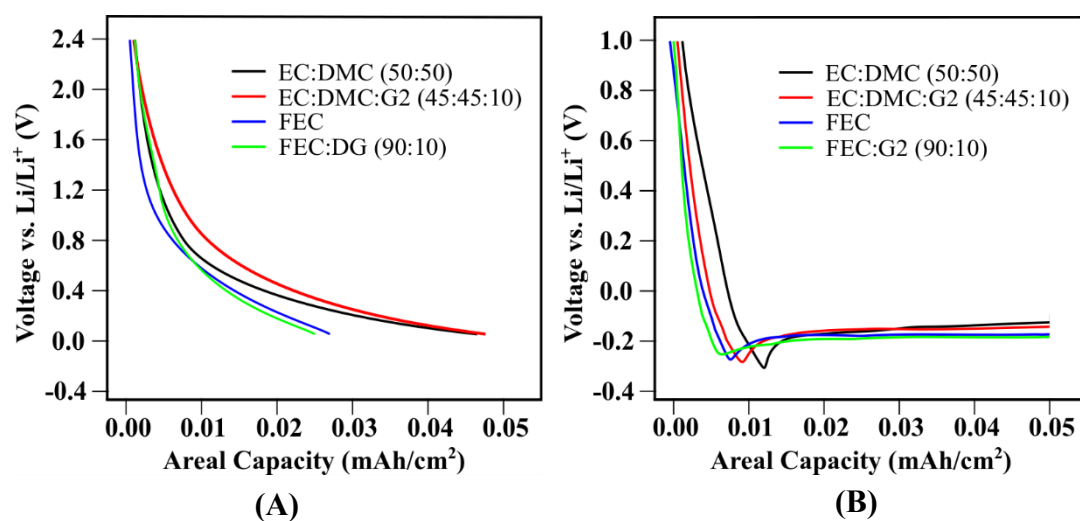


Figure 4.1. Effect of electrolyte chemistry on the morphology and homogeneity of early stage SEI and electrodeposits of Lithium formed on polished stainless steel. **(A)** Experimental voltage profiles of galvanostatic SEI formation for different electrolyte compositions at current densities of 0.5 mA/cm². **(B)** Experimental voltage profiles of Li electrodeposition from electrolyte of different compositions at current densities of 1 mA/cm² and capacities of 0.05 mAh/cm². **(C)** Ex situ SEM images captured of **(a-d)** Li SEI formed galvanostatically at 0.5 mA/cm² **(e-h)** Cu deposited at current densities of 1 mA/cm² and capacity of 0.01 mAh/cm² onto the previously formed Li SEI in different electrolytes **(i-l)** Li deposited at current densities of 1 mA/cm² and capacities of 0.05 mAh/cm² onto the previously formed Li SEI for the range of electrolyte compositions. The electrolyte compositions are 1M LiPF₆ in EC:DMC (50:50), 1M LiPF₆ in EC:DMC:G2 (45:45:10), 1M LiPF₆ in FEC, 1M LiPF₆ in FEC:G2 (90:10). The Li is deposited from the above respective electrolytes corresponding to that of the one that forms the SEI, while copper is deposited from 0.5M Cu(OTF)₂ in EC:DMC (50:50) electrolyte in all cases. All ratios are vol% and G2 here stands for diglyme.

The morphological features of the SEI formed across the range of electrolytes were mapped using SEM as shown in **Figure 4.1(C)(a-d)**. The observed SEI for carbonate electrolytes (**Figure 4.1(C)(a-b)**) has spatial regions of different contrast as opposed to the uniform contrast observed in fluorinated electrolytes (**Figure 4.1(C)(c-d)**). Point spectra chemical analysis of these regions performed via EDX in tandem with the SEM (**Supplementary Figure 4.1(a-d)**) indicates the darker contrasted regions to be rich in fluorine as opposed to the lighter regions having higher carbon wt percentage. The degree of spatial contrast is highest in the case of base carbonate electrolyte (**Figure 4.1(C)(a) & Supplementary Figure 4.1(a)**), suggesting that the SEI formed in this electrolyte is spatially inhomogeneous with alternating fluorine and carbon rich regions.

As an example, **Supplementary Figure 4.1(a)**, darker contrasted region 1a has F and C wt% of 54.2 and 35.7 respectively compared to 24.1 and 69.2 respectively in lighter contrasted region 1b. This is due to the fact that during the electrolyte reduction, the electrolyte components decompose at different potentials to form different products i.e. LiPF_6 decomposes at higher potentials (25,26) to form fluorine rich products (LiF) while the solvent EC:DMC decomposes at relatively lower potentials (25,26) to form carbon rich products (Li_2CO_3 , ROCO_2Li etc) (1). As these products precipitate at the interface, they electronically passivate it, resulting in a patchy SEI. Addition of the diglyme into the base carbonate electrolyte seems to rectify the patchy SEI. The SEI has lesser spatial contrast in morphology and more fluorine rich regions (darker contrast) as shown in **Figure 4.1(C)(b)** and analyzed in **Supplementary Figure 4.1(b)**. This is most likely due to the hypothesized solubilizing action of diglyme on carbon rich precipitates at the interface. The SEI formed in fluorinated electrolytes (FEC & FEC:G2) is rich in fluorine content and lacks any spatial contrast i.e., homogeneously fluorine rich all across the surface as shown in **Figure 4.1(C)(c-d)** and analyzed in **Supplementary Figure 4.1(c-d)**. The higher degree of uniformity is crudely because of similar products (LiF) formed during reduction of LiPF_6 and FEC.

The SEI covered stainless steel substrates are harvested and further studied via deposition of Cu onto them from a carbonate electrolyte. The aim is to further contrast between the ionic transport properties of the spatial regions of the SEI's by analyzing the deposition patterns of a non-reactive metal like Cu. Cu is galvanostatically electrodeposited onto the SEI from 0.5M $\text{Cu}(\text{OTF})_2$ in EC:DMC (50:50) electrolyte at current density of 1 mA/cm^2 and capacity of 0.01 mAh/cm^2 . The capacity of

electrodeposition is deliberately kept low to avoid any modification of the inherent SEI. Further, the potential of electrodeposition recorded are in the range of 2 – 2.2 V vs Li^+/Li , which is well above the reduction potential of the carbonate solvent (0.5M $\text{Cu}(\text{OTF})_2$ in EC:DMC (50:50)) employed (25,26), indicating minimal decomposition of the new electrolyte, hence reduced interference with the previously formed SEI's. **Figure 4.1(C)(e-h)** show the morphology of the Cu electrodeposits on the previously formed SEI's. The chemistry of these morphological features is further analyzed in **Supplementary Figure 4.1(e-h)**. Quite like before, the darker contrasted regions are fluorine rich, while the lighter contrasted regions are carbon rich; also, the spatial and chemical contrast being more vivid in the base carbonate electrolyte (**Figure 4.1(C)(e)** & **Supplementary Figure 4.1(e)**). For e.g., in **Supplementary Figure 4.1(e)**, darker contrasted region e1 is fluorine rich (F - 53.9, C - 8.7 wt%), lighter contrasted region e2 is carbon rich (F - 28.6, C - 69.8 wt%), and Cu deposited region e3 is Cu rich (Cu - 83.4, F - 8.4, C - 6.0 wt%). The proximity and overlap of Cu deposit region e3 with fluorine rich region e1 suggests that Cu ions preferentially diffuses across the fluorine rich spots and charge transfers to form Cu deposits. This is apparent across the entire set of electrolyte chemistries studied as shown in **Figure 4.1(C) (e-h)** and further analyzed in **Supplementary Figure 4.1(e-h)**. In the case of the SEI formed by fluorinated electrolytes (**Figure 4.1(C)(g-h)** & **Supplementary Figure 4.1(g-h)**), the Cu deposits are well distributed across the surface. It can be speculated that the fluorine rich regions have lower energy barrier to ion transport, thereby enabling metal transport and reduction through them. Enhancing the coverage of the surface by the fluorine rich regions can enable uniform and facile nucleation of metal.

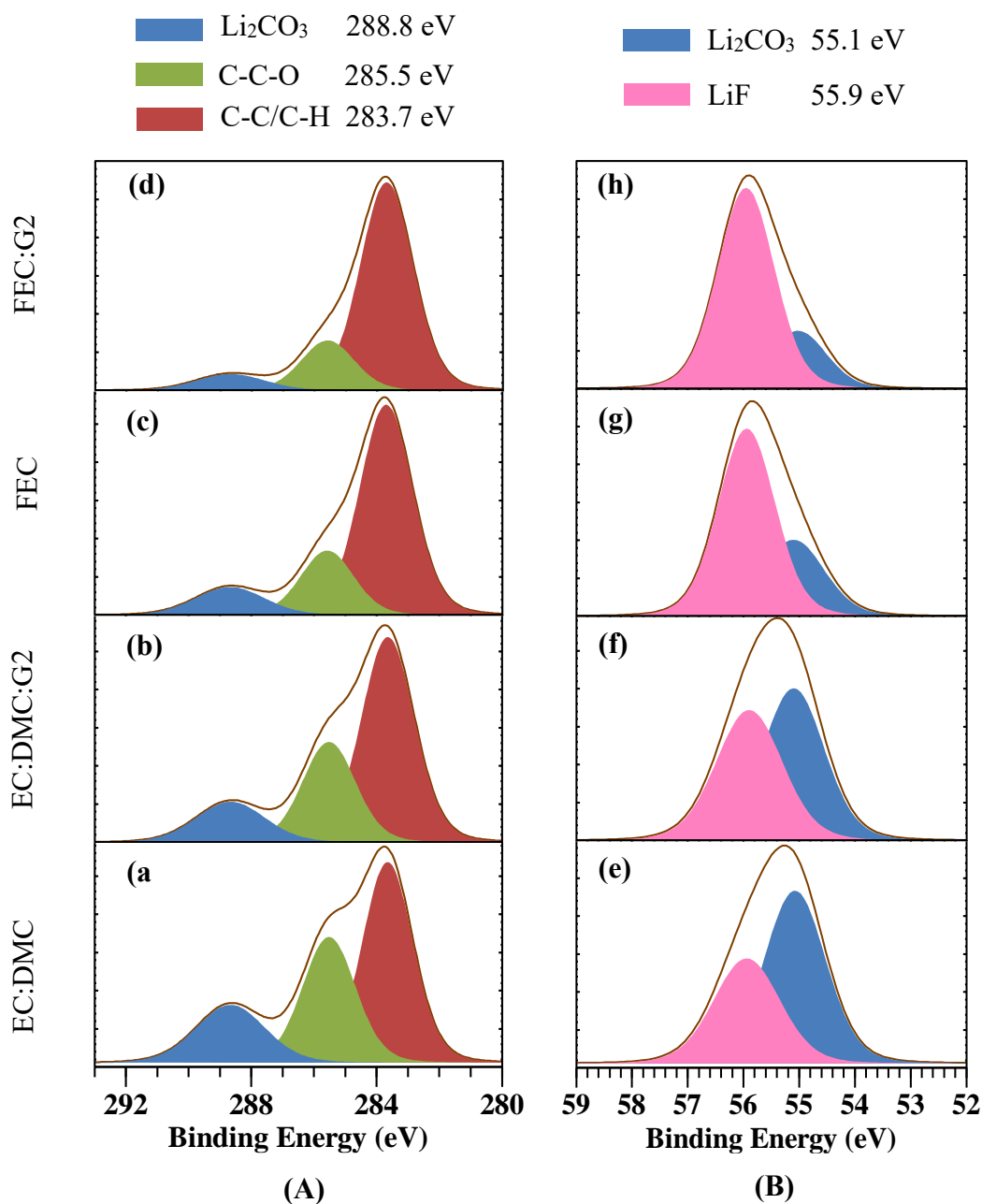


Figure 4.2. Interfacial chemistry of Lithium electrodeposits formed at low capacities. **(A)** C 1s and **(B)** Li 1s high-resolution spectra of SEI layer on Li electrodeposits formed at current density of 1 mA/cm^2 for areal capacity of 0.05 mAh/cm^2 from electrolytes of different compositions **(a,e)** EC:DMC (50:50), **(b,f)** EC:DMC:G2 (45:45:10), **(c,g)** FEC, **(d,h)** FEC:G2 (90:10), each containing 1M LiPF_6 salt.

The SEI covered substrates were further subjected to galvanostatic deposition of metallic Li from the corresponding set of electrolytes at current density of 1 mA/cm^2 and capacity of 0.05 mAh/cm^2 . The small areal capacity equivalent to electrodeposit film thickness of 300 nm if Li electrodeposits have the same density as that of bulk Li metal. The voltage response profiles are shown in **Figure 4.1(B)** and ex-situ postmortem analysis of the substrates are shown in **Figure 4.1(C)(i-l)**. The overpotential curves (voltage response curves) across all electrolytes show a typical behavior of voltage dip due to any remnant SEI formation, voltage peak at about capacity of 0.006 to 0.012 mAh/cm^2 due to metal nucleation, and voltage plateauing due to subsequent electroplating of ions onto the nuclei in the growth phase (4). The areal capacity and overpotential at metal nucleation are observed to vary with the electrolyte composition (0.012 mAh/cm^2 , 0.009 mAh/cm^2 , 0.008 mAh/cm^2 , 0.006 mAh/cm^2 , and 0.31 V , 0.29 V , 0.28 V , 0.25 V , for EC:DMC, EC:DMC:G2, FEC, FEC:G2 respectively) i.e. both values are lower for the fluorinated electrolyte than the carbonate electrolyte, and also addition of diglyme further diminishes them. The decrease in the areal capacity and overpotential of nucleation across the electrolytes suggests that a facile SEI is enabling lower diffusion and charge transfer energy barrier for the electrodeposition of the Li ions. Significant change in morphology of electrodeposits is also observed across the electrolytes as apparent from **Figure 4.1(C)(i-l)**. The carbonate electrolyte (EC:DMC) forms distinct three-dimensional (3-D) spherical structures of radius $1.8 \text{ }\mu\text{m}$ on the stainless steel substrate (**Figure 4.1(C)(i)**). Addition of diglyme diminishes the sizes to $1.1 \text{ }\mu\text{m}$ and increases the areal density of these electrodeposits (**Figure 4.1(C)(j)**), most likely due to increase in spatial homogeneity of the SEI as previously observed. This

can be rationalized as follows: The diglyme added carbonate electrolyte (EC:DMC:G2) forms a more spatially homogeneous SEI than the base carbonate electrolyte (EC:DMC) as previously discussed in **Figure 4.1(C)(a-b)**. A spatially homogeneous SEI imparts a higher number of nucleation points for the incoming Li ions, thereby forming a higher number of smaller nuclei all over the surface for equal capacities of electrodeposition. This effect of spatial homogeneity on the morphology of Li electrodeposits is even more apparent in the case of fluorinated electrolytes (FEC, FEC:G2) as shown in **Figure 4.1(C)(k-l)**. The electrodeposits are planar (2-D), film-like, and entirely cover the surface, rendering the bright stainless-steel background virtually invisible.

To identify root causes for our observations, X-ray photoelectron spectroscopy (XPS) was performed to investigate the surface chemistry of SEI formed in the early stages of Li electrodeposition (i.e., capacity of 0.05 mAh/cm²) across the set of electrolyte chemistries being studied. The results are reported in **Supplementary Figure 4.2(a)**, **Supplementary Table 4.1(a)**, **Supplementary Table 4.2(a)**, and **Figure 4.2**. Distinct changes in the chemical composition of the SEI can be readily observed. The survey spectra in **Supplementary Figure 4.2(a)** shows multiple atomic peaks of which lithium 1s (55.5 eV), carbon 1s (284.5 eV), oxygen 1s (531.6 eV), phosphorous 2p (133 eV), and fluorine 1s (684.9 eV) are relevant. It is observed that the at% of fluorine increases while the at% of carbon and oxygen decreases across the electrolyte chemistries. The fluorinated electrolytes (FEC, FEC:DG) show higher percent of fluorine and lower percent of carbon and oxygen than the carbonate electrolytes (EC:DMC, EC:DMC:G2). For e.g. the SEI of FEC has F(28.46%), C(19.96%), O(12.55%) compared to F(20.1%), C(29.96%), O(22%) of EC:DMC. Also, electrolytes with diglyme additives show a

similar trend in at% of fluorine, carbon, & oxygen when contrasted to their counterparts (w/o diglyme additive). For e.g. the SEI of EC:DMC:G2 has F(24.61%), C(23.02%), O(12.98%) compared to F(20.1%), C(29.96%), O(22%) of EC:DMC. It is noteworthy that the fluorine-to-carbon and fluorine-to-oxygen ratio increases about two-fold and three-fold respectively when comparing the diglyme added fluorinated electrolyte (FEC:G2) with the base carbonate electrolyte (EC:DMC).

A closer look at the high-resolution spectra of carbon and lithium is necessary to further understand the nature of bonding between carbon, oxygen, fluorine, and lithium in the SEI that might produce these observations. **Figure 4.2** reports the high-resolution spectra of carbon (C 1s) and lithium (Li 1s) in the SEI, and the results are tabulated in **Supplementary Table 4.1(a)** and **Supplementary Table 4.2(a)**. There are three distinct peaks observed in the C 1s spectra: Li_2CO_3 at 288.8 eV, C–C–O at 285.5 eV, and C–C/C–H at 283.7 eV (**Figure 4.2A**). The Li_2CO_3 and C–C–O peaks are diminished and the C–C/C–H peak is enhanced across the set of electrolyte chemistries. For e.g. comparing the two ends of the electrolyte spectrum, EC:DMC has 19.17% Li_2CO_3 , 32.12% C–C–O, 48.62% C–C/C–H compared to 7.66% Li_2CO_3 , 17.89% C–C–O, 74.45% C–C/C–H of FEC:G2 (**Supplementary Table 4.1(a)**). Also, there are two distinct peaks observed in the Li 1s spectra: Li_2CO_3 at 55.1 eV and LiF at 55.9 eV (**Figure 4.2B**). The LiF peak is enhanced while the Li_2CO_3 peak is diminished across the set of electrolyte chemistries studied. For e.g. comparing the two ends of the electrolyte spectrum again, EC:DMC has 60.42% Li_2CO_3 , 39.58% LiF compared to 22.42% Li_2CO_3 , 77.58% LiF of FEC:G2 (**Supplementary Table 4.2(a)**). The above observations can be rationalized as follows: The fluorinated electrolyte (FEC)

decomposes to form LiF and oxygen free ethylene species (C-C) as major products, which may electropolymerize at the reducing anode potentials to form a fluorinated SEI enriched in polyene (-C-C-) networks. The SEI formed is deficient in carbonates, polyethers, & alkoxides (for e.g., Li_2CO_3 , ROCO_2Li , ROLi , $-\text{CH}_2\text{O}-$) like oxygen rich species. This observation is consistent with previous reports (29,30,31). Further, the diglyme additive, being a polyether(C-C-O), solubilizes the oxygen rich carbon species (for e.g., Li_2CO_3 & ethylene oxide (C-C-O) rich species) while unaffected the polyene species (-C-C-) in the SEI, thereby enhancing the fluorine and ethylene content of the SEI. The principle of solubility here is based on “Like dissolves like”. For e.g., Li_2CO_3 is determined to be about ten times more soluble than LiF in diglyme as shown in **Supplementary Figure 4.3(b)**. Therefore, the SEI formed in FEC:G2 is observed to have the highest percentage enrichment in fluorine and ethylene linkages across the electrolyte chemistries studied.

Electrochemical impedance spectroscopy and fast cyclic voltammetry performed on the Li electrodeposits formed at low capacities (0.05 mAh/cm^2) on the stainless-steel reveals transport and reaction characteristics of Li ions in the SEI as shown in **Figure 4.3** and **Supplementary Figure 4.4**. All Nyquist plots (**Figure 4.3(a)**) show a depressed semicircle with a Warburg region, which can be fitted to the model in **Supplementary Figure 4.4(a)**, and the extracted data is plotted in **Supplementary Figure 4.4 (b)**. The fluorinated electrolyte (FEC) shows lower SEI and charge transfer (CT) resistances than the carbonate electrolytes (EC:DMC). The addition of diglyme additive to these electrolytes further lowers the resistances, with the interphase formed in FEC:G2 having lowest resistance of all i.e. FEC:G2 ($98.4 \text{ } \Omega/\text{cm}^2$ (SEI), $450.5 \text{ } \Omega/\text{cm}^2$

(CT)) has almost two-fold lower resistances compared to EC:DMC (158.7 Ω/cm^2 (SEI), 82.6 Ω/cm^2 (CT)). Further, the ion diffusivity (D_s) of the SEI, determined from the Warburg region, is shown in **Figure 4.3(c)**. The result indicates that D_s increases four-fold across the set of electrolyte chemistries i.e., the D_s values are as follows: $1.19 \times 10^{-17} \text{ m}^2/\text{s}$ (EC:DMC), $3.02 \times 10^{-17} \text{ m}^2/\text{s}$ (EC:DMC:G2), $3.29 \times 10^{-17} \text{ m}^2/\text{s}$ (FEC), and $4.7 \times 10^{-17} \text{ m}^2/\text{s}$ (FEC:G2). Recent modeling studies have shown the SEI diffusivity (32-35) to be anywhere in between 10^{-16} to $10^{-26} \text{ m}^2/\text{s}$ with values ($10^{-16} \text{ m}^2/\text{s}$) reported for a purely LiF interface. Fast scan CV performed to probe the reaction kinetics of the SEI shows a similar trend in exchange current density of the electrolytes (**Figure 4.3(b)**, **Figure 4.3(c)**). The exchange current density (i_o) increases about four-fold across the electrolyte spectrum i.e., $0.09 \text{ mA}/\text{cm}^2$ (EC:DMC), $0.14 \text{ mA}/\text{cm}^2$ (EC:DMC:G2), $0.30 \text{ mA}/\text{cm}^2$ (FEC), and $0.39 \text{ mA}/\text{cm}^2$ (FEC:G2). These measurements are in accord with the observed lowering of nucleation overpotential (**Figure 4.1(B)**), SEI & CT resistance (**Supplementary Figure 4.4(b)**), as an increased ion diffusivity (D_s) and exchange current density (i_o) suggests facile transport and reduction of Li^+ at the interface. A higher surface diffusivity indicates relatively easier 2D migration of Li ions in the fluorinated SEI, promoting more spread-out/delocalized electrodeposition as shown in **Figure 4.1(C)(k-l)**.

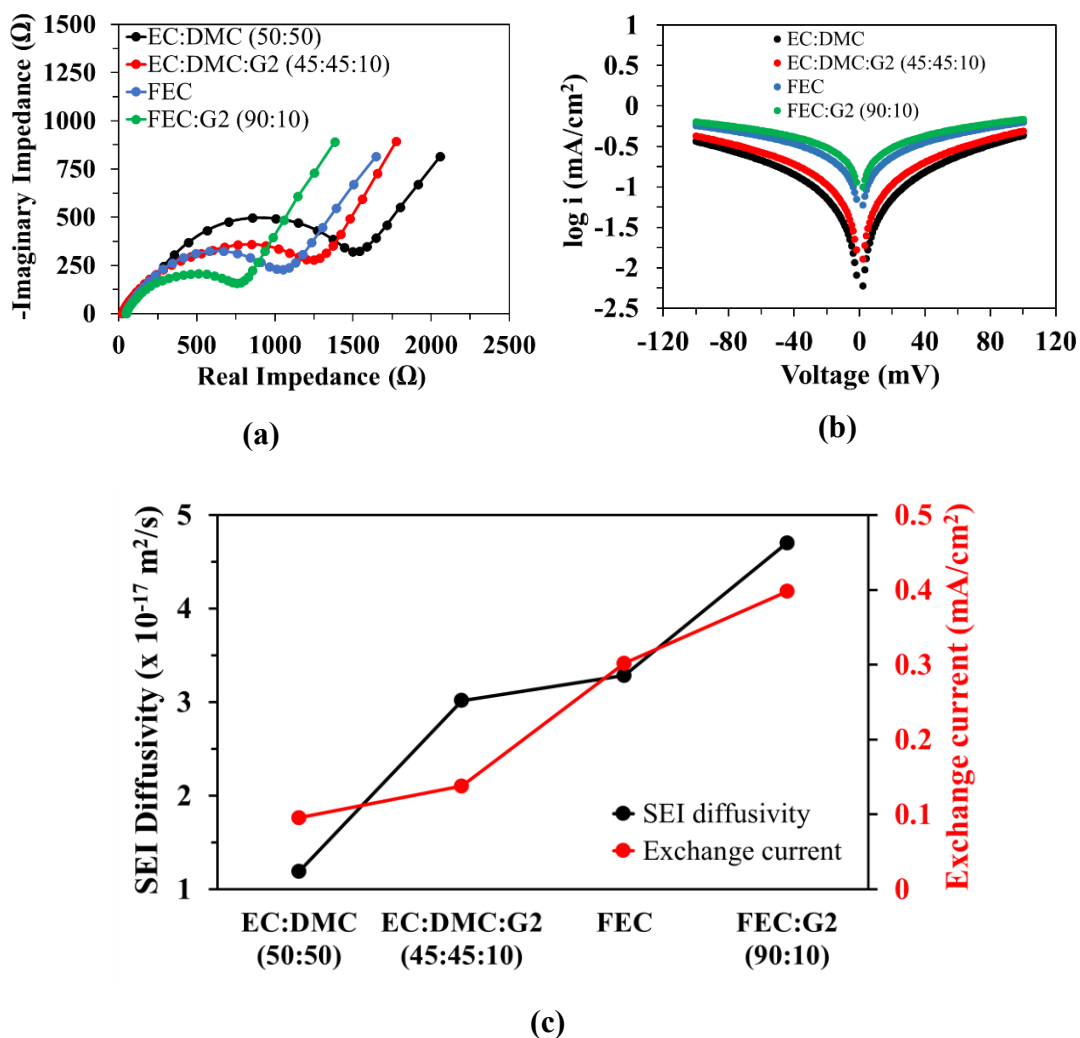
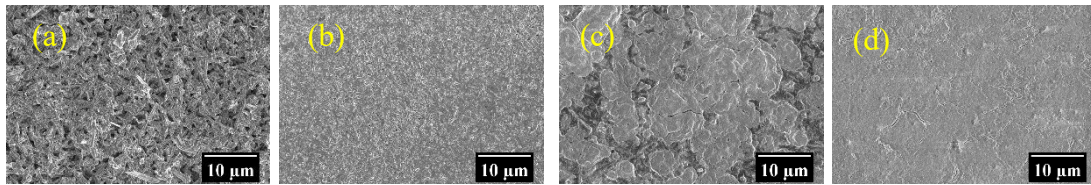


Figure 4.3. Interfacial transport and reaction kinetics of Lithium electrodeposits formed on stainless-steel in electrolytes of different chemistries at current densities of $1 \text{ mA}/\text{cm}^2$ and low capacities of $0.05 \text{ mAh}/\text{cm}^2$. **(a)** Impedance plots (Nyquist) of Li electrodeposits obtained via Electrochemical Impedance spectroscopy. **(b)** Tafel plots for electrodeposited Li obtained via fast CV (i.e., $100 \text{ mV}/\text{s}$ in the range 100 mV to -100 mV). The exchange current was calculated by fitting linear region of the plots (i.e., -80 mV to -40 mV and 40 mV to 80 mV). **(c)** Plot of SEI ion diffusivity (as extracted from impedance plots) and exchange current density (as extracted from tafel plots). The electrolytes are EC:DMC (50:50), EC:DMC:G2 (45:45:10), FEC, FEC:G2 (90:10), each containing 1 M LiPF_6 salt.

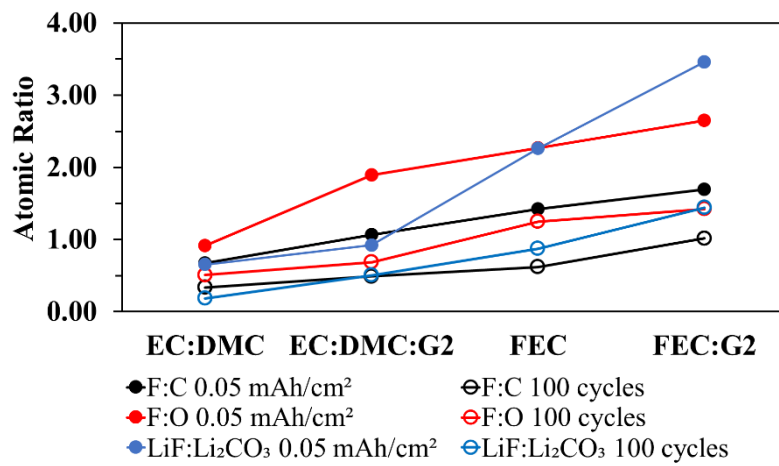
The analysis above provides insights into the role of surface homogeneity, chemistry, and energetics on the uniform plating of Li at low capacities. However, it remains to be determined whether the surface energetics, chemical nature, and uniform morphology observed at low capacities translates to similar morphology and energetics at later stage of charge/discharge cycling at higher capacities relevant for applications in practical LMBs. In this context, we study the morphology, chemical composition, and surface energetics of electrodeposited lithium after a number of charge/discharge cycles (**Figure 4.4, Figure 4.5**). We further investigate the electrochemical reversibility of Li electrodeposits via coulombic efficiency and galvanostatic stripping/plating of symmetric Li cell (**Figure 4.6**). Finally, the electrochemical performance of full cells containing thin Li metal ($\sim 50 \mu\text{m}$) paired against a NCM cathode with the electrolytes is evaluated (**Figure 4.7**).

Li was galvanostatically plated/stripped for 100 cycles onto polished stainless substrate at current density of 1 mA/cm^2 from liquid electrolytes of different compositions, for higher capacity of 1 mAh/cm^2 , i.e., about an order of magnitude higher than the low capacity of 0.05 mAh/cm^2 . **Figure 4.4(A)** shows a panel of ex-situ SEM images of the electrodeposits. It can be observed that the morphology of Li electrodeposits is entwined wire-like mossy dendrites for EC:DMC (**Figure 4.4(A)(a)**) contrasted to relatively smooth morphology observed for EC:DMC:G2 (**Figure 4.4(A)(b)**). Similar contrasting observations can be made for FEC (**Figure 4.4(A)(c)**) and FEC:G2 (**Figure 4.4(A)(d)**) i.e. FEC:G2 case has a more uniform morphology. In other words, the entwined wire-like deposits observed for EC:DMC case have no resemblance to have grown out of the early stage electrodeposits (**Figure 4.1(C)(i)**), while the smooth morphology observed

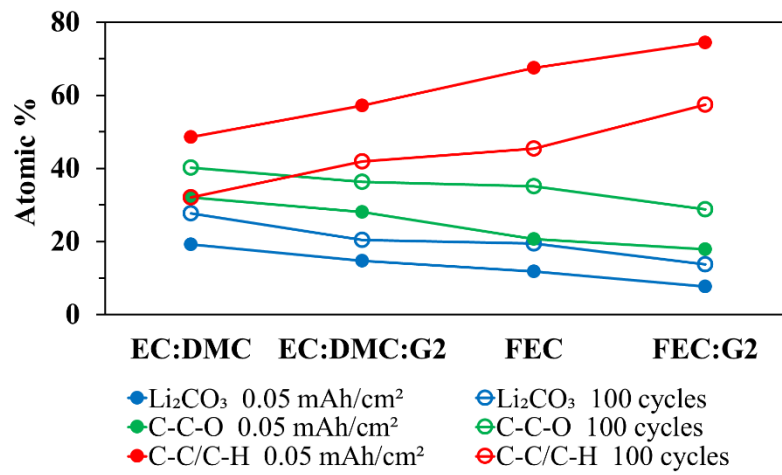
FEC:G2 case retains the spatial uniformity in electrodeposit morphology observed at lower capacities (**Figure 4.1(C)(I)**). The degree of morphological uniformity increases across the electrolyte spectrum as shown in **Figure 4.4(a-d)**. The chemical composition of the SEI after cycling (100 cycles) is examined via XPS survey spectra (**Supplementary Figure 4.2**) along with high-resolution C 1s and Li 1s spectra (**Supplementary Figure 4.5, Supplementary Table 4.1, Supplementary Table 4.2**). For brevity of discussion, the results are briefly summarized and contrasted to that of lower capacity (0.05 mAh/cm², early stage of deposition) in **Figure 4.4B** and **Figure 4.4C**. Similar to the lower capacity case, the F:C and F:O ratio increases about 200%, with increase in ethylene -C-C-/C-H linkage (from 32.12 to 57.46%), and decrease in ethylene oxide C-C-O (from 40.22 to 28.76%) and Li₂CO₃ (from 27.67 to 13.78%) across the range of electrolyte chemistry (EC:DMC to FEC:G2) as shown in **Figure 4.4B** and **Figure 4.4C**. It is also noteworthy that the LiF:Li₂CO₃ ratio increases about 700% across the electrolyte spectrum. Crudely, this suggests that the fluorine enriched polyene SEI formed at lower capacities is retained in its nature of chemical composition during the cycling of electrodeposited Li. It is also observed that the cleaning action of diglyme dissolving the oxygen rich carbonaceous species at the interface lasts throughout the cycle life, further preserving the fluorine enriched interface.



(A)



(B)



(C)

Figure 4.4. Effect of electrolyte chemistry on the morphology and interfacial chemistry of Li electrodeposits on stainless steel substrate after 100 stripping/plating cycles at 1 mA/cm² and 1 mAh/cm². **(A)** Ex-situ SEM images of the electrodeposited Li morphology after 100 cycles for different electrolytes **(a)** EC:DMC (50:50), **(b)** EC:DMC:G2 (45:45:10), **(c)** FEC, **(d)** FEC:G2 (90:10). **(B)** Plot of atomic ratio of Fluorine to Carbon, Fluorine to Oxygen, and Lithium Fluoride to Lithium Carbonate of the SEI formed at 0.05 mAh/cm² and after 100 cycles for different electrolytes **(C)** Plot of atomic % of components of Carbon 1s high resolution spectra of the SEI formed at at 0.05 mAh/cm² and after 100 cycles for different electrolytes. Each of the electrolytes contain 1M LiPF₆ salt.

Electrochemical impedance spectroscopy performed on plated/stripped Li (1 mA/cm², 1 mAh/cm²) on stainless steel for the set of electrolyte composition (EC:DMC to FEC:G2) is shown in **Supplementary Figure 4.6**. The impedance loops in Nyquist plots are relatively smaller than that of lower capacity i.e., compare the Nyquist plots in **Supplementary Figure 4.6(a)** with **Figure 4.3(a)**; which indicates lower SEI and charge transfer (CT) resistance for electrodeposits of Li cycled at higher capacities. Consistent with our previous observations, the FEC:G2 case shows the lowest SEI and charge transfer (CT) resistance of all electrolytes (**Supplementary Figure 4.6(b)**). A study of energy barriers to Li ion movement at the interface can aid our understanding of underlying transport-reaction kinetics of the SEI formed by different electrolytes. To this end, we perform temperature dependent impedance spectroscopy of Li electrodeposits formed on stainless steel at lower capacity (0.05 mAh/cm²) and after 100 cycles capacity (1 mAh/cm²). The resulting SEI and CT resistances (R) are fitted to Arrhenius equation, $k = 1/R = A \exp(-Ea/RT)$, where k (1/s) is the rate constant, A

(1/s) is the pre-exponential factor, E_a (J/mol) is the activation energy, R (8.314 J/(mol K)) is the gas constant, and T (K) is the temperature as shown in **Supplementary Figure 4.7**. The calculated activation energies, E_a and pre-exponential factor, $\ln(A)$ are presented in **Figure 4.5** and **Supplementary Table 4.3**. The activation energy of SEI and CT kinetics follows a decreasing trend across the set of electrolytes at all capacities of electrodeposition/cycling (0.05 mAh/cm², 100 cycles). For e.g. the E_a of the SEI at 0.05 mAh/cm² is 52.42 kJ/mol (EC:DMC), 47.61 kJ/mol (EC:DMC:G2), 38.95 kJ/mol (FEC), & 37.01 kJ/mol (FEC:G2). It is noted that small changes in activation energy can produce considerable effects on the kinetics, as E_a is scaled exponentially in the Arrhenius equation. Cycling at higher capacities increases the activation energy i.e., E_a of 100 cycles > 0.05 mAh/cm². However, the E_a of SEI and CT kinetics is quite similar across 0.05 mAh/cm² and 100 cycles for FEC:G2 (i.e., at 0.05 mAh/cm², the E_a is 37.01 kJ/mol (SEI), 37.99 kJ/mol (CT) compared to 38.12 kJ/mol (SEI), 38.99 kJ/mol (CT) at 100 cycles) contrasted to the large difference seen in the case of EC:DMC (i.e., at 0.05 mAh/cm², the E_a is 52.42 kJ/mol (SEI), 56.26 kJ/mol (CT) compared to 59.64 kJ/mol (SEI), 63.87 kJ/mol (CT) at 100 cycles). Similarly, the E_a of SEI and CT kinetics is more similar across 0.05 mAh/cm² and 100 cycles for the diglyme added one than the base electrolyte (i.e. compare EC:DMC:G2 vs. EC:DMC or FEC:G2 vs. FEC) as shown in **Figure 4.5**. This can be rationalized as follows: The fluorine enriched polyene SEI (FEC:G2) having higher ion diffusivity and exchange current, and chemically preserved through the plating/stripping cycles (as previously observed), shows similar activation energies across the capacities. The effect of diglyme on cleaning the interphase is crucial in preserving the kinetics across cycling

life of Li metal. Fairly similar observations can be made from the trend of the pre-exponential factor ($\ln(A)$) across the set of electrolytes as shown in **Supplementary Table 4.3**. The $\ln(A)$ decreases across the set of electrolytes at all stages of deposition i.e., at 0.05 mAh/cm², $\ln(A)$ of SEI kinetics of EC:DMC is 16.4 compared to 10.6 of FEC:G2. The pre-exponential factor, A is related to the entropy of activation for first order kinetics by the transition state theory (37-39) as: $A = \frac{k_B T e}{h} \exp(\Delta S/R)$, where k_B (1.38 x 10⁻²³ J/K) is the Boltzmann constant, T (K) is the temperature, e is 2.72, h (6.62 x 10⁻³⁴ m² kg/s) is the Planck constant, ΔS (J/K) is the change in entropy of activation, and R (8.314 J/(mol K)) is the gas constant. The calculated ΔS is negative for all electrolytes as shown in **Supplementary Table 4.3**, suggesting that the entropy decreases during the transport-reaction kinetics at the interphase. Moreover, the decreasing trend of $\ln(A)$ previously observed, results in a larger negative ΔS across the set of electrolytes. For e.g., the FEC:G2 electrolyte shows the largest negative ΔS of any electrolytes i.e., -165.1 J/K (SEI) & -174.1 J/K (CT) at 0.05 mAh/cm², which indicates the ionic motions in its interphase are less random (i.e. more correlated) than other electrolytes. Comparing across the capacities (i.e., 0.05 mAh/cm² and 100 cycles), each electrolyte shows an increase in ΔS , quite like the increase in Ea previously observed. For e.g., ΔS of SEI kinetics changes from -116.8 J/K at 0.05 mAh/cm² to -85.2 J/K at 100 cycles for the EC:DMC electrolyte. Therefore, it is reasoned that the interphase of all electrolytes shows signs of impeding kinetics and more randomized motion of Li ions with the progression of plating/stripping cycles.

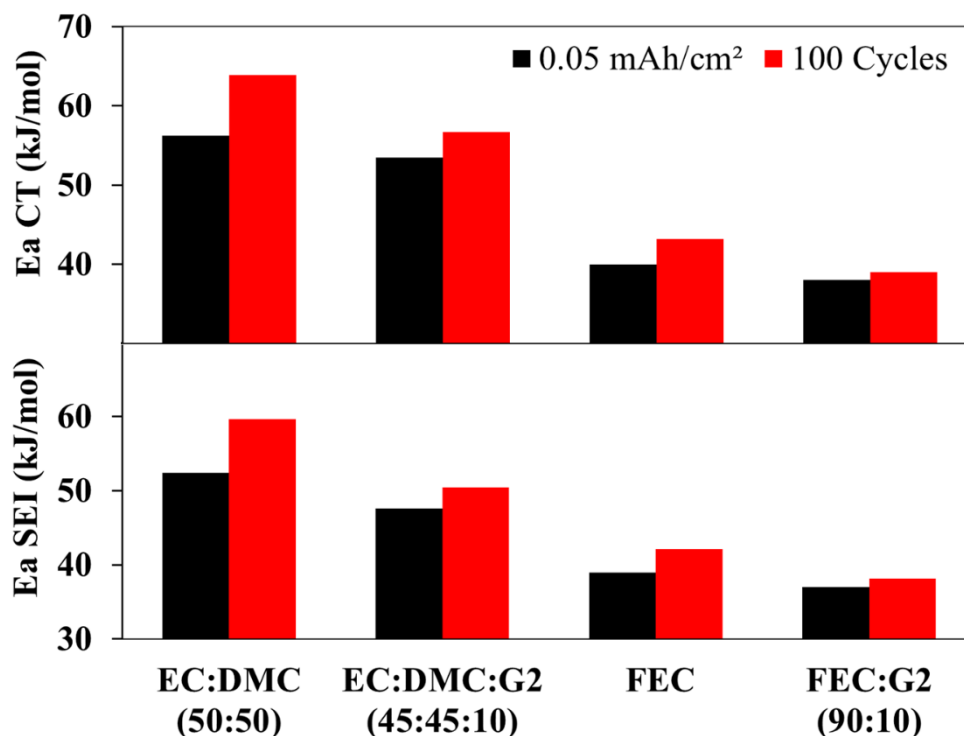
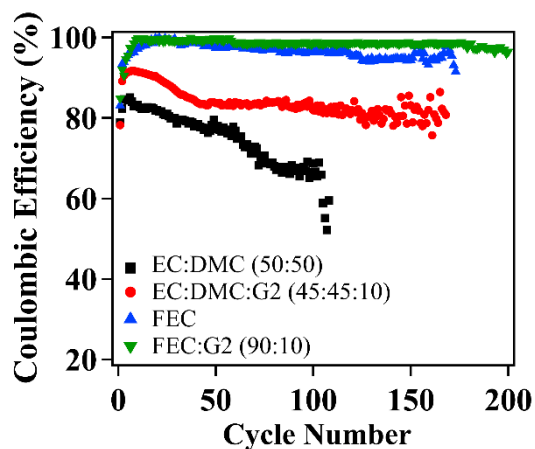


Figure 4.5. Effect of electrolyte chemistry on the activation energies (SEI, CT) of the interphase of Li electrodeposits on stainless steel substrate at 0.05 mAh/cm², and after 100 stripping/plating cycles at 1 mA/cm² and 1 mAh/cm². The electrolytes are EC:DMC (50:50), EC:DMC:G2 (45:45:10), FEC, FEC:G2 (90:10), each containing 1M LiPF₆ salt. The activation energies are obtained through Arrhenius fitting of SEI and CT resistances at different temperatures.

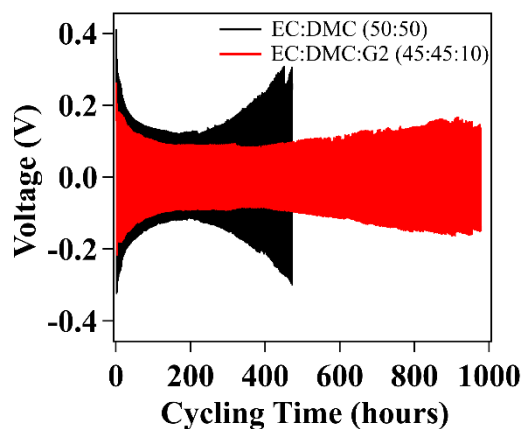
The electrochemical reversibility and cyclability of Li electrodeposits under the influence of the different electrolytes is shown in **Figure 4.6**. Coulombic efficiency (CE) tests performed in electrochemical cells (Li||SS) at a current density of 1 mA/cm² and capacity of 1 mAh/cm² (**Figure 4.6(a)**) corroborate the previous inferences. The CE increases across the set of electrolytes i.e. at 100 cycles, the CE follows the order:

EC:DMC (66.7%) < EC:DMC:G2 (81.2%) < FEC (96.5%) < FEC:G2 (98.8%). Further, the diglyme added fluorinated electrolyte (FEC:G2) shows consistent CE of 97 – 99.5% through its cycle life up to 200 cycles, contrasted to oscillating/drastically dropping CE of other electrolytes. For e.g., the CE of the regular carbonate electrolyte oscillates between 64 – 70% around 80 – 100 cycles, before drastically dropping to below 55% towards the end of its cycle life. While CE is a widely used test to assess the electrochemical reversibility of metals in asymmetric cells (for e.g., Li||SS), the information obtained from it about the dendritic growth of Li metal and its effect on cycle life is rather limited. In other words, different tests are needed to evaluate the interaction of Li anode with electrolyte-separator membrane during cycling in perpetuating short-circuiting of the cell. To this end, we perform galvanostatic plating stripping experiments of Li anode in symmetric cells (Li||Li) under the influence of different electrolytes at a similar current density of 1 mA/cm² and capacity of 1 mAh/cm². The resulting voltage profiles over the cycle life of cells is shown in **Figure 4.6(b)** and **Figure 4.6(c)**, and further elaborated (plotted in time intervals) in **Supplementary Figure 4.8**. Two observations can be easily made (i) the diglyme additive enhances the cycle life (time to short circuit) of the base electrolyte by almost two fold i.e., comparing EC:DMC (470 hrs) with EC:DMC:G2 (980 hrs) or FEC (1230 hrs) with FEC:G2 (2480 hrs). Also, the cycle life increases across the spectrum of electrolytes. (ii) the voltage window of cycling is lower for the diglyme added electrolytes when compared to the base electrolytes, moreover the voltage window decreases across the electrolytes. The voltage window is also arch shaped (U shape), with higher voltages recorded during initial cycles, followed by a plateau during

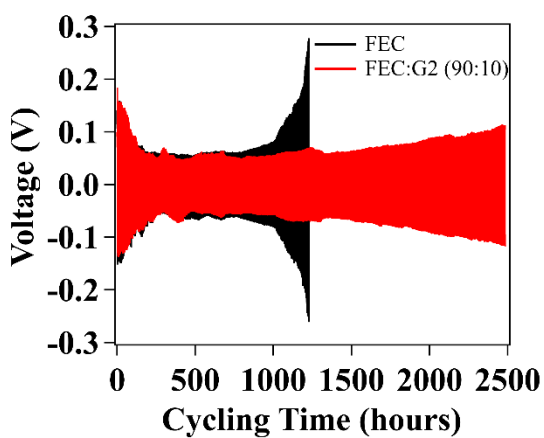
intermediate cycles, and again increase in voltages towards the end of cycle life. This is further elaborated in **Figure 4.6(d)**. The voltage (overpotential) is recorded at the beginning of plating cycles for different electrolytes at different times of cycle life. The arch shape of the voltage and the decrease in voltage window across all electrolytes is even more apparent, for e.g., considering the EC:DMC case, the potentials are 0.329, 0.135, 0.24 V at 10, 100, 400 cycles, respectively. We speculate that the arch shape is a result of (i) higher overpotentials of plating during initial cycling stage due to the ion transport resistance offered by the existing native SEI on Li anode (ii) followed by the plateau region most likely due to facile ion transport through the newly formed SEI (iii) and subsequent increase in overpotential towards the end of cycle life due to increased resistance to ion transport, a result of thickening SEI formed by degradation products of electrolyte and dead lithium in repeated plating/stripping (40-42). The lowest overpotential and longest voltage plateau shown by FEC:G2 electrolyte proves the efficacy of a preserved fluorine enriched SEI in promoting long-lasting ion transport. The CE and galvanostatic stripping plating cycle life evaluated over four coin cells are summarized in **Figure 4.6(e)**. The EC:DMC case shows bigger error bars of CE and cycle life contrasted to other electrolytes, owing to the uncertainty of reversibility and cell failure in the carbonate electrolyte lacking advantages of a facile SEI.



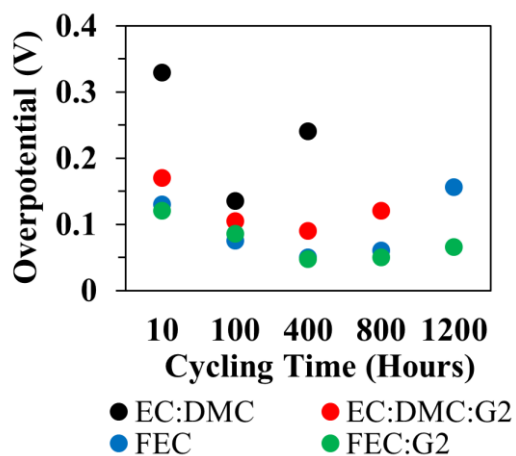
(a)



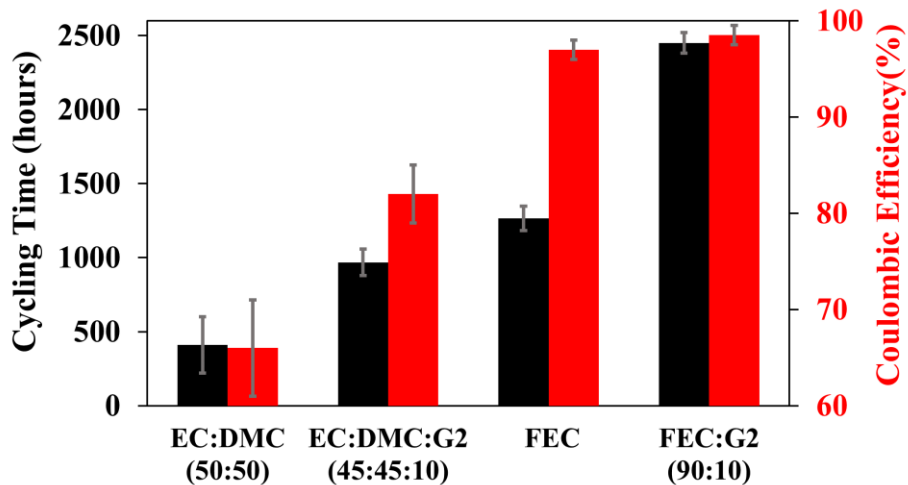
(b)



(c)



(d)



(e)

Figure 4.6. Reversibility and cyclability of Li electrodeposits formed under the influence of electrolyte of different chemistries. **(a)** Coulombic efficiency of electrodeposited Lithium on polished stainless steel for maximum of 200 cycles at 1 mA/cm² and 1 mAh/cm². Galvanostatic plating stripping voltage profile of symmetric Li anode at a current density of 1 mA/cm² and capacity of 1 mAh/cm² in **(b)** EC:DMC & EC:DMC:G2 **(c)** FEC & FEC:G2. **(d)** Nucleation overpotential of different electrolytes at different cycling hours. **(e)** Plot of symmetric cell cycling time and coulombic efficiency (at 100 cycles) for average of 4 coin cells. The standard deviation of the data is represented through error bars. The electrolytes are EC:DMC (50:50), EC:DMC:G2 (45:45:10), FEC, FEC:G2 (90:10), each containing 1M LiPF₆ salt.

The suitability of the electrolytes in LMB's is evaluated by performing voltammetry, floating tests, & full cell electrochemical cycling tests as shown in **Supplementary Figure 4.9** and **Figure 4.7**. Linear scan voltammetry performed at scan rates of 2 mV/s and upto 6.5 V show oxidation (i.e., higher current) of all electrolytes above 5V (**Supplementary Figure 4.9**). Noticeably, a strong oxidation peak is observed around 5.7 – 5.8 V for the carbonate electrolytes with & w/o diglyme (EC:DMC & EC:DMC:G2), indicating that the regular carbonates (EC:DMC) have lower oxidative stability compared to fluorinated ones (FEC) (10,43,44). A more rigorous test of oxidative stability is the floating test, in which the electrolytes are subjected to long time steps (10 hours) of increasing potential (4.3 – 5V) in Li||NCM cells to study the evolution of current (leakage current) as shown in **Figure 4.7(a)**. All the electrolytes show oxidative stability below 4.5 V. The leakage currents increase across all electrolytes above 4.5V, with being strikingly high for the diglyme added ones

(EC:DMC:G2 & FEC:G2), conceivably due to low oxidative stability of diglyme (45). The results of the two aforementioned procedures establish the voltage range of operation for the electrolytes to be below 4.5 V in a LMB.

The electrochemical performance of the electrolytes is evaluated in LMB's containing thin Lithium (50 μm) anode paired against a NCM 622 cathode of areal capacity 2 mAh/cm^2 . The cells are cycled under CC-CV charge mode (constant current of 0.5 C to 4.2 V and constant voltage until the current decreases to 0.2 C) and CC discharge mode at 0.5 C. The resulting charge discharge voltage profiles are reported in **Supplementary Figure 4.10**, and the Coulombic efficiencies (CE) and discharge capacity retention profile are summarized in **Figure 4.7(b)**. The FEC:G2 case shows the highest average CE of 99.85% (5-200 cycles) and discharge capacity retention of 74% (compared to 5th cycle) after 200 cycles. The EC:DMC, EC:DMC:G2, and FEC electrolytes show considerably lower CE and discharge capacity retention. Strikingly, the CE and discharge capacity retention of EC:DMC:G2 is greater than that of FEC case. This measurement is in clear contrast to previously conducted CE study in Li||SS cells (**Figure 4.6(a)**) and oxidative stability studies in **Supplementary Figure 4.9 & Figure 4.7(a)**. We envisage the discrepancy is likely due to beneficial action of the diglyme on the cathode electrolyte interface (CEI) of NCM cathode. Overall, the electrochemical performances of LMB's are significantly improved through the utilization of diglyme enriched fluorinated electrolytes.

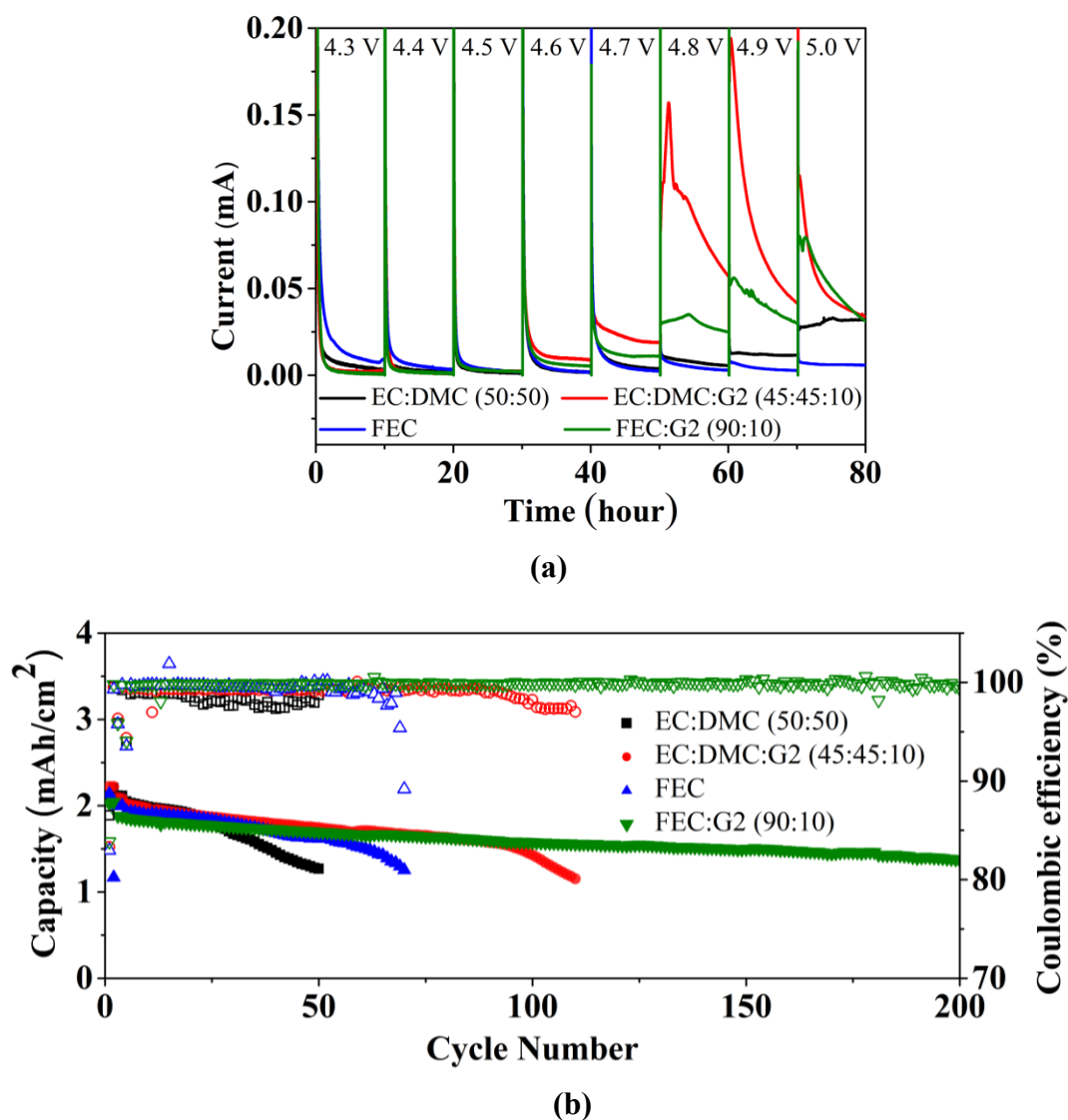


Figure 4.7. Oxidative stability and electrochemical performance of electrolytes in Li||NCM622 cells with thin Li anode (50 μm) and NCM622 cathode (2mAh/cm²). **(a)** Electrochemical floating test of different electrolytes in Li||NCM622 cells. **(b)** Discharge capacity retention and coulombic efficiency over 200 cycles for Li||NCM cells with thin lithium anode (50 μm) and NCM622 cathode (2 mAh/cm²). The cells are cycled under CC-CV charge mode (constant current of 0.5 C to 4.2 V and constant voltage until the current decreases to 0.2 C) and CC discharge mode at 0.5 C. 1C=(2mA/cm²). The electrolytes are EC:DMC (50:50), EC:DMC:G2 (45:45:10), FEC, FEC:G2 (90:10), each containing 1M LiPF₆ salt.

4.4 Conclusion

In summary, we studied the role of carbonate and fluorinated electrolytes with/without ethers as additive on the morphology, chemical composition, interfacial energetics, and electrochemical reversibility of Li anodes during early stages of electrodeposition, as well as later stages of deep cycling of Li anode. Aptly designed experiments shed light into the role of surface energetics (transport-reaction kinetics) of the SEI at different stages of cycle life of Li electrodeposits. The chemical nature of the SEI is deliberately manipulated via electrolytes of contrasting chemistries (carbonate vs fluorinated) to study the physico-chemical nature of Li electrodeposition. The transport-reaction kinetics of the SEI is demonstrated to play an important role in Lithium plating and can be modulated by rational choice of electrolyte components. Furthermore, we demonstrated that incorporation of ether-based additive (diglyme) has a beneficial “cleaning” effect on Li electroplating and is necessary for preserving the surface energetics (transport-reaction kinetics), chemical nature, and uniform morphology observed at initial stages of electroplating through deep cycling of Li anode. Finally, the electrolyte chemistry (ether enriched fluorinated electrolyte) is shown to have superior electrochemical performance in a LMB. Designing and preserving interfaces with enhanced transport-reaction kinetics is a feasible solution to stabilize electrodeposition of reactive metals such as lithium. Additional studies dealing with the fundamental approach of understanding and eliminating morphological and chemical instabilities at the initiation step of dendrite nucleation for a reactive metal electrodeposition are paramount to accelerate the realization of high-energy density, high-performance reactive metal batteries.

4.5 Acknowledgement

The research was supported as part of the Center for Mesoscale Transport Properties, an Energy Frontier Research Center supported by the U.S. Department of Energy (DOE), Office of Science, Basic Energy Sciences, under Award DE-SC0012673. The electron microscopy facilities made use of the Cornell Center for Materials Research Shared Facilities which are supported through the NSF MRSEC program (DMR-1719875). The interface characterization work made use of the facilities available in CESI, Cornell.

4.6 References

- (1) Aurbach, D. (2000). Review of selected electrode–solution interactions which determine the performance of Li and Li ion batteries. *Journal of Power Sources*, 89(2), 206-218.
- (2) Zachman, M. J., Tu, Z., Choudhury, S., Archer, L. A., & Kourkoutis, L. F. (2018). Cryo-STEM mapping of solid–liquid interfaces and dendrites in lithium-metal batteries. *Nature*, 560(7718), 345-349.
- (3) Tikekar, M. D., Choudhury, S., Tu, Z., & Archer, L. A. (2016). Design principles for electrolytes and interfaces for stable lithium-metal batteries. *Nature Energy*, 1(9), 1-7.
- (4) Biswal, P., Stalin, S., Kludze, A., Choudhury, S., & Archer, L. A. (2019). Nucleation and Early Stage Growth of Li Electrodeposits. *Nano Letters*, 19(11), 8191-8200.
- (5) Wood, K. N., Kazyak, E., Chadwick, A. F., Chen, K. H., Zhang, J. G., Thornton, K., & Dasgupta, N. P. (2016). Dendrites and pits: Untangling the complex behavior of

lithium metal anodes through operando video microscopy. *ACS central science*, 2(11), 790-801.

(6) Shi, F., Pei, A., Boyle, D.T., Xie, J., Yu, X., Zhang, X. & Cui, Y., (2018). Lithium metal stripping beneath the solid electrolyte interphase. *Proceedings of the National Academy of Sciences*, 115(34), pp.8529-8534.

(7) Zheng, J., Kim, M. S., Tu, Z., Choudhury, S., Tang, T., & Archer, L. A. (2020). Regulating electrodeposition morphology of lithium: towards commercially relevant secondary Li metal batteries. *Chemical Society Reviews*, 49(9), 2701-2750.

(8) Miao, R., Yang, J., Feng, X., Jia, H., Wang, J., & Nuli, Y. (2014). Novel dual-salts electrolyte solution for dendrite-free lithium-metal based rechargeable batteries with high cycle reversibility. *Journal of Power Sources*, 271, 291-297.

(9) Qian, J., Henderson, W. A., Xu, W., Bhattacharya, P., Engelhard, M., Borodin, O., & Zhang, J. G. (2015). High rate and stable cycling of lithium metal anode. *Nature communications*, 6(1), 1-9.

(10) Suo, L., Xue, W., Gobet, M., Greenbaum, S. G., Wang, C., Chen, Y., ... & Li, J. (2018). Fluorine-donating electrolytes enable highly reversible 5-V-class Li metal batteries. *Proceedings of the National Academy of Sciences*, 115(6), 1156-1161.

(11) Gordin, M. L., Dai, F., Chen, S., Xu, T., Song, J., Tang, D., ... & Wang, D. (2014). Bis (2, 2, 2-trifluoroethyl) ether as an electrolyte co-solvent for mitigating self-discharge in lithium–sulfur batteries. *ACS applied materials & interfaces*, 6(11), 8006-8010.

(12) Aurbach, D., Pollak, E., Elazari, R., Salitra, G., Kelley, C. S., & Affinito, J. (2009). On the surface chemical aspects of very high energy density, rechargeable Li–sulfur batteries. *Journal of The Electrochemical Society*, 156(8), A694-A702.

- (13) Kim, H., Wu, F., Lee, J. T., Nitta, N., Lin, H. T., Oschatz, M., ... & Yushin, G. (2015). In situ formation of protective coatings on sulfur cathodes in lithium batteries with LiFSI-based organic electrolytes. *Advanced Energy Materials*, 5(6), 1401792.
- (14) Choudhury, S. (2019). Lithium fluoride additives for stable cycling of lithium batteries at high current densities. In *Rational Design of Nanostructured Polymer Electrolytes and Solid–Liquid Interphases for Lithium Batteries* (pp. 81-94). Springer, Cham.
- (15) Lu, Y., Tu, Z., Shu, J., & Archer, L. A. (2015). Stable lithium electrodeposition in salt-reinforced electrolytes. *Journal of Power Sources*, 279, 413-418.
- (16) Zhang, X. Q., Cheng, X. B., Chen, X., Yan, C., & Zhang, Q. (2017). Fluoroethylene carbonate additives to render uniform Li deposits in lithium metal batteries. *Advanced Functional Materials*, 27(10), 1605989.
- (17) Choudhury, S., Wei, S., Ozhabes, Y., Gunceler, D., Zachman, M. J., Tu, Z., & Arias, T. A. (2017). Designing solid-liquid interphases for sodium batteries. *Nature communications*, 8(1), 1-10.
- (18) Biswal, P., Kludze, A., Rodrigues, J., Deng, Y., Moon, T., Stalin, S., ... & Archer, L. A. (2021). The early-stage growth and reversibility of Li electrodeposition in Br-rich electrolytes. *Proceedings of the National Academy of Sciences*, 118(2).
- (19) Tamura, T., Hachida, T., Yoshida, K., Tachikawa, N., Dokko, K., & Watanabe, M. (2010). New glyme–cyclic imide lithium salt complexes as thermally stable electrolytes for lithium batteries. *Journal of Power Sources*, 195(18), 6095-6100.

- (20) Suo, L., Hu, Y. S., Li, H., Armand, M., & Chen, L. (2013). A new class of solvent-in-salt electrolyte for high-energy rechargeable metallic lithium batteries. *Nature communications*, 4(1), 1-9.
- (21) Yamada, Y., Wang, J., Ko, S., Watanabe, E., & Yamada, A. (2019). Advances and issues in developing salt-concentrated battery electrolytes. *Nature Energy*, 4(4), 269-280.
- (22) Markevich, E., Salitra, G., Chesneau, F., Schmidt, M., & Aurbach, D. (2017). Very stable lithium metal stripping–plating at a high rate and high areal capacity in fluoroethylene carbonate-based organic electrolyte solution. *ACS Energy Letters*, 2(6), 1321-1326.
- (23) Zhang, Z., Hu, L., Wu, H., Weng, W., Koh, M., Redfern, P. C., ... & Amine, K. (2013). Fluorinated electrolytes for 5 V lithium-ion battery chemistry. *Energy & Environmental Science*, 6(6), 1806-1810.
- (24) Tang, S., & Zhao, H. (2014). Glymes as versatile solvents for chemical reactions and processes: from the laboratory to industry. *RSC advances*, 4(22), 11251-11287.
- (25) Wang, A., Kadam, S., Li, H., Shi, S., & Qi, Y. (2018). Review on modeling of the anode solid electrolyte interphase (SEI) for lithium-ion batteries. *NPJ Computational materials*, 4(1), 1-26.
- (26) Delp, S. A., Borodin, O., Olguin, M., Eisner, C. G., Allen, J. L., & Jow, T. R. (2016). Importance of reduction and oxidation stability of high voltage electrolytes and additives. *Electrochimica Acta*, 209, 498-510.
- (27) Hou, T., Yang, G., Rajput, N. N., Self, J., Park, S. W., Nanda, J., & Persson, K. A. (2019). The influence of FEC on the solvation structure and reduction reaction of

LiPF₆/EC electrolytes and its implication for solid electrolyte interphase formation. *Nano Energy*, *64*, 103881.

(28) Westman, K., Dugas, R., Jankowski, P., Wieczorek, W., Gachot, G., Morcrette, M., ... & Johansson, P. (2018). Diglyme based electrolytes for sodium-ion batteries. *ACS Applied Energy Materials*, *1*(6), 2671-2680.

(29) Markevich, E., Salitra, G., & Aurbach, D. (2017). Fluoroethylene carbonate as an important component for the formation of an effective solid electrolyte interphase on anodes and cathodes for advanced Li-ion batteries. *ACS Energy Letters*, *2*(6), 1337-1345.

(30) Markevich, E., Salitra, G., Hartmann, P., Kulisch, J., Aurbach, D., Park, K. J., ... & Sun, Y. K. (2019). New insights related to rechargeable lithium batteries: Li metal anodes, Ni rich LiNi_xCo_yMn_zO₂ cathodes and beyond them. *Journal of the Electrochemical Society*, *166*(3), A5265.

(31) Jin, Y., Kneusels, N. J. H., Marbella, L. E., Castillo-Martínez, E., Magusin, P. C., Weatherup, R. S., ... & Grey, C. P. (2018). Understanding fluoroethylene carbonate and vinylene carbonate-based electrolytes for Si anodes in lithium ion batteries with NMR spectroscopy. *Journal of the American Chemical Society*, *140*(31), 9854-9867.

(32) Benitez, L., & Seminario, J. M. (2017). Ion diffusivity through the solid electrolyte interphase in lithium-ion batteries. *Journal of The Electrochemical Society*, *164*(11), E3159.

(33) Guan, P., Liu, L., & Lin, X. (2015). Simulation and experiment on solid electrolyte interphase (SEI) morphology evolution and lithium-ion diffusion. *Journal of The Electrochemical Society*, *162*(9), A1798.

- (34) Yildirim, H., Kinaci, A., Chan, M. K., & Greeley, J. P. (2015). First-principles analysis of defect thermodynamics and ion transport in inorganic SEI compounds: LiF and NaF. *ACS applied materials & interfaces*, 7(34), 18985-18996.
- (35) Tasaki, K., Goldberg, A., Lian, J. J., Walker, M., Timmons, A., & Harris, S. J. (2009). Solubility of lithium salts formed on the lithium-ion battery negative electrode surface in organic solvents. *Journal of The Electrochemical Society*, 156(12), A1019.
- (36) Arrhenius, S. (1889) *On the reaction rate of the inversion of non-refined sugar upon souring*, *Z. Phys. Chem.*, 4, 226.
- (37) Frost, A.A., & Pearson, R.G. (1971). *Kinetics and Mechanism*, Wiley Eastern, First reprint, New Delhi, page 7.
- (38) Glasstone, S., Laidler, K. J., & Eyring, H. (1941). *The theory of rate processes; the kinetics of chemical reactions, viscosity, diffusion, and electrochemical phenomena* (No. 541.39), McGraw-Hill Book Company.
- (39) Sanjeev, R., Padmavathi, D. A., & Jagannadham, V. (2018). The ‘yard stick’ to interpret the entropy of activation in chemical kinetics: a physical–organic chemistry exercise. *World J Chem Ed*, 6, 78-81.
- (40) Chen, K. H., Wood, K. N., Kazyak, E., LePage, W. S., Davis, A. L., Sanchez, A. J., & Dasgupta, N. P. (2017). Dead lithium: mass transport effects on voltage, capacity, and failure of lithium metal anodes. *Journal of Materials Chemistry A*, 5(23), 11671-11681.
- (41) Lu, Y., Gu, S., Hong, X., Rui, K., Huang, X., Jin, J., ... & Wen, Z. (2018). Pre-modified Li₃PS₄ based interphase for lithium anode towards high-performance Li-S battery. *Energy Storage Materials*, 11, 16-23.
- (42) Xia, S., Lopez, J., Liang, C., Zhang, Z., Bao, Z., Cui, Y., & Liu, W. (2019). High-

Rate and Large-Capacity Lithium Metal Anode Enabled by Volume Conformal and Self-Healable Composite Polymer Electrolyte. *Advanced Science*, 6(9), 1802353.

(43) He, M., Su, C. C., Peebles, C., & Zhang, Z. (2021). The Impact of Different Substituents in Fluorinated Cyclic Carbonates in the Performance of High Voltage Lithium-Ion Battery Electrolyte. *Journal of the Electrochemical Society*, 168(1), 010505.

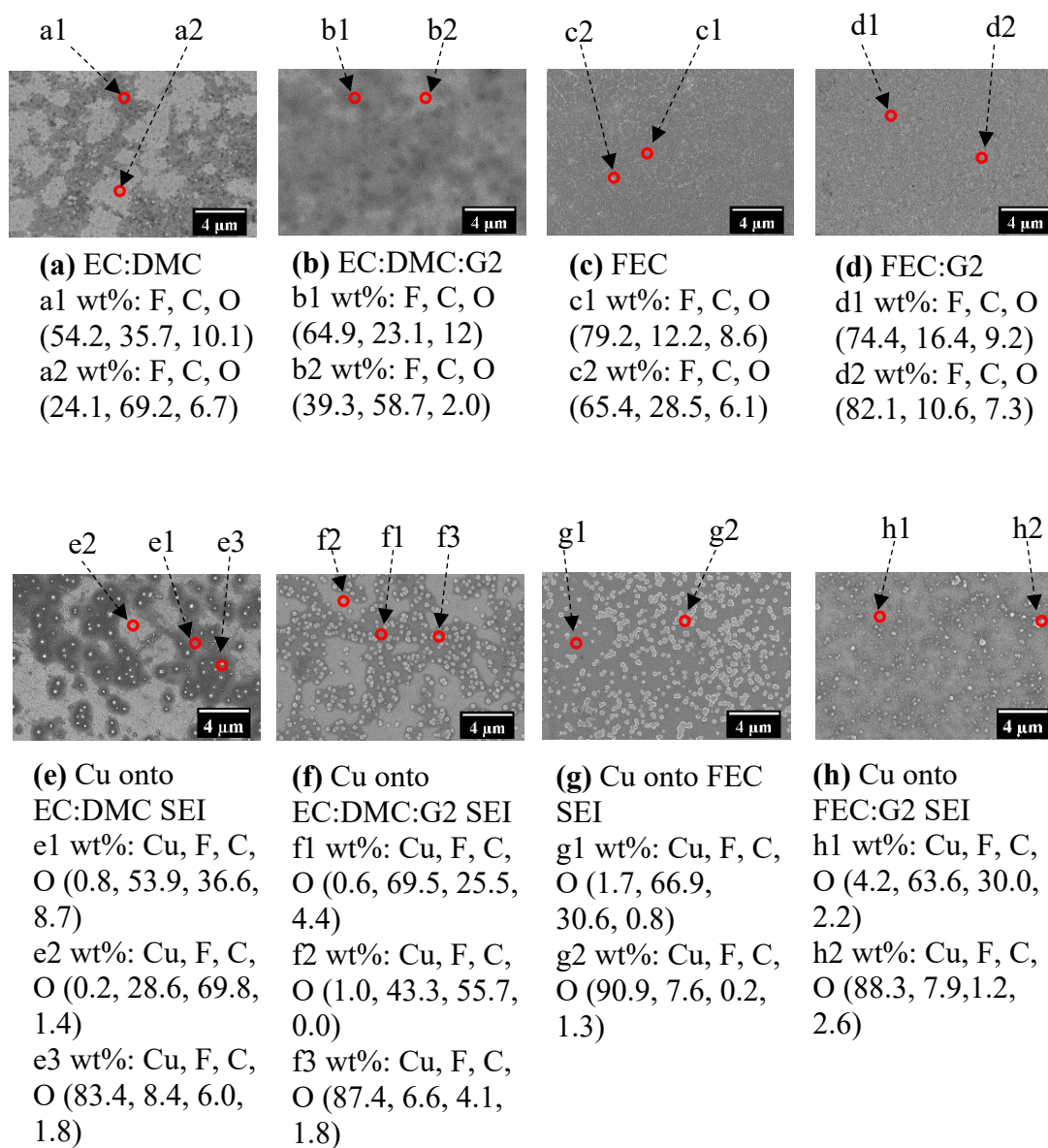
(44) Fan, X., Chen, L., Borodin, O., Ji, X., Chen, J., Hou, S., ... & Wang, C. (2018). Non-flammable electrolyte enables Li-metal batteries with aggressive cathode chemistries. *Nature nanotechnology*, 13(8), 715-722.

(45) Choudhury, S., Tu, Z., Nijamudheen, A., Zachman, M. J., Stalin, S., Deng, Y., ... & Archer, L. A. (2019). Stabilizing polymer electrolytes in high-voltage lithium batteries. *Nature communications*, 10(1), 1-11.

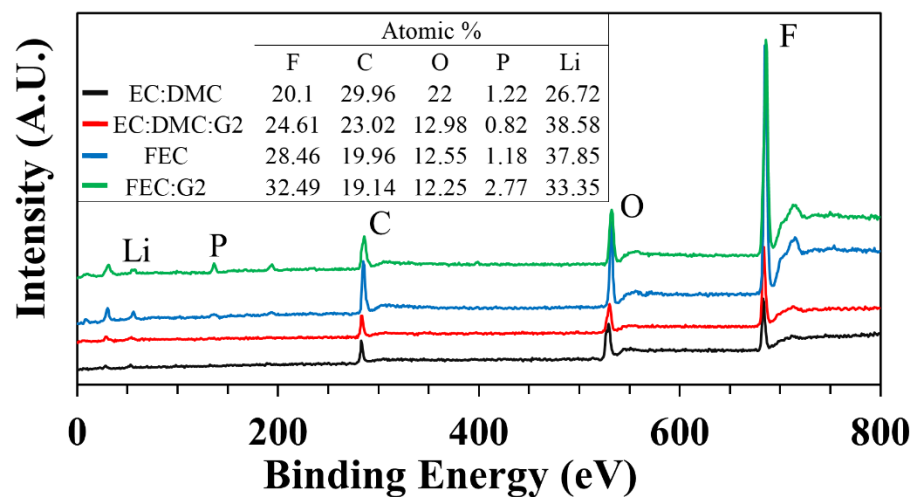
Appendix

Supplementary information for Chapter 4

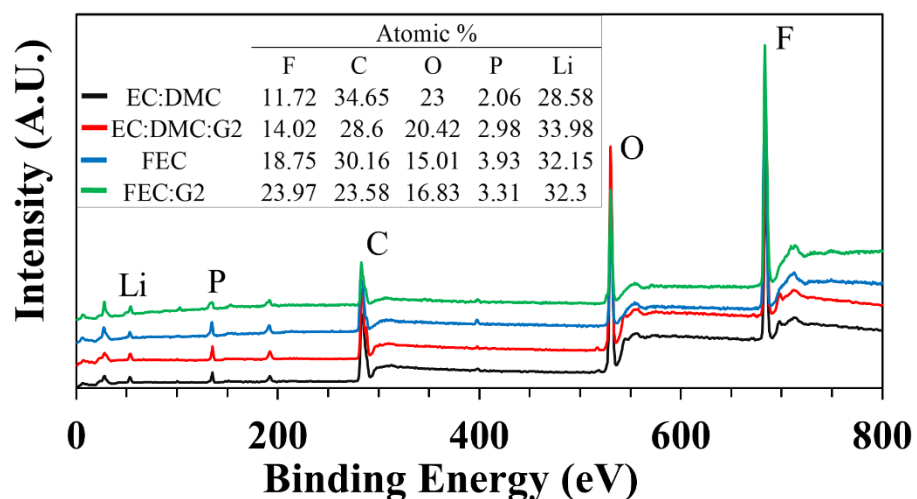
This appendix includes details of SEM, EDX, XPS, solubility characterizations, Impedance spectroscopy, charge discharge profiles, coin cell fabrication, electrochemical testing methods, image analysis, and additional figures.



Supplementary Figure 4.1. Ex situ SEM images and EDX analysis of **(a-d)** SEI formed galvanostatically from electrolyte of different compositions (1M LiPF₆ in EC:DMC (50:50), 1M LiPF₆ in EC:DMC:G2 (45:45:10), 1M LiPF₆ in FEC, 1M LiPF₆ in FEC:G2 (90:10)) at current densities of 0.5 mA/cm² **(e-h)** Cu deposited onto the previously formed SEI from 0.5M Cu(OTF)₂ in EC:DMC (50:50) electrolyte at current densities of 1 mA/cm² and capacities of 0.01 mAh/cm². The chemical composition is measured through point spectra of EDX. All ratios are vol% and G2 here stands for diglyme. The base substrate is polished stainless steel.



(a) 0.05 mAh/cm²



(b) 100 cycles

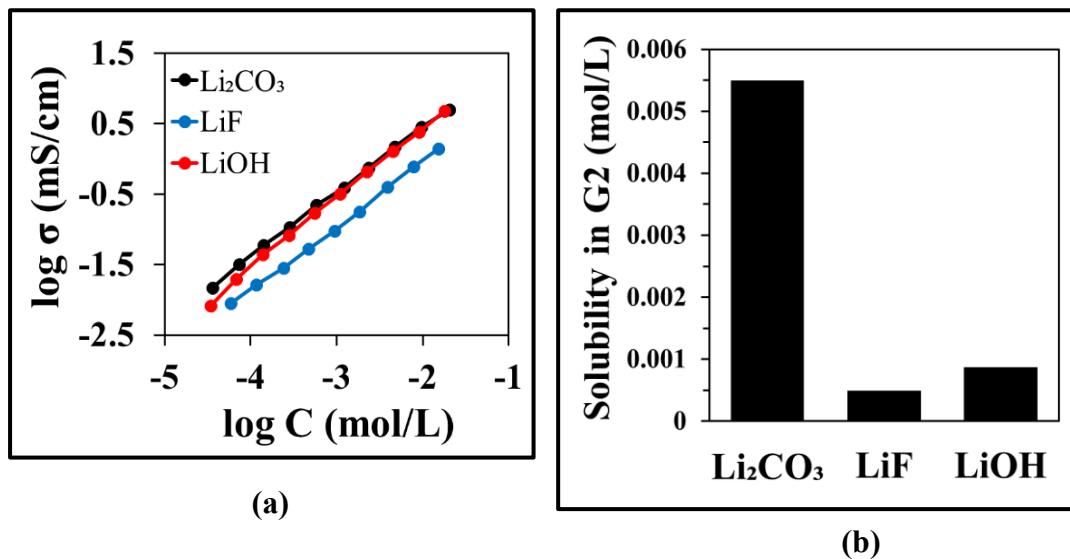
Supplementary Figure 4.2. Chemical spectra of SEI layer obtained via XPS for Li electrodeposits formed under different electrolyte chemistries (a) at current density of 1 mA/cm² and areal capacity of 0.05 mAh/cm² (b) after 100 cycles of stripping/plating at current density of 1 mA/cm² and areal capacity of 1 mAh/cm².

	(a) 0.05 mAh/cm²			(b) 100 cycles		
	Li ₂ CO ₃	C-C-O	C-C/C-H	Li ₂ CO ₃	C-C-O	C-C/C-H
EC:DMC	19.27	32.12	48.62	27.67	40.22	32.12
EC:DMC:G2	14.75	28.02	57.23	20.44	36.26	41.84
FEC	11.78	20.72	67.5	19.49	35.11	45.4
FEC:G2	7.66	17.89	74.45	13.78	28.76	57.46

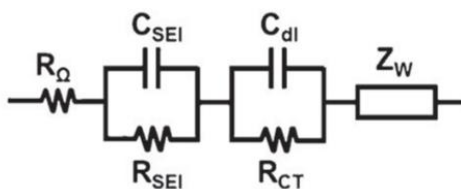
Supplementary Table 4.1. Chemical components obtained via analysis of high-resolution C 1s XPS spectra of the SEI formed in cells with different electrolyte chemistries: **(a)** at current density of 1 mA/cm² and areal capacity of 0.05 mAh/cm², and **(b)** after 100 cycles of stripping plating at current density of 1 mA/cm² and 1 mAh/cm². All values are in atomic percentage.

	(a) 0.05 mAh/cm²		(b) 100 cycles	
	LiF	Li ₂ CO ₃	LiF	Li ₂ CO ₃
EC:DMC	39.58	60.42	15.58	84.42
EC:DMC:G2	48.01	51.99	33.59	66.41
FEC	69.35	30.65	46.69	53.31
FEC:G2	77.58	22.42	59.07	40.93

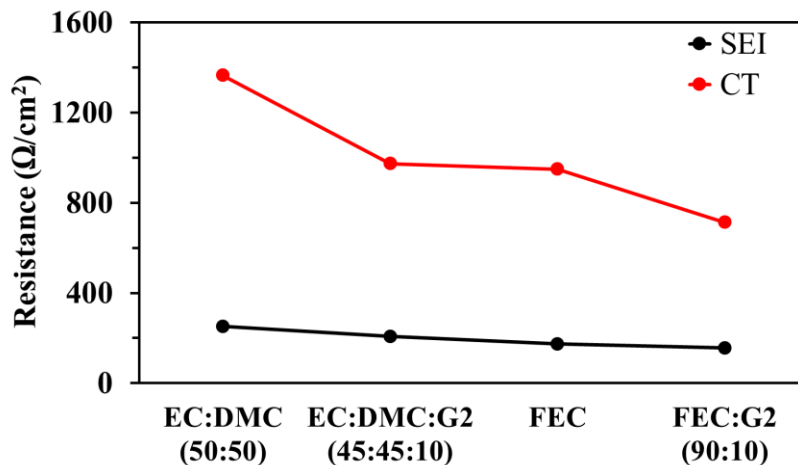
Supplementary Table 4.2. Chemical components obtained via analysis of high-resolution Li 1s XPS spectra of the SEI formed in cells using different electrolyte chemistries: **(a)** at current density of 1 mA/cm² and areal capacity of 0.05 mAh/cm², and **(b)** after 100 cycles of stripping plating at current density of 1 mA/cm² and 1 mAh/cm². All values are in atomic percentage.



Supplementary Figure 4.3. Solubility of different salts in diglyme (G2) at room temperature (20°C). **(a)** Calibration plot of ionic conductivity of different salts at different concentrations in water; **(b)** Solubility of different salts in diglyme (G2). The salts were left for a week in diglyme solvent, followed by extraction of supernatant solution. The supernatant solution was dried in a vacuum oven (50°C) connected to a cold trap. The residual salts were dissolved in a specific amount of water and tested for ionic conductivity against the calibration plot, thereby determining their concentration in water, and the apparent concentration in diglyme was calculated.



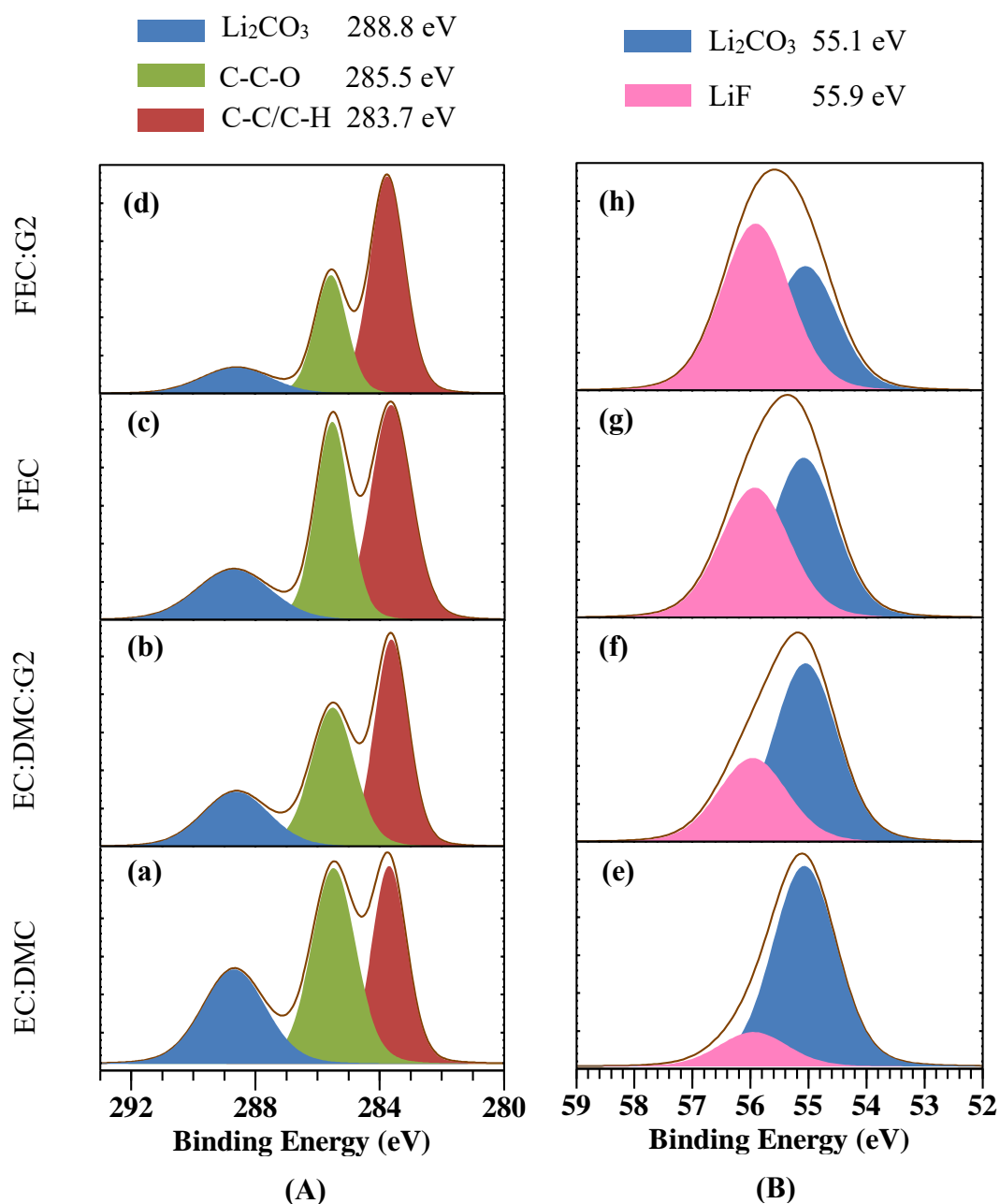
(a)



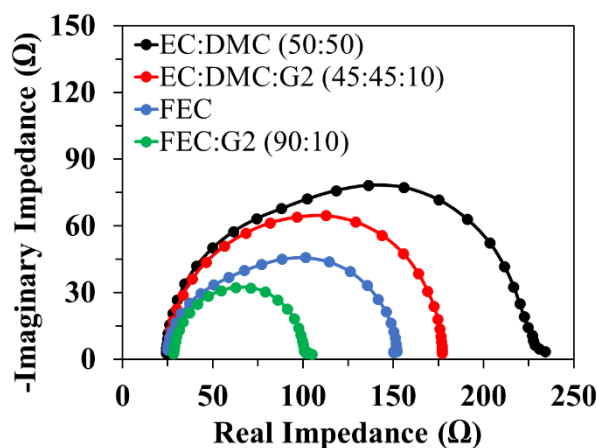
(b)

Supplementary Figure 4.4. (a) EIS model used to fit the electrochemical spectrum data (1-2). (b) SEI and Charge Transfer (CT) resistance per unit area as extracted by the fitted model of the electrochemical spectrum data.

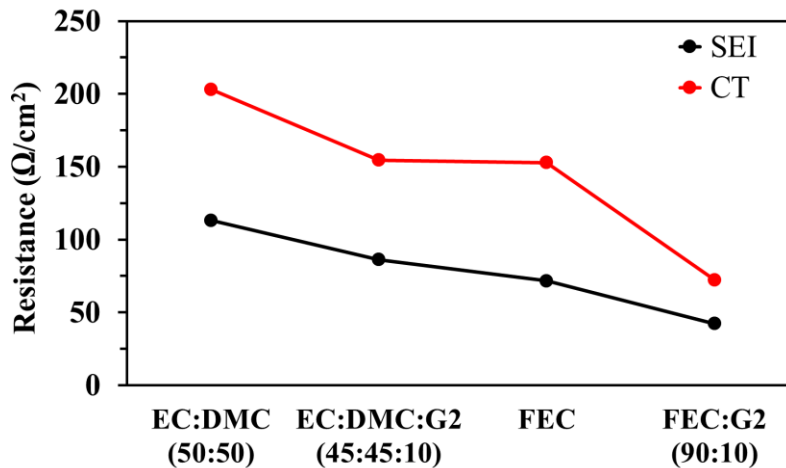
Note: The SEI diffusivity is calculated from the Warburg coefficient (3). The Warburg coefficient is calculated from the plot of low frequency real impedance of Z_w vs $1/\sqrt{\omega}$. The transference number of Li ions in the SEI is assumed to be 1.



Supplementary Figure 4.5. Interfacial chemistry of Lithium electrodeposits formed after 100 plating/stripping cycles. (A) C 1s and (B) Li 1s high-resolution spectra of SEI layer on Li electrodeposits formed after 100 cycles at current density of 1 mA/cm^2 and areal capacity of 1 mAh/cm^2 in electrolytes of different compositions (a,e) EC:DMC (50:50), (b,f) EC:DMC:G2 (45:45:10), (c,g) FEC, (d,h) FEC:G2 (90:10), each containing 1 M LiPF_6 salt.

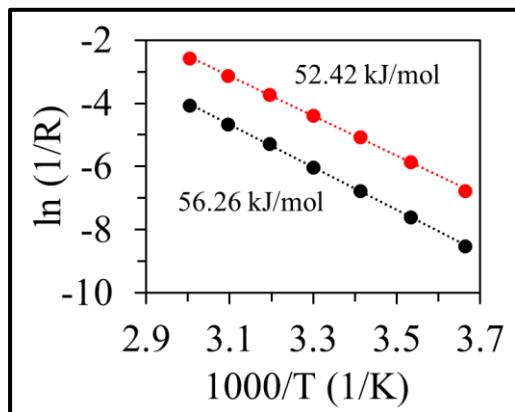


(a)

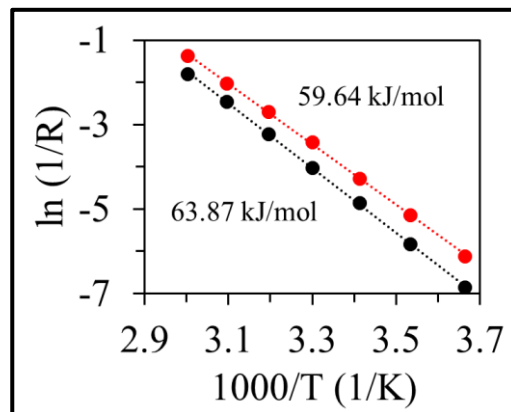


(b)

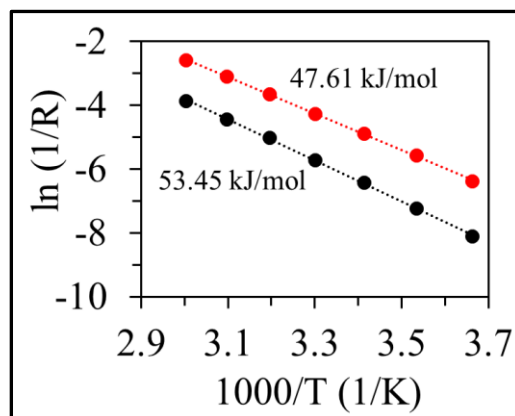
Supplementary Figure 4.6. Electrochemical Impedance Spectroscopy of Li electrodeposits formed on stainless steel after 100 cycles of plating stripping at current density of 1 mA/cm² in electrolytes of different compositions: EC:DMC (50:50), EC:DMC:G2 (45:45:10), FEC, FEC:G2 (90:10), each containing 1M LiPF₆ salt. **(a)** Fitted Nyquist plots **(b)** SEI and charge transfer (CT) resistances for different electrolytes. The data is collected at room temperature (20 °C)



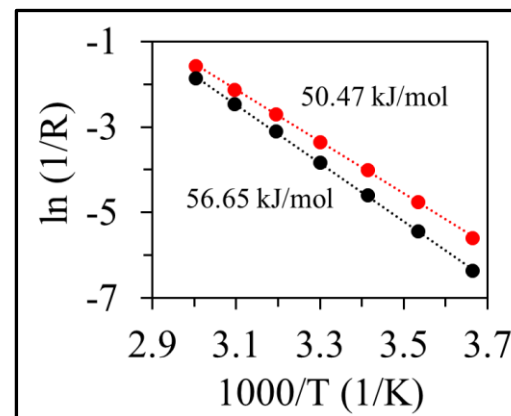
(a) EC:DMC, 0.05 mAh/cm²



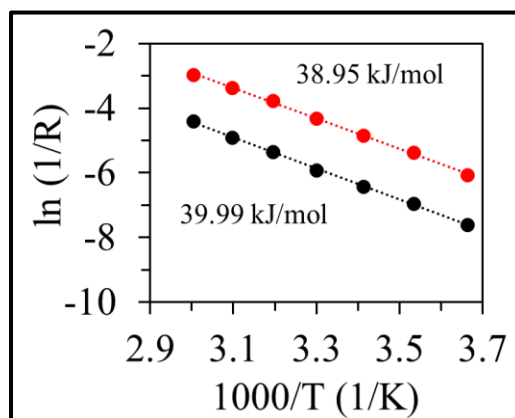
(b) EC:DMC, 100 cycles



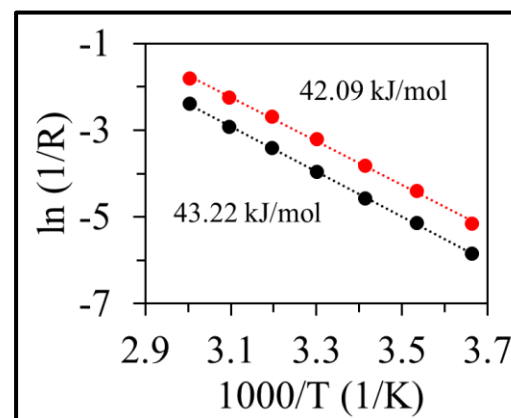
(c) EC:DMC:G2, 0.05 mAh/cm²



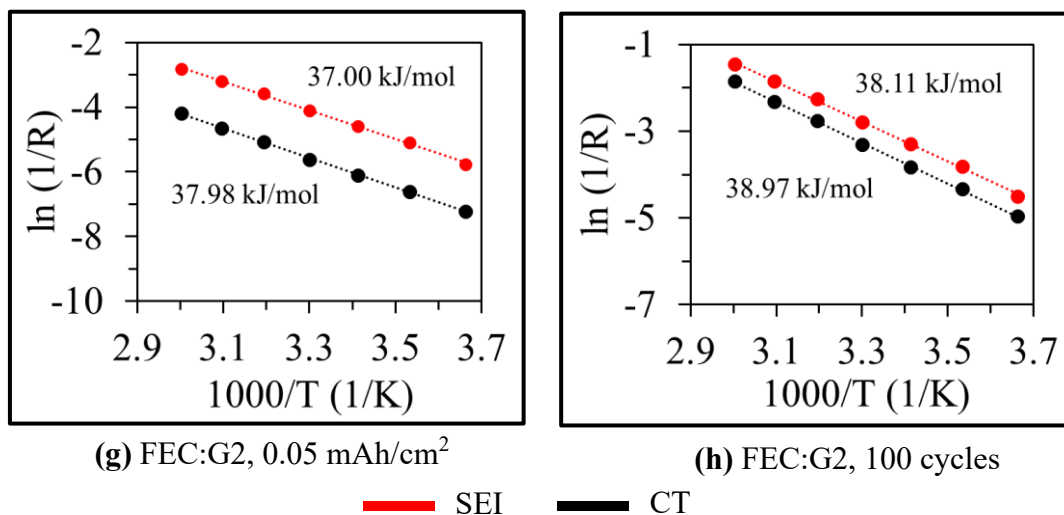
(d) EC:DMC:G2, 100 cycles



(e) FEC, 0.05 mAh/cm²



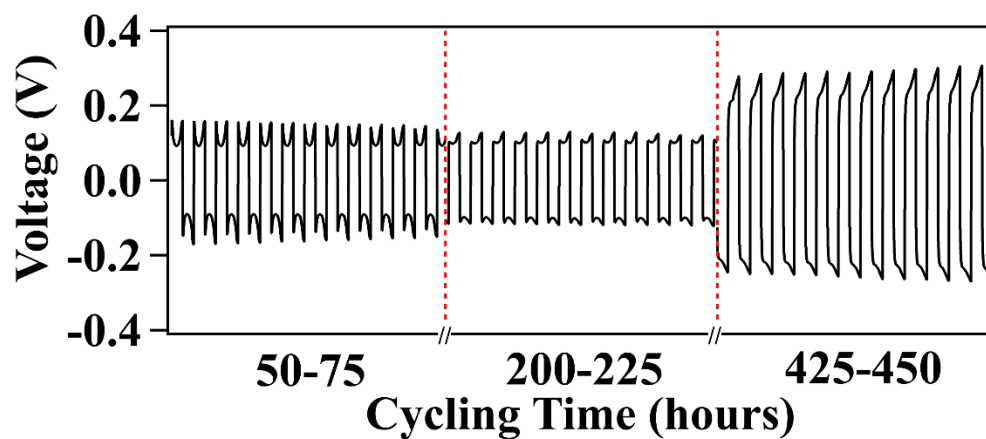
(f) FEC, 100 cycles



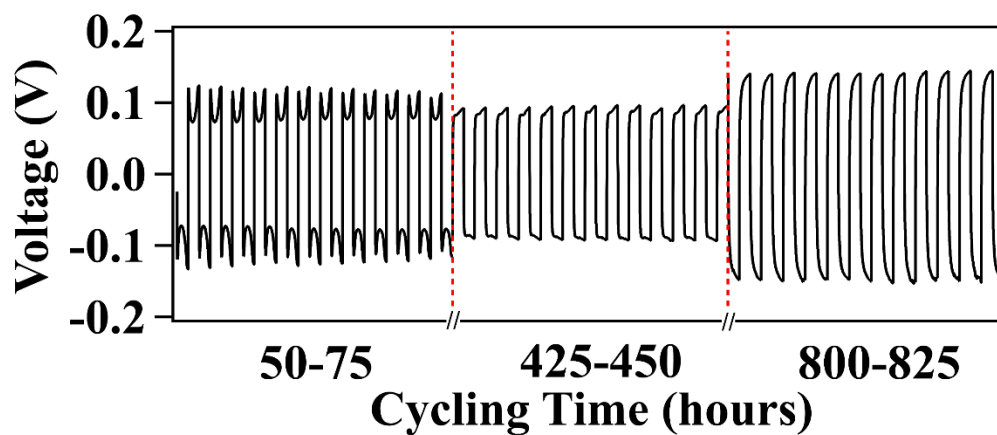
Supplementary Figure 4.7. Arrhenius plots of SEI (red) and charge transfer (CT) (black) resistances of electrodeposits on stainless steel substrate at (a,c,e,g) 0.05 mAh/cm², and (b,d,f,h) after 100 stripping/plating cycles at 1 mA/cm² and 1 mAh/cm². The electrolytes are EC:DMC (50:50), EC:DMC:G2 (45:45:10), FEC, FEC:G2 (90:10), each containing 1M LiPF₆ salt. The activation energies are obtained through Arrhenius fitting of SEI and CT resistances at different temperatures.

	0.05 mAh/cm ²				100 cycles			
	SEI		CT		SEI		CT	
	$\ln(A)$	ΔS	$\ln(A)$	ΔS	$\ln(A)$	ΔS	$\ln(A)$	ΔS
EC:DMC	16.4	-116.8	16.3	-117.6	20.2	-85.2	21.3	-75.9
EC:DMC:G2	14.6	-131.4	15.5	-124.4	16.7	-114.4	18.6	-98.2
FEC	11.1	-160.5	10.0	-170.0	13.5	-141.3	13.2	-143.4
FEC:G2	10.6	-165.1	9.5	-174.1	12.3	-150.5	12.2	-151.6

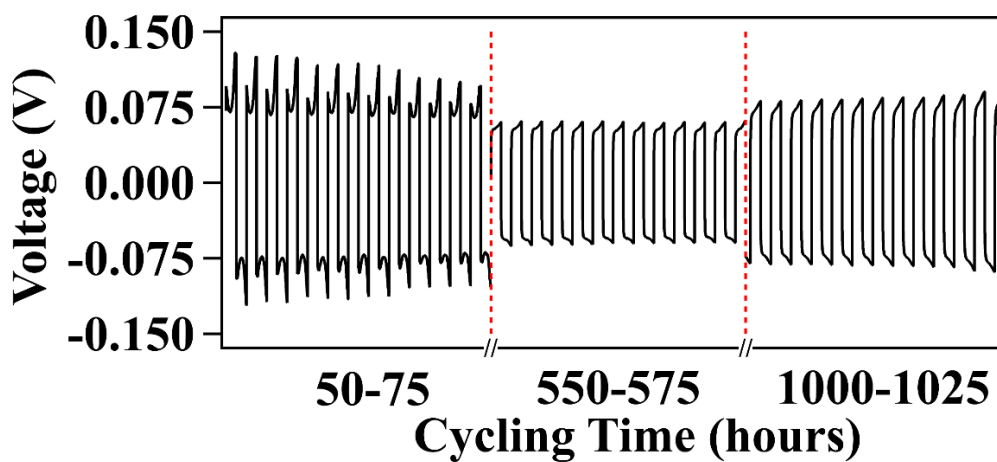
Supplementary Table 4.3. Pre-exponential factor ($\ln(A)$) and change in entropy of activation (ΔS , J/K) calculated from the Arrhenius plots of SEI and charge transfer (CT) resistances of electrodeposits on stainless steel substrate at 0.05 mAh/cm², and after 100 stripping/plating cycles at 1 mA/cm² and 1 mAh/cm². The electrolytes are EC:DMC (50:50), EC:DMC:G2 (45:45:10), FEC, FEC:G2 (90:10), each containing 1M LiPF₆ salt.



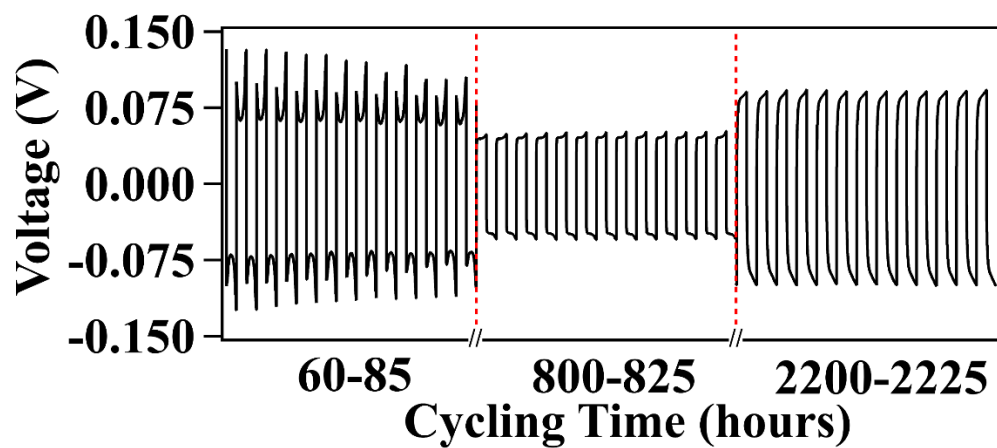
(a) EC:DMC



(b) EC:DMC:G2

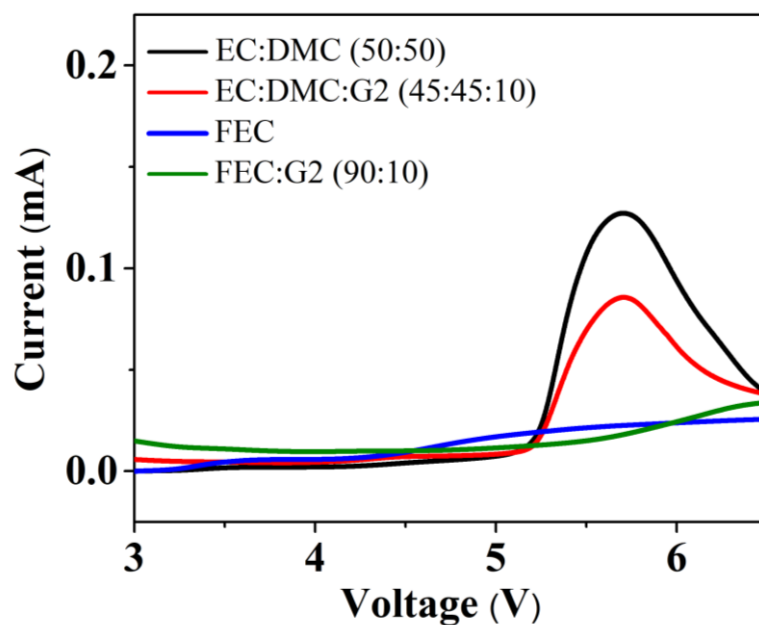


(c) FEC

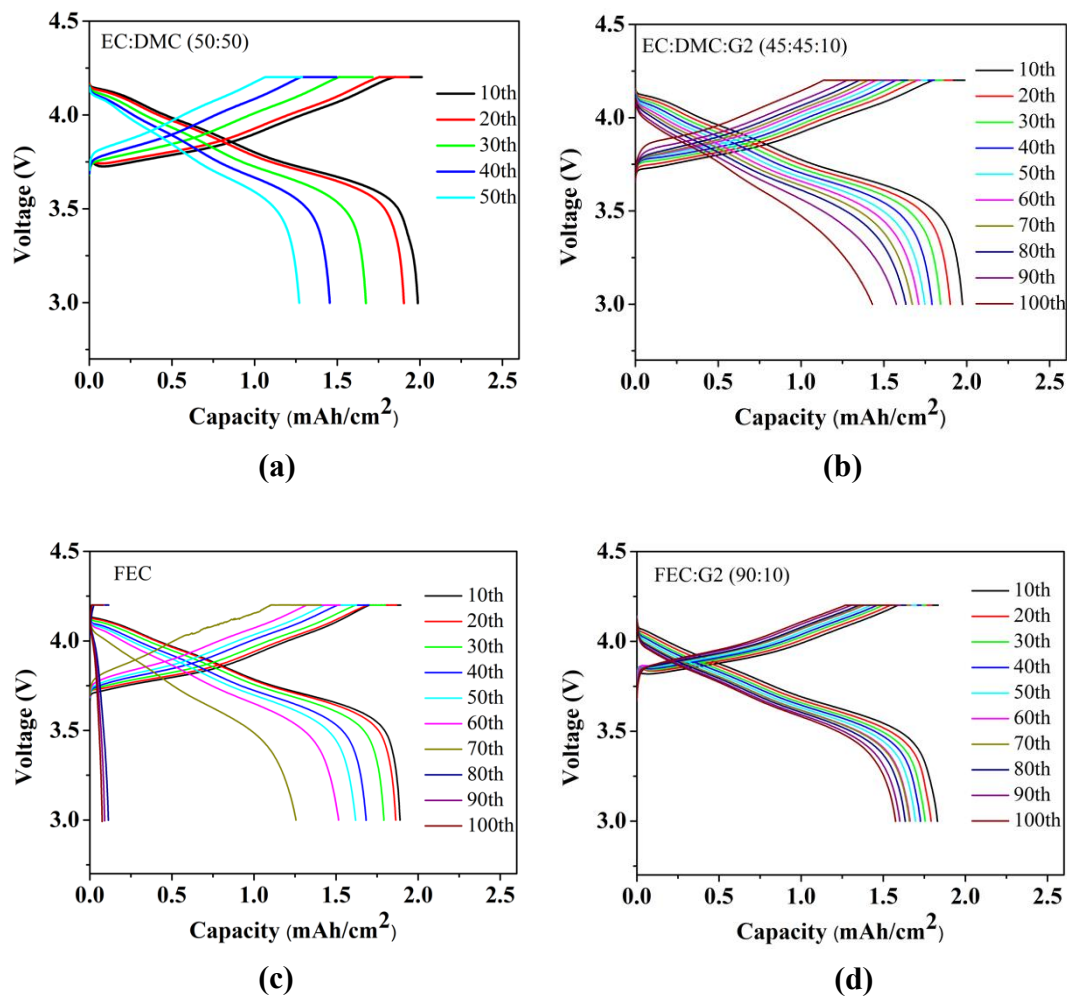


(d) FEC:G2

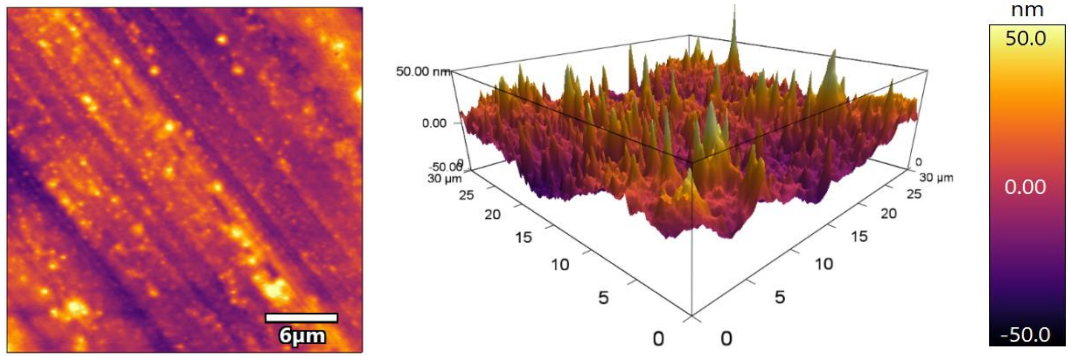
Supplementary Figure 4.8. Galvanostatic plating stripping voltage profile (in intervals) of symmetric Li anode at a current density of 1 mA/cm^2 and capacity of 1 mAh/cm^2 in (a) EC:DMC, (b) EC:DMC:G2, (c) FEC, (d) FEC:G2, each containing 1 M LiPF_6 salt.



Supplementary Figure 4.9. Linear sweep voltammetry from open circuit voltage (OCV) to 6.5 V at a sweep rate of 2 mV s^{-1} . The experiment is performed in a Li||SS cell. The electrolytes are EC:DMC (50:50), EC:DMC:G2 (45:45:10), FEC, FEC:G2 (90:10), each containing 1M LiPF_6 salt.



Supplementary Figure 4.10. Charge-discharge voltage profile of Li||NCM cells with thin lithium anode (50 μm) and NCM622 cathode (2mAh/cm²). The cells are cycled under CC-CV charge mode (constant current of 0.5 C to 4.2 V and constant voltage until the current decreases to 0.2 C) and CC discharge mode at 0.5 C. 1C=(2mA/cm²). The electrolytes are **(a)** EC:DMC (50:50), **(b)** EC:DMC:G2 (45:45:10), **(c)** FEC, **(d)** FEC:G2 (90:10), each containing 1M LiPF₆ salt.



Average surface roughness (Ra) = 9.12 +/- 8.78 nm

Supplementary Figure 4.11. AFM image of the surface topography of polished stainless-steel.

Material and Methods

Materials: All electrolytes are prepared in argon glove box (Inert Inc), in which the content of O₂ and H₂O content are kept below 0.5 ppm. The Li foil of width 0.75 mm and 50 μm was procured from Alfa Aesar. All the electrolytic components including Lithium hexafluorophosphate (LiPF₆), Ethylene Carbonate (EC), Dimethyl Carbonate (DMC), Fluoroethylene Carbonate (FEC), & Diethylene glycol dimethyl ether (Diglyme, G2) were procured from Sigma Aldrich. Celgard 3501 separator was obtained from Celgard Inc.

Polishing/cleaning method: The stainless-steel 304 substrate was polished to a surface roughness of Ra < 10nm through chemical mechanical polishing (CMP) method. The unpolished stainless-steel substrates were fixed in an Alumina slurry of 0.3 Micron particles on a bed of Final-POL Adhesive Back Disc (Allied High-Tech products) in a vibratory polisher at an amplitude of 50% for about 2 days. The polished stainless-steel substrates were cleaned through ultrasonication in a bath of acetone for about 1 hour.

Supplementary Figure 4.11 shows the AFM image of the surface topography of the stainless-steel to have average roughness of about 10 nm. The polished cleaned substrates were stored in a vial of acetone and ultrasonicated again with fresh acetone prior to any usage.

Electrochemical method: For the SEI study, 2032-type coin cells with the polished stainless-steel working electrodes (thickness 1.7 mm) and Li foil (0.75 mm width) counter/reference electrodes were assembled in an argon-filled glove box. A hard Teflon O-ring of internal diameter 0.25 inches and thickness of 0.8 mm was used between the

two electrodes and 150 μL of electrolyte was added to each cell. The electrolyte chemistries are 1M LiPF_6 in EC:DMC (50:50), 1M LiPF_6 in EC:DMC:G2 (45:45:10), 1M LiPF_6 in FEC, 1M LiPF_6 in FEC:G2 (90:10) with room temperature (20 $^\circ\text{C}$) conductivities of 10.1 mS/cm, 9.9 mS/cm, 4.8 mS/cm, 4.7 mS/cm respectively. The Teflon O-ring ensures holding of free liquid electrolyte and minimal stacking pressure. The coin cell crimping pressure is kept at a minimum (< 100 psi) to avoid deformation of Li electrode and subsequent short-circuiting. Galvanostatic deposition was conducted using an 8-channel battery testing unit from Neware Instruments and MACCOR series 4000 battery tester system. The stainless-steel electrode was discharged to 50 mV vs. Li/Li^+ by applying 0.5 mA/cm^2 current to initialize SEI formation, then charged back to 2 V at -0.05 mA/cm^2 to remove any underpotential deposition.

The SEI covered substrates were harvested, washed with DMC for about 5 seconds to remove any leftover salts and solvents, and Cu was galvanostatically electrodeposited onto them from 0.5M $\text{Cu}(\text{OTF})_2$ in EC:DMC (50:50) electrolyte (Teflon O-ring) at current density of 1 mA/cm^2 and capacity of 0.01 mAh/cm^2 in a $\text{Cu}||\text{SS}(\text{SEI})$ cell. The galvanostatic electrodeposition of Li were carried out in the cells after SEI formation with the respective electrolytes, at current density of 1 mA/cm^2 and capacities of 0.05 mAh/cm^2 . The higher capacity cycles (100 cycles at 1 mA/cm^2 and 1 mAh/cm^2) were carried out in $\text{Li}||\text{SS}$ cell with Celgard 3501 as the separator, and 60 μL of electrolyte. Symmetric cell cycling ($\text{Li}||\text{Li}$) and Coulombic efficiency tests ($\text{Li}||\text{SS}$) also employed Celgard 3501 with 60 μL of electrolyte. No SEI formation cycles were carried out in the Symmetric cell cycling or Coulombic efficiency tests.

The electrochemical floating tests were performed in Li||NMC622 cells. The batteries were firstly charged to 4.2 V at a constant current density of 0.1 C, then held at higher voltages from 4.3 V to 5.0 V to observe the leakage current. The full cell tests involved Li||NMC622 with thin lithium anode (50 μm) and NCM622 cathode (2mAh/cm²). The cells were activated at 0.1 C for 2 cycles and 0.2 C for 2 cycles, then cycled under CC-CV charge mode (constant current at 0.5 C to 4.2 V and constant voltage until the current decreases to 0.2 C) and CC discharge mode at 0.5 C. 1C=(2mA/cm²).

The voltammetry experiments were performed using a Gamry CH 600E potentiostat. The cyclic voltammetry measurements (for determining exchange current) were conducted in a Li||SS cell at a fast scan rate of 100 mV s⁻¹ within the voltage range of 100 to -100 mV. The linear scan voltammetry measurements (for determining oxidative stability) were conducted in a Li||SS cell at a scan rate of 2 mV s⁻¹ from open circuit voltage (OCV) to 6.5 V.

A Novocontrol Broad band with frequency analyzer was used for obtaining impedance spectra at different temperatures. The frequency range was adjusted to be in between 1 MHz to 1 mHz at an amplitude of 10mV. Prior to the impedance spectroscopy, Lithium of areal capacity corresponding to 0.05 mAh/cm² or 100 cycles (1mAh/cm²) was electrodeposited on to the polished stainless-steel at 1 mA/cm². These electrodes were extracted and re-assembled in a symmetric cell fashion in 2032-type coin cells. The assembly consisted of electrolyte in a Teflon O-ring (0.25 inches in diameter) in between two Polished stainless-steel with electrodeposited Lithium. A 1 hr resting OCV time was

ensured before impedance spectroscopy to allow the SEI to fully mature. Further impedance spectroscopy performed on symmetric Li cells with Teflon O-ring holding the electrolyte were used to determine conductivity of Li ions in the electrolyte.

Electrode Characterization: After electrodeposition (Li, Cu, SEI) onto polished stainless-steel, the cells were opened in the Argon glove box and the stainless-steel electrodes were rinsed with fresh Dimethyl Carbonate for about 5 seconds and vacuum dried in the antechamber of the glovebox. Electrodes were mounted onto SEM stage puck and sealed in Argon filled transfer vessels for immediate SEM observation (Zeiss Gemini SEM). Unavoidable contact with air was brief (< 10 secs) and may have slightly altered the surface features of the electrodeposited Li metal seen in SEM images. The images were captured at 2 kV with an aperture of 20 μm . The EDX point spectra was performed in conjunction at 5 kV using an Oxford Instruments Ultim Max detector.

The chemical composition of the surface of Li electrodeposits were analyzed using a Scienta Omicron ESCA-2SR with operating pressure ca. 1×10^{-9} mBar. Monochromatic Al K α X-rays (1486.6 eV) were generated at 300W (15kV; 20mA). Analysis spot size was 2 mm in diameter with a 0° photoemission angle and a source to analyzer angle of 54.7°. A hemispherical analyzer determined electron kinetic energy, using a pass energy of 200 eV for wide/survey scans and 50 eV for high resolution scans. A flood gun was used for charge neutralization of non-conductive samples. The data analysis was performed with CasaXPS software, with Tougaard background fitting of the peaks.

Solubility characterization: Predetermined amounts of salts were dissolved instantly in 5 mL of water and tested for ionic conductivity via liquid cell of Novo Dielectric

Spectrometer in the frequency range of 1 MHz to 100 MHz and an amplitude of 10 mV. Based on the data, calibration plot of ionic conductivity vs salt concentration was designed as shown in **Supplementary Figure 4.3(a)**. Next, the salts were left for a week in diglyme solvent (10 mL), followed by extraction of supernatant solution. The supernatant solution was dried in a vacuum oven (50°C) connected to a cold trap for 2 days. The residual salts were collected and dissolved in a definite amount of water (2 mL) and tested for ionic conductivity using the liquid cell of Novo Dielectric Spectrometer in the same range as before. The resultant ionic conductivity was matched against the calibration plot, thereby determining the concentration of salt in water, and therefore the moles of salt residue. The apparent concentration of the salt in diglyme was calculated and plotted in **Supplementary Figure 4.3(b)**. The procedure closely follows the reported literature (4).

Image / Data Analysis: Nuclei sizes were measured using ImageJ software. Gaussian blurring to remove excessive noise, Thresholding to restrict color contrast of images to black and white, and adjustable watershed to identify nuclei were performed. The radius of a Nuclei was calculated by assuming the nuclei to be hemispherical and the projected area was approximated to that of a circle.

References for Appendix

- (1) Zhang, S. S., Xu, K., & Jow, T. R. (2006). EIS study on the formation of solid electrolyte interface in Li-ion battery. *Electrochimica acta*, 51(8-9), 1636-1640.
- (2) Huang, J., Li, Z., Ge, H., & Zhang, J. (2015). Analytical solution to the impedance of electrode/electrolyte interface in lithium-ion batteries. *Journal of The Electrochemical Society*, 162(13), A7037-A7048.
- (3) Warburg, E. (1899). Ueber das Verhalten sogenannter unpolarisierbarer Elektroden gegen Wechselstrom. *Annalen der Physik*, 303(3), 493-499.
- (4) Tasaki, K., Goldberg, A., Lian, J. J., Walker, M., Timmons, A., & Harris, S. J. (2009). Solubility of lithium salts formed on the lithium-ion battery negative electrode surface in organic solvents. *Journal of The Electrochemical Society*, 156(12), A1019.